Raport sintetic intermediar
(ianuarie 2019-decembrie 2019)

Etapa 1: Teorie si simulare; preparare tinte; crestere straturi epitaxiale feroelectrice; caracterizare structurala si chimica a filmelor epitaxiale; caracterizare electrica a filmelor epitaxiale si a dispozitivelor feroelectrice (ferotronice) associate

Activitati prevazute:
Act. 2.1
Denumire Activitate:
Modelarea proprietatilor electronice si a interfetelor cu electrozii in structuri feroelectrice.

Act. 2.2
Denumire Activitate:
Prepararea si caracterizarea primelor tinte de puritate inalta (nedopate).

Act. 2.3
Denumire Activitate:
Depunerea de filme nedopate, depunerea primelor structuri BFO/BCO.

Act. 2.4
Denumire Activitate:
Caracterizare structurala si chimica avansata a _lmelor/structurilor depuse.

Act. 2.5
Denumire Activitate:
Caracterizare electrica pentru a pune in evidenta legatura dintre defectele intrinseci si proprietatile macroscopice.

Act. 2.6
Denumire Activitate:
Raportare, publicare, prezentari conferinte.

Rezultatele obtinute sunt prezentate, in continuare, mai in detaliu, cu mentiunea ca cele care au fost publicate deja vor fi prezentate in rezumat, cu lucrarea atasata in anexe.
Act. 2.1
Denumire Activitate:
Modelarea proprietatilor electronice si a interfetelor cu electrozii in structuri feroelectrice.
Activitati la INCDFM, echipa coordinator si echipa P1.
Activitatile au constat in:

- Modelarea unei structuri metal-feroelectric-metal (MFM) de tip $SrRuO_3$-$PbTiO_3$-$SrRuO_3$ (SRO-PTO-SRO) folosind metoda DFT si calcule ab-initio. S-a urmarit efectul interfetelor asupra stabilitatii polarizarii spontane feroelectrice. S-a evidentiat faptul ca polarizarea spontana reversibila sub actiunea unui camp electric extern este stabila pentru grosimi ale stratului de PTO mai mari de aproximativ 2 nm (5 constante de retea). Sub aceasta grosime polarizarea dispare pentru ca interfetele induc stari in banda interzisa, care duc la acumulare de sarcina ce destabilizeaza faza feroelectrics. Rezultatele au fost publicate in New Journal of Physics (vezi anexa 1 la raport)
- Calcule teoretice privind dopajul de tip p.

- Studiu experimental si teoretic al blantei intre lucrul de extractie si starea de polarizare in stabilirea inaltimii barierei Schottky la contactul intre Cu si feroelectric. S-a constatat ca inaltimea barierei de potential depinde nu numai de diferenta intre lucrul de extractie in Cu si in feroelectric, ci si de orientarea polarizarii feroelectrice. De asemenea, mecansimul de compensare a campului de depolarizare difera in functie de grosimea stratului de Cu, fiind intrinsec pentru grosimi de pana la 3 nm Cu, cu generare de vacante de oxigen donoare in feroelectric, si extrinsec pentru grosimi mai mari de 3nm Cu, cu compensare pe baza de sarcini electronice din metal. Rezultatele au fost publicate in Applied Surface Science (anexa 2 la raport).

Aditional la cele prezentate mai sus, a fost elaborata o metoda de selectie a valorii corecte a polarizarii in modelarile first principle cuplate cu faza Berry. Rezultatele au fost publicate in Modelling and Simulation in Materials Science and Engineering (anexa 3 la raport).

Act. 2.2
Denumire Activitate:
Prepararea si caracterizarea primelor tinte de puritate inalta (nedopate).

I.1. Memoriu justificativ

Materialele de tip PZT sunt intens studiate datorită excelentelor proprietăţi, dielectrice, feroelectrice şi piezoelectrice, ceea ce le face utilizabile într-o gamă diversă de aplicaţii aparţinând micro-, nano şi opto-electronicii, precum senzori şi actuatori, diverse tipuri de traductori, filtre, etc.

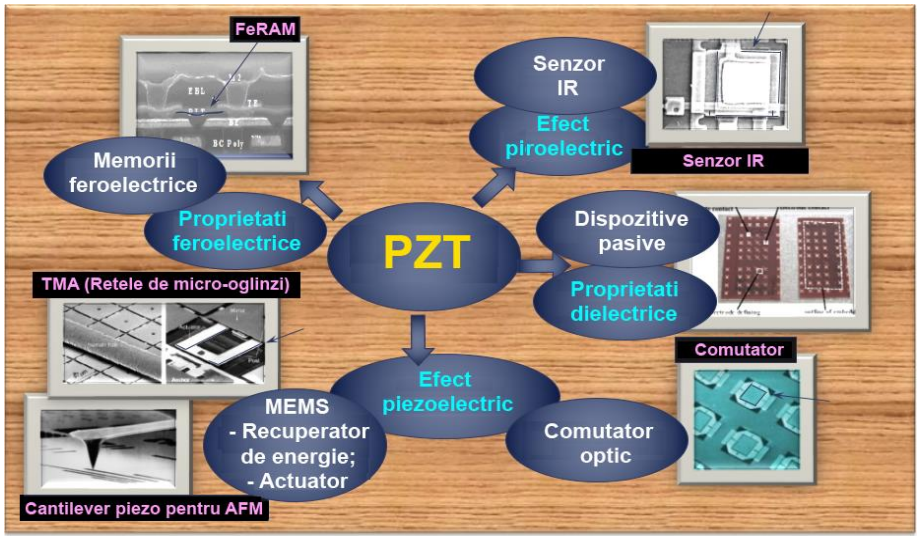

Fig. I.1. Proprietăţi şi aplicaţii ale ceramicilor de tip PZT.

Lucrarea de faţă are în vedere analiza unor compoziţii feroelectrice în sistemul $PbTiO_3$ – $PbZrO_3$, propunându-şi un studiu comparativ al caracteristicilor morfo-structurale ale unor ceramici de tip $PbZr_{1-x}Ti_xO_3$ (PZT) (x = 0,2 – 0,8) obţinute prin sinterizare convenţională şi stabilirea de corelaţii complexe compoziţie - procesare - structură cristalină - microstructură - sinterabilitate.

Principalele obiective ale studiului sunt:

- sinteza unor pulberi de tip PZT prin varianta "acetat" a metodei sol-gel;

- studiul mecanismului de formare al soluţiilor perovskitice de tip PZT din precursorii gelici obţinuţi pe ruta sol-gel;
- elaborarea prin sinterizare convenţională a unor ceramici PZT derivate din pulberile sintetizate;
- caracterizarea compoziţională, structurală şi microstructurală a materialelor obţinute.

I.2. Alegerea compoziţiilor şi procedură experimentală

I.2.1. Alegerea compoziţiilor

Compoziţiile selectate în vederea cercetării sunt soluţii solide ce aparţin sistemului pseudo-binar $PbZrO_3$ – $PbTiO_3$ din cadrul sistemului ternar PbO – ZrO_2 – TiO_2. Plasarea compoziţiilor analizate în sistemul ternar menţionat este prezentată în Fig. I.2.

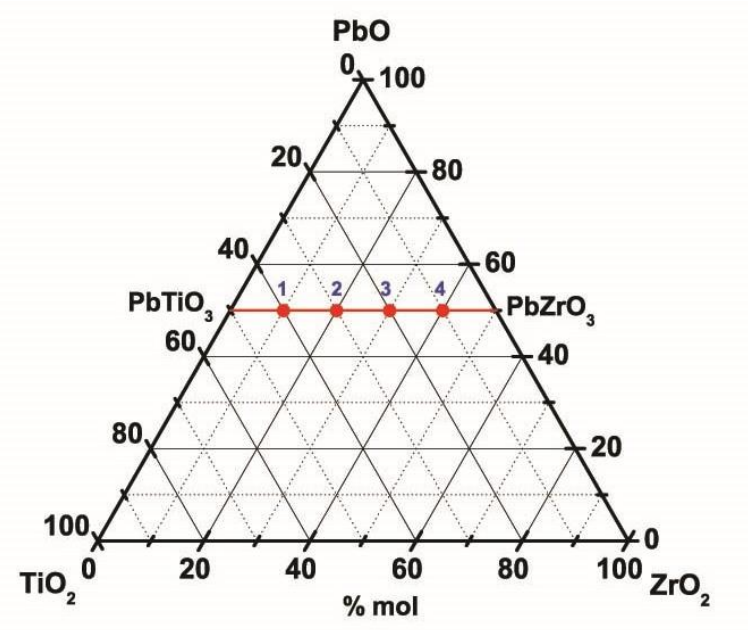

Fig. I.1. Plasarea compoziţiilor selectate şi analizate în sistemul ternar PbO – ZrO_2 – TiO_2.

I.2.2. Procedura experimentală

I.2.2.1. Prepararea pulberilor şi a ceramicilor aferente de PZT

Pulberile de zirconat titanat de plumb $PbZr_{1-x}Ti_xO_3$ (x = 0,8; 0,6; 0,4 şi 0,2) au fost preparate folosind ruta "acetat" a metodei sol-gel, pornind de la: acetat de plumb ($Pb(CH_3CO_2)_2 \cdot 3H_2O$, puritate ACS >99,99%, Sigma-Aldrich), izopropoxid de titan ($Ti(OC_3H_7)_4$, soluţie 97% în 2-propanol, Sigma-Aldrich), propoxid de Zr ($Zr(OCH_2CH_2CH_3)_4$, solutie 70 wt. % in 1-propanol, Sigma-Aldrich), acid acetic (CH_3CO_2H, 99%, Sigma-Aldrich), izopropanol ($(CH_3)_2CHOH$, 99,5%, Aldrich) şi acetilacetonă ($CH_3COCH_2COCH_3$, >99%, Aldrich). Acetatul de plumb a fost solubilizat în apă distilată şi acid acetic, obţinându-se o soluţie de concentraţie 1M.

Separat, se prepară o soluţie de propoxid de Zr şi izopropoxid de Ti care se solubilizează în 2-propanol la 100°C sub agitare magnetică timp de 30 minute. Se adaugă acetilacetona, ca stabilizator, atât in solutia de acetat de Pb, cât şi în soluţia mixtă de propoxid de Zr şi izopropoxid de Ti. Soluţia de acetat de Pb se adaugă peste soluţia mixtă de (Zr+Ti), constatându-se o modificare a culorii soluţiei iniţiale care devine tot mai limpede pe măsură ce se adaugă acetatul de plumb. Astfel, se obţine o soluţie clară, de culoare galbenă, care se încălzeşte pe plită, sub agitare magnetică la 80°C timp de 2 ore, până când aceasta se transformă în gel. Gelul galben-maroniu obţinut se supune unui tratament termic la 100°C timp de 6 ore până când acesta se transformă în pulbere precursoare. Tratament termic final în vederea obţinerii pulberilor oxidice de tip PZT s-a realizat în aer, la temperaturile de 700, respectiv 800°C, timp de 2 ore, cu viteza de încălzire de 5°C/min.

Din pulberile oxidice obţinute au fost elaborate ceramici, prin sinterizare convenţională. În acest scop, pulberile oxidice de PZT au fost introduse într-o matriţă de oţel, cu diametrul de 13 mm şi presate uniaxial, la o presiune de 160 MPa, cu ajutorul unei prese manuale. Pastilele crude rezultate au fost supuse tratamentului termic de sinterizare. În vederea analizării efectului temperaturii de ardere asupra caracteristicilor ceramicilor rezultate, sinterizarea convenţională s-a realizat într-un cuptor electric de tip cameră, în aer, la trei temperaturi diferite, şi anume, 1000, 1100 şi 1200°C, cu palier de menţinere la temperatura maximă de 2 ore, pentru toate cele 3 temperaturi menţionate. De asemenea, pentru a evalua şi influenţa duratei de palier asura sinterabiltăţii şi microstructurii corpurilor ceramice, pentru probele sinterizate la temperatura de 1000°C s-a aplicat şi un palier de 4 ore. Viteza de încălzire a fost de 10°C/min, iar răcirea a fost lentă, la viteza normală de răcire a cuptorului. Este de menţionat faptul că, în vederea conservării stoechiometriei nominale, pastilele crude au fost acoperite cu pulbere PZT şi introduse in creuzete cu capac, pentru ca în timpul sinterizării să se creeze o atmosferă saturată în vapori de Pb, evitatându-se astfel migrarea ionilor de Pb din reţea în atmosfera de ardere.

I.2.2.2. Caracterizarea precursorilor gelici, a pulberilor oxidice şi a ceramicilor de PZT

În vederea evaluării gradului de cristalinitate a precursorilor, precum şi a compoziţiei fazale (purităţii fazei perovskitice) în pulberile oxidice finale şi în ceramcile de PZT au fost efectuate măsurători difractometrice cu ajutorul unui difractometru *SHIMADZU XRD 6000*, utilizând radiaţie CuK□ (□□= 1.5418 Å) şi filtru de Ni. Analizele au fost efectuate, în intervalul de ubghiuri de difracţie 2□ = 20 – 80°, cu incresemnt al pasului de scanare de 0.02° şi timp de numărare de 10 sec./pas. Pentru determinarea factorilor structurali (parametrii de reţea, volumul celulei elementare, dimensiunea de cristalit şi microtensiunile interne) a fost utilizat formalismul Rietveld.

Mecanismul de formare al soluţiilor solide perovskitice de tip PZT din precursorii gelici a fost monitorizat prin metode de analiză termică (calorimetrie diferenţială şi termogravimetrie) cuplate cu spectroscopie FTIR *in situ* a gazelor degajate în funcţie de temperatură. Analiza termică s-a realizat cu ajutorul unui echipament STA Netzsch Jupiter F3, conectat cu un spectrometru FTIR Bruker Tensor 27, în atmosferă statică de aer, cu viteza de 10 K/min, în intervalul de temperatură 20 – 900°C. Spectrele FTIR au fost colectate pentru domeniul de frecvenţă 400 – 4500 cm^{-1}. Întrucat spectrele FTIR se înregistrează în mod continuu, se obţin suprafaţe 3D care pot fi secţionate la orice temperatură pentru a vedea cum arată spectrul gazelor emise în acel moment.

Morfologia pulberilor şi ceramicilor de PZT, precum şi dimesniunea medie de particulă/ granulă au fost determinate prin tehnici de microscopie electronică (FE-SEM, TEM, HR-TEM), cu ajutorul unui microscop electronic de baleiaj *FEI QUANTA INSPECT F*, cuplat cu spectroscopie de energie dispersivă a razelor X (EDX), în vederea verificării compoziţiei chimice elementale (cantitativă şi calitiativă), precum şi prin intermediul unui microscop electronic de transmisie *TecnaiTM G2 F30 S-TWIN*, cuplat cu analiză de difracţie de electroni pe arie selecţionată (SAED) pentru evaluarea gradului de cristalinitate.

Pe probele rezultate în urma sinterizării prin cele două tehnici, în diferite condiţii, s-au determinat: proprietăţile ceramice: densitatea aparentă (prin metoda hidrostatică (Archimedică)) şi porozitatea aparentă (deschisă). Aceste caracteristici au permis estimarea aptitudinii la sinterizare (sinterabilitatea) corespunzătoare compoziţiilor considerate.

Schema de preparare şi caracterizare a materialelor de tip PZT este prezentată în Fig. I.3.

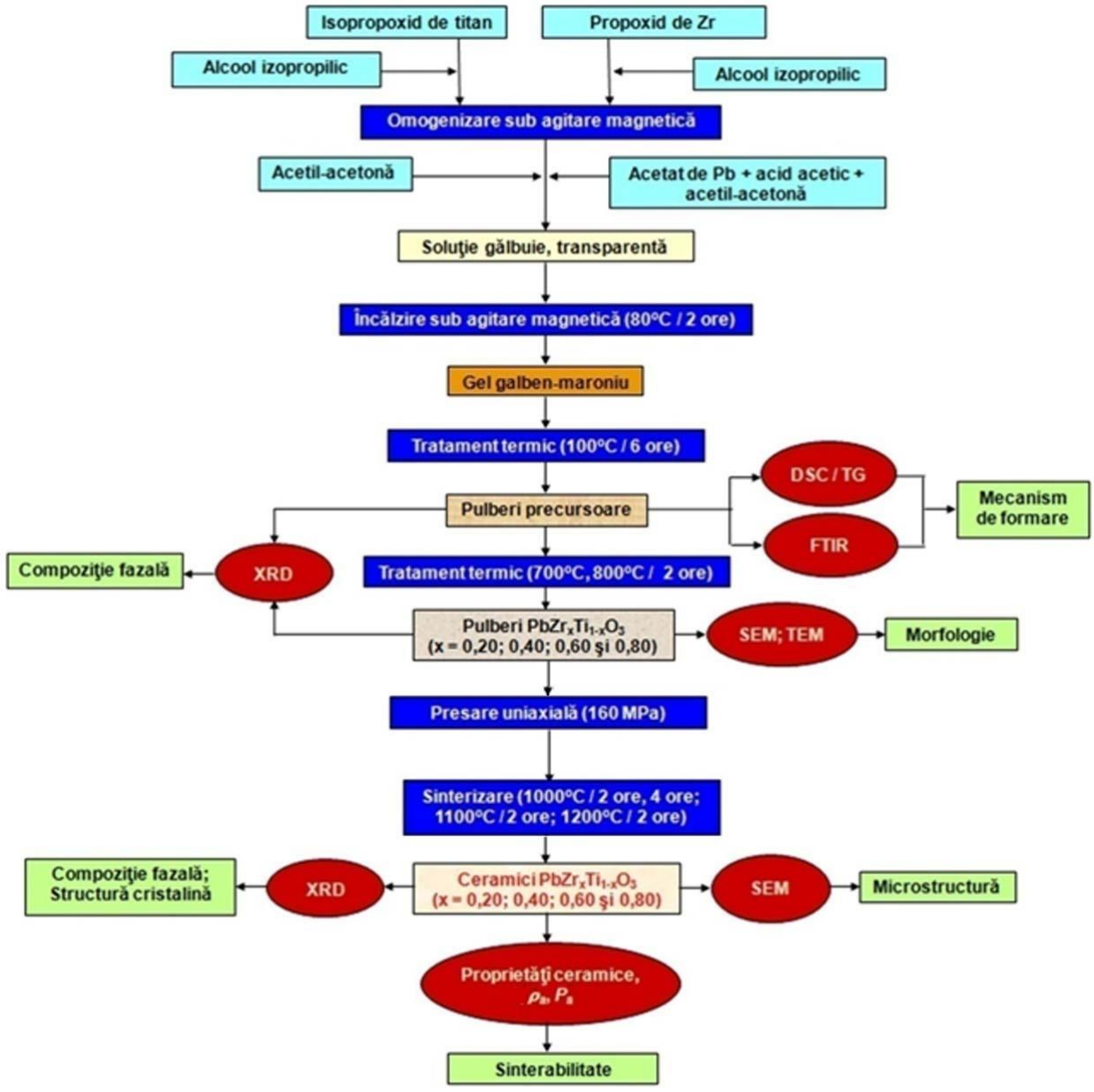

Fig. I.2. Schema de preparare şi caracterizare a precursorilor, pulberilor şi ceramicilor de PZT.

I.3. Caracterizarea precursorilor gelici

Pulberile precursoare obţinute în urma sintezei sol-gel au culoare diferită, şi anume, gălbuie în cazul compoziţiei 1, cu proporţie maximă de titan (x = 0,8), alb-cenuşiu în cazul compoziţiilor 2 şi 3 (x = 0,6 şi 0,4) şi gălbui deschis, în cazul compoziţiei 4 cu proporţie maximă de Zr (Fig. I.4).

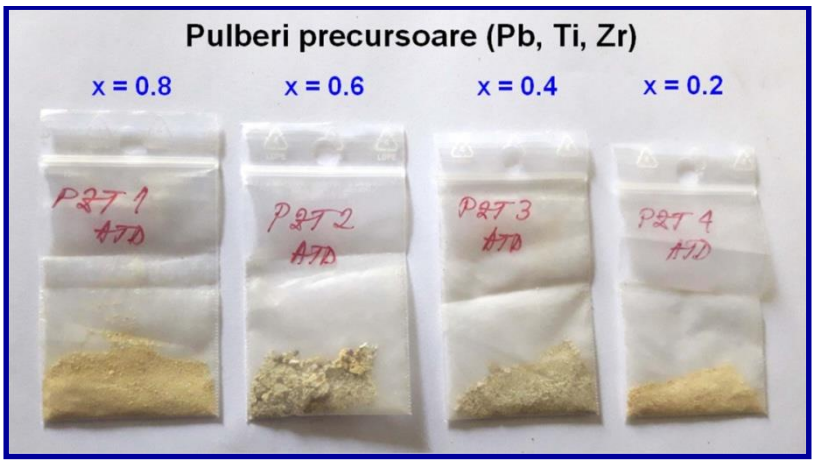

Fig. I.4. Pulberile precursoare de (Pb, Zr, Ti) rezultate în urma sintezei sol-gel pe ruta "acetat".

I.3.1. Compoziţia fazală a precursorilor

Difracţia de raze X efectuată pe precursori evidenţiază prezenţa fazelor perovskitice bine cristalizate de tip PZT, decelate după răcirea la 100°C timp de 6 ore a pulberilor rezultate în urma sintezei sol-gel (Fig. I.5).

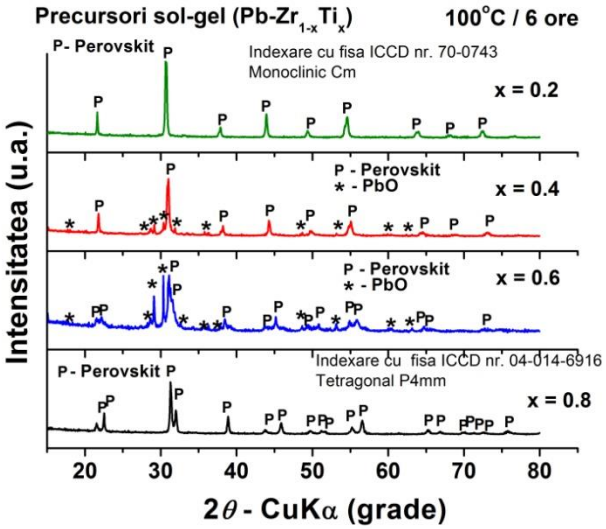

Fig. I.5. Difractogramele înregistrate la temperatura camerei, corespunzătoare pulberilor precursoare

de (Pb, Zr, Ti).

Compoziţiile cu concentraţie maximă de Ti, respectiv de Zr (PZT1 şi PZT4) sunt monofazice, în timp ce, în precursorii de compoziţie PZT2 şi PZT3 cu x = 0,6 şi respectiv x = 0,4, se identifică PbO ca fază secundară. Toate probele menţionate conţin şi o oarecare proporţie de fază amorfă, fapt demonstrat de fondul mai înalt al difractogramelor (Fig. I.5).

I.3.2. Comportarea termică a precursorilor şi mecanismul de formare al fazelor perovskitice

A fost analizată comportarea termică a precursorilor cu proporţie maximă de Zr, şi respectiv cu proporţie maximă de Ti (compoziţiile 1 şi 4). Probele au o comportare termică destul de diferită. În cazul precursorlui 1, reziduul obţinut în urma analizei termice este galben mai închis, în timp ce în cazul precursorului 4, reziduul este galben mai deschis.

Pulberea precursoare 1, cu proporţie maximă de Ti, prezintă o uşoară pierdere de masă până la temperatura de 267°C (0,71% până la 180°C şi 0,51% între 180 – 267°C (Fig. I.6). Efectul termic care însoţeşte această pierdere de masă este endoterm, cu minim la 132,6°C. Cel mai probabil procesul poate fi atribuit eliminării unor molecule de solvent şi grupări -OH ramase pe suprafaţa particulelor. Între 267 – 400°C are loc principala pierdere de masa de 1,97%, însoţită de două efecte slab exoterme cu maxime la 306 si 366°C. Cel mai probabil acestea pot fi atribuite unor resturi de compuşi organici (grupări acetat, agent complexant adaugat în cursul sintezei). Fiind vorba de efecte exoterme acestea por fi atribuite combustiei (arderii) acestor resturi organice. După această combustie, în intervalul 400 – 540°C are loc arderea resturilor carbonice (în general substanţele organice lasă in urma arderii un reziduu carbonic, care apoi este oxidat la CO_2), simultan cu creşterea cristalinităţii structurii perovskitice corespunzătoare soluţiei solide $PbZr_{0,2}Ti_{0,8}O_3$. Şi în acest interval, pe curba DSC există două efecte exoterme slabe, cu maxime la 442 şi 495°C. Pe diagrama 3D FTIR se observă exact că cele patru maxime exoterme corespund unor maxime ale concentraţiei de CO_2 (Fig. I.7).

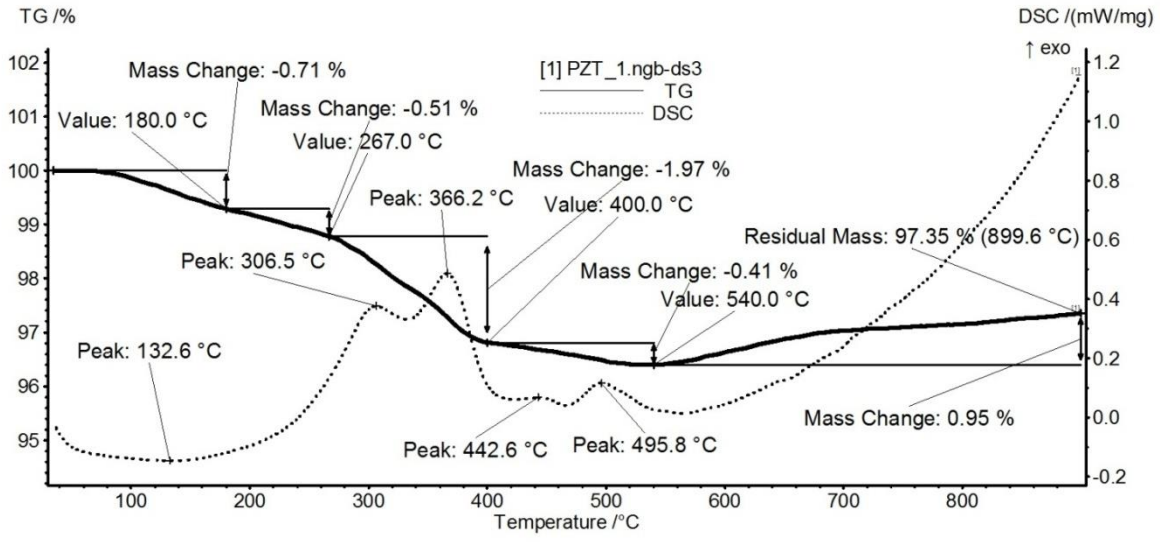

Fig. I.6. Curbele de analiză termică corespunzătoare precursorului 1,

cu concentraţie maximă de titan.

În ultima etapă, 540 – 900°C are loc o creştere de masă de 0,95%. Aceasta poate fi atribuită unui proces de reoxidare a unor ioni Ti^{3+} rezultaţi ca urmare a unui proces de reducere parţială a ionilor Ti^{4+} într-o etapă anterioară a tratamentului termic, ca o consecinţă a contactului cu masa carbonică (Fig. I.6). Cu toate acestea, din cauza faptului că acest proces de reoxidare se produce lent, într-un inverval larg se temperatură, efectul termic exoterm aferent pe curba DSC este foarte aplatizat şi se lasă doar ghicit, acesta fiind ecranat şi de evoluiţia crescătoare a curbei DSC la temperaturi mai mari de 600°C, din cauza modificării capacităţii calorice a probei (Fig. I.6).

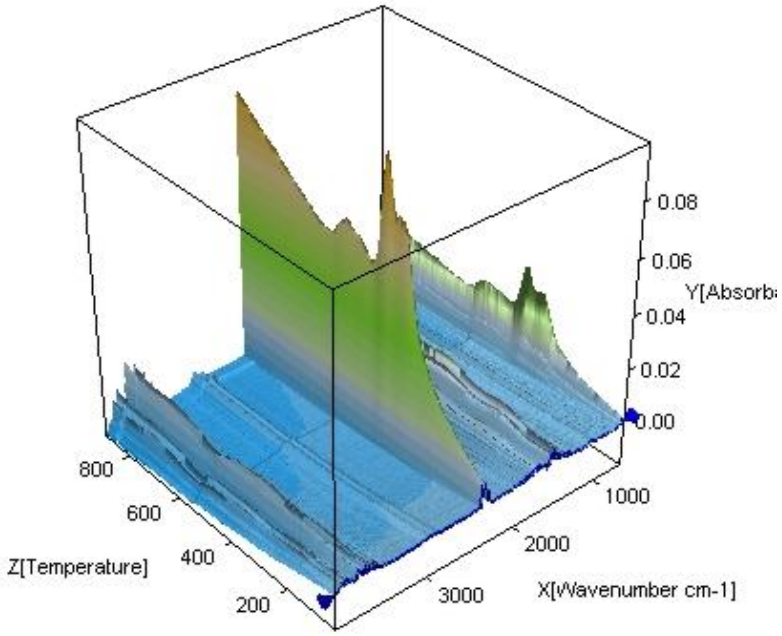

Fig. I.7. Spectre FTIR *in situ*, corespunzătoare gazelor emise în timpul descompunerii precursorului 1.

În ceea ce priveşte pulberea precursoare 4, cu concentraţie maximă de Zr, aceasta prezintă o uşoară pierdere de masă până la 237°C (2,03% până la 184°C şi 0,61% între 184 – 237°C. Efectul termic care însoţeşte această pierdere de masă este endoterm, cu minim la 79,5°C. Cel mai probabil procesul reprezintă, ca şi în cazul probei 1, eliminarea unor molecule de solvent şi grupări -OH adsorbite pe suprafaţa particulelor (Fig. I.8).

Între 237 – 448°C are loc principala pierdere de masă ce se produce, de asemenea în două trepte (2,96% până la 337°C şi 3,34% în intervalul 337 – 448°C, ţinând seama de faptul că există un punct de inflexiune, care indică etape distincte de oxidare). Pierderea de masă este însoţită de două efecte slab exoterme, cu maxime la 257 şi 297°C, care pot fi atribuite oxidării unor resturi de compuşi organici. În intervalul 448 – 587°C are loc arderea resturilor carbonice. Şi în acest caz, pe curba DSC se semnalează

prezenţa a două efecte exoterme, mult mai intense, parţial suprapuse, cu maxime la 500 şi 546°C. Aceste procese decurg simultan cu desăvârşirea edificiului cristalin al fazei perovskitice corespunzătoare soluţiei solide $PbZr_{0,8}Ti_{0,2}O_3$. În intervalul 587 – 668°C există o uşoară creştere de masă, de 0,21%, datorată oxidării ionilor de titan care au fost reduşi în prezenţa C/CO în etapa anterioară. Procesul este insotit de un mic efect exoterm cu maxim la 662°C. Între 668 – 900°C are loc ultimul proces exoterm de descompunere osidativă, pierderea de masă fiind de 1,05% (Fig. I.8).

Şi în cazul precursorului 4, pe diagrama 3D FTIR se observă prezenţa celor patru maxime exoterme corespunzătoare unor maxime ale concentraţiei de CO_2 (Fig. I.9).

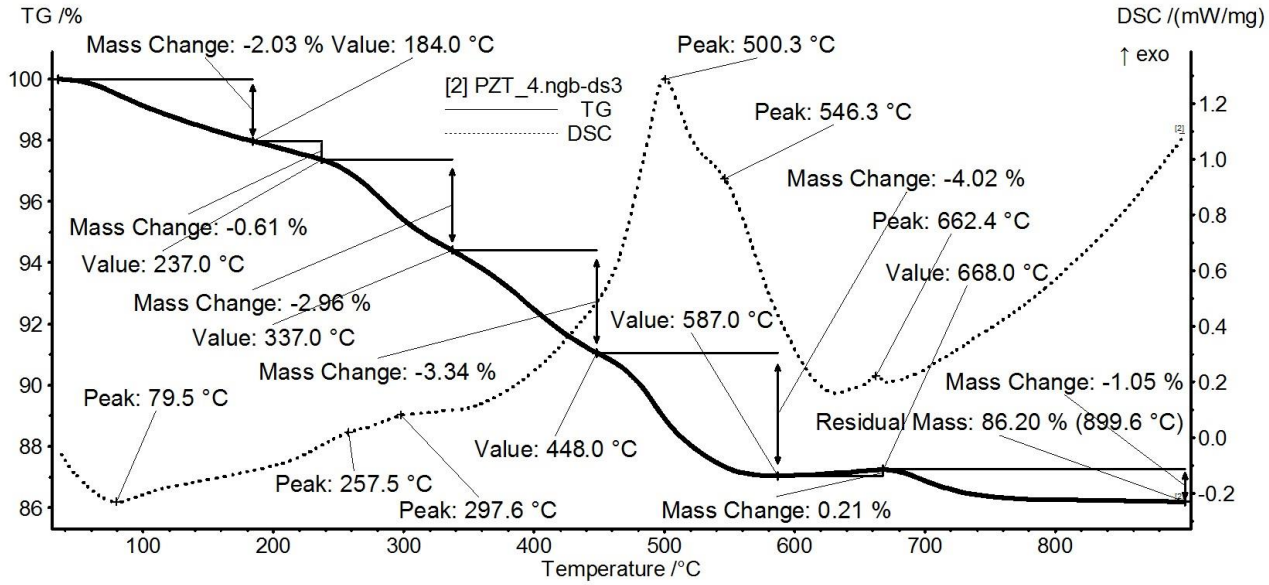

Fig. I.8. Curbele de analiză termică corespunzătoare precursorului 4,

cu concentraţie maximă de zirconiu.

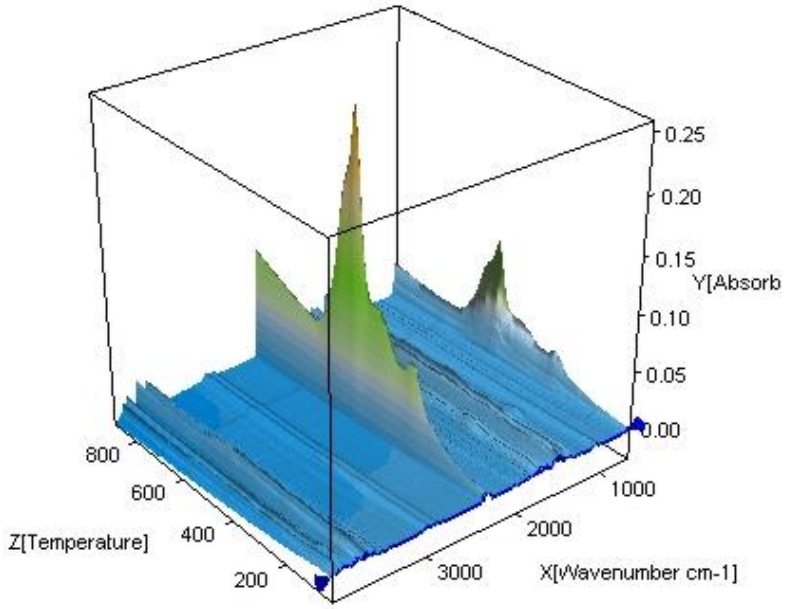

Fig. I.9. Spectre FTIR *insitu*, corespunzătoare gazelor emise în timpul descompunerii precursorului 4.

Studiul comparativ al comportării termice corespunzătoare precursorilor cu concentraţie maximă de titan, respectiv zirconiu, indică faptul că o creştere a concentraţiei de Zr implică o pierdere mai importantă de masă şi o deplasare a proceselor exoterme principale de combustie către temperaturi mai ridicate, datorită refractarităţii mai ridicate a $PbZrO_3$ (T_{topire} = 1570ºC), cu pondere majorotară în compoziţia 4 ($PbZr_{0,8}Ti_{0,2}O_3$), faţă de $PbTiO_3$ (T_{topire} = 1281ºC), cu pondere majoritară în compoziţia 1 ($PbZr_{0,2}Ti_{0,8}O_3$) (Fig. I.10).

În ambele cazuri, pierderea de masă destul de redusă, indică faptul că scheletul perovskitic al soluţiilor solide de tip PZT era deja bine format încă de la faza de precursori, aşa cum a dovedit şi analiza difractometrică. Pierderea de masă de ~ 14%, mai mare în cazul precursorului 4 cu concentraţie maximă de Zr sugerează faptul că porporţia de fază amorfă a fost mai ridicată în această probă, faţă de pulberea precursoare 1, cu concentraţie maximă de Ti, care a înregistrat o pierdere de masă de doar ~ 3%.

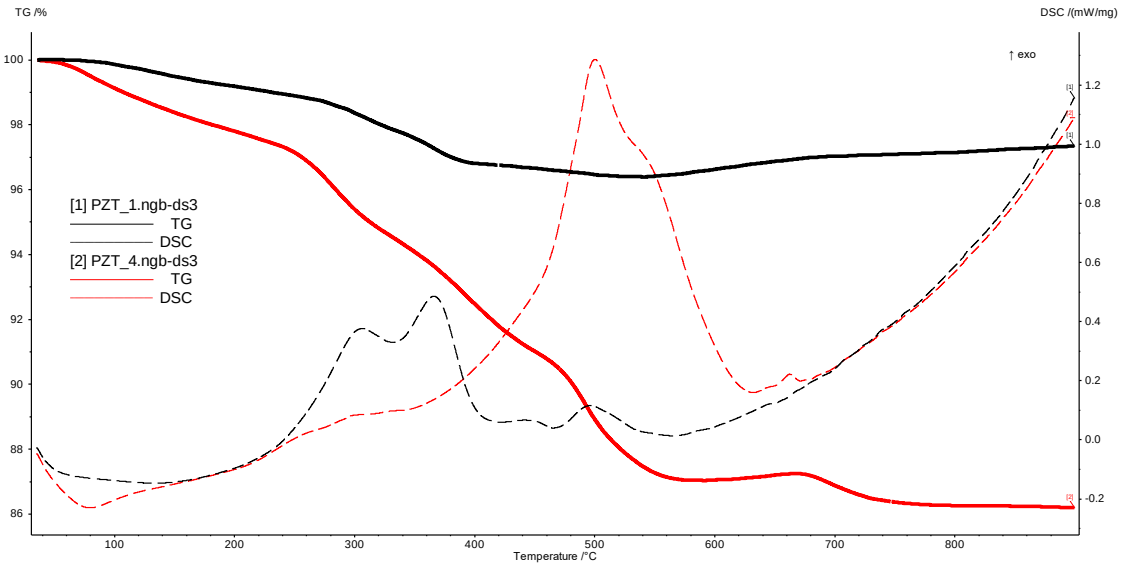

Fig. I.10. Prezentarea comparativă a curbelor de analiză termică pentru precursorii cu compoziţia 1, şi respectiv, cu compoziţia 4.

De asemenea, este de remarcat faptul că procesul de reoxidare a ionilor Ti^{3+} la Ti^{4+} este mult mai evident pe curba TG a precursorului 1 decât pe cea corespunzătoare precursorului 4, datorită conţinutului mult mai ridicat de Ti din precursorul 1 (x = 0.8) faţă de precursorul 4 (x = 0,2).

I.4. Caracterizarea pulberilor de tip $Pb(Zr,Ti)O_3$ (PZT)

I.4.1. Compoziţia fazală a pulberilor sol-gel de PZT

Din punct de vedere al compoziţiei fazale se constată că, indiferent de temperatura de tratament termic utilizată (700, respectiv 800ºC), ceramicile PZT obţinute sunt monofazice. Astfel, difractogramele din Fig. I.11 şi I.12 evidenţiază prezenţa principalelor maxime de difracţie corespunzătoare soluţiilor solide perovskitice de tip PZT cu structura tetragonală (grup spaţial P4mm), pentru compoziţiile cu proporţie mai redusă de zirconiu, $PbZr_{0,2}Ti_{0,8}O_3$ şi $PbZr_{0,4}Ti_{0,6}O_3$ (Fig. I.11(a), (b) şi Fig. I.12(a), (b)), cu structură romboedrică (grup spaţial R3m) pentru compoziţia $PbZr_{0,6}Ti_{0,4}O_3$ (Fig. I.11(c) şi Fig. I.12(c)) şi, respectiv, cu structură monoclinică (grup spaţial Cm) pentru compoziţia cu conţinutul cel mai ridicat de zirconiu (Fig. I.11(d), Fig. I.12(d)).

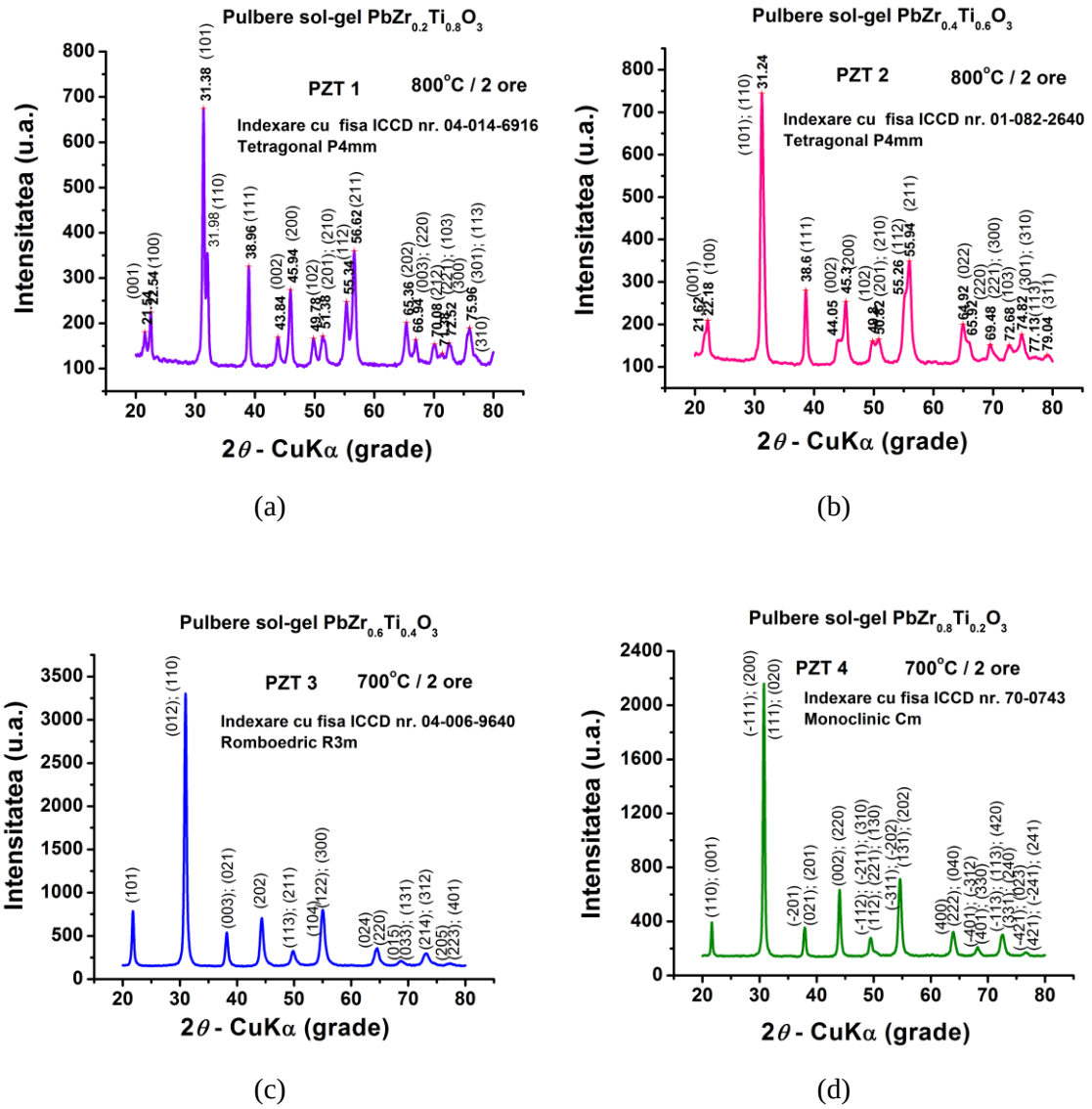

Fig. I.11. (a) Difractogramele înregistrate la temperatura camerei, corespunzătoare pulberilor de tip $PbZr_{1-x}Ti_xO_3$ (PZT) obţinute pe ruta "acetat" a metodei sol-gel şi procesate termic la 800°C timp de 2 ore: (a) x = 0,8; (b) x = 0,6; (c) x = 0,4 şi (d) x = 0,2.

I.1.3. Caracteristici morfologice ale pulberilor sol-gel de PZT

Pulberea de compoziţie $PbZr_{1-x}Ti_xO_3$ cu conţinut maxim de titan (x = 0,8) este alcătuită din formaţiuni poliedrale, neregulate din punct de vedere al formei, cu dimensiuni de ordinul 200 - 300 nm, aşa cum evidenţiază imaginea TEM de mărire mai mică din Fig. I.12(a). Imaginea TEM de mărire mai mare din Fig. I.12(b) indică faptul că, aceste formaţiuni nu sunt particule individuale, ci conglomerate de particule primare, mici, poliedrale, omogene din punct de vedere dimensional şi morfologic, cu dimensiuni de 13 - 25 nm. Aceeaşi morfologie duplex este prezentată şi de pulberile de PZT cu conţinut mai ridicat de Zr (x = 0,6 şi x = 0,4) (Fig. I.13(a) şi Fig. I.14(a)). Tendinţa de aglomerare creşte cu creşterea concentraţiei de Zr în soluţia solidă perovskitică de tip PZT, astfel că, pentru pulberile de compoziţie $PbZr_{0,6}Ti_{0,4}O_3$ şi $PbZr_{0,8}Ti_{0,2}O_3$, cu proporţiile cele mai mari de Zr, se constată apariţia unor blocuri dense, parţial sinterizate, de dimensiuni la scară micronică (2 - 6 □m), alcătuite din granule poliedrale foarte bine sudate între ele, cu

dimensiuni de de 350 - 550 nm (Fig. I.14(b) şi Fig. I.15(a)). Şi în aceaste pulberi, se observă, de asemenea, prezenţa unor particule primare izolate, cu dimensiuni ce se menţin la scară nanometrică (~ 22 - 45 nm), dar uşor mai mari în comparaţie cu dimensiunea particulelor primare din pulberile PZT cu concentraţie mai redusă de Zr (Fig. I.15(b)).

Toate pulberile de tip PZT analizate sunt constituite din particule bine cristalizate. Gradul ridicat de cristalinitate este relevat atât de imaginea de microecopie de transmisie de înaltă rezoluţie (HRTEM) din Fig I.13(c), care evidenţiază prezenţa franjelor ordonate la lungă distanţă, precum şi de imaginile de difracţie de electroni pe arie selecţionată (SAED) din Fig. I.12(c), I.13(c), I.14(c) şi I.15(c)), care indică spoturi luminoase ce formează inele concentrice, specifice diverselor plane cristaline ale particulelor de PZT cu diferite orientări.

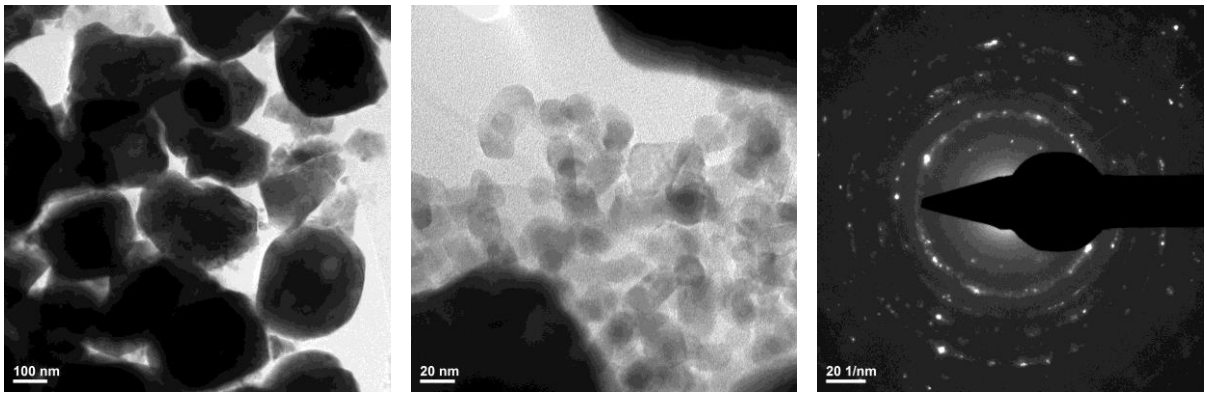

(a) (b) (c)

Fig. I.12. (a), (b) Imagini TEM la diverse măriri pentru pulberea de $PbZr_{0,2}Ti_{0,8}O_3$ preparată prin metoda sol-gel şi tratată termic la 800ºC timp de 2 ore; (c) imagine de difracţie de electroni pe arie selecţionaţă (SAED).

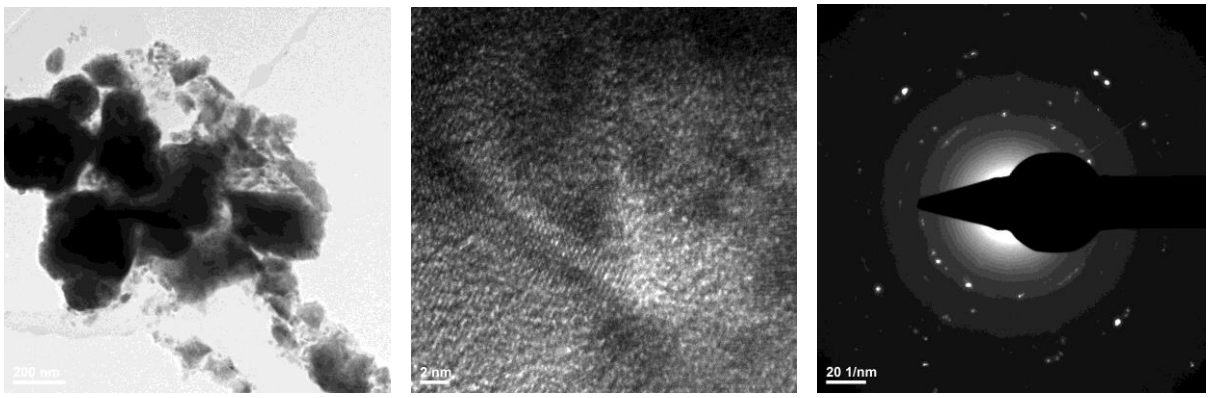

(a) (b) (c)

Fig. I.13. (a), (b) Imagine TEM şi, respectiv HRTEM pentru pulberea de $PbZr_{0,4}Ti_{0,6}O_3$ preparată prin metoda sol-gel şi tratată termic la 800ºC timp de 2 ore; (c) imagine de difracţie de electroni pe arie selecţionaţă (SAED).

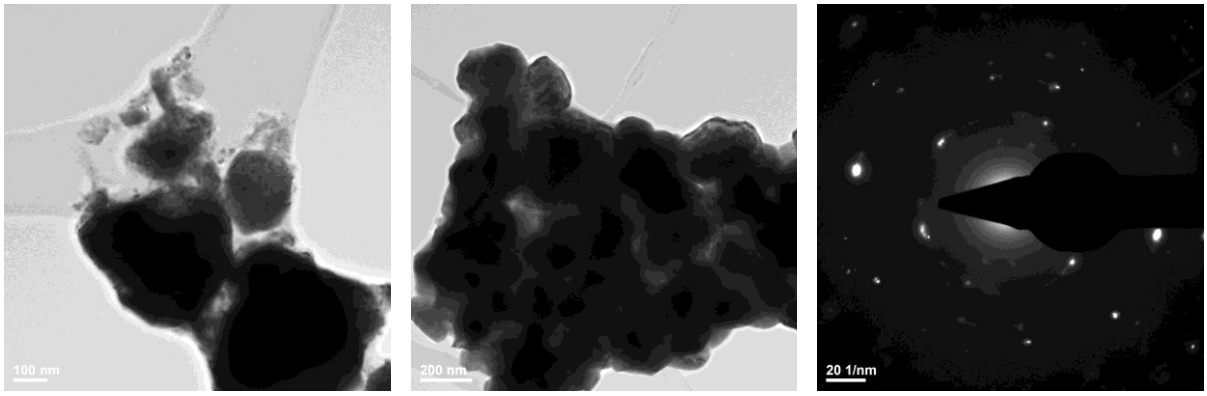

(a) (b) (c)

Fig. I.14. (a), (b) Imagini TEM la diverse măriri pentru pulberea de $PbZr_{0,6}Ti_{0,4}O_3$ preparată prin metoda sol-gel şi tratată termic la 800°C timp de 2 ore; (c) imagine de difracţie de electroni pe arie selecţionaţă (SAED).

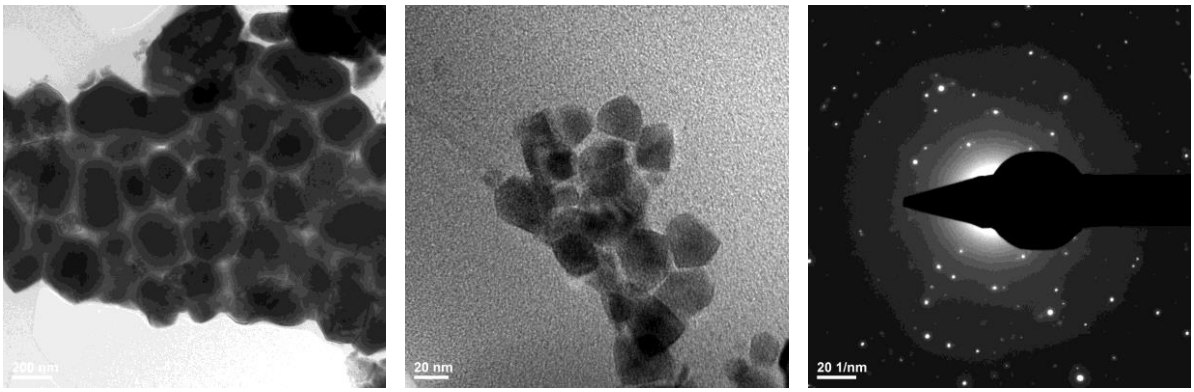

(a) (b) (c)

Fig. I.15. (a), (b) Imagini TEM la diverse măriri pentru pulberea de $PbZr_{0,8}Ti_{0,2}O_3$ preparată prin metoda sol-gel şi tratată termic la 800°C timp de 2 ore; (c) imagine de difracţie de electroni pe arie selecţionaţă (SAED).

I.5. Caracterizarea ceramicilor de tip $Pb(Zr,Ti)O_3$ (PZT)

I.5.1. Caracteristicile ceramicilor de PZT obţinute prin sinterizare convenţională

Din pulberile oxidice obţinunte au fost elaborate corpuri ceramice prin sinterizare convenţională în diferite condiţii de temperatură şi palier (1000°C / 2 ore, 1000°C / 4 ore, 1100°C / 2 ore şi 1200°C / 2 ore), urmărindu-se efectul temperaturii de tratament termic şi al duratei de palier asupra compoziţiei fazale, gradului de cristalinitate şi microstructurii ceramicilor obţinute. Ceramicile obţinute prin sinterizare convenţională sunt prezentate în Fig. I.16.

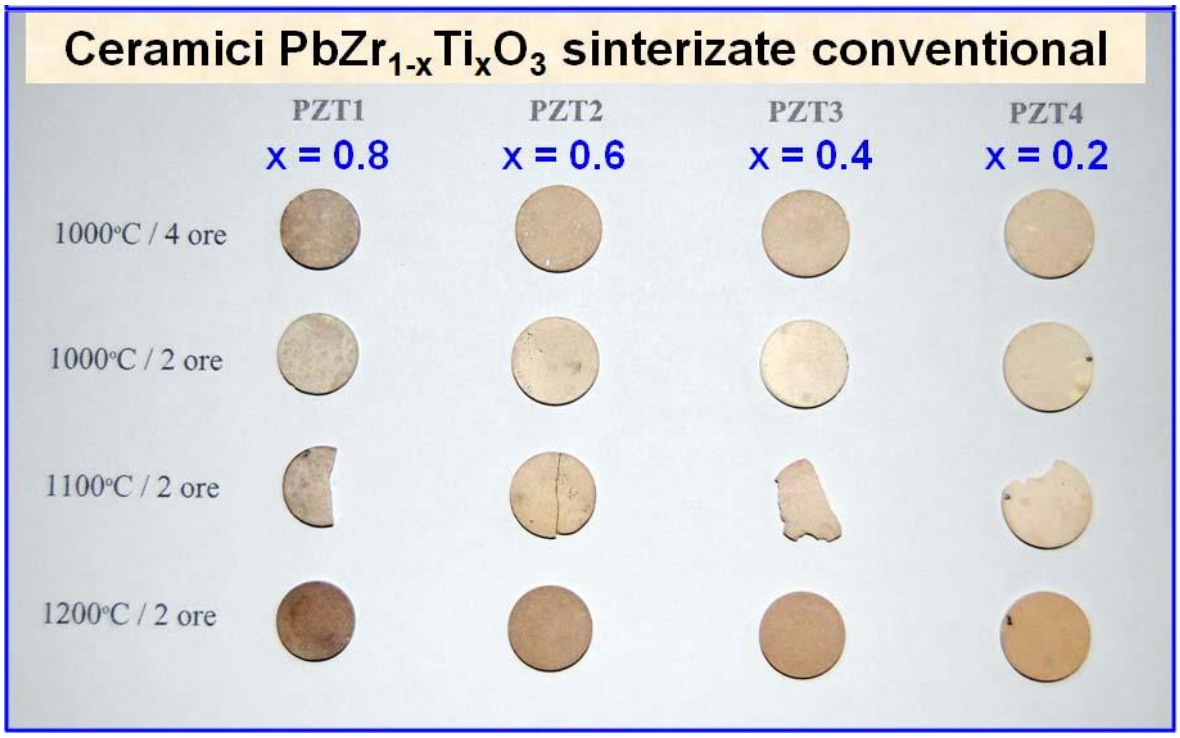

Fig. I.16. Ceramicile de tip PZT obţinute în urma sinterizării convenţionale, în diferite condiţii de temperatură şi palier de ardere.

Din punct de vedere al culorii, se constată faptul că, ceramicile obţinute prezintă o nuanţă ce variază de la gălbui la cenuşiu, pe măsură ce proporţia de titan creşte în detrimentul celei de zirconiu în soluţiile solide de PZT tratate termic în intervalul 1000 - 1100°C. De asemenea, indiferent de compoziţie, creşterea duratei de palier, şi, mai ales, a temperaturii de sinterizare duce la obţinerea unor ceramici de nuanţă mai închisă. Astfel, pentru ceramicile sinterizate la 1200°C timp de 2 ore, culoarea variază de la ocru închis, pentru proba cea mai bogată în Zr (x = 0,2), la brun-cenuşium pentru proba mai bogată în Ti (x = 0,8) (Fig. I. 16).

I.5.1.1. Compoziţia fazală

Toate ceramicile obţinute prin sinterizare convenţională sunt monofazice, constând din fazele perovskitice de tip PZT, cu structură ce variază (ca şi în cazul pulberilor oxidice din care provin) de la simetria tetragonală a celulei elementare specifică $PbTiO_3$, în cazul compoziţiilor 1 şi 2 bogate în titan, către simetria romboedrică şi, respectiv, monoclinică, pentru compoziţiile 3 şi 4, bogate în zirconiu (Fig. I.17(a)-(d)).

Se constată că atât creşterea temperaturii de tratament termic, cât şi a duratei de palier contribuie la desăvârşirea edificiului cristalin (creşterea gradului de cristalinitate) al soluţiilor solide perovskitice de tip PZT (Fig. I.17(a)-(d)).

În cazul reprezentării comparative a difractogramelor probelor de compoziţie diferită (cu raport Zr/Ti diferit), se observă că, odată cu integrarea izomorfă a Zr (creşterea concentraţiei de Zr) în structura perovskitică, indiferent de simetria celulei elementare, picurile de difracţie caracteristice sunt deplasate către unghiuri de difracţie 2 din ce în ce mai mici, aşa cum este reprezentat cazul ceramicilor sinterizate la 1200°C, timp de 2 ore (Fig. I.18(a), (b)).

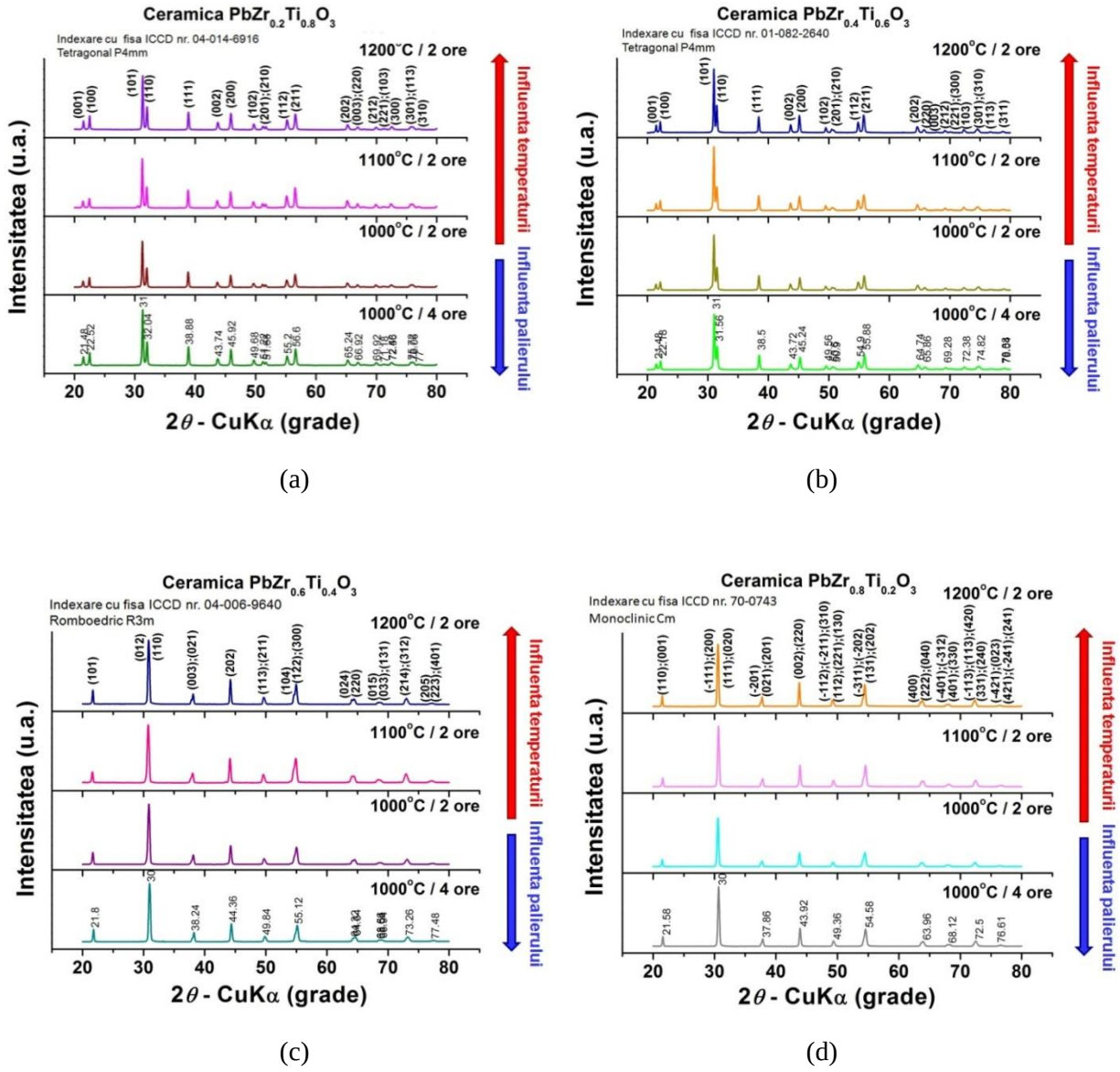

Fig. I.17. Difractogramele înregistrate la temperatura camerei, corespunzătoare ceramicilor de tip $PbZr_{1-x}Ti_xO_3$ sinterizate convenţional în diferite condiţii: (a) x = 0,8; (b) x = 0,6, (c) x = 0,4 şi (d) x = 0,2.

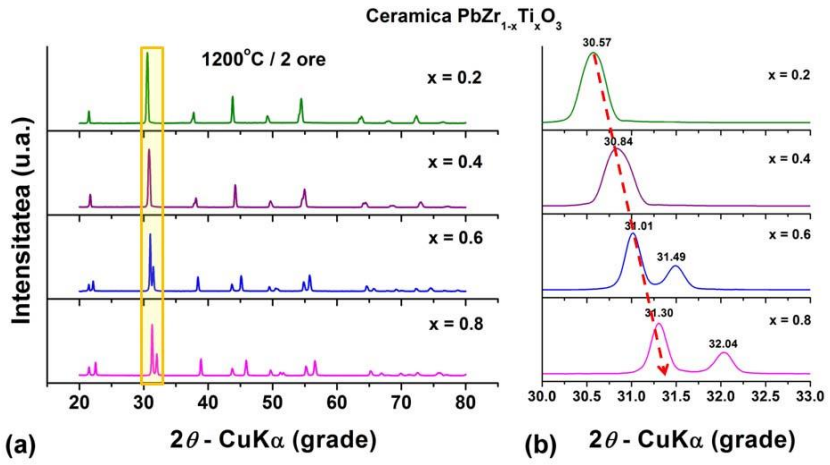

Fig. I.18. (a) Difractogramele ceramicilor de PZT rezultate în urma sinterizării convenţionale la temperatura de 1200ºC timp de 2 ore şi (b) detaliu al domeniului de unghiuri de difracţie 2 = 30 – 33º (dreptunghiul galben din Fig. I.18(a)) care indică evoluţia maximului de difracţie de 100% în funcţie de proporţia de Zr din structura ceramicilor PZT.

I.5.2. Microstructura

Ceramica de compoziţie $PbZr_{0,2}Ti_{0,8}O_3$ rezultată în urma sinterizării la 1000ºC, timp de 2 ore prezintă o microstructură destul de densă, uniformă, alcătuită din granule poliedrale cu limite granulare continue, bine definite şi cu îmbinări aproape perfecte la punctele de joncţiune triplă, ceea ce indică un grad avansat de sinterizare. Distribuţia granulometrică este monomodală, mai largă , grăunţii cristalini prezentând dimensiuni între 1 - 6 m (Fig. I.19(a)). Creşterea conţinutului de Zr de la x = 0,2 la x = 0,4 conduce la o rafinare microstructurală. Microstructura se menţine uniformă, iar distribuţia granulometrică este, de asemenea, monomodală, dar dimensiunea granulelor scade la în domeniul 0,7 - 2.5 m. Se constată apariţia unei porozităţi reziduale la limitele granulare (Fig. I.19(b)).

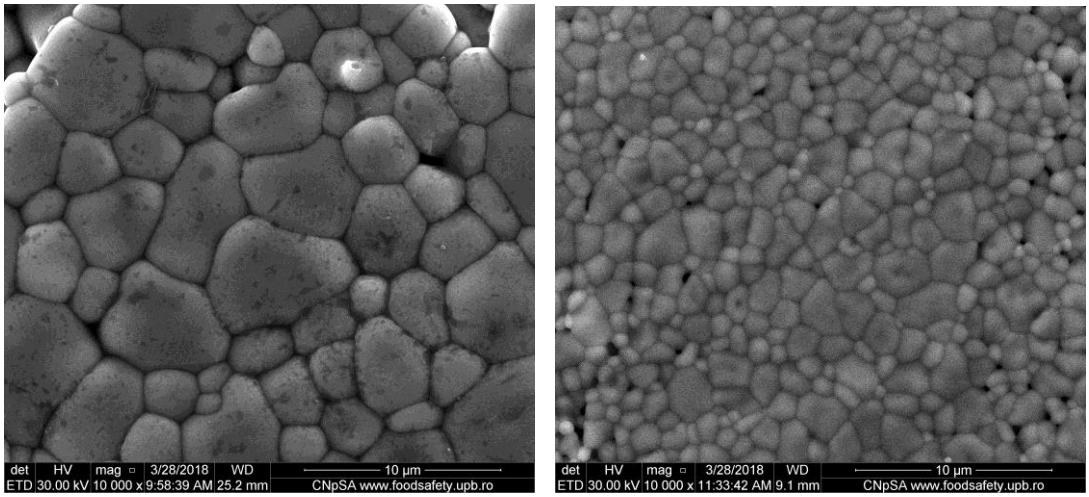

(a) (b)

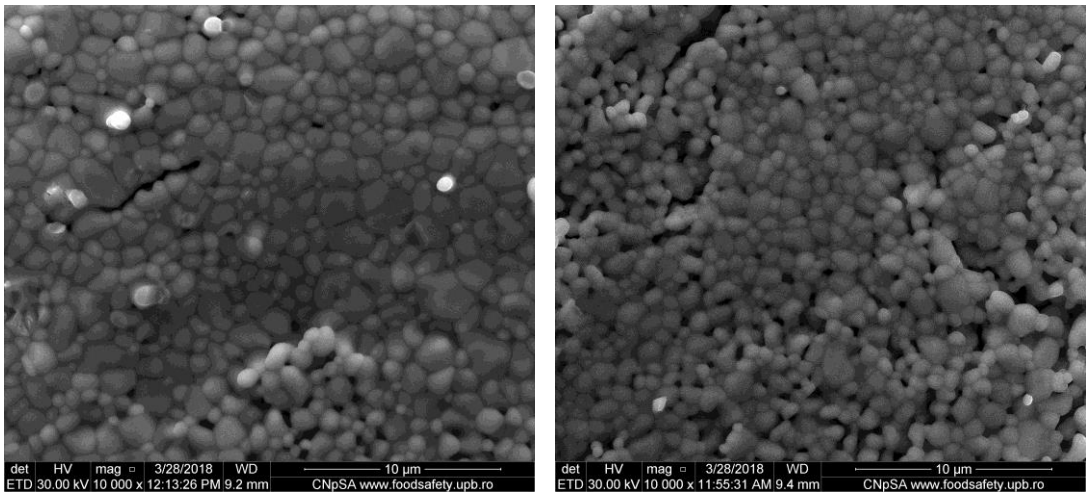

(c) (d)

Fig. I.19. Imagini SEM ce relevă microstructură ceramicilor de tip $PbZr_{1-x}Ti_xO_3$ derivate din pulberi sol-gel şi sinterizate la 1000ºC timp de 2 ore: (a) x = 0,8; (b) x = 0,6; (c) x = 0,4 şi (d) x = 0,2.

Tendinţa de scădere a dimensiunii granulare şi de creştere a cantităţii de porozitate intergranulară se manifestă cu creşterea în continuare a concentraţiei de Zr la x = 0,6 şi, respectiv la x = 0,8 (Fig. I.19(c),(d)). Astfel, ceramicile de compoziţie $PbZr_{0,6}Ti_{0,4}O_3$ şi, respectiv $PbZr_{0,8}Ti_{0,2}O_3$ prezintă microstructuri uniforme din punct de vedere al formei şi dimensiunii granulelor, dar sunt mult mai poroase şi mai fin granulate, dimensiunea granulelor situându-se în domeniul submicronic (0.4 - 0.8 □m) (Fig. I.19(c),(d)).

Creşterea palierului de sinterizare de la 2 la 4 ore, în condiţiile menţinerii temperaturii de sinterizare de 1000ºC, nu determină modificări esenţiale din punct de vedere al dimensiunii medii granulare, în schimb contribuie la creşterea tendinţei de densificare, în special în cazul compoziţiilor bogate în Zr (PZT3 şi PZT4) (Fig. I.20(a)-(d)).

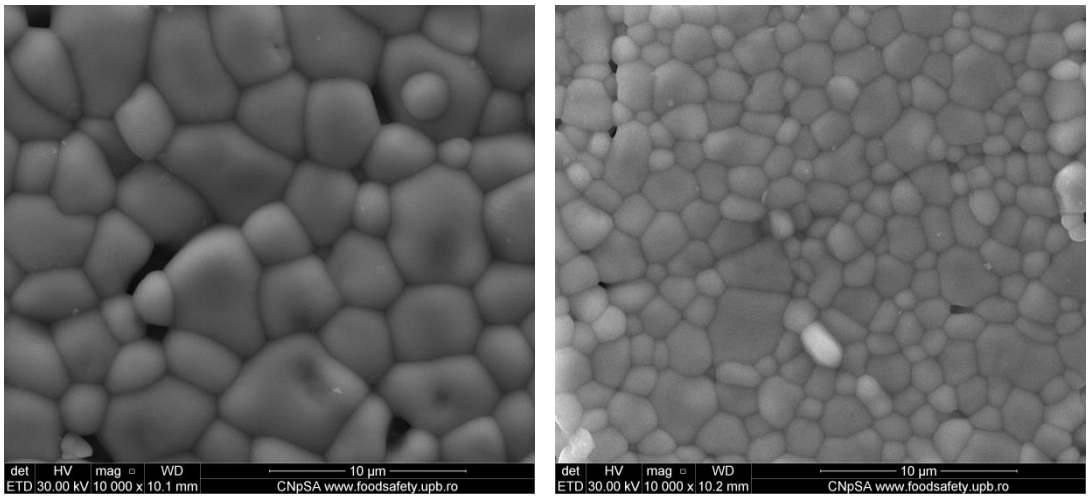

(a) (b)

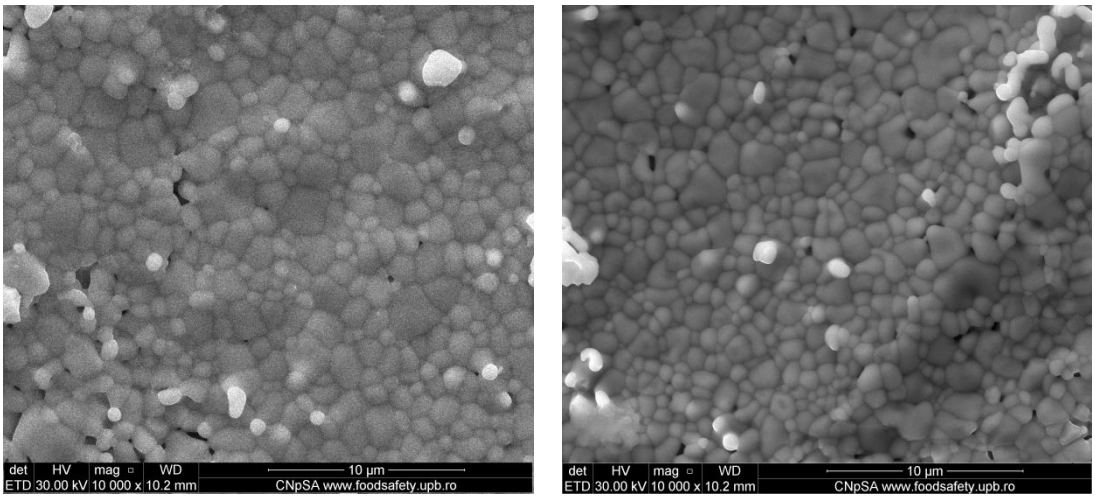

(c) (d)

Fig. I.20. Imagini SEM ce relevă microstructură ceramicilor de tip $PbZr_{1-x}Ti_xO_3$ derivate din pulberi sol-gel şi sinterizate la 1000ºC timp de 4 ore: (a) x = 0,8; (b) x = 0,6; (c) x = 0,4 şi (d) x = 0,2.

Creşterea temperaturii de tratament termic la 1100ºC determină densificarea ceramicilor, simultan cu intensificarea procesului de creştere granulară prin mecanisme difuzionale, indiferent de raportul Zr/Ti din compoziţiile analizate (Fig. I.21(a)-(d)). Astfel, chiar dacă tendinţa de scădere a dimensiunii medii granulare se manifestă şi în acest caz pe măsură ce creşte proporţia de Zr, porozitatea intergranulară este foarte scăzută chiar şi în cazul ceramicii cu proporţie maximă de Zr (Fig. I.21(d)).

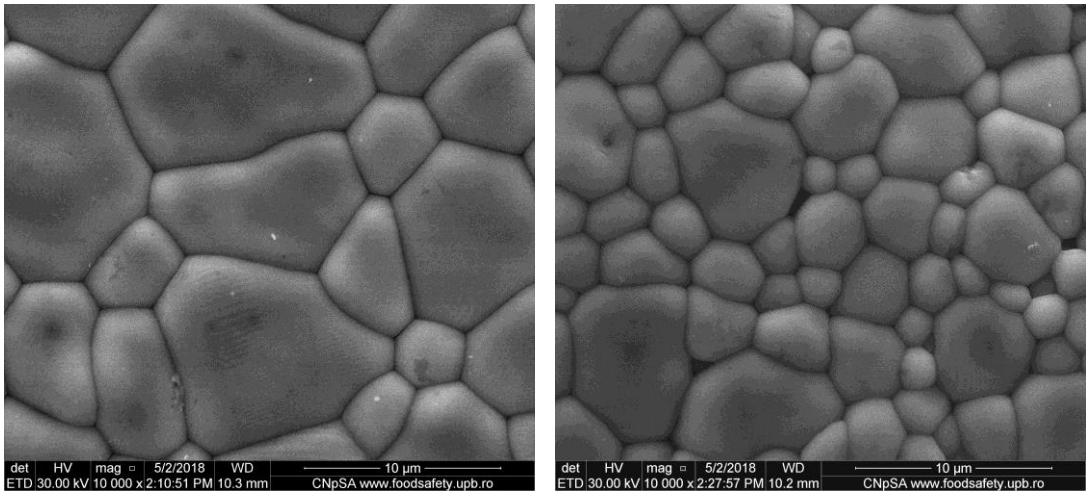

(a) (b)

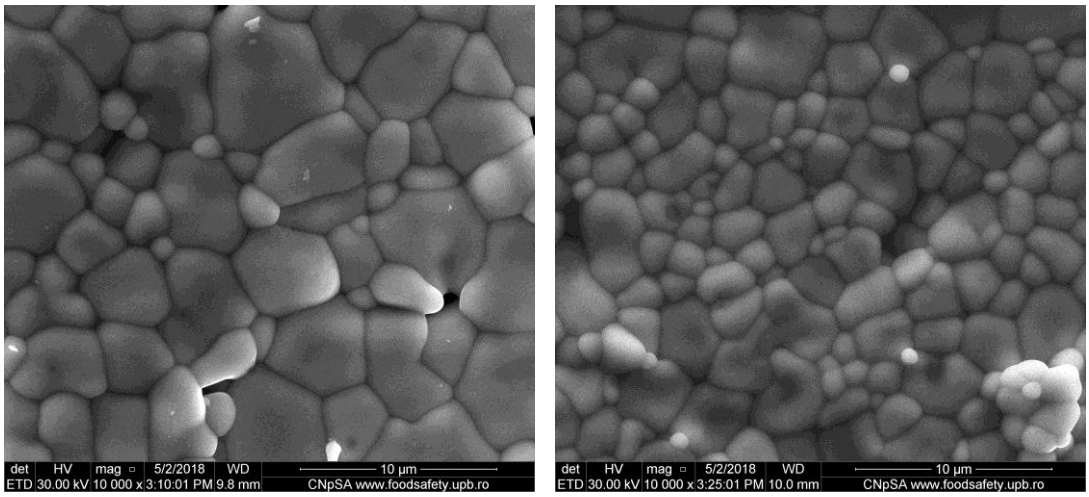

(c) (d)

Fig. I.21. Imagini SEM ce relevă microstructură ceramicilor de tip $PbZr_{1-x}Ti_xO_3$ derivate din pulberi sol-gel şi sinterizate la 1100ºC timp de 2 ore: (a) x = 0,8; (b) x = 0,6; (c) x = 0,4 şi

(d) x = 0,2.

Creşterea în continuare a temperaturii de tratament termic la 1200ºC determină creşterea dimensiunii medii granulare, precum şi a densificării materialelor ceramice, indiferent de proproția de Zr din compoziția PZT. Se menține tendința de scădere a dimensiunii medii granulare odată cu creşterea proporției de Zr (Fig. I.22(a)-(d)). În toate cazurile distribuția granulometrică tinde către una de tip monomodal, dar destul de largă.

Variația dimensiunii medii granulare în funcție de gradul de substituție x pentru diversele condiții de sinterizare este prezentată în Fig. I.23.

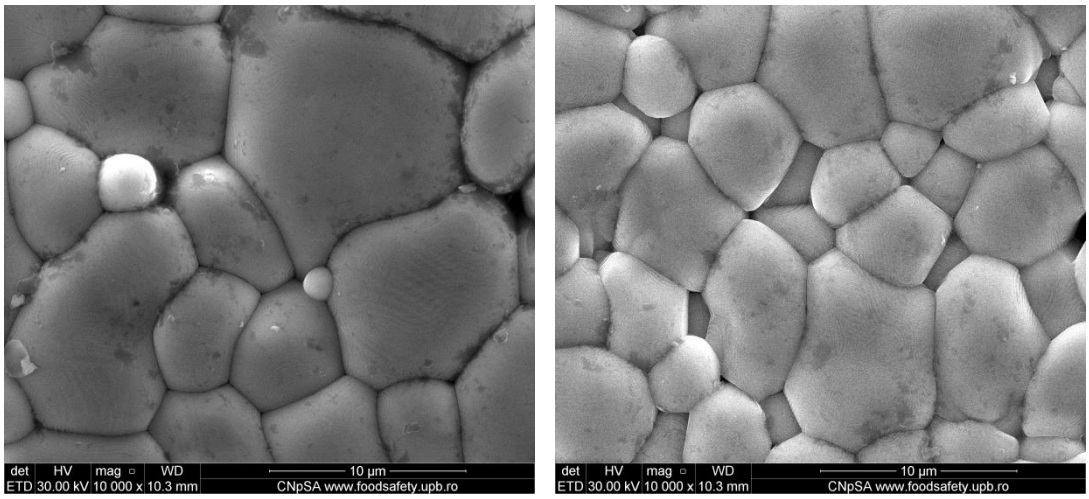

(a) (b)

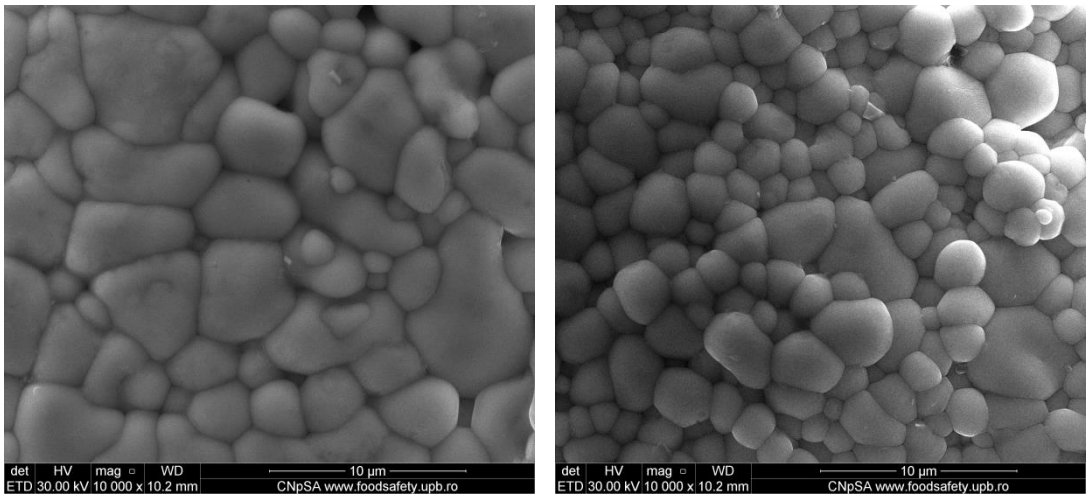

(c) (d)

Fig. I.22. Imagini SEM ce relevă microstructură ceramicilor de tip $PbZr_{1-x}Ti_xO_3$ derivate din pulberi sol-gel şi sinterizate la 1200ºC timp de 2 ore: (a) x = 0,8; (b) x = 0,6; (c) x = 0,4 şi (d) x = 0,2.

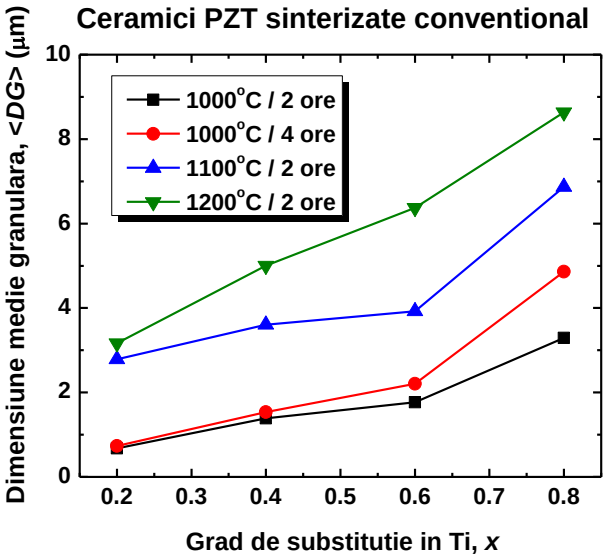

Fig. I.23. Variația dimensiunii medii granulare în funcție de proporția de Ti în ceramicile PZT sinterizate convențional în diferite condiții

I.5.3. Sinterabilitatea

Observațiile de microscopie electronică de baleiaj sunt susținute de valorile proprietăților ceramice (Fig. I.24(a), (b)). Astfel, se constată că atât o temperatură de sinterizare mai ridicată la un palier constant de 2 ore, cât şi un palier mai îndelungat (de 4 ore) în condițiile menținerii unei temperaturi de sinterizare constante (1000ºC) determină densificarea superioară a materialului ceramic prin eliminarea porozității de tip intergranular. Prin urmare, creşterea palierului şi tremperaturii de sinterizare va conduce la creşterea

valorii de densitate aparentă, respectiv la scăderea porozității aparente (Fig. I.24(a), (b)). Este de menționat faptul că o creştere a proporției de Zr determină valori mai scăzute ale densității aparente, respectiv, valori mai ridicate ale porozității aparente pentru toate condițiile de sinterizare analizate. Ținând seama de faptul că densitatea aparentă este o rezultantă a două componente: (*i*) densitatea structurală, care creştere cu creşterea proporției de Zr datorită masei atomice mai mari a acestuia față de cea a Ti pe care îl substituie şi (*ii*) densitatea microstructurală, care determină scăderea valorilor de densitate cu creştere a porporției de Zr din cauza refractarității acestuia, reiese faptul că densitatea microstructurală prevalează, evoluția valorilor densității aparente indicând efectul nefavorabil pe care îl prezintă creşterea proporției de Zr în soluția solidă de tip PZT.

Este de sublinat faptul că ceramica cu proporţie maximă de Ti, descrisă de formula $PbZr_{0,2}Ti_{0,8}O_3$ obţinută în urma sinterizării în aer la 1200ºC timp de 2 ore prezinţă o densitate relativă apropiată de cea teoretică ($\square_r$ = 98,9 %).

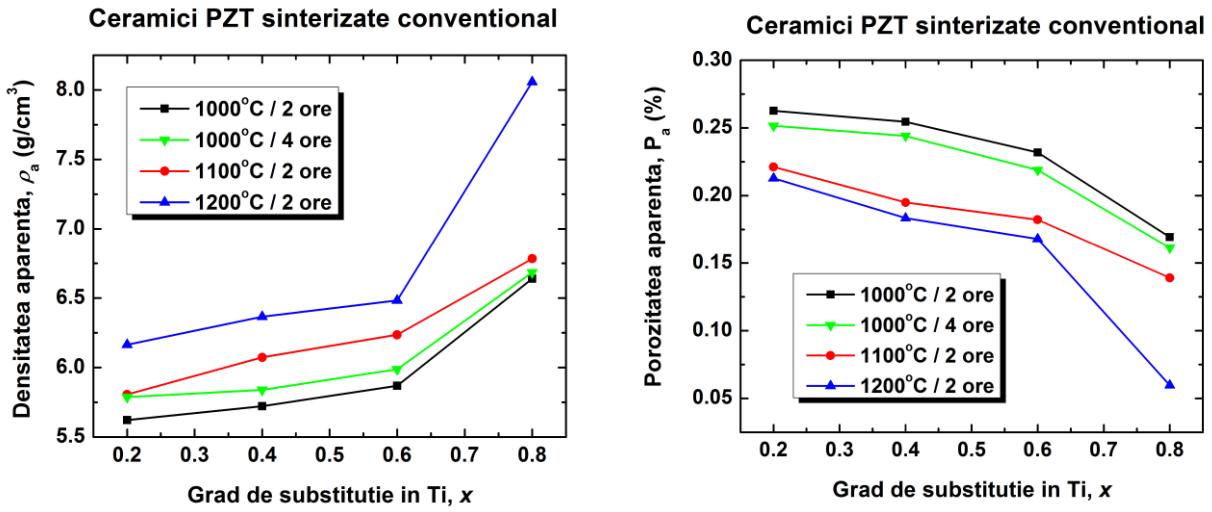

(a) (b)

Fig. I.24. Variația proprietăților ceramice în funcție de proporția de Ti în materialele de tip PZT sinterizate convențional în diferite condiții: (a) densitatea aparentă şi (b) porozitatea aparentă.

I.6. Concluzii

- Au fost sintetizate pe ruta acetat a metodei sol-gel pulberi de compoziţie $PbZr_{1-x}Ti_xO_3$ (PZT) (x = 0,2 – 0,8).
- Toate pulberile preparate sunt bine cristalizate, monofazice, unica fază decelată fiind cea perovskitică, corespunzătare soluţiilor solide de tip PZT;
- Pulberile de PZT cu conţinut mai redus de Ti au prezentat o structură tetragonală, caracteristică $PbTiO_3$, în timp ce pulberile mai bogate în Zr prezintă structură monoclinică;
- Pulberile mai bogate în Ti prezintă o morfologie duplex datorită tendinţei de aglomerarea a unor cristalite mici, de 13 – 25 nm în conglomerate mai mari de 200 – 300 nm; tendinţa de aglomerare creşte cu creşterea concentraţiei de Zr în soluţia solidă perovskitică de tip PZT, astfel că, pentru pulberile de compoziţie $PbZr_{0,6}Ti_{0,4}O_3$ şi $PbZr_{0,8}Ti_{0,2}O_3$, cu proporţiile cele mai mari de Zr, se constată apariţia unor blocuri dense, parţial sinterizate, de dimensiuni la scară micronică (2 – 6

□m), alcătuite din granule poliedrale foarte bine sudate între ele, cu dimensiuni de de 350 – 550 nm;

- Din aceste pulberi au fost elaborate ceramici prin sinterizare convenţională în aer la temperaturi de 1000 – 1200ºC;
- Toate ceramicile sinterizate convenţional în diferite condiţii au fost monofazice, simetria celulei elementare variind în funcţie de raportul Ti/Zr în acelaşi mod ca şi în cazul pulberilor sol-gel din care au provenit;
- Creşterea proporţiei de Zr determină o scădere a dimensiunii medii granulare şi o creştere a porozităţii intergranulare, cu efect nefavorabil asupra densificării în ceramicile sinterizate convenţional, indiferent de temperatura de sinterizare şi palierul de ardere utilizat;
- Creşterea atât a duratei de palier, cât şi a temperaturii de tratament termic determină creşterea dimesnsiunii medii granulare datorită intensificării proceselor de difuzie, precum şi scăderea prorozităţii aparente şi creşterea densităţii aparente datorită avansării procesului de sinterizare.

Aditional fata de rezultatele prezentate mai sus, amai fost preparate tinte din material BST si s-a studiat dependent proprietatilor dielectrice in functie de concentratia de Sr si dimensiunea de graunte cristalin. Rezultatele au fost publicate in Ceramics International (anexa 4 la raport).

Act. 2.3

Denumire Activitate:

Depunerea de filme nedopate, depunerea primelor structuri BFO/BCO.

In aceasta etapa au fost depuse filme subtiri de PZT20/80 (raport Zr/Ti egal cu 20/80) din tinte comerciale (furnizor Parxair) si din tintele nominal nedopate preparate in cadrul proiectului. Au fost depuse prin PLD straturi de PZT 20/80 cu grosimi de 50 si 200 nm, pe suport monocristalin de $SrTiO_3$ (STO) si avand electrozi de $SrRuO_3$ (SRO). Masuratorile electrice preliminare, efectuate la temperatura camerei, au relevat unele diferente in ceea ce priveste proprietatile electrice ale filmelor nominal nedopate si cele ale filmelor depuse din tinta comerciala, care contine anumite impuritati provenite din materiile prime utilizate la fabricare. In tintele preparate in proiect, materiile prime au fost de puritate cat mai ridicata, pentru a se elimina cat mai mult din impuritatile care ar putea actiona ca centrii donori sau acceptori in PZT.

Intr-adevar, masuratorile efectuate pe mai multe contact au relevat faptul ca exista diferente, in special in ceea ce priveste magnitudinea curentului de scurgeri, dupa cum se poate observa si din figurile de mai jos.

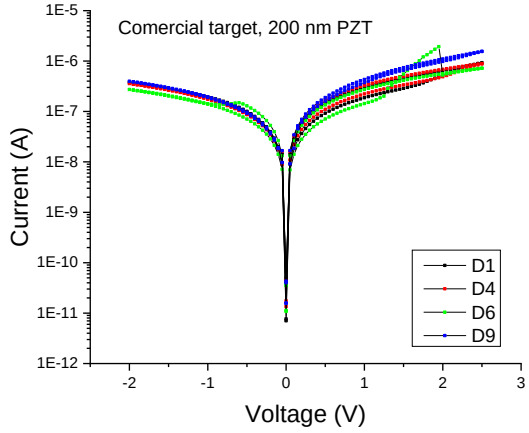

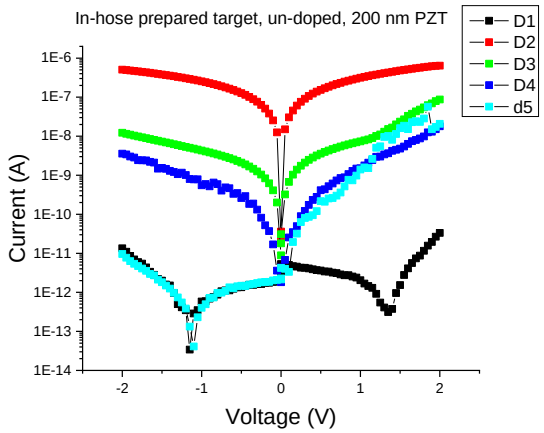

Se o scadere cu cel putin un ordin de marime, statistic vorbind, a curentului de scurgeri in straturile de PZT depuse din tinta nominal nedopata preparata in cadrul proiectului. Aceasta scadere se reflecta si in curbele de histerezis inregistrate pentru straturile de PZT cu grosime de 200 nm.

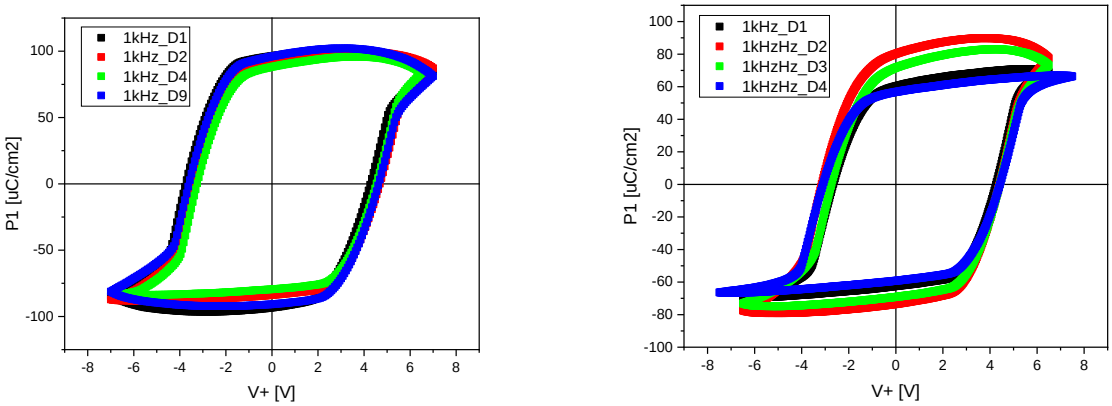

Curbe de histerezis inregistrate pentru diferite contacta depuse pe strat PZT de 200 nm crescut din tinta comerciala (stanga) si depuse pe strat PZT de 200 nm crescut din tinta nominal nedopata preparata in cadrul proiectului.

Din analiza curbelor de histerezis se contata ca:

- Dispersia de valori de polarizare este neglijabila pentru PZT crescut din tinta comerciala, dar este semnificativa pentru PZT crescut din tinta nedopata.
- Valorile polarizarii remanente sunt, statistic, mai mici pentru stratul PZT depus din tinta nedopata, fata de cel depus din tinta comerciala. Acest lucru poate fi corelat cu faptul ca si curentul de scurgeri este mai mic, deci sarcina libera disponibila pentru compensarea campului de depolarizare este mai mica, ceea ce poate duce la o polarizare remanenta mai mica.

Tot in cadrul acestei activitati au fost depuse si unele stratiri de tip BFCO sau BZTO, pentru aplicatii de tip fotovoltaic. Analizele preliminare privind fazele prezente, au relevant prezenta de faze parasite, detrimentale pentru proprietatile electrice macroscopice.

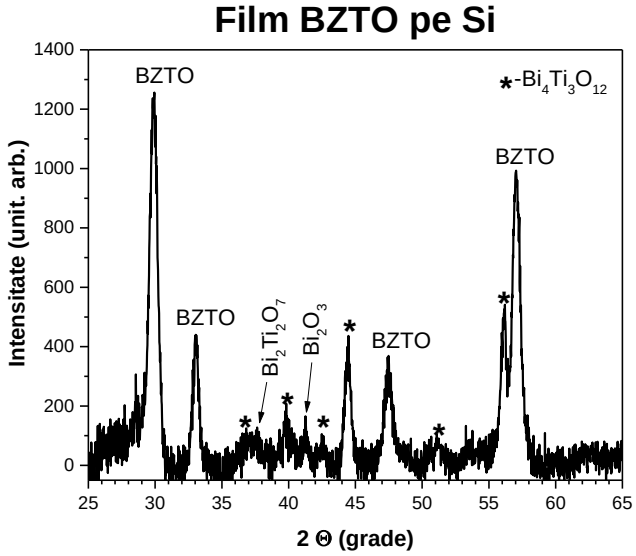

Difractograma de raze X a unui film de BZTO depus pe Si

Eforturile depuse pentru a elimina fazele secundare prin tratamente termice ulterioare nu au dus pana acum la rezultate satisfacatoare. In urmatoarele luni se va decide daca acest studiu va fi continuat sau nu, pentru a evita risipa de resurse pe aceasta directive.

Act. 2.4
Denumire Activitate:
Caracterizare structurala si chimica avansata a filmelor/structurilor depuse.
Aceasta activitate s-a derulat in stransa legatura cu actvitatile 2.3 si 2.5, prepararea, caracterizarea structurala si investigarea proprietatilor electrice fiind puternic intercorelate.
Principalele rezultate sunt urmatoarele:

- Prin spectroscopie XPS a fost pus in evidenta faptul ca curbura de benzi la interfete Au-feroelectric este controlata de polarizare si nu depinde de diferenta dintre lucrurile de extractie ale celor doua materiale. Rezultatele au fost publicate in Physica Status Solidi-Rapid Research Letters (anexa 5 la raport).
- A fost pus in evidenta, prin masuratori combinate de XPS si electrice, prezenta unui histerezis in sens invers acelor de ceasornic in straturi similare grafenei depuse pe PZT epitaxial (a se vedea figura de mai jos).

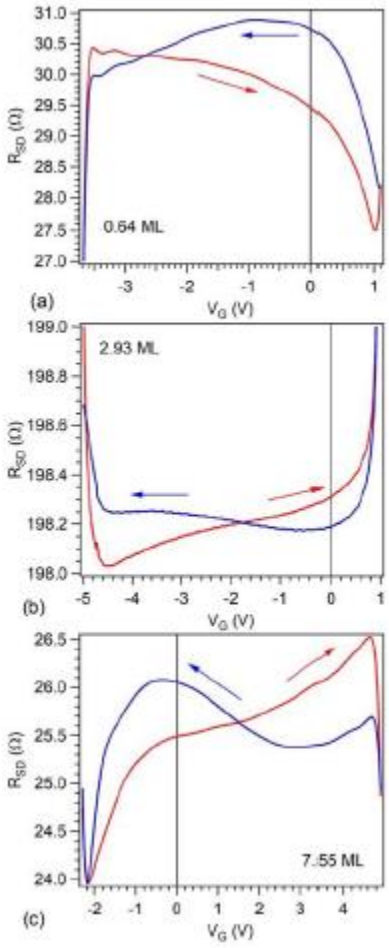

Cicluri resistive de histerezis pentru PZT cu acoperiri diferite de grafena. Ciclul de histerezis este atribuit comutarii polarizarii in stratul ferroelectric.

Rezultatele au fost trimise spre publicare la RSC Advances.

Act. 2.5
Denumire Activitate:
Caracterizare electrica pentru a pune in evidenta legatura dintre defectele intrinseci si proprietatile macroscopice.
In cadrul acestei activitati au fost obtinute 2 rezultate importante:

- A fost pusa la punct o metoda de masura statica a caracteristicii capacitate-tensiune (C-V), in sensul ca valoarea capacitatii se masoara fara tensiune dc aplicata pe capacitorul feroelectric, aceasta fiind utilizata numai pentru schimbarea starii de polarizare dupa care este indepartata de pe proba. Rezultatele obtinute sunt diferite de cele inregistrate in cazul caracteristicilor C-V clasice, la care tensiunea dc este aplicata continuu pe proba si variata in trepte in valori maxime negative si pozitive. Coreland masuratorile C-V cu analiza Rayleigh a curbei de histerezis la campuri sub campul corecitiv si cu studii structurale, s-au constatat urmatoarele: 1) valoarea capacitatii statice este constanta cu tensiunea aplicata, in afara domeniului de tensiuni in care are loc reversarea polarizarii, ceea ce sugereaza ca, in conditii statice si fara tensiune aplicata capacitoril feroelectric este total depletat; 2) valoarea constantei dielectrice fara camp aplicat este foarte mica, in jur de 20-25 pentru un strat subtire de 20 nm, chiar si la frecvente joase, de ordinul kHz; 3)constanta dielectric creste pe masura ce grosimea filmului de PZT creste, pe de o parte pentru ca apar defecte structurale purtatoare de sarcina electrica care poate raspunde la campul aplicat, si pe de alta parte datorita aparitiei domeniilor fereoelectrice si a peretilor de domenii, care raspund usor la orice variatie a campului electric aplicat. Rezultatele au fost publicate in Scientific Reports (anexa 6 la raport).
- Functionalitati noi au fost puse in structuri cu 3 straturi de tip PZT-STO-PZT, cu potentiale aplicatii in memorii cu stari multiple, memorii nevolatile, porti logice cu posibilitate de memorare (dispozitive de tip memcapacitor), sau in memorii analogice si retele neuromorfice. Rezultatele au fost publicate in Physical Review Applied (anexa 7 la raport).

Act. 2.6
Denumire Activitate:
Raportare, publicare, prezentari conferinte.
Lista lucrari

Nr.	Titlu, jurnal, etc.	Autori	IF	AIS
1	**Memcomputing and Nondestructive Reading in Functional Ferroelectric Heterostructures** PHYSICAL REVIEW APPLIED **12,** 024053 (2019)	Georgia A. Boni, Lucian D. Filip,* Cristina Chirila, Alin Iuga, Iuliana Pasuk, Luminita Hrib, Lucian Trupina, Ioana Pintilie, and Lucian Pintilie	4.532	1.832
2	**Polarization branches and optimization calculation strategy applied to ABO(3) ferroelectrics** MODELLING AND SIMULATION IN MATERIALS SCIENCE AND ENGINEERING Volume: 27 Issue: 4 Article Number: 045008 Published: JUN 2019	Filip, Lucian D.; Plugaru, Neculai; Pintilie, Lucian	1.826	0.672

3	**Low value for the static background dielectric constant in epitaxial PZT thin films** **Scientific Reports** | *(2019) 9:14698* | https://doi.org/10.1038/s41598-019-51312-8	Georgia Andra Boni, Cristina F lorentina Chirila, Luminita Hrib, Raluca Negrea, Lucian Dragos Filip, Ioana Pintilie & Lucian Pintilie	4.011	1.286
4	**Designing functional ferroelectric interfaces from first-principles: Dipoles and band bending at oxide heterojunctions** New Journal of Physics (accepted)	Rusu, Dorin; Filip, Lucian; Pintilie, L; Butler, Keith; Plugaru, Neculai	3.783	1.489
5	**Impact on Ferroelectricity and Band Alignment of Gradually Grown Au on BaTiO3** PHYSICA STATUS SOLIDI-RAPID RESEARCH LETTERS Volume: 13 Issue: 7 Article Number: 1900077 Published: JUL 2019	Popescu, Dana Georgeta; Husanu, Marius Adrian; Chirila, Cristina; Pintilie, Lucian; Teodorescu, Cristian Mihail	3.729	0.790
6	**The interplay of work function and polarization state at the Schottky barriers height for Cu/BaTiO3 interface** Applied Surface Science, accepted	D.G. Popescu[1,*], M.A. Husanu[1], C. Chirila[1], L. Pintilie[1] and C.M. Teodorescu[1]	5.155	0.671
7	**(Ba,Sr)TiO_3 solid solutions sintered from sol-gel derived powders: An insight into the composition and temperature dependent dielectric behavior** Ceramics International, accepted	Roxana Elena Patru[1], Constantin Paul Ganea[1], Catalina-Andreea Stanciu[2], Vasile-Adrian Surdu[2], Roxana Trusca[2], Adelina-Carmen Ianculescu[2*], Ioana Pintilie[1*], Lucian Pintilie[1]	3.450	0.454
			26.486	7.194

Anexa 1

IOP Publishing New J. Phys. 21 (2019) 113005 https://doi.org/10.1088/1367-2630/ab4d8b

New Journal of Physics
The open access journal at the forefront of physics

DPG IOP Institute of Physics

Published in partnership with: Deutsche Physikalische Gesellschaft and the Institute of Physics

PAPER

Designing functional ferroelectric interfaces from first-principles: dipoles and band bending at oxide heterojunctions

Rusu Dorin[1], Lucian Dragos Filip[2,4], Lucian Pintilie[2], Keith Tobias Butler[3] and Neculai Plugaru[2]

[1] University of Warwick, Dept. Phys, Coventry CV4 7AL, W Midlands, United Kingdom
[2] National Institute of Materials Physics, Atomistilor Str. 405A, Magurele, 077125 Ilfov, Romania
[3] Rutherford Appleton Lab, Sci Comp Div, SciML, Didcot OX11 0QX, Oxon, United Kingdom
[4] Author to whom any correspondence should be addressed.

E-mail: lucian.filip@infim.ro and plug@infim.ro

Keywords: ferroelectrics, capacitors, interfaces, polarization, heterojunctions

Supplementary material for this article is available online

OPEN ACCESS

RECEIVED
19 July 2019

REVISED
3 October 2019

ACCEPTED FOR PUBLICATION
14 October 2019

PUBLISHED
1 November 2019

Abstract

The fundamental phenomena at ferroelectric interfaces have been the subject of thorough theoretical and computational studies due to their usefulness in a large variety of emergent electronic devices, solar cells and catalysts. Ferroelectricity determines interface band-bending and shifts in electron energies, which can be beneficial or detrimental to device performance. However, the underlying mechanisms are still the subject of debate and investigation, as a deeper understanding of the electrochemistry is required to develop *bona fide* design principles for functional ferroelectric surfaces and interfaces. Here, using first principles calculations within the GGA + U formalism, we investigate the problem of band alignment in non-defective, asymmetric $SrRuO_3/PbTiO_3/SrRuO_3$ capacitors with ultra-thin ferroelectric layers. The effects of the dielectric size on the polar distortion stability and interface-specific properties are analyzed. It is shown that the critical size of the dielectric for polarization switching is ≈2 nm (5 $PbTiO_3$ u.c.). Below this limit there is no bulk-like region in the dielectric, the space charge accumulated at interfaces leads to the presence of gap states in the whole $PbTiO_3$ layer and ferroelectricity vanishes. We draw the band alignment diagrams as given by the band line-up and band structure terms, as well as by taking Ti 3*s* semi-core states as reference. In the ferroelectric structures, both approaches predict a strong effect of band-bending on the type of contact, Schottky or Ohmic, at the asymmetric interfaces. The effect of interface states on the interface dipole amplitude and band alignment is discussed.

1. Introduction

Multilayered structures incorporating ferroelectric perovskites and metal/oxide electrodes have extensively been investigated for their use in a wide range of advanced applications, including but not limited to (multiple state) ferroelectric memories [1–5], quantum tunneling junctions [6–14], photo-ferroic solar cells [15–24], and various multilevel architectures with coupled ferroic modes [25–34]. Also, new experimental methods have been envisaged for acquiring an accurate control of polarization when the ferroelectric layer is situated deep into these structures [35–38]. Ferroelectric interfaces are key elements for the functionality of these heterostructures. Their underlying phenomenology is determined by the chemistry of the specific materials, their thickness, as well as the design and quality of interfaces [39–43]. At the interface with a ferroelectric the polar distortions are perturbed, the local strain, bonding across the interface and the built-in electric field promote charge transfers and space charge build-up. In turn, these effects impact on the electronic structure, inducing relative shifts of the energy levels, modifications of band gap values, metal-induced band gap states (MIGS) and interfacial band bending effects [7, 44–48]. The band alignment scheme results as an effect of entangled microscopic mechanisms and plays a major role in setting the operating conditions of practical junctions [49, 50]. Theory and computational methods, particularly those based on first principles calculations, have proven their usefulness in

exploring the fundamental mechanisms at the interface with a ferroelectric, as well as by revealing practical routes for the device design based on predictive behavior; for a review in the field see [51].

Based on their previous work [52, 53], Stengel *et al* have developed a new formalism, referred to as the constrained electric displacement method, for the description of the microscopic phenomena in ferroelectric multilayered systems [54, 55]. It was shown that expressing the internal energy of a periodic crystal in a uniform external field in terms of the electric displacement as the fundamental variable—equivalent to fixing the free charge on the plates of a capacitor- enables one to explain the factors determining the depolarizing field, to model the polarization and response of complex super-lattices, capacitors and interfaces in terms of the electrical properties of the elementary building blocks [10], and also provides a convenient route for the treatment of the couplings between different order parameters [54, 55].

A comprehensive study of the band alignment problem in ferroelectric capacitors is presented in [45]. The authors highlight the possible consequences in the interpretation of the LDA/GGA band offsets at interfaces due to band gap under-estimation. In such a situation, denoted as a 'pathological' case, a spill-out of charge from the metal to the insulator leads to the appearance of conduction band states at the Fermi level and brings about a degree of arbitrariness in assessing the band edges and hence the band alignment scheme, which no longer is a well-defined interface property [45]. It is also rationalized that the errors in establishing accurate realistic Schottky barrier heights (SBHs) from standard (LDA, GGA) first principles calculations affect the amount of transferred charge and induced metallicity in the dielectric. As a result, these will determine errors in the ground state charge density, which in turn may propagate to alter the predicted electronic and structural properties of the system, as well. The authors elaborate a refined strategy, consisting in a sequence of calculations on bulk and supercell systems, in order to detect the pathological cases, and to derive reliable band edge positions relative to Ti 3*s* semi-core states, in the non-pathological cases. Their approach also allows the evaluation of the effects of the interface states on band edge positions when MIGS are present [45].

Here it is worth highlighting that an insightful analysis of the MIGS and their effect on the interface dipole and formation of SBHs in ferroelectric/metal junctions has also been presented in [47]. These authors demonstrate that although the most penetrating bands are located at high symmetry points, for the study of tunneling conductance across ultra-thin layers or integrated quantities (where many k parallel points contribute) it is important to consider complex bands in the whole two dimensional Brillouin Zone (BZ). Also, a general recipe is outlined to estimate from the complex band structure of the bulk insulator the effective decay factor (and its dependence with the energy within the gap) of the MIGS in realistic interfaces [47].

Ferroelectric capacitors with asymmetric interfaces have been investigated with the expectation that asymmetry may furnish an enhanced device functionality comparing to the symmetric realizations (see [48] and the references cited therein). The degeneracy of polarization states in symmetric geometries is broken in asymmetric configurations and hence size effects may determine distinct states for forward–backward polarization. Following this line of research, Chen *et al* [48], carried out a detailed study within LDA on the size effect in ferroelectric $BaTiO_3$ tunnel junctions with metal Pt and/or oxide $SrRuO_3$ electrodes, considering the four possible types of electrode/ferroelectric interfaces. They found a significant dependence of the ferroelectric stability of a tunnel junction on the type and combination of the two interfaces. Also, an abnormal enhancement of ferroelectricity due to bonding at the Pt_2/BaO interface has been predicted. However, on the grounds of the analysis and results presented in [45], the findings reported in [48] may be affected by the shortcomings inherent to LDA.

Umeno *et al* [2] investigated the influence of electrode materials and PTO size on the ferroelectric stability and SBHs in ultra-thin perovskite capacitors, with symmetric $SrRuO_3/PbTiO_3/SrRuO_3$ (SRO/PTO/SRO) or $Pt/PbTiO_3/Pt$ and asymmetric $Pt/PbTiO_3/SrRuO_3$ configurations. The SBHs were obtained by using a macroscopic averaging of the electrostatic potential, with the p-type SBH calculated from the relation $\phi_p = \Delta\overline{V} + \Delta E_{\rm bulk}$, where $\Delta\overline{V}$ is the difference between the macroscopic averages of the electrostatic potentials in the two materials 'far' from the interface and $\Delta E_{\rm bulk}$ is the difference between the Fermi energy of the electrode and the valence-band maximum (VBM) of the dielectric material, with the Fermi and VBM energies obtained from independent bulk calculations at the same structural parameters as in the capacitor calculations. Another approximation in this work is the usage of the experimental PTO bandgap for the estimation of the SBHs for electrons. The authors conclude that the influence of polarization on the Schottky barrier is larger in SRO/PTO/SRO than in Pt/PTO/Pt, and also the contribution of the electrical field generated by the asymmetric electrodes influences the Schottky barriers significantly. Also, a considerable change (about 1.0 eV) in the SBH has been predicted in the Pt/PTO/SRO capacitor when switching polarization [2].

As the thickness of the ferroelectric layer decreases, it may become comparable with the spatial extent of the interface-induced phenomena. Ultra-thin layers (only a few nanometers thick) reach a limit where a bulk-like region, with structural regularity and characteristic potential and charge distributions, may not exist any more, to be taken as a reference for resolving the interface contribution. Actually, one has to make a trade-off between

using elaborate and accurate models, e.g. [45, 47, 55] and a practical approach which encompasses as much as possible the characteristics of the real system. To our knowledge, a proper explanation of size effects and interface specific properties in ferroelectric capacitors with ultra-thin layers is still an open issue.

Therefore, here we have investigated by first principles calculations $SrRuO_3/PbTiO_3/SrRuO_3$ ferroelectric capacitors with asymmetric interfaces. We discuss the effects of size, asymmetry and polarization on the ferroelectric instability and interface-specific properties, including local structure, potential and charge density distributions, interface dipole extension and amplitude, band bending and band alignment.

The paper is organized as follows: in section 2 we present the computational details and describe the models used in this work. The structural results and their imprint on the electrical properties of the systems under study are presented in section 3. The electronic structure, including partial and local density of states, the potential and charge density variation, as well as the size effect on polarization are discussed in section 4. In section 5, starting from a corrected band gap for the dielectric, we derive the band alignment diagrams both by using the band line-up and band structure terms, as well as by taking Ti 3*s* semi-core states as reference. The contrasting features predicted by the two different approaches are discussed by considering both the effect of interface states as well as the limitations due to our assumptions. The main conclusions of the work are summarized in section 6 of the paper.

2. Computational details and model structures

2.1. Method

The calculations were performed within the generalized gradient approximation (GGA) using the quantum ESPRESSO plane-wave code [56, 57], and the exchange and correlations functional in the parametrization for solids (PBESol) [58, 59]. We used Vanderbilt ultrasoft pseudopotentials [60] from the QE library [61], with Pb *5d10 6s2 6p2*, Sr *4s2 4p6 5s2 5p0*, Ti *3s2 3p6 4s2 3d2*, Ru *4d7 5s1 5p0* and O *2s2 2p4* states in the valence band. The kinetic-energy cut-off for the plane waves was set at 100 Ry and for the charge density at 800 Ry. The BZ integration was performed on an automatically generated Monkhorst–Pack [62] $4 \times 4 \times 1$ k-mesh, for all slabs, with Gaussian energy level smearing of 0.02 Ry. The total energy per atom was converged to less than 1×10^{-3} eV. A dipole correction was applied in order to remove the electrostatic interaction between the electric dipoles in neighboring slabs along the z-axis of broken symmetry [52, 63].

The DFT + U rotationally invariant method, in the atomic projection [64–66], was used to treat orbital-dependent correlations for Ti *3d* and O *2p* orbitals, and thus to correct their effect on the $PbTiO_3$ band gap. An effective Hubbard term, $U_{\text{eff}} = U - J$, was applied to the correlated orbitals, with U being the screened on-site Coulomb interaction and J the Stoner exchange parameter. The corrective U_{eff} values used in this study are 7 eV for the Ti *3d* orbitals and 6 eV for the O *2p* orbitals, as determined empirically on bulk tetragonal $PbTiO_3$, leading to a band gap of 2.98 eV. This value is still a little underestimated with respect to experiment (giving values in the range 3.45–3.6 eV (see [67] and references cited therein), but significantly improved relative to the GGA result (1.68 eV). Applying the correction also on Ru *4d* states had no noticeable effect on the present results and therefore was discarded.

We evaluated the layer-by-layer spontaneous polarization of the $PbTiO_3$ using the following equation [68]:

$$P_k(z) \simeq \sum_i \frac{\partial P}{\partial u_{ki}^{(0)}}(u_{ki} - u_{ki}^{(0)}) = \frac{1}{V_k} \sum_i Z_{ki}^* \, \Delta u_{ki}, \tag{1}$$

where Z_{ki}^* and Δu_{ki} are the dynamical charge and displacement of ion i in cell k, respectively, and V_k is the volume of the cell. The superscript zero refers to a non-polar equivalent of the relaxed $PbTiO_3$ sub-structure. This was constructed by keeping the Pb sublattice fixed and moving the rest of the atoms to equivalent centro-symmetric positions within each $PbTiO_3$ unit cell. Z_{ki}^* were calculated using the linear response to an atomic perturbation [69] at the gamma point, within the Density Functional Perturbation Theory framework, implemented in the PHonon package. Equation (1) can be used with either A or B cation-centered cells.

The spontaneous polarization of the PTO layer was also calculated within the Berry's phase approach [70] as implemented in the Quantum ESPRESSO package [71]. In order to minimize the number of calculation steps for deriving unambiguous polarization values we applied the method described in [72].

2.2. Model structures

The ferroelectric capacitors were modeled as slabs, schematically depicted in figure 1, with the atomic layers in the sequence $(3(SrO - RuO_2) - SrO)/m(TiO_2 - PbO)/4(RuO_2 - SrO)$, where $m = 3, 5, 7$ and 9. The asymmetry of the structures emerges from the two different interfaces. The thickness of the SRO layers is close to the experimentally detected limit for metallic conduction [73]. We also carried out calculations on 9-PTO models with double numbers of SRO unit cells, both in the slab as well as supercell geometry. This enables a

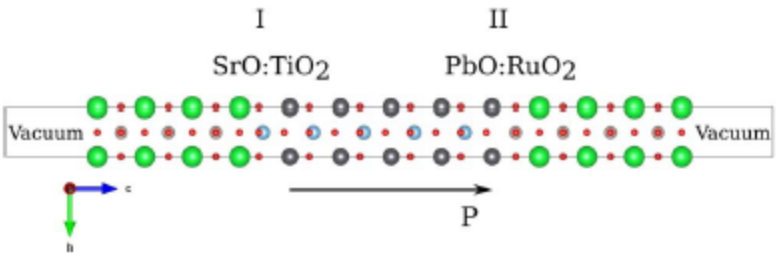

Figure 1. Schematic illustration of the model structures used in this study, with the two interfaces SrO/TiO_2 left and PbO/RuO_2 right. Color code: Sr light green, Pb dark gray, Ru light brown, Ti light blue, and O red.

comparison between data for open and short-circuit conditions, as well as of the interface specific properties and effects in both type of systems [74].

The slabs are separated by ≈15 Å vacuum along z-axis, see figure 1. In all model structures the atomic positions were relaxed until the Hellmann–Feynman forces were less than 0.01 $eVÅ^{-1}$ on each atom. In the initial state, before relaxation, both $\pm z$ ferroelectric distortions, denoted as P^+ and P^-, were considered.

We implicitly assumed that the structures were grown coherently on a cubic $SrTiO_3$ (001) substrate, with the bulk lattice constant, $a = 3.905$ Å [75], which is slightly less (by 0.64%) than that of pseudocubic $SrRuO_3$ with $a = 3.93$ Å [35], and matches the in-plane lattice constant of tetragonal PTO [76]. Thus, the experimental lattice constants were used in the present study, as suggested in [77]. Also, it has previously been shown that such a geometry determines the direction of PTO layer polarization perpendicular to the capacitor plane [78].

The band structure of interfaces between different materials is a complex interplay of symmetry, strain and chemistry. We have chosen in this work to consider the effects of chemistry and strain at the interface, by choosing to impose the substrate perovskite structure (Pm-3 m) on the SRO layers. Previously it has been shown that very thin layers of SRO constrained by a substrate symmetry has octahedral tilt angles determined by the substrate, rather than bulk SRO, up to 3 or 4 layers deep [79]. Moreover experimental characterization of SRO grown epitaxially on PZT up to 25 nm, displays a pseudo-cubic symmetry [80]. In future work it will be interesting to consider also how symmetry effects can influence the interface band structure, but in the interests of clarity and motivated by these previous studies, herein we use a model without the bulk aac-tilting of bulk SRO.

Recently, the magnetism of $SrRuO_3$ thin films has thoroughly been discussed in relationship with size, lattice distortions and electronic correlations [81]. It has been shown that the application of standard methods (LDA and GGA) to describe the magnetic ground state leads to contrasting solutions in complex oxide thin films or their heterostructures. Since in this work our primary goal is to describe the role of bonding, space charge and polarization on band alignment in the studied systems, we have assumed non-magnetic $SrRuO_3$, thus neglecting the effects of interfacial magnetism.

3. Structural results

The layer-by-layer cation-oxygen (M–O) relative z-displacements, $Z_M - Z_O$, where $Z_{M/O} = Z^{(r)}_{M/O} - Z^{(0)}_{M/O}$ stand for the cation and anion positions in the relaxed layers relative to their positions in the centro-symmetric layers, are plotted in figure 2 and the corresponding data for the 9-PTO slab with thick electrodes are shown in figure S1 (supporting information is available online at stacks.iop.org/NJP/21/113005/mmedia). The positions of the geometric interfaces (GI 1/2) are marked by vertical dashed lines at half distance between adjoining SRO and PTO monolayers. In the case of the 9- and 7-PTO slabs the initial $\pm z$ polar distortions are preserved in the relaxed structures: the Pb–O and Ti–O relative shifts are larger at interfaces and gradually decrease towards inside the layer, where a regular, bulk-like behavior may be observed. However, their values are smaller than in bulk $PbTiO_3$. In the relaxed 5- and 3-PTO structures, the negative values of the relative ionic displacements show that the P^- state is favored. A similar behavior was previously reported for the $SrRuO_3/BaTiO_3/SrRuO_3$ capacitors [82, 83]. These results are consistent with the unit cell tetragonality, c/a, in the relaxed state, shown in figure 3. The PTO tetragonality decreases with the layer thickness, from 1.064 in the bulk (marked by the blue dashed line) to ~1.03 for 9-PTO, to ~1.02 for 7-PTO, to 1.01 – 1.02 for 5-PTO and to ~1.00 for 3-PTO.

In figures 2 and S1 one should also remark the presence of cation-oxygen relative z-displacements in the SRO electrodes, for the 9- and 7-PTO structures, which are driven by the ionic relaxations in the dielectric at interfaces. These ionic displacements, larger at interfaces and decreasing inside the electrode, as well as the cubic

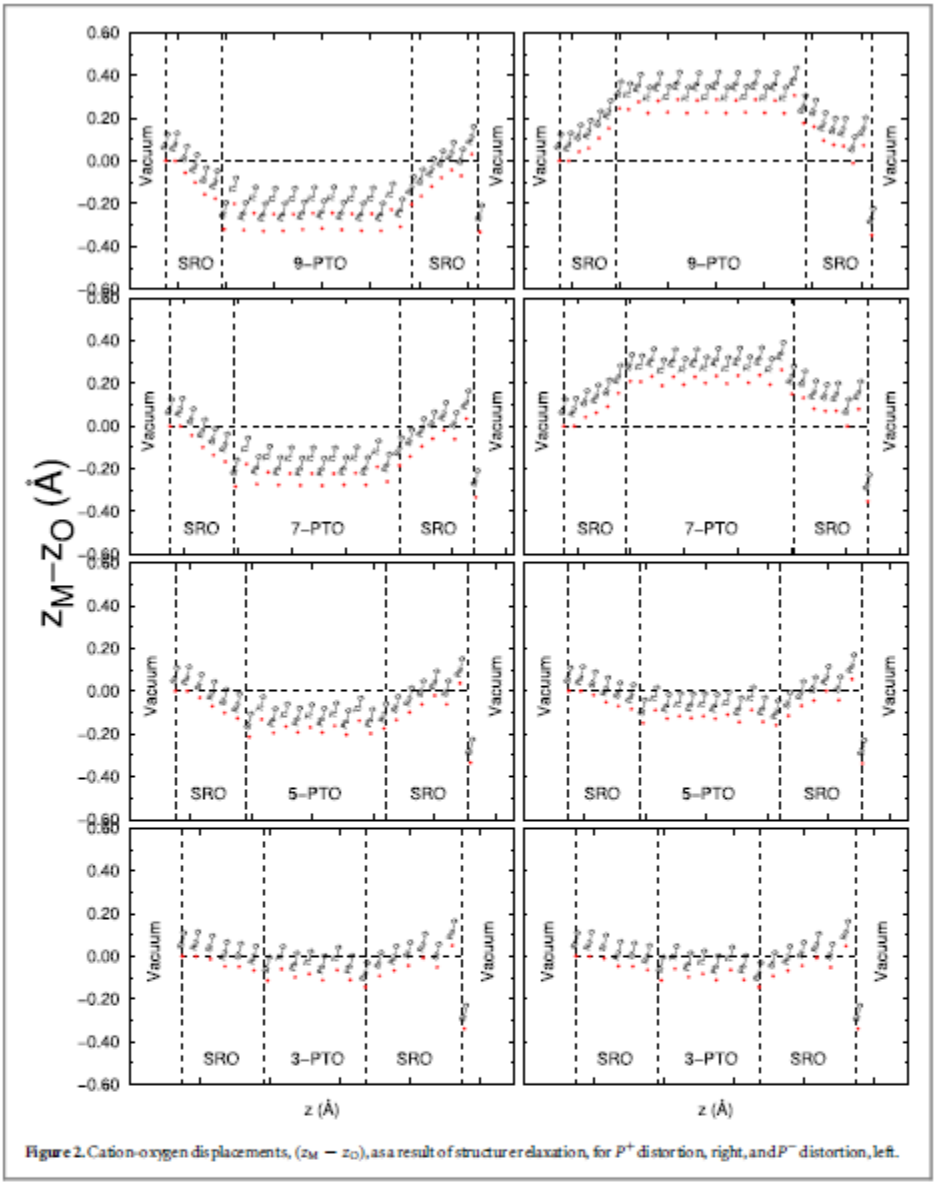

Figure 2. Cation-oxygen displacements, ($z_M - z_O$), as a result of structure relaxation, for P^+ distortion, right, and P^- distortion, left.

to tetragonal distortion of the SRO unit cell show that a polar state may onset in the metallic phase at the interface with a ferroelectric, in agreement with previous results, [7, 84]. The phenomenon has been explained by the softness of the metallic oxide lattice, which allows the ferroelectric displacements in PTO to penetrate into the metal electrode, acting toward the stabilization of a ferroelectric phase in a narrow region at the interface [7]. More recently, Filippetti *et al* reported that $Bi_5Ti_5O_{17}$ complies with the sufficient symmetry requirements for a switchable polarization to exist and the material can sustain a sizeable potential drop along the polar direction, in spite of being a metal [84]. However, in the present case the results do not reveal the presence of a ferroelectric polarization in the SRO electrodes, as discussed further.

The values of the bond lengths across the SRO–PTO interfaces, collected in table S1, show that Ru–O, Pb–O and Pb–Ru bonds are larger than the Ti–O, Sr–O and Sr–Ti, respectively, due to the larger Shannon–Prewitt radii of Ru (0.760) and Pb (1.63) than the radii of Ti (0.745) and Sr (1.58) [85]. In the case of the 9- and 7-PTO slabs, the M–O bonds show variations of the order of the M–O displacements, when switching polarization along $\pm z$. Increasing the electrode thickness does not effect the bond lengths at interfaces, as evidenced by a

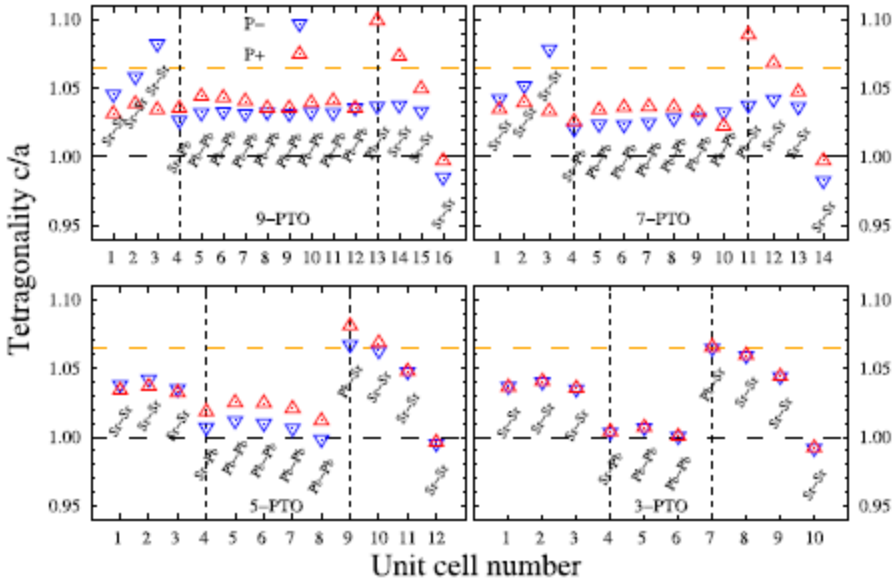

Figure 3. Position dependence of the c/a ratio (unit cell tetragonality) as a result of ionic relaxations. Unit cells are set-up on Sr and Pb ions. The yellow dashed line marks the experimental value, 1.064, for bulk $PbTiO_3$, while for bulk $SrRuO_3$ this ratio is 1.00 before relaxation.

comparison between the values for the 9-PTO slabs with thin and thick SRO layers. The relaxation of the 5-PTO slab determines only very small differences between the corresponding bond lengths in the two polar states. In the case of the 3-PTO slabs one obtains identical bond lengths after relaxation, consistent with only a slight difference in the total energy between the two states (less than 5 meV).

These structural results indicate that the ferroelectric states along $\pm z$ are not equivalent, as expected for asymmetric interfaces, and that a switchable polarization can exist only in the 9 and 7-PTO slabs, albeit with smaller values than calculated in bulk PTO (0.88 $C\,m^{-1}$). In the case of the 5-PTO slab, only one stable polarization state is revealed, while the polar distortion in the 3-PTO slab is suppressed.

4. Electronic structure results

4.1. Partial and local density of states

The total and partial densities of states of the thin electrode structures, plotted in figure S2, reveal the following features: (i) the Fermi level is pinned in the PTO band gap by Ru *4d* and (SRO) O *2p* states; (ii) a significant dependence on the polarization direction in the 9- and 7-PTO slabs, only slight differences for the 5-PTO slabs, and no difference for the 3-PTO slabs; (iii) the PTO band gap is smaller than the value in the bulk material; (iv) the presence of PTO band gap states.

More insight is brought by inspecting the PTO local DOS, (LDOS), displayed in figure 4 for the 9-PTO system and figure S3(a)–(c) for the 7-, 5- and 3-PTO ones. These data show a layer dependence of the position of the VBM and CBM in the 9, 7 and 5 layer systems, but not in the 3 layer system. The reason for this is discussed in more detail in the next section on electrostatic potential. Band gap states are visible in the LDOS of the first PTO unit cell (one or two monolayers) at an interface. They form bands at certain energy values, a feature which is associated with the formation of chemical bonds across the interface.

4.2. Electrostatic potential and charge density

We calculated the electrostatic potential, $V(r) = V_b + V_H$, where V_b is the inter-ionic term, and V_H is the electron–electron term given by:

$$V_H = \int dr' \rho(r') \frac{1}{r - r'}, \tag{2}$$

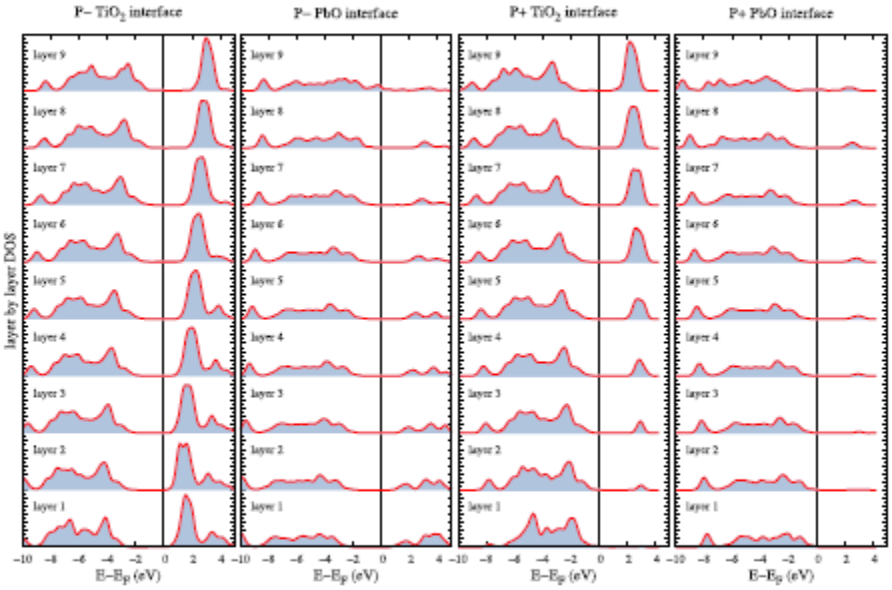

Figure 4. Layer-by-layer LDOS for the 9-PTO system. For a given polarization direction, LDOS for TiO_2 are in the left-hand column and for the PbO in the right-hand column. TiO_2 monolayer 1 is located at the TiO_2/SrO interface, and PbO monolayer 9 is located at the PbO/RuO_2 interface.

with $\rho(r')$ being the electron density. Then, the planar average $\overline{V}(z)$ and the nanoscale smoothed electrostatic potential, $\overline{\overline{V}}(z)$, were obtained [86]. Their profiles along z-axis are plotted in figure 5 for the slabs with thin electrodes and in figures S4 and S5 for the 9-PTO slab and 9-PTO supercell, respectively.

Figure 5 shows that in the 9- and 7-PTO thin electrode structures, the nano-smoothed potential varies linearly with z in the PTO layers, with the sign of the slope dependent on the polarization direction. This explains the observations in the previous section on the layer dependence of the local density of states. In the case of the 5-PTO system, the stable polarization state is that for P^- direction. In the 3-PTO slab the potential shows no slope along z axis, supporting its non ferroelectric state, in agreement with the ionic displacements and LDOS data. The potential gradient is the source of the built-in electric field, which is responsible for the energy level shift in the LDOS diagrams of figures 5 and S3(a), (b). Because the thickness of the thin electrodes is comparable with the penetration length of the ionic distortions from the PTO into the SRO layers, the nano-smoothed potential is not flat within these electrodes. The different vacuum levels on the left and right-hand sides of the slabs are due to the electrostatic dipolar interaction between surface charges in the neighboring slabs along z axis. By doubling the size of the SRO layers, e.g. the case of the 9-PTO capacitors, see figures S4 and S5, the potential recovers its flat profile within the electrodes. Also, it acquires the same value in the vacuum regions on each side of the slab, due to a better screening of the interface charges by the thicker SRO electrodes.

In the case of the thick electrode 9-PTO capacitor, at the SrO/TiO_2 interface, the observable flat portion of the macroscopic potential suggests a better *in situ* compensation of the polarization charges in the dielectric by the transferred charge from the electrode, than in the case of the PbO/RuO_2 interface. This implies that the amount of charge transferred at interface *I* is larger than that at interface *II*. Therefore, a larger interface dipole may be expected at the SrO/TiO_2 interface than at the PbO/RuO_2 interface.

In order to reveal the build-up of interface charge from the calculated charge density data we calculated the charge density difference, $\delta(\rho)$, by subtracting the charge densities calculated individually for each component of the capacitor from the slab total density, [87]. As a result, one obtains the charge density at interfaces due to bonding and charge transfer, i.e. the microscopic dipole [88], all other effects being removed. These results are displayed in figure 6 for the thin electrode slabs and in figure 7 for the 9-PTO slabs with thick electrodes. Referring to the nano-smoothed data, these plots indicate the formation of distinct interface dipoles in all slabs, with larger amplitude at the SrO/TiO_2 interface than at the PbO/RuO_2 one in the 9 and 7-PTO capacitors. Also, the interface dipoles are larger for the P^+ than for the P^- direction. It is interesting to note that in the metallic SRO layer the effects of charge redistribution can penetrate beyond the interface as shown in figure 7 where there is an additional sub-surface redistribution of charge in SRO when polarization is P^-.

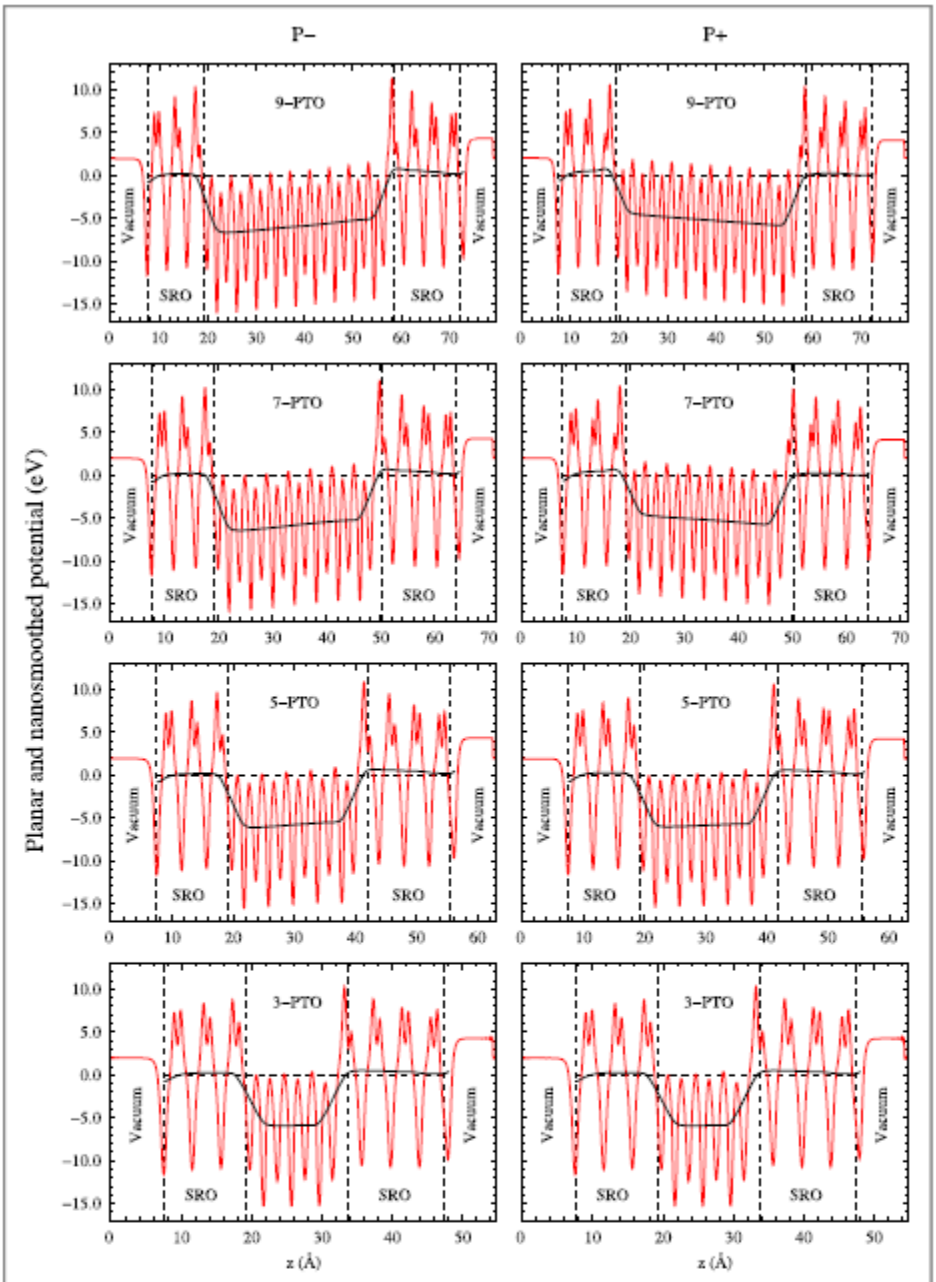

Figure 5. The planar average (red) and the nanoscale smoothed (black) electrostatic potential, V_{ES} along z-axis. The SrO/TiO_2 interface is on the PTO layer left side, and the PbO/RuO_2 interface is on the right side.

We have also analyzed the charge transfer at interfaces using an alternative approach and found the same effects (see figures S6–S8 in supporting information for details).

4.3. Polarization

The values of the layer-by-layer polarization calculated using equation (1) are plotted in figure 8. The relaxed ionic displacements in the SRO–PTO–SRO capacitors uphold a stable, switchable polarization, of about 0.6 C m^{-2} and 0.5 C m^{-2} in the 9- and 7-PTO capacitors, respectively. When the thickness of the dielectric is

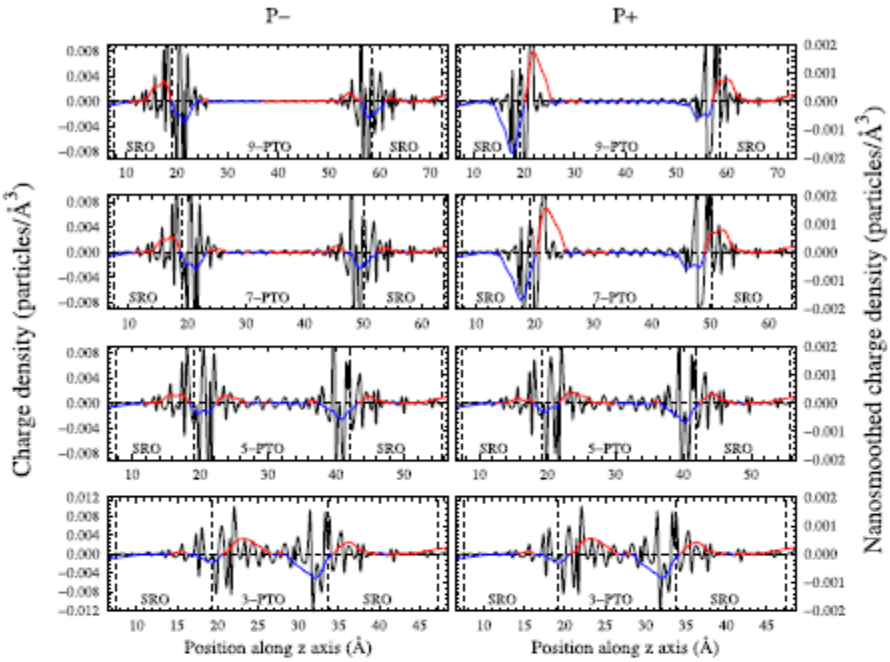

Figure 6. Charge density difference plots obtained by subtracting the partial charge densities calculated individually for each component of the slab from the total quantity: the macroscopic averaged data, black line, and the corresponding nano-smoothed data, red–blue line.

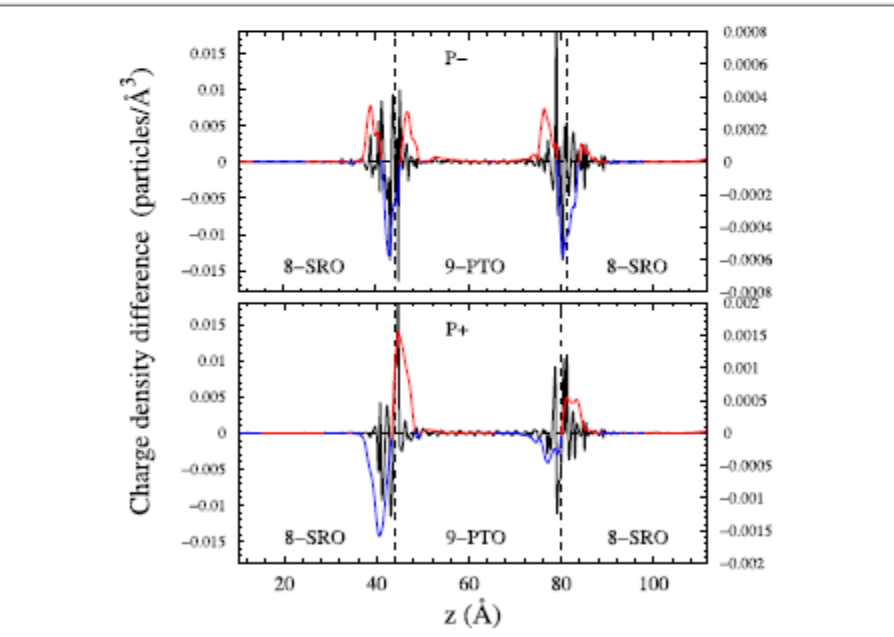

Figure 7. Charge density difference plots for the thick electrodes slab: the macroscopic averaged data, black line, and the corresponding nano-smoothed data, red–blue line.

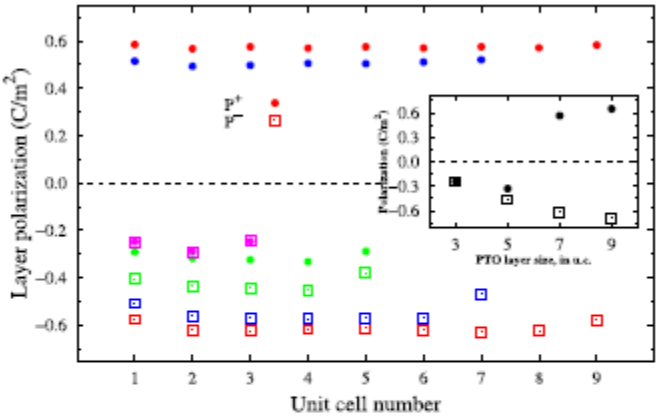

Figure 8. Layer-by-layer polarization calculated within DFPT. Solid symbols, P^+, hollow symbols, P^-. Color code: red, blue, green and magenta stand for the 9-PTO, 7-PTO, 5-PTO and 3-PTO slabs, respectively. Inset: PTO layer polarization obtained from Berry phase calculations. Solid symbols, P^+, hollow symbols, P^-.

down-sized to 5 unit cells, (~2 nm) a critical limit of polarization bi-stability is reached and only one energy minimum is effective in setting the spontaneous polarization direction, along $-z$. A further decrease of the PTO layer thickness to three PTO u.c. (about 1.2 nm) leads to space charge build-up throughout the whole structure, see figure S6, and the material loses ferroelectricity although it still experiences a finite polarization value.

A similar trend in the size effect on the ferroelectric state was also reported for ultrathin $SrRuO_3/BaTiO_3/SrRuO_3$ epitaxial heterostructures and was ascribed to a fixed, unfavorable interface dipole at the BaO/RuO_2 interface [82].

The ionic and electronic contributions to polarization were also calculated on supercells of the PTO layers at the structural parameters in the slab geometry, by employing the Berry's phase formalism [70]. This approach avoids the potential error due to metallic state in PTO unit cells at interfaces [51]. The results are plotted in the inset in figure 8 and show a fair agreement with the values of the layer-by-layer polarization calculated by using the Born charges.

5. Discussion

Based on the LDOS and electrostatic potential data shown in figures 4, S3(a)–(c) and figure 4, we have drawn the energy level schemes for the systems with thin electrodes in figure 9. The segments that mark the valence and conduction band edges of the individual PTO unit cells extend over the length of a lattice constant along z, and their colors, black and red, correspond to TiO_2 and PbO monolayers.

While most of the SBHs have positive values, (here we adhere to the sign convention on SBHs as also adopted in [45], at the SrO/TiO_2 interface in the case of 9- and 7-PTO capacitors we note negative SBHs (Ohmic contact, possible 'pathological' situation) for electrons and P^-, and negative SBHs for holes and P^+. At the PbO/RuO_2 interface, negative SBHs for holes are predicted for the 7- and 5-PTO slabs, for P^-.

One may observe a relative large shift in energy, of about 2 eV, for the VBM and CBM when switching the orientation of polarization in the 9- and 7-PTO capacitors. This is about twice the value previously reported for symmetric SRO–PTO-SRO capacitors, 1 eV [2]. The SBHs and ΔV_H values referring to the band alignment diagrams in figure 9 are also collected in table 1.

We suggest that at the SrO/TiO_2 interface, for $P+$, the 9- and 7-PTO systems show blocking contacts for holes, considering that the PTO layer is an (undoped) insulator [89]. A similar behavior is predicted at the PbO/RuO_2 interface, for $P-$, in the case of the 7- and 5-PTO systems. Actually, the systems under study show a transition of the Schottky barrier type for holes between the interfaces when changing the dielectric size and polarization direction.

The SBHs values derived from the energy level scheme drawn in figure 9 are affected by the presence of interface states due to bonding across interfaces and charge transfer from the metallic SRO to the dielectric PTO. An estimation of the effect of the interface states on the band alignment may be obtained by taking the Ti 3*s* semi-core states as reference for the VBM energy. These states are situated deep, at about −58 eV below the Fermi level, and hence their energy is barely sensitive to valence charge redistribution. Therefore, we have followed a

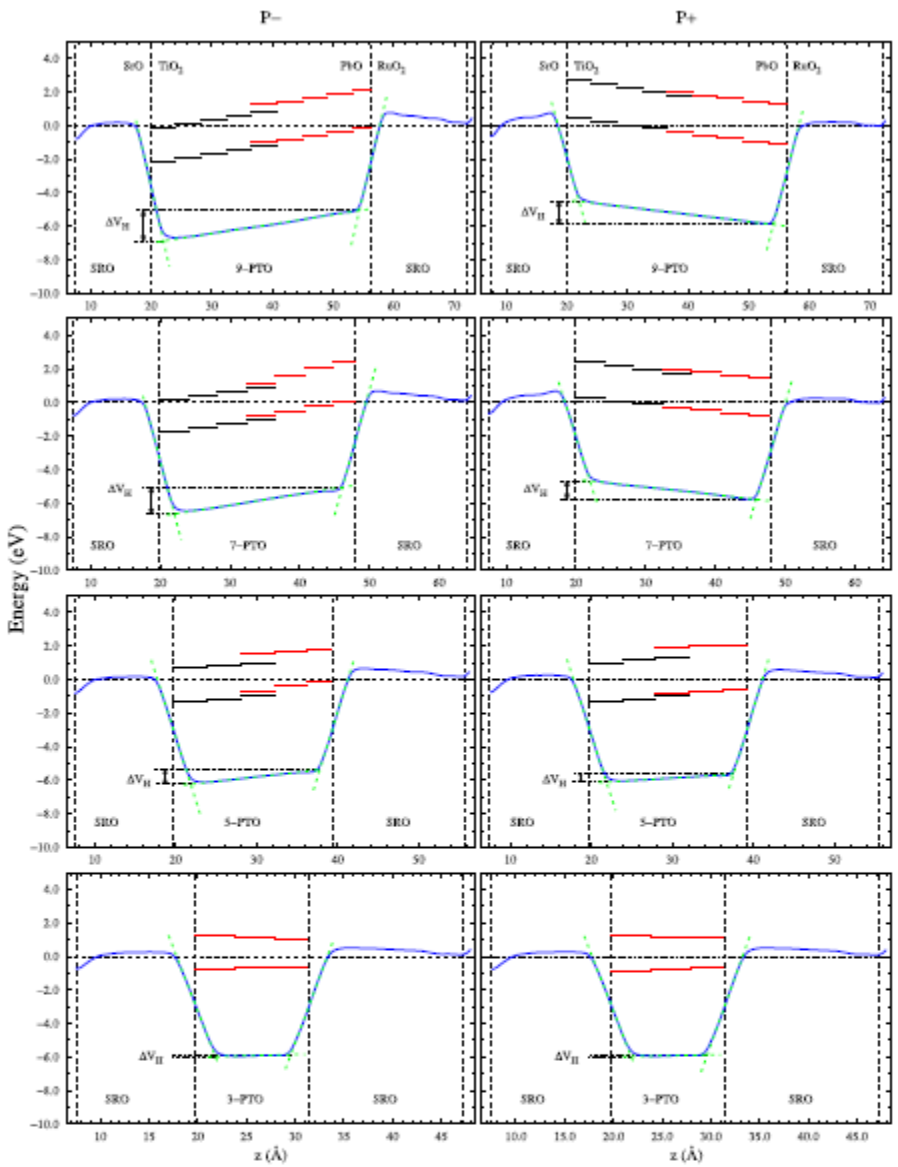

Figure 9. Band alignment diagrams considering the band line-up and band structure terms The black segments correspond to TiO_2 and red segments to PbO monolayers. Only the levels of half of the monolayers are marked, toward the corresponding interface, SrO/TiO_2 and PbO/RuO_2. The Fermi level is set at zero energy.

route as basically described in [17, 45] in order to align the band edges in the slabs with reference to Ti 3*s* states. First, we performed a bulk self-consistent calculation at the PTO structural parameters before the relaxation of the atomic positions in the slabs, to determine the Ti 3*s* energy level in the bulk, $E_{sc,b}(\mathrm{Ti}-3s) = -57.95$ eV, with $E_{\mathrm{VBM},b} = 0$ eV (the VBM energy in the bulk calculation). Then, we performed self consistent calculations on slabs in order to obtain the energy of the Ti 3*s* states, $E_{sc,s}$, with $E_{\mathrm{VBM},s}$ set at 0 eV. The VBM position with the Ti 3*s* level in the slab aligned to that in the bulk is given by:

$$E_{\mathrm{VBM},s} = E_{sc,s} + \Delta E_b, \tag{3}$$

Table 1. Schottky barrier heights (SBHs) for electrons (holes) Φ_n (Φ_p) and ΔV_H in eV.

		I_1		I_2		
		Φ_n	Φ_p	Φ_n	Φ_p	ΔV_H
9	P+	2.690	—	1.297	1.103	1.38
	P−	Ohmic	2.110	0.135	2.125	1.81
7	P+	2.477	—	1.476	0.824	1.1
	P−	Ohmic	1.776	2.486	—	1.6
5	P+	1.007	1.304	2.040	0.659	0.46
	P−	0.687	1.369	1.731	—	0.86

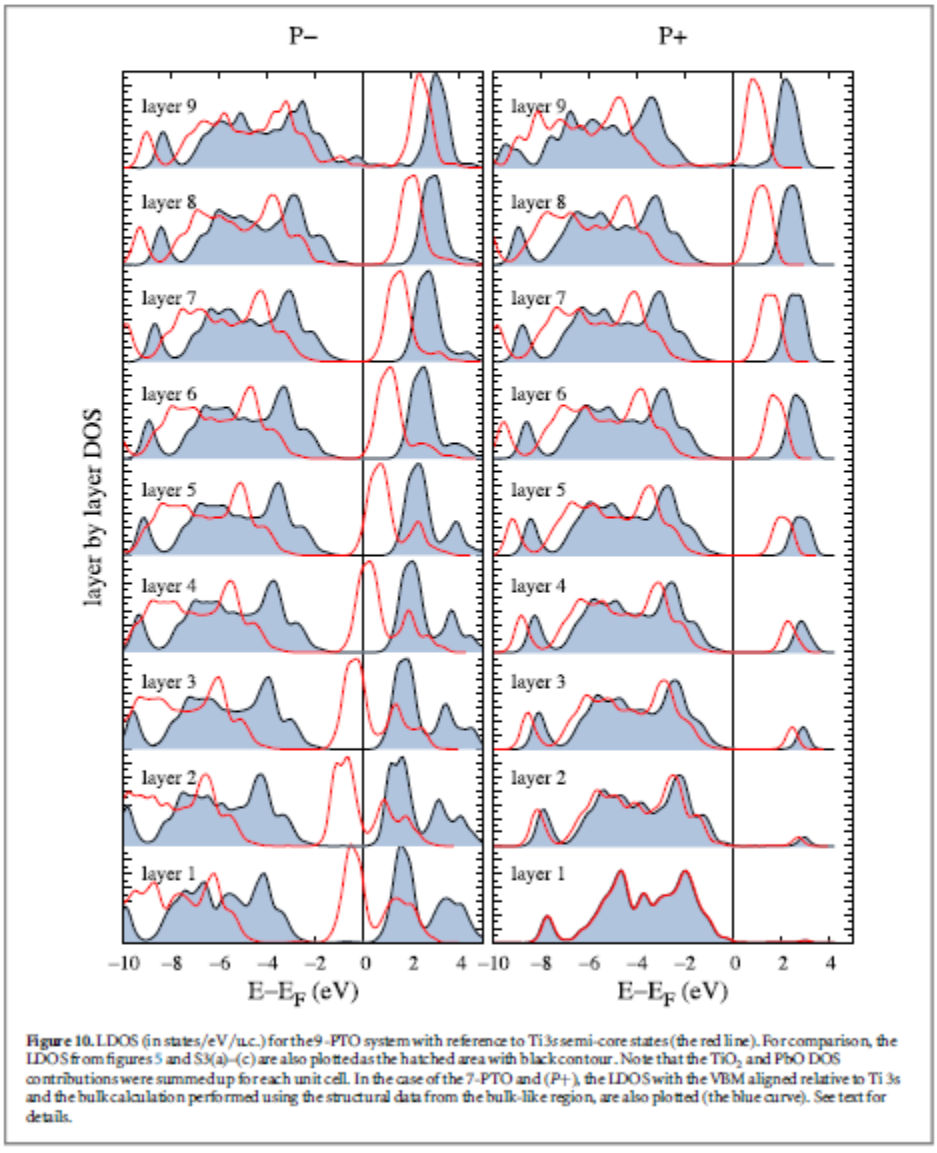

Figure 10. LDOS (in states/eV/u.c.) for the 9-PTO system with reference to Ti 3*s* semi-core states (the red line). For comparison, the LDOS from figures 5 and S3(a)–(*c*) are also plotted as the hatched area with black contour. Note that the TiO_2 and PbO DOS contributions were summed up for each unit cell. In the case of the 7-PTO and (*P*+), the LDOS with the VBM aligned relative to Ti 3*s* and the bulk calculation performed using the structural data from the bulk-like region, are also plotted (the blue curve). See text for details.

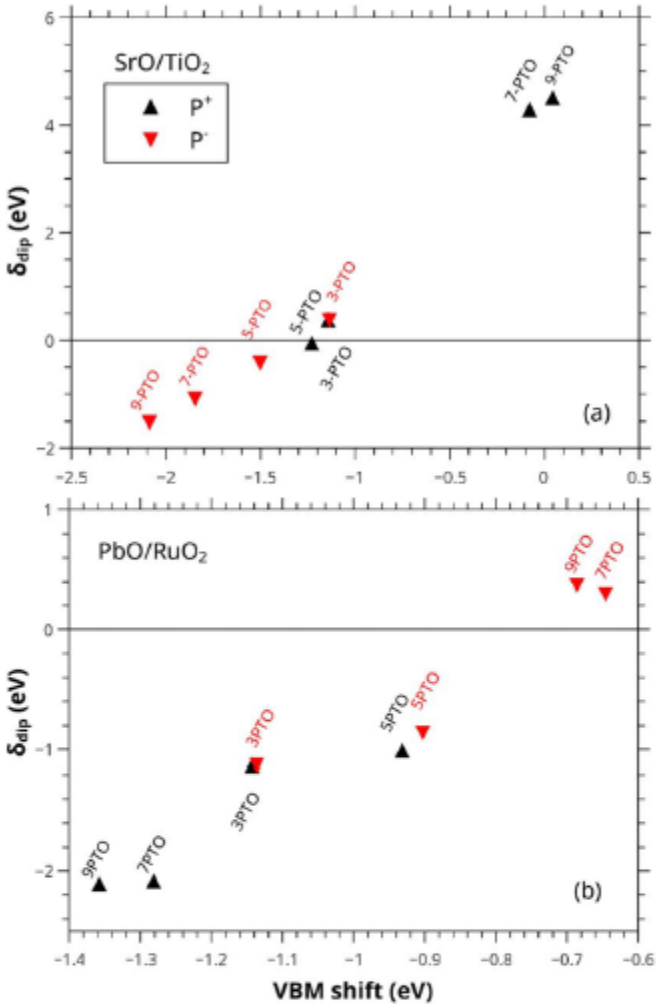

Figure 11. The interface dipole as a function of the VBM shift due to the presence of interface states. The potential drop at each interface was calculated as $\text{delta}_{dip} = V_{PTO} - V_{SRO}$ where V_{PTO} and V_{SRO} denote the potential values on the PTO and SRO sides of the interface, respectively.

where $\Delta E_b = E_{VBM,b} - E_{sc,b}$. The LDOS plots calculated according to this approach are shown as red curves in figure 10 and S9(a)–(c), superposed on the LDOS in figures 5 and S3(a)–(c), to enable a comparison between the results.

The approximation to use an unique Ti 3*s* energy value from bulk calculation for all the slabs is made in order to allow a straight comparison of the results, having in view the lack of bulk-like regions in the 5 and 3-PTO slabs, see figure 2). As an error check, we have made an evaluation of the variation in the Ti 3*s* energy level when the structural parameters of a PTO cell in the bulk-like region of the slab were used for the SCF bulk calculation, as proposed in [45], instead of an unique reference as described herein. For example, bulk calculations for the 9- and 7-PTO slabs, were performed at the structural parameters of the bulk-like cells in these slabs. We found that the term $\Delta E_b = E_{VBM,b} - E_{c,b}$, varies by 76 meV for 9-PTO and 81 meV for 7-PTO with respect to the initial value calculated for the bulk PTO before relaxation. Based on these results, we suggest that such small shifts in the LDOS, shown in figure S9(a) for the 7-PTO slab P^+ (in blue), as an example, can not determine qualitative changes in the predicted positions of the band edges. The LDOS plots in figures 10 and S9(a)–(c) reveal significant differences between the positions of the valence and conduction band edges in the two data sets, particularly for the 9- and 7-PTO capacitors. Referring to the LDOS results in the alignment

relative to the Ti 3*s* semi-core states, the presence of MIGS and the Fermi level location relative to the conduction band edge points to a 'pathological' regime at the PbO/RuO_2 interface, according to [45], for the 9 and 7-PTO slabs, for P^+, and at the SrO/TiO_2 interface for P^-. In the case of the 5-PTO slab, a 'pathological' regime may be invoked at the SrO/TiO_2 interfaces for both directions of polarization. Nevertheless, taking into account that the present results have been obtained using a band gap corrective approach, with a calculated band gap of about 3 eV in the bulk PTO, we suggest that the predicted behaviors are not artefacts of the DFT calculations, but real Ohmic contacts. We emphasize that in such cases, the experimental verification of the calculation results is highly recommended.

Information on the charge re-arrangement and formation of interface dipoles may provide useful hints for understanding the factors contributing to the interface properties, such as bonding across interface, interface states and effect of the built in electric field. Therefore, we evaluated the magnitude of the interface dipoles in the systems under investigation, starting from the charge density difference data in figure 6 and solving the 1D Poisson equation for the electrostatic potential. Then, the microscopic interface dipole, δ_{dip}, was evaluated as the potential drop at each interface [88, 90]. Figure 11 displays the δ_{dip} values for the thin electrode capacitors as a function of the VBM shift when the Ti 3*s* semi-core states are used as reference with respect to the band line-up scheme (see figure 9). This difference reflects the effect of the interface states on the VBM (CBM) positions. In the case of the 9- and 7-PTO capacitors, figure 11 shows the followings: (i) the dipoles change sign according to the polarization direction, at both interfaces; (ii) also, for a given interface, the dipoles are bigger, in absolute value, for P^+ than for P^- orientation. (iii) The dipoles are bigger at the SrO/TiO_2 interface than at the PbO/RuO_2 interface, for $\pm z$ polarization. (iv) In the case of the 5- and 3-PTO slabs, the dipoles do not change sign with the polarization direction, in accordance with polar displacement and polarization results.

We also note a direct correlation between the magnitude of δ_{dip} and the VBM shift at the PbO/RuO_2 interface, for the 9-, 7- and 5-PTO slabs. However, at the SrO/TiO_2 interface we note a direct correlation for P^-, and a reciprocal correlation for P^+. In the open-circuit condition of the capacitors under investigation, we suggest that the bonding at the SrO/TiO_2 interface favors local charge build-up and therefore the creation of a larger dipole than that at the PbO/RuO_2 interface.

6. Conclusions

We performed first principles calculations of the polar distortions and electronic properties in $SrRuO_3/PbTiO_3/SrRuO_3$ ferroelectric capacitors with asymmetric interfaces, in order to examine the band bending, band alignment and interface dipoles in their dependence on the dielectric size. The main results of this work are summarized as follows.

- It is shown that a switchable polarization, of about 0.5 C m^{-2} is preserved in capacitors with dielectric size larger than 2 nm.
- A monostable polarization state is evidenced in capacitors with PTO layer of about 2 nm.
- No band bending and a loss of ferroelectricity is predicted below this limit.
- The band alignment scheme drawn from the local density of states calculated within the GGA+U framework shows possible Ohmic contact at an interface and Schottky barrier at the other interface in the 9- and 7-PTO structures, for a given polarization direction. If experimentally proven realistic, such characteristics may be of interest to achieve tunneling electro-resistive junctions.
- The LDOS plots with the VBM aligned relative to Ti 3*s* semicore states clearly evidence Ohmic contacts at the PbO/RuO_2 interface for P^+, and at the SrO/TiO_2 interface for P^-, in the case of the 9 and 7-PTO slabs. Possible Ohmic contact is predicted at the SrO/TiO_2 interface for the 5-PTO slab.
- The interface dipoles re-orient themselves with the forward–backward polarization only in the 9- and 7-PTO capacitors. They are significantly bigger at the SrO/TiO_2 interfaces than at the PbO/RuO_2 ones. It is found that at the PbO/RuO_2 interface, the larger is the VBM shift, the larger is the interface dipole. Contrasting correlations for forward–backward polarization are predicted at the SrO/TiO_2 interfaces. These results suggest intricate effects of bonding across interfaces, internal electrostatic field and dielectric size on local charge transfers.
- The size of the barrier and the switching effect can be changed by changing the thickness of the PTO layer.

- Finally, it is worth highlighting the significant polar displacements induced by the ferroelectric dielectric into the SRO electrodes. However, taking into account the high density of states at the Fermi level in the SRO layer, we rule out a possible onset of a ferroelectric metallic state at the SRO–PTO interfaces.

Acknowledgments

The authors LDF, LP and NP thank the financial support of the Romanian Ministry of Research and Innovation through the Core Program of NIMP (contract PN18-110101), PFE-CDI-339 (contract PFE nr. 12 din 2018) and the PCCF project nr. PN-III-P4-ID-PCCF-2016-0047 (contract PCCF nr. 16 din 2018) funded by the Ministry of Research and Innovation though UEFISCDI.

ORCID iDs

Lucian Dragos Filip https://orcid.org/0000-0001-7319-1758

References

[1] Junquera J and Ghosez P 2003 Critical thickness for ferroelectricity in perovskite ultrathin films *Nature* 422 506–9
[2] Umeno Y, Albina J M, Meyer B and Elsässer C 2009 *Ab initio* calculations of ferroelectric instability in $PbTiO_3$ capacitors with symmetric and asymmetric electrode layers *Phys. Rev.* B 80 205122
[3] Garcia V and Bibes M 2014 Ferroelectric tunnel junctions for information storage and processing *Nat. Commun.* 5 4289
[4] Boni A-G, Filip L, Chirila C, Pasuk I, Negrea R, Pintilie I and Pintilie L 2017 Multiple polarization states in symmetric ferroelectric heterostructures for multi-bit non-volatile memories *Nanoscale* 9 19271
[5] Yin L, Wang X and Mi W 2018 Ferromagnetic, ferroelectric, and optical modulated multiple resistance states in multiferroic tunnel junctions *ACS Appl. Mater. Interfaces* 11 1057–64
[6] Dawber M, Rabe K M and Scott J F 2005 Physics of thin-film ferroelectric oxides *Rev. Mod. Phys.* 77 1083–130
[7] Gerra G, Tagantsev A K, Setter N and Parlinski K 2006 Ionic polarizability of conductive metal oxides and critical thickness for ferroelectricity in $BaTiO_3$ *Phys. Rev. Lett.* 96 107603
[8] Duan C-G, Sabirianov R F, Mei W-N, Jaswal S S and Tsymbal E Y 2006 Interface effect on ferroelectricity at the nanoscale *Nano Lett.* 6 483–7
[9] Velev J P, Duan C-G, Belashchenko K D, Jaswal S S and Tsymbal E Y 2007 Effect of ferroelectricity on electron transport in $Pt/BaTiO_3/Pt$ tunnel junctions *Phys. Rev. Lett.* 98 137201
[10] Wu X, Stengel M, Rabe K M and Vanderbilt D 2008 Predicting polarization and nonlinear dielectric response of arbitrary perovskite superlattice sequences *Phys. Rev. Lett.* 101 087601
[11] Velev J P, Duan C-G, Burton J D, Smogunov A, Niranjan M K, Tosatti E, Jaswal S S and Tsymbal E Y 2008 Magnetic tunnel junctions with ferroelectric barriers: prediction of four resistance states from first principles *Nano Lett.* 9 427–32
[12] Zhuravlev M Y, Sabirianov R F, Jaswal S S and Tsymbal E Y 2005 Giant electroresistance in ferroelectric tunnel junctions *Phys. Rev. Lett.* 94 246802
[13] Lorenz M *et al* 2016 The 2016 oxide electronic materials and oxide interfaces roadmap *J. Phys. D: Appl. Phys.* 49 433001
[14] Tornos J *et al* 2019 Ferroelectric control of interface spin filtering in multiferroic tunnel junctions *Phys. Rev. Lett.* 122 037601
[15] Walsh A and Butler K T 2013 Prediction of electron energies in metal oxides *Acc. Chem. Res.* 47 364–72
[16] Butler K T, Buckeridge J, Catlow C R A and Walsh A 2014 Crystal electron binding energy and surface work function control of tin dioxide *Phys. Rev.* B 89 115320
[17] Butler K T, Frost J M and Walsh A 2015 Ferroelectric materials for solar energy conversion: photoferroics revisited *Energy Environ. Sci.* 8 838–48
[18] Liu Y *et al* 2018 Chemical nature of ferroelastic twin domains in $CH_3NH_3PBI_3$ perovskite *Nat. Mater.* 17 1013
[19] Plugaru N, Nemnes G A, Filip L, Pintilie I, Pintilie L, Butler K T and Manolescu A 2017 Atomistic simulations of methylammonium lead halide layers on $pbtio_3$ (001) surfaces *J. Phys. Chem.* C 121 9096–109
[20] Yang Y *et al* 2019 An ultrathin ferroelectric perovskite oxide layer for high-performance hole transport material free carbon based halide perovskite solar cells *Adv. Funct. Mater.* 29 1806506
[21] Wilson J N, Frost J M, Wallace S K and Walsh A 2019 Dielectric and ferroic properties of metal halide perovskites *APL Mater.* 7 010901
[22] Ji C, Liu S, Han S, Tao K, Sun Z and Luo J 2018 Towards a spectrally customized photoresponse from an organic–inorganic hybrid ferroelectric *Angew. Chem. Int. Ed.* 57 16764–7
[23] Cordero F, Craciun F, Trequattrini F, Imperatori P, Paoletti A M and Pennesi G 2018 Competition between polar and antiferrodistortive modes and correlated dynamics of the methylammonium molecules in $MaPbI_3$ from anelastic and dielectric measurements *J. Phys. Chem. Lett.* 9 4401–6
[24] Young J and Rondinelli J M 2018 Inducing spontaneous electric polarizations in double perovskite iodide superlattices for ferroelectric photovoltaic materials *Phys. Rev. Mater.* 2 065406
[25] Fiebig M, Lottermoser T, Meier D and Trassin M 2016 The evolution of multiferroics *Nat. Rev. Mater.* 1 16046
[26] Ferenstein W, Mathur N D and Scott J F 2006 Multiferroic and magnetoelectric materials *Nature* 442 759
[27] Gajek M, Bibes M, Fusil S, Bouzehouane K, Fontcuberta J, Barthelemy A and Fert A 2007 Tunnel junctions with multiferroic barriers *Nat. Mater.* 6 296
[28] Ramesh R and Spaldin N A 2007 Multiferroics: progress and prospects in thin films *Nat. Mater.* 6 21
[29] Velev J P, Jaswal S S and Tsymbal E Y 2011 Multi-ferroic and magnetoelectric materials and interfaces *Phil. Trans. R. Soc.* A 369 3069–97
[30] Imam M, Stojić N and Binggeli N 2017 Ferroelectric switching of band alignments in ISMO/PZT/Co multiferroic tunnel junctions: an *ab initio* study *Nanotechnology* 28 315202
[31] Hausmann S *et al* 2017 Atomic-scale engineering of ferroelectric-ferromagnetic interfaces of epitaxial perovskite films for functional properties *Sci. Rep.* 7 10734

[32] Narayan A, Cano A, Balatsky A V and Spaldin N A 2019 Multiferroic quantum criticality *Nat. Mater.* 18 223
[33] Spaldin N A and Fiebig M 2005 The renaissance of magnetoelectric multiferroics *Science* 309 391–2
[34] Spaldin N A and Ramesh R 2019 Advances in magnetoelectric multiferroics *Nat. Mater.* 18 203
[35] Callori S J, Gabel J, Su D, Sinsheimer J, Fernandez-Serra M V and Dawber M 2012 Ferroelectric $Pbtio_3/Srruo_3$ superlattices with broken inversion symmetry *Phys. Rev. Lett.* 109 067601
[36] De Luca G, Strkalj N, Manz S, Bouillet C, Fiebig M and Trassin M 2017 Nanoscale design of polarization in ultrathin ferroelectric heterostructures *Nat. Commun.* 8 1419
[37] Kwon O *et al* 2018 Direct probing of polarization charge at nanoscale level *Adv. Mater.* 30 1703675
[38] Tănase L C *et al* 2018 Polarization orientation in lead zirconate titanate (001) thin films driven by the interface with the substrate *Phys. Rev. Appl.* 10 034020
[39] Granozio F M, Koster G and Rijnders G 2013 Functional oxide interfaces *MRS Bull.* 38 1017–23
[40] Pintilie L *et al* 2015 Polarization induced self-doping in epitaxial $Pb(Zr_{0.2}Ti_{0.80})O_3$ thin films *Sci. Rep.* 5 14974
[41] Nguyen M D, Houwman E P and Rijnders G 2018 Energy storage performance and electric breakdown field of thin relaxor ferroelectric plztfilms using microstructure and growth orientation control *J. Phys. Chem. C* 122 15171–9
[42] Liao Z *et al* 2017 Thickness dependent properties in oxide heterostructures driven by structurally induced metal-oxygen hybridization variations *Adv. Funct. Mater.* 27 1606717
[43] Li L *et al* 2018 Epitaxial stress-free growth of high crystallinity ferroelectric $PbZr_{0.52}Ti_{0.48}O_3$ on GaN/ALGaN/Si (111) substrate *Adv. Mater. Interfaces* 5 1700921
[44] Morozovska A N, Eliseev E A, Svechnikov S V, Krutov A D, Shur V Y, Borisevich A Y, Maksymovych P and Kalinin S V 2010 Finite size and intrinsic field effect on the polar-active properties of ferroelectric-semiconductor heterostructures *Phys. Rev.* B 81 205308
[45] Stengel M, Aguado-Puente P, Spaldin N A and Junquera J 2011 Band alignment at metal/ferroelectric interfaces: insights and artifacts from first principles *Phys. Rev.* B 83 235112
[46] Zubko P, Gariglio S, Gabay M, Ghosez P and Triscone J-M 2011 Interface physics in complex oxide heterostructures *Annu. Rev. Condens. Matter Phys.* 2 141–65
[47] Aguado-Puente P and Junquera J 2013 First-principles study of metal-induced gap states in metal/oxide interfaces and their relation with the complex band structure *MRS Commun.* 3 191–7
[48] Chen W J, Zheng Y, Luo X, Wang B and Woo C H 2013 *Ab initio* study on the size effect of symmetric and asymmetric ferroelectric tunnel junctions: a comprehensive picture with regard to the details of electrode/ferroelectric interfaces *J. Appl. Phys.* 114 064105
[49] Burton J D and Tsymbal E Y 2010 Evolution of the band alignment at polar oxide interfaces *Phys. Rev.* B 82 161407
[50] Margaritondo G 2012 *Electronic Structure of Semiconductor Heterojunctions* vol 1 (Berlin: Springer)
[51] Hong S, Nakhmanson S M and Fong D D 2016 Screening mechanisms at polar oxide heterointerfaces *Rep. Prog. Phys.* 79 076501
[52] Meyer B and Vanderbilt D 2001 *Ab initio* study of $Batio_3$ and $Pbtio_3$ surfaces in external electric fields *Phys. Rev.* B 63 205426
[53] Stengel M and Spaldin N A 2007 *Ab initio* theory of metal-insulator interfaces in a finite electric field *Phys. Rev.* B 75 205121
[54] Stengel M, Spaldin N A and Vanderbilt D 2009 Electric displacement as the fundamental variable in electronic-structure calculations *Nat. Phys.* 5 304
[55] Stengel M, Vanderbilt D and Spaldin N A 2009 First-principles modeling of ferroelectric capacitors via constrained displacement field calculations *Phys. Rev.* B 80 224110
[56] Giannozzi P *et al* 2009 Quantum espresso: a modular and open-source software project for quantum simulations of materials *J. Phys.: Condens. Matter* 21 395502 (19pp)
[57] Giannozzi P *et al* 2017 Advanced capabilities for materials modelling with quantum espresso *J. Phys.: Condens. Matter* 29 465901
[58] Perdew J P, Burke K and Ernzerhof M 1996 Generalized gradient approximation made simple *Phys. Rev. Lett.* 77 3865
[59] Perdew J P, Ruzsinszky A, Csonka G I, Vydrov O A, Scuseria G E, Constantin L A, Zhou X and Burke K 2008 Restoring the density-gradient expansion for exchange in solids and surfaces *Phys. Rev. Lett.* 100 136406
[60] Vanderbilt D 1990 Soft self-consistent pseudopotentials in a generalized eigenvalue formalism *Phys. Rev.* B 41 7892
[61] Dal Corso A 2014 Pseudopotentials periodic table: From H to Pu *Comp. Mat. Sci.* 95 337–50
[62] Monkhorst H J and Pack J D 1976 Special points for brillouin-zone integrations *Phys. Rev.* B 13 5188
[63] Bengtsson L 1999 Dipole correction for surface supercell calculations *Phys. Rev.* B 59 12301
[64] Anisimov V I, Zaanen J and Andersen O K 1991 Band theory and mott insulators: Hubbard U instead of stoner I *Phys. Rev.* B 44 943–54
[65] Dudarev S L, Botton G A, Savrasov S Y, Humphreys C J and Sutton A P 1998 Electron-energy-loss spectra and the structural stability of nickel oxide: an lsda + ustudy *Phys. Rev.* B 57 1505
[66] Cococcioni M and De Gironcoli S 2005 Linear response approach to the calculation of the effective interaction parameters in the LDA +U method *Phys. Rev.* B 71 035105
[67] Brehm J A, Takenaka H, Lee C-W, Grinberg I, Bennett J W, Schoenberg M R and Rappe A M 2014 Density functional theory study of hypothetical pbtio 3-based oxysulfides *Phys. Rev.* B 89 195202
[68] Nakhmanson S M, Rabe K M and Vanderbilt D 2005 Polarization enhancement in two- and three-component ferroelectric superlattices *Appl. Phys. Lett.* 87 102906
[69] Baroni S, De Gironcoli S, Corso A D and Giannozzi P 2001 Phonons and related crystal properties from density-functional perturbation theory *Rev. Mod. Phys.* 73 515
[70] King-Smith R D and Vanderbilt D 1993 Theory of polarization of crystalline solids *Phys. Rev.* B 47 1651
[71] Giannozzi P *et al* 2009 QUANTUM ESPRESSO: a modular and open-source software project for quantum simulations of materials *J. Phys.: Condens. Matter* 21 395502
[72] Filip L D, Plugaru N and Pintilie L 2019 Polarization branches and optimization calculation strategy applied to Abo_3 ferroelectrics *Modell. Simul. Mater. Sci. Eng.* 27 045008
[73] Shen X, Qiu X, Su D, Zhou S, Li A and Wu D 2015 Thickness-dependent metal-insulator transition in epitaxial $Srruo_3$ ultrathin films *J. Appl. Phys.* 117 015307
[74] Kolpak A M, Sai N and Rappe A M 2006 Short-circuit boundary conditions in ferroelectric $Pbtio_3$ thin films *Phys. Rev.* B 74 054112
[75] Madelung O, Rössler U and Schulz M 2000 Landolt-börnstein new series, group: iii. Condensed matter, ternary compounds, organic semiconductors
[76] Glazer A M and Mabud S A 1978 Powder profile refinement of lead zirconate titanate at several temperatures: II. pure $Pbtio_3$ *Acta Crystallogr.* B 34 1065–70
[77] Rabe K M 2010 First-principles calculations of complex metal-oxide materials *Annu. Rev. Condens. Matter Phys.* 1 211–35
[78] Pertsev N A, Zembilgotov A G and Tagantsev A K 1998 Effect of mechanical boundary conditions on phase diagrams of epitaxial ferroelectric thin films *Phys. Rev. Lett.* 80 1988–91

[79] He J, Borisevich A, Kalinin S V, Pennycook S J and Pantelides S T 2010 Control of octahedral tilts and magnetic properties of perovskite oxide heterostructures by substrate symmetry *Phys. Rev. Lett.* **105** 227203
[80] Chirila C, Ibanescu G, Hrib L, Negrea R, Pasuk I, Kuncser V, Pintilie I and Pintilie L 2013 Structural, electric and magnetic properties of $Pb(Zr_{0.2}Ti_{0.8})O_3 - -CoFe_2O_4$ heterostructures *Thin Solid Films* **545** 2–7
[81] Ryee S and Han M J 2017 Magnetic ground state of srruo3 thin film and applicability of standard first-principles approximations to metallic magnetism *Sci. Rep.* **7** 4635
[82] Liu X, Wang Y, Lukashev P V, Burton J D and Tsymbal E Y 2012 Interface dipole effect on thin film ferroelectric stability: first-principles and phenomenological modeling *Phys. Rev.* B **85** 125407
[83] Lu H *et al* 2012 Enhancement of ferroelectric polarization stability by interface engineering *Adv. Mater.* **24** 1209–16
[84] Filippetti A, Fiorentini V, Ricci F, Delugas P and Íñiguez J 2016 Prediction of a native ferroelectric metal *Nat. Commun.* **7** 11211
[85] Shannon R D 1976 Revised effective ionic radii and systematic studies of interatomic distances in halides and chalcogenides *Acta Crystallogr.* A **32** 751–67
[86] Junquera J, Cohen M H and Rabe K M 2007 Nanoscale smoothing and the analysis of interfacial charge and dipolar densities *J. Phys.: Condens. Matter* **19** 213203
[87] Jung Y-K, Butler K T and Walsh A 2017 Halide perovskite heteroepitaxy: bond formation and carrier confinement at the PbS-CsPBBr3 interface *J. Phys. Chem.* C **121** 27351–6
[88] Wager J F 2008 Transparent electronics: Schottky barrier and heterojunction considerations *Thin Solid Films* **516** 1755–64
[89] Kao K C 2004 Charge carrier injection from electrical contacts *Dielectric Phenomena in Solids* ed K C Kao (New York: Academic) pp 327–80
[90] Yajima T, Hikita Y, Minohara M, Bell C, Mundy J A, Kourkoutis L F, Muller D A, Kumigashira H, Oshima M and Hwang H Y 2015 Controlling band alignments by artificial interface dipoles at perovskite heteroi interfaces *Nat. Commun.* **6** 6759

Anexa 2

Applied Surface Science 502 (2020) 144101

Contents lists available at ScienceDirect

Applied Surface Science

journal homepage: www.elsevier.com/locate/apsusc

Full Length Article

The interplay of work function and polarization state at the Schottky barriers height for Cu/$BaTiO_3$ interface

Dana Georgeta Popescu[a,*], Marius Adrian Husanu[a], C. Chirila[a], L. Pintilie[a], C.M. Teodorescu[a]

[a] National Institute of Materials Physics, Atomistilor 405A, 077125 Magurele, Romania

ARTICLE INFO

Keywords:
X-ray photoelectron spectroscopy
First principle calculation
Band bending
Barium titanate

ABSTRACT

The emerging field of electronics based on ferro-functional materials relies on driving effectively and predictably a ferroelectric system between different polarization states through bias applied to metallic contacts. This requires detailed understanding of the growth mechanisms and electronic properties of the interface, including ferroelectric and material – dependent band alignment and Schottky barrier heights. Whether the major contribution at the interface band alignment comes from the work function difference or from the ferroelectric state is still under debate. Here, using X-ray photoemsion and *ab-initio* calculations, we derive the complex microscopic picture of metal/ferroelectric interface formation, including growth mechanism, valence alteration, ferroelectric-dependent electrostatic potential and thickness – dependent compensation mechanisms of ferroelectricity, starting from the ultrathin growth of Cu up to 100Å on $BaTiO_3$. One establishes the evolution of the band bending and of the build-in potential from the initial probed thickness of the ferroelectric in the range of 3λ (λ – the inelastic mean free path) while gradually approaching the contact region with the metal at higher thickness of the top layer. We find that the well-defined orientation of the ferroelectric polarization lead to a band bending at the interface, which add at the bending expected from the work function difference of the two joining materials.

1. Introduction

The spontaneous polarization of ferroelectric (FE) materials is reversible at a certain voltage below the coercive field [1]. Their fundamental property of electrically switchable spontaneous polarization below Curie temperature made them be promising materials for a different number of applications such as non-volatile memory storage devices [2], nonlinear optics [3], for their piezoelectricity and pyroelectricity [4], in ferroelectric capacitors [5]. Usually the ferroelectric system is driven through a metallic electrode, thus the metal-ferroelectric interface becomes an important issue to address in device physics. In contrast to lead titanate $PbZrTiO_3$ (PZT), barium titanate $BaTiO_3$ (BTO) demonstrate several advantages regarding non-volatile memories like non-toxic elements, crystallizing at lower temperature, lower fatigue effects and higher compatibility with integrated circuits [6–9]. The semiconducting character of ferroelectric thin films, exceeding sometimes 100 nm, is involved in stabilization of single-domain ferroelectric states having the polarization perpendicular to the film [10]. Mobiles charge carriers from the ferroelectric thin film may be transferred by the internal field P/ε (with P= polarization perpendicular to the surface of the ferroelectric, $\varepsilon = \varepsilon_0\varepsilon_r$= dielectric permittivity of the ferroelectric), close to the surface or across the interface. In absence of any other sources of extrinsic screening these electrons and holes form layers which screen the depolarization field inside the film accompanied by band bending occurring near the free ferroelectric surface. Its magnitude is given by $eP\delta/\varepsilon$ ratio, where δ is distance between the surface and the polarization charge sheet and e the elementary charge [11]. For a polarization oriented inwards, the bands are bending toward lower binding energies near surfaces, while for an outwards polarization the bending is toward higher binding energies [12]. It was shown that core levels shift rigidly with respect the vacuum level and with the valence band maximum, following the band alignment direction [12–17], thus X-ray Photoelectron Spectroscopy (XPS) investigation emerges as a useful tool to extract important information on the band bending close to the surfaces and their corresponding interfaces with different electrodes. It is known that valence band (VB) investigation using soft X-rays photoemission is notoriously difficult due to its decrease of the photoexcitation cross section by orders of magnitude compared to the core levels. Moreover, the valence band maximum may be hindered by the larger density of states at the Fermi level of the metal and by the consequent attenuation of the VB signal of the semiconductor by the top metal [18]. Hence, from a practical

* Corresponding author.
E-mail address: dana.popescu@infim.ro (D.G. Popescu).

https://doi.org/10.1016/j.apsusc.2019.144101
Received 18 December 2018; Received in revised form 21 August 2019; Accepted 18 September 2019
Available online 19 October 2019

perspective, XPS technique offers the possibility to infer the band alignment in semiconductors near the contact region with a metal deposited on its surface, by inspecting the core-level shifts instead of monitoring the valence band (VB) changes. Generally, migration of the electrons from the system with lower work function (WF) into the one with a higher WF operates in the contact region of a metal with a semiconductor. This mechanism develops until the internal field at the interface prevents further charge migration and results in a band bending for the semiconductor. Its magnitude is comparable to the WF difference between the metal and the semiconductor. Indeed, recent experiments evidenced the importance of the build-in-potential at metal-ferroelectric interface depending on of the nature of the electrode used in these contacts. PZT was used in the previous studies due to to its large saturation polarization (about 1 Cm^{-2}). Nevertheless, for future practical applications, switching to Pb free materials is strongly encouraged. Barium-titanate represents an environment-friendly, affordable ferroelectric material with considerably lower saturation polarization, thus easily switcheable between opposed ferroelectric states. Chen and co-workers showed that by *in situ* biasing a ferroelectric system, all core levels vary as a function of the bias – switched ferroelectric polarization [19]. Namely, the polarization dependent core level shift of a BTO film sandwiched between top Pt or RuO_2 and bottom Pt electrode is of −1.1 eV for the symmetric structure and of −0.6 eV for the asymmetric one. By considering the additional effect of the depolarization charge-induced bending at free ferroelectric surfaces, one can extend this approach to ferroelectrics [12,18]. By studying gold and copper grown on lead zircon-titanate (PZT), some intricate phenomena were identified, where top deposition initiate first with unconnected metallic clusters and their corresponding positive or negative charging effects and shifts towards higher or lower binding energies, depending on the substrate ferroelectric state and the WF difference of the two materials. Later, at higher metal coverage, these clusters coalesce, finally connecting to the ground of the system and acting as a charge reservoir [14]. In the Au case the effect of FE polarization-induced band bending and Schottky barrier formation add up, while in the Cu case, the initial band bending term (due to FE polarization) vanishes, and the second, due to the different WFs of the heterointerface is enhanced when the layers become continuous. Indeed, Bucur et al. have shown that in the case of Pt deposited on PZT, the shift towards higher binding energies is associated with a band bending downwards due to the occurrence of an out-of-plane $P^{(+)}$ state of the film near the surface, and that the corresponding electric field outside the film promotes electrons from the metal towards the film, to compensate for the depolarization field [20].

In the following, we investigate the polarization dependent Schottky barrier heights (SBH) at Cu/BTO interfaces by using XPS, starting from the early stage of its formation at sub-monolayer thickness. During successive metal deposition steps (2, 4, 16, 24, 40, 100 Å) on BTO substrate we establish gradual band alignment from the shift of the core levels with respect the Fermi level of the metal which add at the bending expected from the WF difference. The mechanisms involved points at the ferroelectric induced polarization effects. The results are supplemented by first-principle calculations, adding information regarding the preferences of the copper layers deposition on the different polarization domains on the BTO substrate and on the different compensation mechanisms for ferroelectric polarization pointing towards or away from the metallic electrode.

2. Experimental and computational methods

Epitaxial BTO layers 150 nm thick are grown by pulsed laser deposition (PLD) on $SrTiO_3$(1 0 0) (STO) with $SrRuO_3$ bottom electrode. The PLD parameters used are KrF radiation at 248 nm wavelength with 5000 pulses, repetition rate 5 Hz and laser fluence 1.5 J/cm^2. The substrate was heated at 700 °C and the partial O_2 pressure was 14 Pa when growing the ferroelectric BTO. Since the PLD setup and the surface science cluster (where metals are deposited and XPS measurements are performed) are not in vacuum connected, after the preparation, the sample was extracted from PLD setup and introduced into surface science cluster (Specs). Cu was gradually deposited at room temperature after reducing the surface contamination by annealing the samples at about 180 °C. Deposition is performed close to normal incidence, in a molecular beam epitaxy (MBE) chamber, connected in vacuum to the analysis XPS chamber, from a properly outgassed Knudsen cell at a rate of 3.5 ± 0.2 Å/min (Au) and 2.7 ± 0.2 Å/min (Cu), as calibrated with a quartz thickness monitor, in a pressure of 1.5×10^{-7} Pa. The samples were then transferred *in situ* in the photoemission chamber and the experiments performed in ultrahigh vacuum (UHV) at a base pressure of 2×10^{-8} Pa. X-ray photoelectron spectroscopy measurements were conducted by using a monochromatized Al $K\alpha_1$ X-ray source (1486.74 eV), with the photoelectrons recorded by a Phoibos (150 mm radius) electron energy analyser operating in fixed analyser transmission (FAT) mode with pass energy of 30 eV. The estimated combined (source + analyser) resolution is around 0.9 eV total full width at half maximum.

First principles calculations were performed within the density functional theory framework using Quantum Espresso code [21], by employing ultrasoft pseudopotentials and the generalized gradient approximation functional in PBE parameterization [22] of the exchange and correlation term. The code uses plane wave to expand the electronic wave function considering explicitly valence and semicore electrons. The generalized gradient approximation in the formulation of Perdew and Wang GGA+ U and PW91 – is used to treat the correlation contribution and the exchange to the total Hamiltonian [23]. For our system we employ 8 unit cell ferroelectric slabs with two different ferroelectric polarization states with one end kept with the inter-atomic distances at the bulk values and the other in contact with the metal layer. During calculation the coordinates of the first, bulk-like two unit cells are fixed, while the rest of the system is allowed to relax along the z-axis until the Hellman-Feynman forces on each atom are less than 30 meV/Å. A 30 Ry cutoff for the plane wave expansion and 400 Ry for the charge density integration is used. We could achieve the convergence when relaxing the coordinates in the supercell for a 7x7x1 k-point mesh. The in-plane lattice constant value was deduced from a previous bulk calculation to be $a = 3.936$ Å and used for our structure fixing the $SrTiO_3$ substrate.

3. Results and discussion

Fig. 1((a)–(c)) presents the XPS spectra of Cu/BTO systems, in the increasing order of Cu thickness (2, 4, 16, 24, 40, 100 Å) deposited on $BaTiO_3$ ferroelectric sample. Each X-ray photoelectron spectrum is 'deconvoluted' by using Voigt lines [24]. All the spectra are simulated with a minimum number of components in order to obtain a reasonable fit. The Ba 3*d* and Cu 2*p* spectra are fitted with 2 components (represented with green and blue curves, the green one having the lower binding energy), with imposed branching ration $(l + 1)/l$ between $j_{max} = l + \frac{1}{2}$ and $j_{min} = l - \frac{1}{2}$ components (l is the orbital quantum number and j the total angular momentum in the L-S coupling scheme). The relative binding energy shifts between these two main components is 1.15 ± 0.01 eV. For the O 1*s* and Ti 2*p* spectra, three components were necessary. The results are in agreement with the ones obtained for Cu deposited on PZT (0 0 1) [14,25]. The evolution of the binding energies are seen in Fig. 2.

The photoemission spectra of Ba 3*d*, in the Cu/BTO system is presented in Fig. 1(a), where the main component at lower binding energies (LBE - green curve) is assigned to Ba atoms in the perovskite state, and the one at higher binding energy (HBE - blue curve) to surface related emission due to uncoordinated surface Ba atoms [26,27]. The main component of Ti 2*p* spectra (Fig. 2(b)) is associated to Ti ions in perovskite phase having a + 4 valence state and the smaller component at HBE is attributed to TiO_2 surface termination, thus one

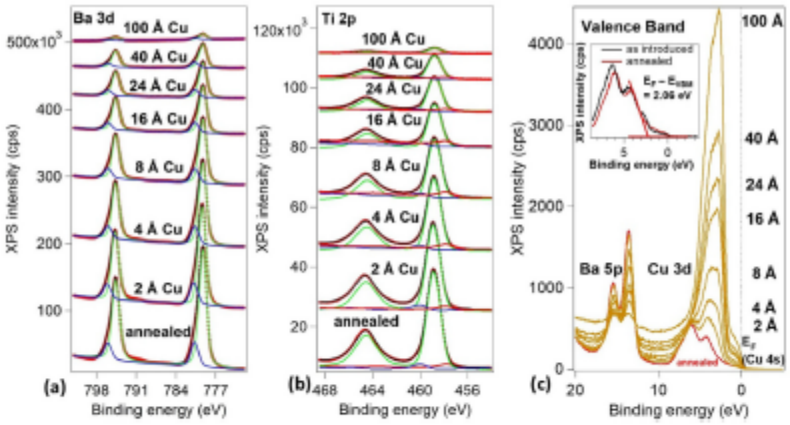

Fig. 1. (a) Ba 3*d* and (b) Ti 2*p* XPS spectra after successive Cu deposition on BTO substrate. Red symbols represent the experimental data, black lines are the fits, green and blue lines represent individual components. (c) Valence band maximum obtained with monochromatized Al K_α source upon Cu deposition. The red line represents the annealed surface prior metal deposition used to extract the Fermi level and to estimate the VBM (see the Inset). (For interpretation of the references to colour in this figure legend, the reader is referred to the web version of this article.)

deduce that BTO surface has a mixed, BaO and TiO_2 termination. It is reasonable to assume that only atoms in perovskite environment give a net contribution at the ferroelectric polarization, while under-coordinated species contribute at the P^0 state (no out-of-plane FE polarization). Additionally, a lower binding energy component was used in order to describe the Ti^{3+} states, which are in direct connection with the oxygen vacancies.

One can easily observe that the Ba 3*d* and Ti 2*p* intensities during Cu deposition are not dropping to zero, even after growing an overlayer of 100 Å. At this thickness and with the inelastic mean free path in the range of 1 – 2nm, the attenuation of substrate Ba 3*d* and Ti 2*p* spectra should have been of orders of magnitude compared to their initial amplitudes [13]. This behavior is reasonable in the assumption that Cu film grow as discontinuous coating – clusters or nanoparticles, accompanied by additional formation of a reacted CuO_x layer, with intermediate valence between metallic Cu and CuO. The amplitude variation of LBE/HBE components with Cu thickness is quite similar, obeying an exponential attenuation law (see Fig. S2). The evolutions of O 1*s* and Cu 2*p* spectra in the increasing order of metal overlayer are presented in Fig. S1(a,b).

The valence band spectra from Fig. 1(c) reveal the evolution of the system with Cu deposition, where the Fermi level is automatically extracted by the analysis software, regularly calibrated for the XPS setup to 0 eV. It is difficult to assess any binding energy shifts in the valence band during metal depositions, as the O 2*p* - Ti 3*d* signature at 2 – 4 eV is gradually replaced by that of Cu 3*d*, accompanied by the attenuation of Ba 5*p* signal. The inset reveals the valence band maximum (VBM) position determined from the spectra of the annealed BTO substrate. Extrapolating the leading edge of the valence band spectra recorded on the bare BTO sample (Figure S3) we determine the VBM: $E_F - E_{VBM} = 2.06$ eV, corresponding to the Schottky barrier height (SBH) for holes. This also indicates the n-doped character of our BTO layer

Fig. 2(a)–(c) shows gradual shifts of the signals coming from the substrate (Ba 3*d*, Ti 2*p*) towards lower BE with increasing metal thickness, up to 0.1eV. The values of the core levels obtained for the main component of the clean surface are $E_{Ba} \cong 779.3$ eV for Ba $3d_{5/2}$, $E_{Ti} \cong 458.8$ eV for Ti $2p_{3/2}$, $E_O \cong 530$ eV for O *1s* agree well with previous data [16,28]. For a survey of the Ti *2p* and Ba *3d* binding energies in the literature and more details about the Cu *2p* and O *1s* evolution during layer growth see Supporting Information).

What can we observe in Fig. 2(d) is first a drop of the O/Ti ratio, signalizing some increase of the oxygen deficient state, followed by its gradual recovery with increasing Cu thickness. The initial existence of some oxygen deficient state can be understood as an effect of mild vacuum annealing, while the intrinsic compensation mechanisms of the out-of-plane ferroelectric state is responsible for their accumulation more towards the surface [18]. On the other hand, the further increase of oxygen vacancies, and consequent build-up of free electrons is unexpected for a ferroelectric polarization "inwards" intrinsically compensated by holes rather by negative charge carriers [18]. This indicates that the main compensation mechanism, at thin Cu over layers is intrinsic, involving the accumulation of negative charges close to the interface and the transfer of free charges from BTO to the Cu clusters. Indeed, Cu is negatively charged (Fig. 1(c)) [28], featuring a BE shift towards LBE of 1 eV in the first deposition stages until the Cu clusters get connected at higher metal coverage, and the top electrode becomes a true electron reservoir. From that moment on, any electron transfer from BTO to Cu is excluded. Indeed, starting with 30 Å thickness of deposited Cu, no major shift in the Cu *2p* BE is detected anymore. Hence, that thickness represents the crossover from intrinsic to extrinsic compensation mechanism of the ferroelectric polarization. At higher Cu

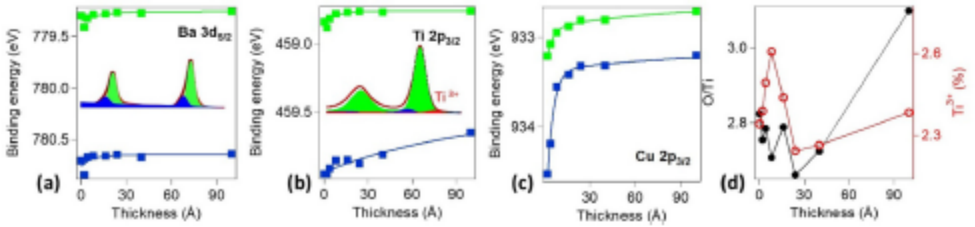

Fig. 2. Evolution of binding energy of (a) Ba $3d_{5/2}$, (b) Ti $2p_{3/2}$, (c) Cu 2*p* components resulted from the fit of spectra recorded in Fig. 1(a),(b) and Fig. S1(b) as function on the Cu nominal thickness. (d) O/Ti ratio after successive Cu deposition and Ti^{3+} contribution at the total integral intensity of Ti 2*p* spectra.

thickness the gradual recovery of r = O/Ti ratio, going up to oxygen excess (100 Å Cu) indicate that the screening of the out-of-plane ferroelectricity relies on positive charges (holes and ionized donors), involving a *p*-self doped regime [10,18]. Remarkably, the relative integral amplitude of the component associated to Ti^{3+} states, confirms the trend described by the O/Ti ratio, sharply increasing in the early Cu deposition stages where the increase of the oxygen deficient state is identified, while remaining almost constant at higher Cu thickness. In this context, the accompanying intensity between VBM and the Fermi level is a clear indication of localized in-gap states of Ti^{3+} origin [29,30], similar to STO-derived states in STO[31] and at LAO/STO interfaces [32,33].

While in STO – derived systems, the oxygen vacancies are involved in the particular manifestation of the two dimensional gases [31–33], with direct implications in electronic transport, in our case, the functionality of the oxygen vacancies stems from their role in stabilizing a well-defined orientation of the ferroelectric polarization at the BTO surface through intrinsic mechanisms, while gradually replaced by conventional, extrinsic compensation through the electrons from the top metallic contact at higher Cu coverage.

In Fig. 3 we sketched the mechanisms involved in the evolution of the binding energies identified in Fig. 2. We establish a band bending with the curvature depending *(i)* on the difference between the WF of the metal and that of the ferroelectric and (*ii*) on the ferroelectric polarization orientation. We imagine first the situation when no out-of-plane ferroelectric polarization is present (Fig. 3a); as for example in the case of $P^{(0)}$ domains, where FE polarization lacks or of the regions featured by FE polarization oriented within the sample plane, which do not contribute to surface band bending[13]. We additionally assume a hypothetical situation with no bending despite the different WFs of the joining materials. By considering the effect of the different work functions, such as in a metal-semiconductor contact with metal having higher work function than BTO (Φ_{Cu} = 4.65 eV [34] and for Φ_{BTO} = 4.8 eV [35–37]), one would obtain a downwards band bending and should have experimentally identified shifts of the BE towards higher energies (Fig. 3(b)). Such shifts are excluded by the experimental evidence, and one have to assume, for a consistent picture, the effect triggered by the ferroelectric polarization which lead to opposite shift of the BEs, thus FE pointing inwards ($P^{(-)}$) (Fig. 3(c)). Indeed, the shift of the VBM of the as-introduced sample towards the Fermi level by 0.2 eV upon vacuum annealing (inset of Fig. 1c) is an indication of such direction of the ferroelectric polarization with its corresponding band bending upwards.

Moreover, one has to accept that the band bending upwards close to the contact region is consistent with a mechanism of interface formation involving the combined effect of a $P^{(-)}$ orientation of the FE polarization and a FE-dependent WF value [18], as illustrated in Fig. 3c. As previously explained, the values of the WF in ferroelectrics depend on the polarization state, termination and doping [18,38–40]. For example it is well established that the surface potential of ferroelectrics is higher for $P^{(-)}$ domains than for $P^{(+)}$ ones [18,38–41], with values of WFs larger by 0.3–0.4 eV for $P^{(+)}$ domains than for the $P^{(-)}$ FE orientation. The explanation involves combined electrostatic considerations [38] and more complex, doping-dependent mechanisms of concomitant change of the band structure, electron affinities and Fermi level position [18,36,41].

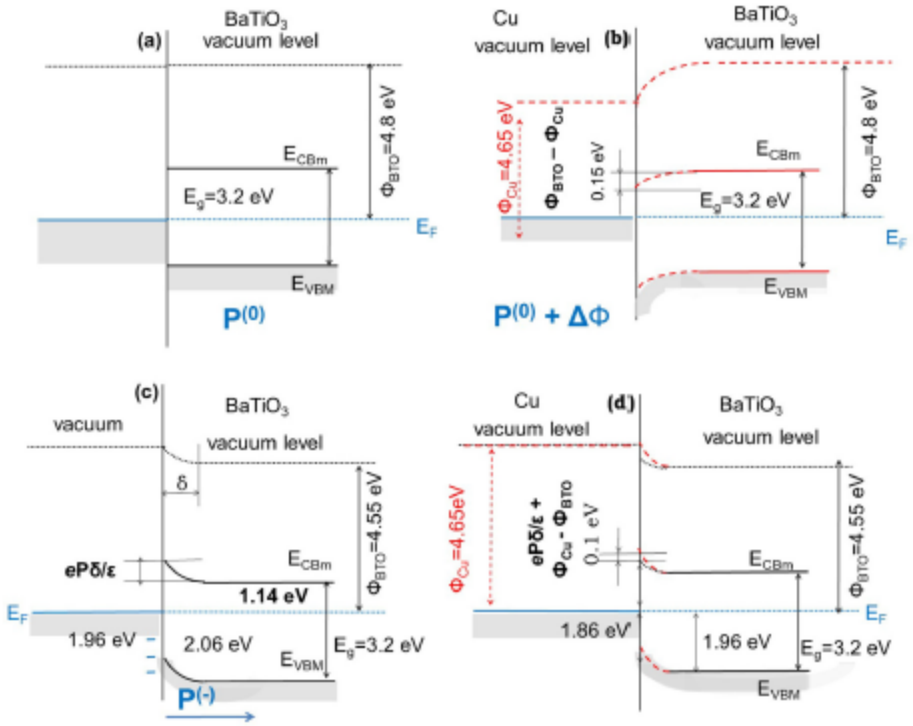

Fig. 3. Mechanisms explaining the evolution of binding energies from Fig. 2. (a) energy band diagram of BTO without polarization perpendicular to the surface ($P^{(0)}$ or in-plane) and assuming no WF difference and no band bending; (b) Schottky-Mott band bending mechanism when Cu is deposited on BTO; (c) energy band diagram of BTO exhibiting a FE polarization oriented inwards (↓) with its corresponding band bending; (d) our case where the ferroelectric maintain its polarization adding at the bending due to the Schottky contact.

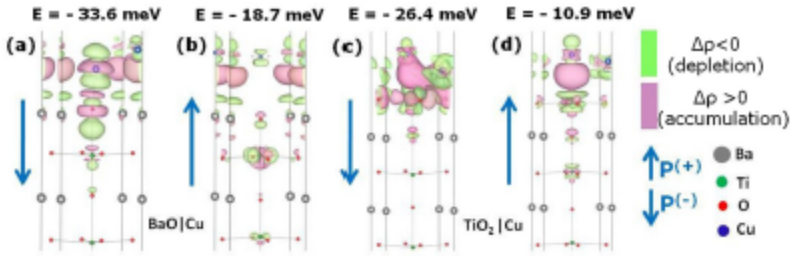

Fig. 4. First-principle calculation of bonding charge distribution on Cu/BTO interface for different terminated substrate and ferroelectric polarization. Cu tends to grow $P^{(-)}$ domains for a BaO terminated surface. Pink represents the regions with charge accumulation, and green represents the charge-depletion regions. (For interpretation of the references to colour in this figure legend, the reader is referred to the web version of this article.)

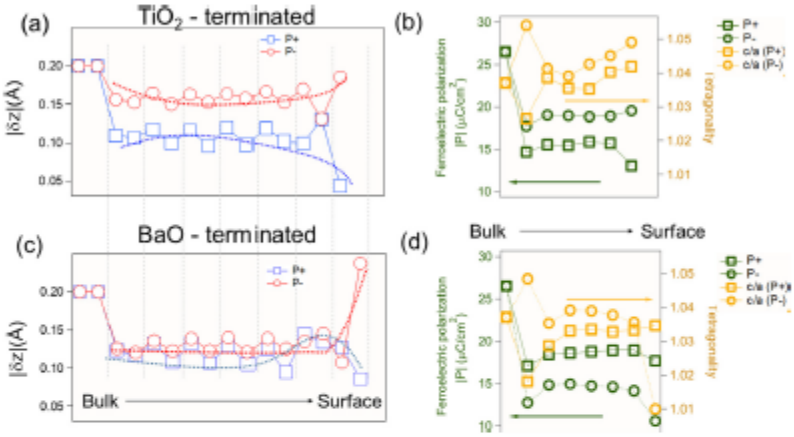

Fig. 5. Calculated Ba – O and Ti – O displacements along the z direction for the TiO_2 and BaO- terminated slabs (a,c). For compact visualization, we represented their absolute values. Dotted lines are guides for the eyes, depicting individual unit cells. Variation of the tetragonality and the consequent variation of the ferroelectric polarizations per unit cell for TiO_2 – terminated slab featured by two polarization directions are in (b) and the same quantities calculated for BaO – terminated slab in (d).

The $P^{(-)}$ orientation of the film polarization then adds at the difference between the metal-semiconductor WFs, resulting in a SBH defined as $\frac{ed\delta}{\varepsilon}+(\Phi_{BTO}-\Phi_{Cu})$, where $\Phi_{Cu}>\Phi_{BTO}$, $\Phi_{Cu}-\Phi_{BTO}=0.1$ eV, in line with the mechanism suggested in Fig. 3c, d and with the apparent shift towards LBE by 0.1 eV of BTO core levels upon Cu deposition [25]. The image extracted from the BE variations is schematized in Fig. 3(d), with the shift towards LBE upon Cu deposition corresponding to upwards band bending in absolute values [25]. The SHB for electrons is calculated using the BTO band gap of 3.2eV, $E_{CB}-E_F=1.14$ eV. We can deduce the SHB for electrons at the interface after metal deposition, $\Phi_e^{Cu}=1.86$ eV, assuming a rigid shift of VBM and core-levels of 0.1 eV.

With these values and the mechanism invoked in Fig. 3, we obtain the ferroelectric term $\frac{ed\delta}{\varepsilon}=0.2$ eV, with $P=25$ $\mu C/cm^2$[19] and effective dielectric constant $\varepsilon_r=140$ [42] and, deduce that $\delta_{Cu/BTO(P-)}\simeq 1.5$ nm. This means that the main effect of the interface charge reorganization lies in approximately the first two unit cells of BTO. The value is larger than the width involved in the stabilization of a P^+ FE state by a factor of ~4 [37,43].

The formation energy calculated from first-principles for a BTO slab in the initial stage of Cu growth (Fig. 4) confirm that the most favorable scenario is with Cu presumably growing on domains with $P^{(-)}$ orientation either on BaO terminated surface and to smaller extent to TiO_2 regions (Fig. 4(a,c)) which have the smallest formation energy, with significant differences for the formation energy in the case of $P^{(+)}$ domains. Regarding the stability of the interface formation as deduced from DFT calculations, Cu lattice constant $a_{Cu}=3.615$ Å is significantly smaller than that of BTO strained at the in-plane STO lattice constant [18], $a_{STO}=3.905$ Å. Consequently, the lattice mismatch between Cu and BTO imply that the basic condition for epitaxial growth is not fulfilled; hence the growth is likely to result, at least in the early deposition stage, in clusters and islands unconnected, while they will connect each other only at higher thickness of the top metal. This scenario corresponds precisely to our experimental case. Taking under consideration that thick BTO layers are commonly featured by mixed termination domains, it is expected that the growth will proceed on domains featured by the smallest formation energy (largest in absolute values), resulting in clusters and islands connected to each other only at high metal coverage [13,25]. Indeed, this hypothesis is in line with the attenuation of the substrate signal of 94.4% at 100 Å thick metal coverage and with the value of the total attenuation thickness, considerably larger than the estimate based on the inelastic mean free path.

Insight into the microscopic mechanism of charge compensation at the interfaces and stabilization of a well-defined out-of-plane polarization direction is given by the calculated bonding charge distribution as the difference between the charge density of the entire slab and of Cu and BTO, lying in identical supercells [44,45]. It shows that in $P^{(-)}$ states (Fig. 4(a,c)) charge depletion occurs indeed in the first unit cells occurs close to the metal contact. This can be assimilated to hole state localized orbitals oriented along the Ti-O hybridized bond in the z direction. $P^{(+)}$ states, on the other hand, are featured mostly by charge accumulation as expected. Moreover, the alteration in the charge distribution propagates in the first two unit cell close to the interface, in accordance with the deduced value of δ 1.5 nm and this behavior is particularly evident for the BaO – terminated domains, invoking intrinsic compensation mechanism, while for the TiO_2 – terminated interface, the compensation of the ferroelectricity involves drastic reorganization of the charge distribution around the top metal layer (*i.e.* extrinsic compensation).

We further explore the relationship between the relative atomic displacements of Ti, O and Ba species along the z axis, which directly impact the out-of-plane polarization and the results are presented in Fig. 5.

The polarization can be expressed as:

$$P = \frac{1}{v}\sum_i \delta_i Z_i \quad (1)$$

with the sum running over the whole set of unit cells, v is the volume of the unit cell, δ_i the displacement of atom i from the centrosymmetric position and Z_i the Born effective charge of the atom i. With the values of δ collected from the DFT-relaxed slabs for both BaO and TiO_2 terminations (Fig. 5(a,c)) one would expect a decrease of the polarization, compared with the bulk values, gradually recovering ($P^{(-)}$, TiO_2 termination), decreasing ($P^{(+)}$, both terminations) or exceeding the bulk value ($P^{(-)}$, BaO termination) while approaching the surface.

The other term in Eq. (1), regulating the net ferroelectric polarization represents the Born charges, which for BTO were calculated in [46]. Taking the plane containing the Ba atoms as reference, we express the ferroelectric polarization per unit cell as follows [47,48]:

$$P = \frac{e}{v}(\delta_0^{Ba} + \delta_0^{Ti})Z_{O,\perp} + \frac{e}{v}\delta_{Ti}Z_{Ti} \quad (2)$$

which sum up the two contribution.

The deduced cell-resolved polarizations (Fig. 5(b,d)) shows clearly that the bulk values capture the experimental P of 25 $\mu C/cm^2$, but within the slab the values tend to decrease while approaching the surface. The drastic drop deduced for the BaO –terminated domains and $P^{(-)}$ state, surprisingly featured by the largest relative atomic displacements is due to cell tetragonality which approaches the cubic, paraelectric state close to the surface. To better illustrate the subtle balance between atom off-centering and tetragonal distortion, in the TiO_2 termination ($P^{(+)}$) case for example, the large tetragonality of the cell close to the interface is not enough to compensate for the small relative atomic displacements, thus the value of the FE polarization close to the surface decreases to 13 $\mu C/cm^2$. The rest of the values, for the two remaining cases care in the $15 - 20$ $\mu C/cm^2$ range. This observation concludes that large relative atomic displacements reflect in large FE polarization given that the cell remains tetragonal, with the transition to a cubic configuration triggering the disappearance of any out-of-plane FE polarization. Another interesting observation is the selective drop of P, the FE polarization value close to the surface only for the TiO_2 –terminated P+ domains and BaO – terminated P- ones while BaO (P^+) and TiO_2(P^-) seem to keep their bulk values. This behavior should be useful in understanding the polarization behavior in artificial heterostructures involving well-defined, engineered terminations. Our results thus shed light on the complex metal/ferroelectric interface formation mechanisms, and clarify practical aspects involved in the fabrication of ferro - functional devices.

4. Conclusions

We have presented a comprehensive study by means photoelectron spectroscopy and first-principles calculations of the band bending during the contact formation of Cu with the $BaTiO_3$ surface. Careful analysis of the core level spectra allowed us to trace the origin of each fit component and to establish the influence of FE polarization and surface stoichiometry on the interface band bending. From the evolution of these components with the thickness of the metal top layer, we conclude that Cu layer, in the incipient state, at thickness below 3 nm is not continuous. This regime is associated with intrinsic compensation mechanism of the out of plane ferroelectric polarization direction. It involves oxygen vacancies-derived negative charges which build-up in BTO close to the interface, accompanied by electron transfer towards the Cu islands. For Cu thickness exceeding 3 nm, the islands coalesce and the stabilization of $P^{(-)}$ domains involves the compensation of the depolarizing field by the charges from the metal overlayer, thus the system switches to the conventional, extrinsic compensation mechanism. We find that the valence band maximum of BTO at the interface is 2.06 eV, defining a Schottky barrier height of 1.14 eV for the electrons. These values, correlated with the shifts of the valence band maximum and of the core levels are consistent with ferroelectric dependent work-function value of BTO, which, in combination with the $P^{(-)}$ direction of BTO accounts for the upwards band bending in the interface region. *Ab-initio* calculations point towards a scenario with copper growing more likely on the $P^{(-)}$ domains, while rather insensitive to the different terminations of the surface.

Acknowledgements

This work was funded by the Romanian Ministry of Research and Innovation through Project PN-III-P4-ID-PCCF2016-0047 granted through the UEFISCDI Agency, and by the Project 18-ELI/2016 granted through the Institute of Atomic Physics. Authors gratefully acknowledge Mr. Charles Fiesel for constructive suggestions and English-proofreading of the final version of the manuscript.

Appendix A. Supplementary material

Supplementary data to this article can be found online at https://doi.org/10.1016/j.apsusc.2019.144101.

References

[1] M.E. Lines, A.M. Glass, Principles and Applications of Ferroelectrics and Related Materials, Clarendon, Oxford, 1977.
[2] J.F. Scott, Ferroelectric Memories, Springer, Berlin, 2000.
[3] R.W. Wessels, Ferroelectric oxide epitaxial thin films: synthesis and non-linear optical properties, J. Cryst. Growth 195 (1998) 706.
[4] V. Vaithyanathan, J. Lettieri, W. Tian, A. Sharan, A. Vasudevarao, Y.L. Li, A. Kochhar, H. Ma, J. Levy, P. Zschack, J.C. Woicik, L.Q. Chen, V. Gopalan, D.G. Schlom, c-axis oriented epitaxial $BaTiO_3$ films on (001) Si, J. Appl. Phys. 100 (2006) 024108.
[5] R. Bruchhaus, D. Pitzer, M. Schreiter, W. Wersing, Optimized PZT thin films for pyroelectric IR detector arrays, J. Electroceram. 3 (1999) 151.
[6] S.K. Hong, C.W. Suh, C.G. Lee, S.W. Lee, E.Y. Hang, N.S. Kang, Protection of $SrBi_2Ta_2O_9$ ferroelectric capacitors from hydrogen damage by optimized metallization for memory applications, Appl. Phys. Lett. 77 (2000) 76.
[7] S.T. Zhang, B. Yang, Y.F. Chen, Z.G. Liu, X.B. Yin, Y. Wang, M. Wang, N.B. Ming, $SrBi_4Ti_4O_{15}$ thin films and their ferroelectric fatigue behaviors under varying switching pulse widths and frequencies, J. Appl. Phys. 91 (2002) 3160.
[8] S.R. Shannigrahi, H.M. Jang, Fatigue-free lead zirconate titanate-based capacitors for nonvolatile memories, Appl. Phys. Lett. 79 (2001) 1051.
[9] R. Guo, Z. Wang, S.W. Zeng, K. Han, L.S. Huang, D.G. Schlom, T. Venkatesan, Ariando, J.S. Chen, Functional ferroelectric tunnel junctions on silicon, J. Sci. Rep. 5 (2015) 12576.
[10] L. Pintilie, C. Ghica, C.M. Teodorescu, I. Pintilie, C. Chirila, I. Pasuk, L. Trupina, L. Hrib, A.G. Boni, N.G. Apostol, L.E. Abramiuc, R. Negrea, M. Stefan, D. Ghica, Polarization induced self-doping in epitaxial $Pb(Zr_{0.20}Ti_{0.8}0)O_3$ thin films, Sci. Rep. 5 (2015) 14974.
[11] L. Pintilie, M. Alexe, Metal-ferroelectric-metal heterostructures with Schottky contacts. I. Influence of the ferroelectric properties, J. Appl. Phys. 98 (2005) 124103.
[12] N.G. Apostol, L.E. Stoflea, G.A. Lungu, C.A. Tache, D.G. Popescu, L. Pintilie, C.M. Teodorescu, Band bending at free $Pb(Zr, Ti)_O3$ surfaces analyzed by X-ray photoelectronspectroscopy, Mater. Sci. Eng., B 178 (2013) 1317.
[13] N.G. Apostol, L.E. Stoflea, G.A. Lungu, C. Chirila, L. Trupina, R.F. Negrea, C. Ghica, L. Pintilie, C.M. Teodorescu, Charge transfer and band bending at $Au/Pb(Zr_{0.2}Ti_{0.8})O_3$ interfaces investigated by photoelectron spectroscopy, Appl. Surf. Sci. 273 (2013) 415.
[14] N.G. Apostol, L.E. Stoflea, L.C. Tanase, I.C. Bucur, C. Chirila, R.F. Negrea, C.M. Teodorescu, Band bending at copper and gold interfaces with ferroelectric Pb (Zr, Ti)$_O3$ investigated by photoelectron spectroscopy, Appl. Surf. Sci. 354 (2015) 459.
[15] F. Chen, R. Schafranek, A. Wachau, S. Zhukov, J. Glaum, T. Grannow, H. von Seggern, A. Klein, Barrier heights, polarization switching, and electrical fatigue in $Pb(Zr, Ti)_O3$ ceramics with different electrodes, J. Appl. Phys. 108 (2010) 104106.
[16] D.G. Popescu, N. Barrett, C. Chirila, I. Pasuk, M.A. Husanu, Influence of hole depletion and depolarizing field on the $BaTiO_3/La_{0.7}Sr_{0.3}MnO_3$ interface electronic structure revealed by photoelectron spectroscopy and first-principles calculations, Phys. Rev. B 92 (2015) 235442.
[17] S. Hüfner, Photoelectron Spectroscopy: Principles and Applications, Springer, Berlin, 2003.
[18] L.C. Tanase, L.E. Abramiuc, D.G. Popescu, A.M. Trandafir, N.G. Apostol, I.C. Bucur, L. Hrib, L. Pintilie, I. Pasuk, L. Trupina, C.M. Teodorescu, Polarization Orientation in Lead Zirconate Titanate (001) Thin Films Driven by the Interface with the Substrate, Phys. Rev. Appl 10 (2018) 034020.
[19] F. Chen, A. Klein, Polarization dependence of Schottky barrier heights at interfaces of ferroelectrics determined by photoelectron spectroscopy, Phys. Rev. B 86 (2012) 094105.

[20] I.C. Bucur, L. Tanase, L.E. Abramiuc, G.A. Iungu, C. Chirila, L. Trupina, N.G. Apostol, R.M. Costescu, R.F. Negrea, L. Pintilie, C.M. Teodorescu, Triggering surface ferroelectric order in Pb(Zr, Ti)$_{1-x}$O$_3$(001) by deposition of platinum, Appl. Surf. Sci. 432 (2018) 27.
[21] P. Giannozzi, S. Baroni, N. Bonini, M. Calandra, R. Car, C. Cavazzoni, D. Ceresoli, G.L. Chiarotti, M. Cococcioni, I. Dabo, A. Dal Corso, S. de Gironcoli, S. Fabris, G. Fratesi, R. Gebauer, U. Gerstmann, C. Gougoussis, A. Kokalj, M. Lazzeri, L. Martin-Samos, N. Marzari, F. Mauri, R. Mazzarello, S. Paolini, A. Pasquarello, L. Paulatto, C. Sbraccia, S. Scandolo, G. Sclauzero, A.P. Seitsonen, A. Smogunov, P. Umari, R.M. Wentzcovitch, Quantum ESPRESSO: a modular and open-source software project for quantum simulations of materials, J. Phys.: Condens. Matter 21 (2009) 395502.
[22] J.P. Perdew, K. Burke, M. Ernzerhof, Generalized gradient approximation made simple, Phys. Rev. Lett. 77 (1996) 3865.
[23] J.P. Perdew, K. Burke, Y. Wang, Generalized gradient approximation for the exchange-correlation hole of a many-electron system, Phys. Rev. B 54 (1996) 16533.
[24] C.M. Teodorescu, J.M. Esteva, R.C. Karnatak, A. El Afif, An approximation of the Voigt I profile for the fitting of experimental x-ray absorption data, Nucl. Instrum. Methods Phys. Res., Sect. A 345 (1994) 141.
[25] I. Pintilie, C.M. Teodorescu, C. Ghica, C. Chirila, A.G. Boni, L. Hrib, I. Pasuk, R. Negrea, N. Apostol, L. Pintilie, Polarization-control of the potential barrier at the electrode interfaces in epitaxial ferroelectric thin films, ACS Appl. Mater. Interfaces 6 (2014) 2929.
[26] S.M. Mukhopadhyay, T.C.S. Chen, Surface chemical states of barium titanate: influence of sample processing, J. Mater. Res. 10 (1995) 1502.
[27] K. Moriwawa, T. Mizokawa, A. Fujimori, Y. Taguchi, Y. Tokura, Photoemission spectral weight distribution in $Y_{1-x}Ca_xTiO_3$, Phys. Rev. B 54 (1996) 8446.
[28] L.E. Stoflea, N.G. Apostol, C. Chirila, L. Trupina, R. Negrea, L. Pintilie, C.M. Teodorescu, Schottky barrier versus surface ferroelectric depolarization at Cu/Pb(Zr, Ti)$_{1-x}$3 interfaces, J. Mater. Sci. 49 (2014) 3387.
[29] S. Muff, N. Pilet, M. Fanciulli, A.P. Weber, C. Wessler, Z. Ristić, Z. Wang, N.C. Plumb, M. Radović, J.H. Dil, Influence of ferroelectric order on the surface electronic structure of $BaTiO_3$ films studied by photoemission spectroscopy, Phys. Rev. B. 98 (2018) 045132.
[30] P. Lutz, S. Moser, V. Jovée, Y.J. Chang, R.J. Koch, S. Ulstrup, J.S. Oh, L. Moreschini, S. Fatale, M. Grioni, C. Jozwiak, A. Bostwick, E. Rotenberg, H. Bentmann, F. Reinert, Phys. Rev. Mater. 2 (2018) 094411.
[31] S. McKeown Walker, F.Y. Bruno, Z. Wang, A. de la Torre, S. Riccó, A. Tamai, T.K. Kim, M. Hoesch, M. Shi, M.S. Bahramy, P.D.C. King, F. Baumberger, Carrier-Density control of the $SrTiO_3$ (001) surface 2D electron gas studied by ARPES, Adv. Mater. 27 (2015) 3894–3899.
[32] C. Cancellieri, A.S. Mishchenko, U. Aschauer, A. Filippetti, C. Faber, O.S. Barišić, V.A. Rogalev, T. Schmitt, N. Nagaosa, V.N. Strocov, Polaronic metal state at the $LaAlO_3/SrTiO_3$ interface, Nature Commun. 7 (2016) 10386.
[33] A. Chikina, F. Lechermann, M.-A. Husanu, M. Caputo, C. Cancellieri, X. Wang, T. Schmitt, M. Radovic, Vladimir N. Strocov, Orbital ordering of the mobile and localized electrons at oxygen-deficient $LaAlO_3/SrTiO_3$ interfaces, ACS Nano 12 (2018) 7927–7935.
[34] D.E. Eastman, Photoelectric work functions of transition, rare-earth, and noble metals, Phys. Rev. B 2 (1970) 1.
[35] T. Schulmeyer, S.A. Paniagua, P.A. Veneman, S.C. Jones, P.J. Hotchkiss, A. Madhiige, J.E. Pemberton, S.R. Marder, N.R. Armstrong, Modification of $BaTiO_3$ thin films: adjustment of the effective surface work function, J. Mater. Chem. 17 (2007) 4563.
[36] J. Fujisawa, T. Eda, M. Hanaya, Comparative study of conduction-band and valence-band edges of TiO_2, $SrTiO_3$ and $BaTiO_3$ by ionization potential measurements, Chem. Phys. Lett. 685 (2017) 23.
[37] **D.G. Popescu, M. Husanu, C. Chirila, L. Pintilie, C. M. Teodorescu, Impact of ferroelectricity and band alignment of gradually grown Au on BaTiO3, Phys. Stat Solidi – RRL 13 (7) (2019) 1900077.**
[38] N. Barrett, J. Rault, I. Krug, B. Vilquin, G. Niu, B. Gautier, D. Albertini, P. Lecoeur, O. Renault, Surf. Interf. Anal. 42 (2010) 1690.
[39] J.E. Rault, W. Ren, S. Prosandeev, S. Lisenkov, D. Sando, S. Fusil, M. Bibes, A. Barthelemy, L. Bellaiche, N. Barrett, Thickness-dependent polarization of strained $BiFeO_3$ films with constant tetragonality, Phys Rev. Lett. 109 (2012) 267601.
[40] J.L. Wang, B. Vilquin, N. Barrett, Screening of ferroelectric domains on $BaTiO_3$(001) surface by ultraviolet photo-induced charge and dissociative water adsorption, Appl. Phys. Lett. 101 (2012) 092902.
[41] A. Novikov, Experimental measurement of work function in doped silicon surfaces, Solid-State Electron. 54 (2010) 8.
[42] Y. Qi, S.M. Anlage, H. Zheng, R. Ramesh, Local dielectric measurements of $BaTiO_3$-$CoFe_2O_4$ nanocomposites through microwave microscopy, J. Mater. Res. 22 (2007) 1193.
[43] B.C. Huang, Y.T. Chen, Y.P. Chiu, Y.C. Huang, J.C. Yang, Y.C. Chen, Y.H. Chu, Direct observation of ferroelectric polarization-modulated band bending at oxide interfaces, Appl. Phys. Lett. 100 (2012) 122903.
[44] D.G. Popescu, M.A. Husanu, Epitaxial growth of Au on Ge(001) surface: photoelectron spectroscopy measurements and first-principles calculations, Thin Solid Films 552 (2014) 241.
[45] D.G. Popescu, M.A. Husanu, Au-Ge bonding on a uniformly Au-covered Ge(001) surface, Phys. Status Solidi RRL 7 (2013) 274.
[46] Ph. Ghosez, X. Gonze, Ph. Lambin, J.P. Michenaud, Born effective charges of barium titanate: band-by-band decomposition and sensitivity to structural features, Phys. Rev. B 51 (1995) 6765.
[47] C.L. Jia, V. Nagarajan, J.Q. He, L. Houben, T. Zhao, R. Ramesh, K. Urban, R. Waser, Unit-cell scale mapping of ferroelectricity and tetragonality in epitaxial ultrathin ferroelectric films, Nat. Mater. 6 (2007) 64.
[48] S.R. Spurgeon, P.V. Balachandran, D.M. Kepaptsoglou, A.R. Damodaran, J. Karthik, S. Nejati, L. Jones, H. Ambaye, V. Lauter, Q.M. Ramasse, K.K.S. Lau, L.W. Martin, J.M. Rondinelli, M.L. Taheri, Polarization screening-induced magnetic phase gradients at complex oxide interfaces, Nature Commun. 6 (2017) 6735.

Anexa 3

IOP Publishing Modelling and Simulation in Materials Science and Engineering
Modelling Simul. Mater. Sci. Eng. 27 (2019) 045008 (17pp) https://doi.org/10.1088/1361-651X/ab146e

Polarization branches and optimization calculation strategy applied to ABO_3 ferroelectrics

Lucian D Filip, Neculai Plugaru and Lucian Pintilie

National Institute of Materials Physics, Atomistilor str., nr. 405A, PO Box MG7, Magurele, Bucharest, Romania

E-mail: lucian.filip@infim.ro

Received 23 January 2019, revised 21 March 2019
Accepted for publication 28 March 2019
Published 15 April 2019

Abstract

Berry phase (BP) polarization calculations have been investigated for several ferroelectric materials from the point of view of practical calculations. It was shown that interpretation of the results is particular to each case due to the multivalued aspect of polarization in the modern theory. Almost all of the studied examples show ambiguous polarization results which can be difficult to solve especially for super-cells containing large number of atoms. For this reason, a procedure has been proposed to minimize the number of calculations required to produce an unambiguous polarization result from BP polarization investigations.

Keywords: Berry phase, polarization, ferroelectrics, Born effective charges

(Some figures may appear in colour only in the online journal)

1. Introduction

Ferroelectric materials, have been under intense research for the better part of the last three decades due to the tremendous integration potential into applications ranging from high-density non-volatile memories to solar cells and logic gates [1–13].

Most ferroelectrics belong to the *perovskite* ABO_3 family which is a versatile group of materials that can be obtained through a wide range of synthesis methods [14]. One important property for real life applications is the large polarization value obtained in some ferroelectric compounds such as $Pb(Zr_xTi_{1-x})O_3$ (PZT) thin films (around $1\,C\,m^{-2}$) [15]. Unfortunately these high polarization values are mostly obtained in lead-containing materials which have a rather harmful environmental footprint. For this reason, a sustained experimental and theoretical effort is made in order to find lead-free perovskites that ideally retain the high

0965-0393/19/045008+17$33.00

polarization value but have a much lower toxicity. The theoretical approach for this search is based on high throughput calculations using automated scripts searching for particular material properties (such as a high polarization value) [16–19]. The most reliable theoretical model to date for computing the spontaneous polarization is an implementation of the Berry phase (BP) formalism [20] adapted by Resta [21] in 1992 to correctly define and calculate the bulk polarization value of a ferroelectric. It was later implemented by King-Smith and Vanderbilt [22] in first-principles density functional theory numerical calculations routine and together have become what is now called the *modern theory of polarization*. This method has been used to compute polarization values for various bulk ferroelectric materials. However, special attention is required for each studied material. The difficulty lies behind the definition of the spontaneous polarization within the modern theory of polarization as the time integral of the electric current appearing when the system is distorted adiabatically from a reference centrosymmetric state (CS) towards a final ferroelectric state (FS) [21, 23–26], as one needs the polarization values for at least two different system states (CS and FS) in order to calculate the spontaneous polarization, which is the difference between the two. Therefore such an approach is fundamentally different than previously used models where the bulk polarization was viewed as a collection of neatly arranged electrical dipoles [26]. In addition, the calculated polarization is **not** single valued but a multivalued function of the system state; it can only be obtained up to an integer number (indexing polarization branches) multiplied by a certain geometrical system constant [21, 23, 25, 26].This intricacy complicates the interpretation of numerical results considerably, since the obtained polarization values for the required CS and FS may not have the same indeterminacy (i.e. they may belong to different polarization branches). As such, the difference in polarization of the CS and FS is multivalued, contradicting experimental spontaneous polarization measurements. This ambiguity is corrected by repeating calculations for a large number of intermediary system states, so as to identify the polarization branches of the CS and FS. However, the procedure is system dependent and can also lead to incorrect results if the proper corrections are not used, as pointed out by Neaton *et al* [27].

It is at this point where a distinction between the analytical theoretical description of the modern theory of polarization and its numerical implementation and usage, should be made. While the BP theory of polarization is general to all materials, the interpretation of results obtained from the numerical implementations is strongly system dependent. This fact implies that almost always one must resort to calculating the polarization for multiple intermediary system states which can be very time consuming especially for larger systems.

The present paper aims to illustrate the BP polarization theory from the perspective of practical density functional theory [28] calculations and to introduce a strategy for choosing the optimum calculation points required to resolve the polarization ambiguity in a minimum number of steps. The manuscript is structured as follows: in the next section, the materials used in this study are presented, followed by the computational details in section 3. BP calculations are briefly described in section 4 and the polarization calculations results for the materials introduced in section 2 are individually discussed in section 5. The proposed optimization strategy is introduced in section 6 using the example of a larger system, followed by a discussion on the calculation of Born effective charges in section 7. The manuscript will be concluded with a discussion of all the results obtained in this study and the implemented strategy in section 8.

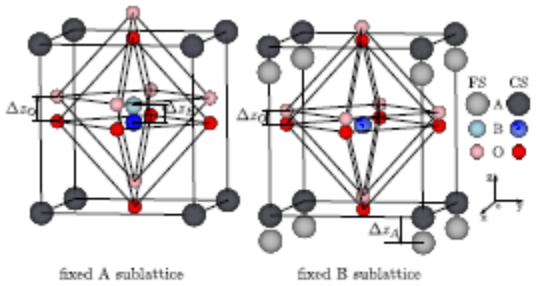

Figure 1. Schematic of a tetragonal unit-cell prototypal ABO_3 ferroelectric perovskite. Two possible distortion paths are exemplified with respect to the A and B sublattices, respectively.

Table 1. Lattice parameters and atomic coordinates of the optimized $PbTiO_3$, $BaTiO_3$ and $KNbO_3$ unit-cells.

	a (Å)	c (Å)	z_A	z_B	z_{O_1}	$z_{O_{2,3}}$
$BaTiO_3$	3.9925	4.036 5	0.00	0.4785	0.025 3	0.5105
$PbTiO_3$	3.8775	4.207	0.00	0.5380	0.116 6	0.6211
$KNbO_3$	3.997	4.063	0.00	0.4770	0.017 0	0.519

2. Materials and structures

The application of the BP polarization theory can be better understood if practical calculations are discussed. For this reason, in this study, four materials have been used to exemplify various aspects of polarization calculations: $BaTiO_3$ (BTO), $PbTiO_3$ (PTO), $KNbO_3$ (KNO) and $Pb(Zr_{0.25}Ti_{0.75})O_3$ (PZT). Although very similar in structure, it will be shown that one cannot rely on assessing the correct polarization branch in one compound based on the data of the others. The choice for the first three materials was motivated by the simplicity of their respective unit-cells which allowed for a large number of calculations to be performed for intermediary system distortion states. The symmetry of the systems is tetragonal and they each have five atoms in the unit-cell (see figure 1). The lattice parameters and atomic coordinates for the first three materials have been summarized in table 1.

$Pb(Zr_{0.25}Ti_{0.75})O_3$ has been used to exemplify BP polarization calculations for a larger system. The 40 atom super-cell was obtained by arranging eight PTO unit-cells in a $2 \times 2 \times 2$ grid and replacing two Ti atoms by Zr. For this system there are five symmetrically inequivalent configurations available where the two Zr atoms can be placed. The chosen example used in this manuscript replaced the diagonal Ti atoms on the second layer of the $2 \times 2 \times 2$ super-cell. The optimization strategy that will be presented in this manuscript can be applied for all five configuration without modification and for this reason we have restricted the discussion for just one of them. Being a larger system the polarization calculations took considerably longer time to complete compared to calculations for the smaller studied systems. While the relative time it takes for a polarization calculation to finish is not relevant when individual structures are tested, it becomes important when an entire range of different materials is investigated.

3. Computational details

All calculation for the present study were performed using the generalized gradient approximation density functional theory [28] as implemented in the Quantum Espresso suite [29]. Projected augmented-wave Perdew–Burke–Ernzerhof pseudo-potentials optimized for solids (PBEsol) [30], from the THEOS library [31], have been used for all the numerical results obtained in this study. However, it should be noted that while small differences can be obtained for the value of the spontaneous polarization, the ambiguities generated by the multivalued aspect remain. For this reason the precision of the numerical results in this paper is less important since they were used only for visualization of the peculiarities involved with the BP polarization calculations.

For the first three materials, a kinetic energy cut-off of 100 Ry was chosen and the Brillouin zone was sampled in a $5 \times 5 \times 5$ Monkhorst–Pack [32] uniform k-point grid for all self-consistent calculations. The polarization calculations (non-self-consistent) were performed with a $5 \times 5 \times 20$ k-point grid. For the BTO and PTO materials, structural optimization was performed starting from experimental data found in the literature [33, 34]. The optimized lattice parameters were obtained by minimizing the total energy with respect to the volume of the unit cell and the final atomic coordinates were obtained by relaxing the internal coordinates until the Hellmann–Feynman forces converge 10^{-5} eV Å^{-1}. The KNO case has been treated using the same lattice parameters and atomic coordinates as obtained by Dal-l'Olio *et al* [35].

The $Pb(Zr_{0.25}Ti_{0.75})O_3$ material was also investigated as an example of a larger system described by a super-cell formed with eight PTO unit-cells disposed in a $2 \times 2 \times 2$ grid where two Ti atoms have been replaced by Zr. The lattice parameters of the PZT super-cell are twice the ones obtained for PTO (see table 1). The atomic coordinates were further relaxed to account for the presence of the two Zr atoms. Since the larger system will take considerably longer time for each polarization calculation run to complete, it was used to highlight the consequences of randomly choosing intermediary system distortion states between CS and FS in order to solve the polarization ambiguity. Lastly, as a language convention, a polarization calculation run is a set of two consecutive calculations for a given system state: first a self-consistent calculation on a uniform k-point grid, followed by a non-self-consistent calculation with an increased number of k points along the axis where the polarization is calculated.

4. BP primer and usage

The modern theory of polarization defines ferroelectric polarization as the time integral of the current that appears through the sample when the studied system is adiabatically distorted from a reference state to a final FS. This is valid as long as the system remains insulating in all the intermediate states along the distortion path [26]. A visual representation of two such processes are given in figure 1 where the tetragonal ABO_3 system is distorted from the CS to the FS along the z axis with respect to the A and B sublattices, respectively. For all materials studied in this paper, the polarization direction is parallel to the z axis of the unit-cell and thus the systems will only be distorted along this axis. For the cases shown in figure 1 we can write the system distortion as a linear function of a dimensionless parameter λ:

$$z_i(\lambda) = z_i^{\mathrm{CS}} + (z_i^{\mathrm{FS}} - z_i^{\mathrm{CS}})\,\lambda, \tag{1}$$

where the index i spans all the atoms in the unit cell and $\lambda \in [0, 1]$. The coordinates z_i^{CS} and z_i^{FS} represent the z coordinates of atom i for the centrosymmetric and the FS, respectively,

while $z_i(\lambda)$ is the coordinate of the same atom i for an intermediary distortion λ. This means that all the atoms in the unit-cell will be moved together by a fraction λ of their corresponding final displacements $\Delta z_i = z_i^{\mathrm{FS}} - z_i^{\mathrm{CS}}$. Following the definition of polarization in the modern theory, the difference between the values obtained for the FS and CS should represent the spontaneous polarization of the studied system

$$P_s = P_{\mathrm{FS}} - P_{\mathrm{CS}}, \tag{2}$$

where P_s is the measurable spontaneous polarization, P_{FS} the computed polarization in the FS state and P_{CS} the computed polarization in the reference state (in our case, the CS). This is a measurable quantity and the modern theory mimics the generic experimental measurement method, where the system state is switched between the two stable FSs using an external electric field along a hysteresis cycle.

However, since the polarization is a multivalued function, equation (2) does not strictly represent the spontaneous polarization [23, 26]. Indeed it can be shown that polarization is only well-defined modulo a polarization quantum given by: $P_q = \frac{e\mathbf{R}}{\Omega}$, where Ω is the unit-cell volume, e is the unit charge and $\mathbf{R}$ is any lattice vector. This means that the calculated polarization for any system state P_{state} is actually an entire family of values separated by integer multiples of P_q (also called branches) and given by [23, 26]:

$$\boldsymbol{P}_{\mathrm{state}} = \boldsymbol{P}_{\mathrm{Berry}} + n\,\boldsymbol{P}_q,\ n \in \mathbb{Z}, \tag{3}$$

where P_{Berry} is the calculated polarization and n is an integer indexing the polarization branch [23, 26]. It is now clear that, if the polarization values for the CS and FS do not belong to the same branch, then the spontaneous polarization will continue to have the form given in equation (3), contradicting experimental findings.

Equation (3) is not only an important consequence of the modern approach to ferroelectric polarization but also the key to the correct application of the numerical implementation of this theory for practical cases. From the theoretical perspective the polarization is a continuous function of the system distortion λ and while in principle, the polarization values are multivalued, they all belong to the same branch. Thus the polarizations of the CS and FS can be used in equation (2) without modifications. For numerical calculations this is not always the case. The calculated values not always belong to the same polarization branch and different strategies are proposed to discern weather this is the case or not. For example, one can check if the polarization values for the CS and FS belong to the same branch by looking at their difference and comparing it to the polarization quantum [22, 25, 26]. If the difference is much smaller than the polarization quantum then no ambiguity has appeared and equation (2) is valid. For the case when the difference is comparable to the polarization quantum, intermediary system distortions should be considered in order to clarify what branch the two polarization values belong to and which corrections should be made. However, there is no clear indication what it means for the polarization difference to be 'much smaller' and it will be shown that this comparison cannot be used effectively to solve the ambiguity. Figure 2 summarizes the calculation steps in order to obtain the spontaneous polarization using the BP polarization method.

5. Numerical calculations and polarization branches

5.1. $BaTiO_3$

The first choice of distortion path shown in figure 3(a) returns the ideal result: all the calculated polarization values belong to a single polarization branch. It is then clear that by

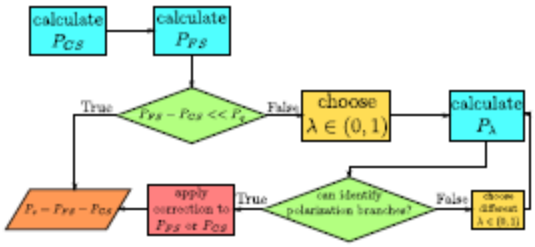

Figure 2. Berry phase polarization method calculation work-flow. The blue rectangles represent polarization calculation runs, green diamonds are decisional steps. Red, yellow and orange rectangles are regular arithmetic operations.

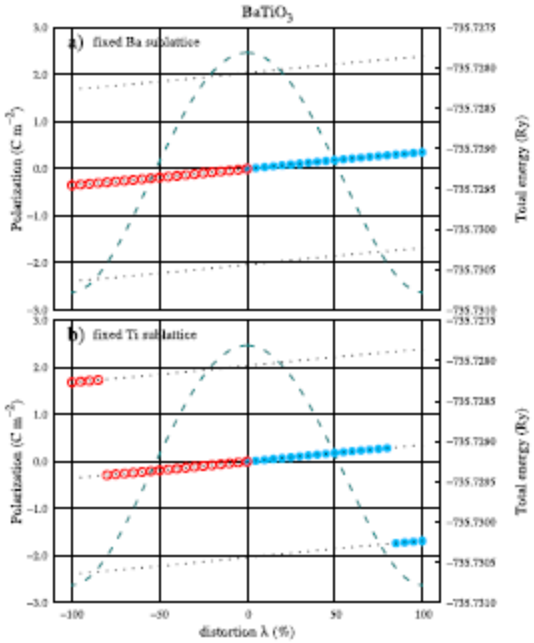

Figure 3. Polarization lattice for $BaTiO_3$ (black dots given by equation (3)) with distortion from the CS to the 'DOWN' FS (red empty circles) and from the CS to the 'UP' FS (solid blue circles) with respect to the Ba sublattice (a) and with respect to the Ti sublattice (b). The distortion parameter λ was modified in 5% steps, with the negative values for the 'DOWN' intended for a better clarity of the figure. The green dashed line is the total energy as a function of distortion showing a continuous variation for each distortion path.

applying equation (2) with the FS and CS values one obtains the correct polarization value of $0.351\,\mathrm{C\,m^{-2}}$. Using the checkpoints at the end of section 4, the values for the 'UP' directions are as follows: $P_{CS} = 0\,\mathrm{C\,m^{-2}}$, $P_{FS} = 0.351\,\mathrm{C\,m^{-2}}$ and $P_q = 2.036\,\mathrm{C\,m^{-2}}$. The difference between the FS and CS values is almost six times smaller than the polarization quantum and this could have been considered sufficient to conclude that an unambiguous result can be obtained without any other intermediary system distortions. However, the situation changes drastically if the unit-cell of the system is now distorted with respect to the B atom site (see figure 3(b)). From the CS to around 80% distortion, the calculated polarizations are neatly arranged on the same branch just like in the previous example. Nevertheless for the rest of the 20% left to the final FS the values jump suddenly on a different branch. Analyzing the end values of interest, one obtains: $P_{CS} = 0\,\mathrm{C\,m^{-2}}$ and $P_{FS} = -1.685\,\mathrm{C\,m^{-2}}$, while the polarization quantum remains the same, $P_q = 2.036\,\mathrm{C\,m^{-2}}$.

According to the calculations steps outlined in figure 2 the difference is now $-1.685\,\mathrm{C\,m^{-2}}$ which is almost the same as P_q in absolute value. This means that an ambiguity has arisen and a correction is needed. In this case, with that many calculated values, it is easy not only to identify where the calculated polarization values reside on their corresponding branch but also what correction should be used. For this case, by adding one polarization quanta to P_{FS} will bring its value on the same branch as P_{CS} (for the 'UP' direction). The spontaneous polarization in equation (2) becomes: $P_s = P_{FS} + P_q - P_{CS} = 0.351\,\mathrm{C\,m^{-2}}$.

5.2. $PbTiO_3$

For the first distortion path in figure 4(a) more polarization jumps appear not only towards the end of the distortion interval, but also at around 30% distortion. This only reflects the 'random' nature of these polarization jumps driven by the numerical implementation of the BP polarization theory. In order to verify that these jumps are not related to any numerical errors, the total energy is plotted (dashed green line) as a function of the system distortion. If the irregularities in the dependence of polarization on the system distortion had a different source, a corresponding discontinuity in the energy dependence should be observed.

This is clearly not the case in any of the studied examples. Apart from the appearance of irregular polarization jumps, the important FS and CS polarization are located on different branches similar to the case in figure 3(b): $P_{CS} = 0\,\mathrm{C\,m^{-2}}$, $P_{FS} = -1.185\,\mathrm{C\,m^{-2}}$ and $P_q = 2.130\,\mathrm{C\,m^{-2}}$. The spontaneous polarization can be obtained in a similar fashion, by adding one polarization quanta (for the 'UP' direction): $P_s = P_{FS} + P_q - P_{CS} = 0.944\,\mathrm{C\,m^{-2}}$. It should be noted that the value of the obtained spontaneous polarization in this case is not 'much smaller' than the polarization quanta and this can add more confusion when analyzing calculated data. For the second distortion path in figure 4(b), the irregular jumps from the previous case have disappeared but the polarization ambiguity is solved just like in the previous case. In fact, if it was not for the one instance in figure 3(a), one could be inclined to conclude at this point that, by always adding one polarization quanta to P_{FS} for the 'UP' direction, equation (2) would lead to an unambiguous result. Unfortunately this is not true, as the next example will reveal.

5.3. $KNbO_3$

Figure 5 shows the same type of polarization calculations as the previous two cases, however the results are entirely different, starting with the CS polarization value. Contrary to the results in figures 3 and 4 the CS polarization in figure 5 does not vanish for the CS. This result

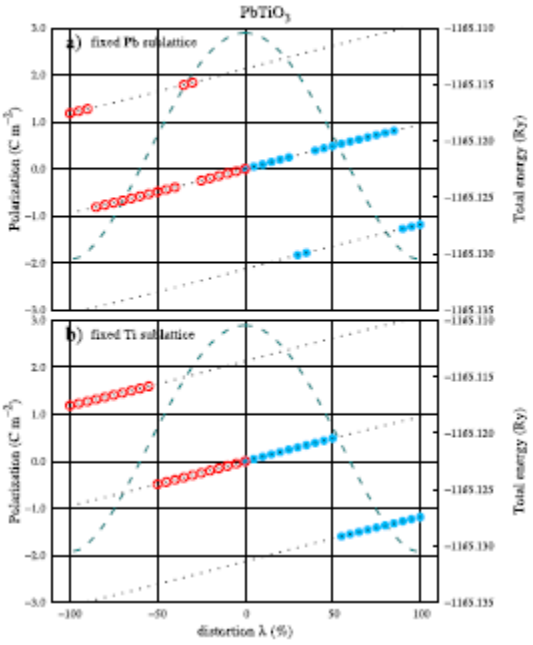

Figure 4. Polarization lattice for $PbTiO_3$ (black dots given by equation (3)) with distortion from the CS to the 'DOWN' FS (red empty circles) and from the CS to the 'UP' FS (solid blue circles) with respect to the Pb sublattice (a) and with respect to the Ti sublattice (b). The distortion parameter λ was modified in 5% steps, with the negative values for the 'DOWN' intended for a better clarity of the figure. The green dashed line is the total energy as a function of distortion showing a continuous variation for each distortion path.

appears to be in contradiction with the expectation that for a CS of a system the polarization must vanish, yet this is only true if the polarization was single valued [26, 36]. Once again it is shown that using the current approach it is impossible to successfully apply the same strategy to different materials. Another difference in the results obtained for KNO is the polarization jump that appears in the near vicinity of the CS. This only appears for one polarization direction but not the other. This is a fortuitous result because it reinforces the fact that in order for equation (2) to be applied, both the CS and the FS polarizations must belong to the same branch. For this case the CS and FS values for the 'UP' direction in figure 5(a) were: $P_{CS} = -0.501 \text{C m}^{-2}$, $P_{FS} = 0.870 \text{ C m}^{-2}$ and $P_q = 1.002 \text{ C m}^{-2}$. By correcting either value, the spontaneous polarization can be obtained to be $P_s = 0.369 \text{ C m}^{-2}$. Another interesting aspect of this example is the value of the polarization quanta which is about two times smaller than the values obtained for $PbTiO_3$ and $BaTiO_3$. This result has been thoroughly discussed in the specialized literature and the reader should consult [26] for a complete explanation.

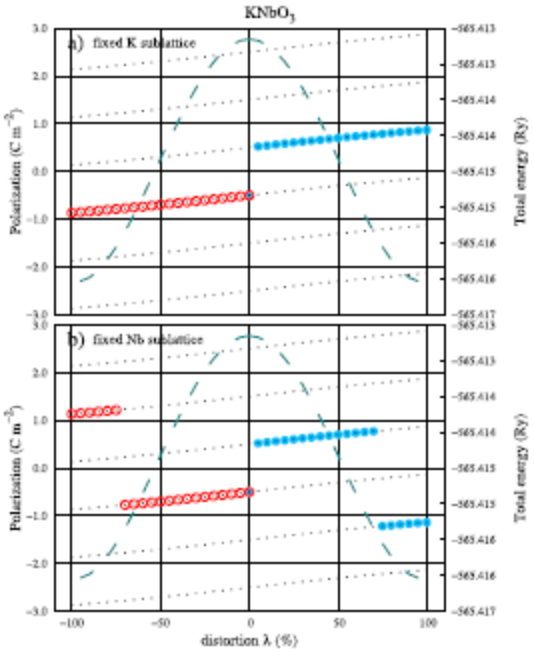

Figure 5. Polarization lattice for $KNbO_3$ (black dots given by equation (3)) with distortion from the CS to the 'DOWN' FS (red empty circles) and from the CS to the 'UP' FS (solid blue circles) with respect to the *K* sublattice (a) and with respect to the Nb sublattice (b). The distortion parameter λ was modified in 5% steps, with the negative values for the 'DOWN' intended for a better clarity of the figure. The green dashed line is the total energy as a function of distortion showing a continuous variation for each distortion path.

6. Optimization strategy for BP polarization calculations

The examples shown in figures 3–5 have been presented using a large number of calculations in order to help visualize polarization branches. As stated above, the calculations were performed using the *Quantum Espresso* simulation package and the branch jumps in figures 3–5 can be replicated for these three systems almost exactly if the same initial conditions are met. However, it must be pointed out that using other packages such as *VASP*, *Wien2k* or *ABINIT* may lead to branch jumps at different positions or indeed, a smaller number of them. Nevertheless, the random occurrence of these jumps should be expected. In a regular scenario, some cases can be clarified using a smaller number of calculations. On average, depending on the choice of the distortion parameter value λ, four calculations should be enough to correctly identify the polarization branches and obtain the spontaneous polarization for the first three cases presented in section 5. Yet the only common feature that remains is that each material requires an individual treatment to obtain the spontaneous polarization. This process is far more tedious for larger system sizes. In order to illustrate our

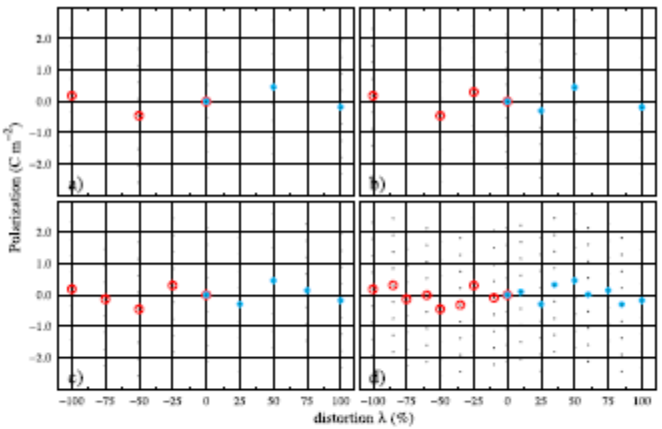

Figure 6. Polarization lattice for $Pb(Zr_{0.25}Ti_{0.75})O_3$ super-cell (black dots) with the calculated values in filled blue circles for the 'UP' polarization direction and empty red circles for 'DOWN': (a) one intermediary point at 50% distortion; (b) two intermediary points: 25% and 50% distortion; (c) three intermediary points: 25%, 50% and 75% distortion; (d) seven intermediary points: 10%, 25%, 35%, 50%, 60%, 75% and 85% distortion.

optimized method, PZT will be used as the test material and the data will be shown for an ever increasing intermediary number of system distortion states.

Due to the size and the large number of atoms in the super-cell it becomes difficult to fix a sublattice and perform the distortion with respect to it. As an alternative, in this case, all atoms in the unit cell have been moved as described in equation (1) from the CS to the corresponding FS. The calculated polarization values for the CS and FS are: $P_{CS} = 0.0\,C\,m^{-2}$, $P_{FS} = -0.186\,C\,m^{-2}$ and the polarization quanta $P_q = 0.532\,C\,m^{-2}$. This seems to be an ambiguous situation and generally for an unknown material it is difficult to know for sure the spontaneous polarization just from the difference between the FS and CS polarization values. For this reason, an extra point has been introduced in figure 6(a) corresponding to a 50% system distortion. The purpose for adding more intermediary states is to obtain a clear image of the polarization branches in order to identify what correction is needed for the values of interest. In this case, the extra point does not help to clarify the situation completely since no polarization branches are revealed and we make another choice for the next system distortion. This time, a 25% distortion is added to the plot in figure 6(b) and the result does not bring the conclusion any closer. Moving on, a 75% distortion is added next in figure 6(c) with the same result. It is only when smaller distortion steps are added in figure 6(d) that a real image of the PZT polarization branches emerges and a correction can be made by adding two polarization quanta to the FS value in order to bring it on the same branch as the CS case.

Figure 6(d) provides the best clue to introducing an optimization procedure. Let us consider the CS system state and an infinitesimally distorted one by a value $d\lambda$. If $d\lambda$ is small enough we will assume that between these two polarization values there are no other branch jumps such that the following represents the local slope for the variation of polarization with distortion λ:

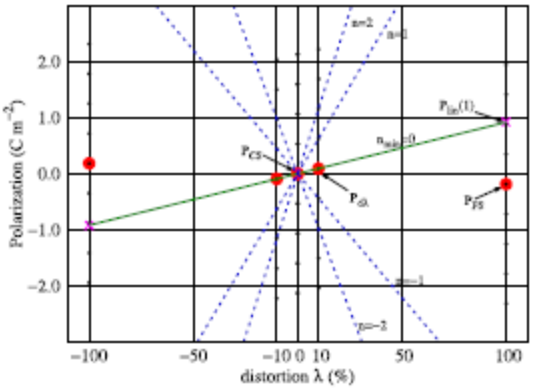

Figure 7. Demonstrating the optimization procedure for finding the correct polarization branch for PZT in the 'UP' direction. Red circles represent calculated points while the black points are the corresponding polarization lattice. The green line is the linear approximation defined in equation (6). The blue dashed lines exemplify the linear approximation for a slope parameter different than the minimal value obtained for n_{min}. The magenta colored crosses are the interpolated values for the two FS.

$$\Lambda = \frac{P_{d\lambda} - P_{CS}}{d\lambda}, \tag{4}$$

where $P_{d\lambda}$ is the *calculated* polarization for an 'infinitesimal' system distortion $d\lambda$ in the vicinity of the reference CS. Unfortunately, both these values are determined up to an integer value of polarization quanta. Therefore the difference is still multivalued and, by extension, the slope parameter has a similar behavior. This problem is much easier to solve if one considers for example the calculated value of P_{CS} as a reference (regardless of what branch it resides on) and replaces the entire family of values for $P_{d\lambda}$ in equation (4):

$$\Lambda(n) = \frac{P_{d\lambda} + n\, P_q - P_{CS}}{d\lambda}, \; n \in \mathbb{Z}. \tag{5}$$

It is now possible to find the integer number n_{min} such that $|\Lambda(n_{min})|$ in equation (5) is minimum. This operation essentially ensures that the calculated polarization $P_{d\lambda}$ is brought to the same branch as P_{CS}. Figure 7 shows the slopes for different values of the branch index n corresponding to the calculated $P_{d\lambda}$ polarization. The continuous green line is obtained for the minimum $|\Lambda(n_{min})|$, where $n_{min} = 0$ in this case. Using n_{min}, equation (5) returns the local slope of the branch-independent $P(\lambda)$.

The materials presented in this work have all shown a rather linear dependence for the polarization values belonging to the same branch. Resta *et al* suggest in [23] that this behavior is a general feature for all materials, however the results obtained by Neaton *et al* in [27] show a departure from the linear dependence. Nevertheless, using the corrected slope calculated with equation (5) one can obtain a reasonable extrapolation for the expected value of the FS polarization at $\lambda = 1$:

$$P_{lin}(\lambda) = \Lambda(n_{min})\, \lambda + P_{CS}. \tag{6}$$

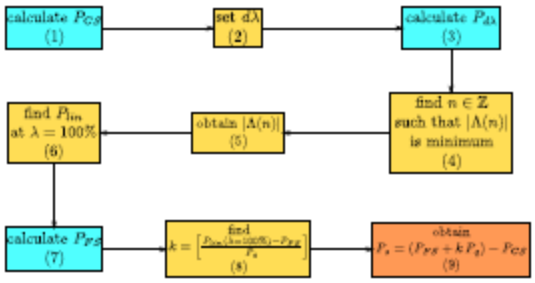

Figure 8. Optimized work-flow for Berry phase calculations. The blue rectangles are polarization calculation runs and in yellow and orange are regular arithmetic operations.

Comparing the extrapolated polarization $P_{\text{lin}}(\lambda = 1)$ from equation (6) with the calculated value P_{FS} one can obtain the necessary correction in order to bring all polarization points on the same branch:

$$k = \left[\frac{P_{\text{lin}}(\lambda = 1) - P_{\text{FS}}}{P_q}\right], k \in \mathbb{Z}. \tag{7}$$

Finally, the spontaneous polarization can be obtained using equation (2) and the corrected P_{FS} value:

$$P_s = (P_{\text{FS}} + k\ P_q) - P_{\text{CS}}. \tag{8}$$

All the steps of the proposed optimization procedure have been summarized in a simple work flow in figure 8. For materials such as the ones presented in this study, where the polarization direction is parallel to one of the principal axes, the total number of calculations is reduced to only three system states (steps 1, 3 and 7). The rest of the steps can be performed with simple arithmetic operations that could potentially be included in a high throughput calculation automated script. For a more general case, the ferroelectric polarization can take any direction in the crystal and the operations proposed by this strategy must be repeated for each of the three cartesian axes.

7. Born effective charges and the BP

Before moving on to commenting results of the proposed strategy, the calculation of Born effective charges via the BP method should also be discussed. The Born effective charge is a tensor that can be defined (among other ways) as the change of polarization induced by a sublattice displacement of atom s in the absence of a macroscopic electric field [26, 37, 38]. When the displacement takes place in the direction of polarization one can write the Born effective charge as:

$$Z_s^* = \frac{\Omega}{e}\frac{\partial P}{\partial u_s}, \tag{9}$$

where Ω is the volume of the unit cell and e is the electron charge. The polarization in this definition is calculated using the BP theory and it has been shown that its values are only defined up to an integer number of a polarization quanta [23, 26]. Since this is a derivative,

Table 2. Calculated polarizations for the Nb sublattice in KNO and the Pb sublattice in PTO, displaced by $\lambda = 1\%$ in the 'UP' and 'DOWN' directions. The values are shown in units of polarization multiplied by the electron charge and divided by the volume of the unit cell.

	Nb (KNO)		Pb(PTO)	
	DOWN	UP	DOWN	UP
$P_{\Delta u_z}$	3.102	−3.103	−0.288	0.288
P_{CS}	−3.838	−3.838	−0.000	−0.000
P_q	7.677	7.677	15.899	15.899
Z^*	9.588		3.629	

the Born effective charge is uniquely defined. From a practical perspective equation (9) can be numerically calculated via several methods, such as the linear-response theory or the more straightforward approach of finite differences, where two polarization calculations are performed, one for a CS state and a second for a small displacement Δu_z. Using the second method, the two calculated polarization values are also defined up to an integer number of polarization quanta and equation (9) becomes:

$$Z_z^{fd} = \frac{\Omega}{e} \frac{P_{\Delta u_z} - P_{CS} + (n-m)P_q}{\Delta u_z}, \tag{10}$$

where fd represents the finite difference value, n and m are integer numbers indexing the branches of the two calculated polarization values, $P_{\Delta u_z}$ and P_{CS}. Nevertheless, the Born effective charges in equations (10) and (9) should lead to the same value as $\Delta u_z \to 0$ and this can only happen if $n = m$, i.e. the two polarizations belong to the same branch!

This raises a very important question of how small should the displacement be in order to ensure that the polarization values calculated for the states with an infinitesimal displacement between them, belong to the same branch. Unfortunately the answer is that no infinitesimal amount can guarantee that, as the examples given in table 2 clearly show. Performing the finite difference calculation of the Born effective charge associated to the Nb atom in the KNO unit cell and also to the Pb atom in the PTO unit cell as described in the Quantum Espresso documentation [39] one obtains the following values when performing a $\lambda = 1\%$ displacement of the sublattices in the 'UP' and 'DOWN' polarization directions:

It is quite clear from the data in table 2 that simply using the finite difference formula in equation (10) one does not obtain the correct Born effective charge for Nb when the sublattice is displaced in the 'DOWN' direction. due to the fact that the two values do not belong to the same branch! This is in stark contrast with the Pb Born charge calculation. Without a branch ambiguity, the finite difference formula can be readily applied and the correct result can be obtained without other modifications to the method. It is thus apparent that, before the finite difference formula is applied, an extra step must be introduced to ensure that the two polarization values belong to the same branch. This can be achieved using the strategy proposed in the previous section.

The answer to the question of how small the displacements must be for the optimization strategy to work is not definitive and, at this point, given all the studied examples, the only clear rule that emerges is that the distortions should be kept below the 10% range. For the PZT example in figure 6 we have used a 10% distortion only after it became clear that no branch jumps were taking place in the vicinity of the CS state, but this should not be considered the norm for all materials!

8. Results

The most important result obtained in this study is the optimization strategy summarized in figure 8. By comparison with the original method for BP calculations in figure 2 the proposed approach does not contain any interrogations steps and algorithm branches. Also, the method is a series of nine consecutive steps and only three calculation runs. The original approach however, may need considerably more calculations if multiple polarization jumps occur for the chosen distortion path of the system.

Using the steps summarized in figure 8 one can obtain the spontaneous polarization for all the cases presented in this study in figures 3–6 using only three of the calculated points for each distortion path. The results can be analyzed in table 3 where the values obtained for each step are shown separated between the two polarization directions (formally denoted as 'UP' and 'DOWN'). The third column of table 3 indicates the sublattice with respect to which the systems were distorted. As described in section 3, for the PZT case all atoms were moved from their corresponding centrosymmetric positions in the super-cell toward the FS positions following the same rule in equation (1).

The application of the proposed optimization strategy is straightforward yet there are some aspects that should be pointed out. First of all, the optimization strategy is based on the theory of polarization as a function of the system distortion as discussed by Resta *et al* [23]. This was shown to be true for the KNO case [23] and it was shown in this work that similar results are obtained for PTO and BTO. However, in a study by Neaton *et al* on $BiFeO_3$ it is shown that the polarization dependence on the system distortion is linear only up to about 20% distortion. For situations where the materials have strong nonlinear polarization dependence on the internal distortion, the proposed optimization strategy may need more calculated points in order to obtain a non-ambiguous result. Another important point to be considered, is one of the crucial conditions for the application of the BP theory: the system must be insulating in any state on the distortion path. This aspect is difficult to control,and such materials will require a more detailed investigation.

9. Conclusions

In summary, the results presented in the current study provide a detailed view of the numerical implementation of the modern theory of polarization from the point of view of actual calculations on various ferroelectric materials. Most of the studies have been purposely performed with an exaggerated fine distortion mesh in order to provide a better visual image of the multivalued aspect of polarization and the emergence of polarization branches. We illustrate this using $BaTiO_3$, $PbTiO_3$ and $KNbO_3$ as test materials. It has been shown that using the approach proposed in the usual BP polarization calculations, each material must be treated individually which makes it difficult to integrate such a study in an automated workflow. For this reason, a unified optimization procedure has been proposed that can provide a starting point for polarization investigation for ferroelectric materials. The procedure uses a minimal number of calculations in order to obtain the spontaneous polarization value, thus reducing the computational effort. We hope the present study will enhance the current efforts in the theoretical investigation of known ferroelectrics and accelerate the design of new ferroelectric materials. The current study and the proposed calculation strategy provides both a visual representation of the multivalued aspect of polarization in the modern theory and a practical approach for such calculations which should complement the theoretical descriptions found in the specialized literature.

Table 3. Spontaneous polarization obtained using the proposed optimization strategy for all the studied materials shown in figures 3–6.

	DOWN								UP							
	BTO		PTO		KNO		PZT		BTO		PTO		KNO		PZT	
	Ba	Ti	Pb	Ti	K	Nb	none		Ba	Ti	Pb	Ti	K	Nb	none	
P_{CS} (C m^{-2})	0.000	0.000	0.000	0.000	−0.501	−0.501	0.000		0.000	0.000	0.000	0.000	−0.501	−0.501	0.000	
dA	5%	5%	5%	5%	5%	5%	10%		5%	5%	5%	5%	5%	5%	10%	
P_{RA} (C m^{-2})	−0.019	−0.019	−0.050	−0.050	−0.522	−0.522	−0.093		0.019	0.019	0.050	0.050	0.522	0.522	0.093	
n	0	0	0	0	0	0	0		0	0	0	0	−1	−1	0	
Λ (C m^{-2})	−0.003 8	−0.003 8	−0.010	−0.010	−0.004 2	−0.004 2	−0.009 3		0.003 8	0.003 8	0.010	0.010	0.004 2	0.004 2	0.009 3	
$P_{sat}(1)$ (C m^{-2})	−0.380	−0.380	−1.000	−1.000	−0.921	−0.921	−0.930		0.380	0.380	1.000	1.000	−0.081	−0.081	0.93	
P_{RS} (C m^{-2})	−0.350	1.685	1.185	1.185	−0.870	1.135	0.186		0.350	−1.685	−1.185	−1.185	0.870	−1.134	−0.186	
k	0	−1	−1	−1	0	−2	−2		0	1	1	1	−1	1	2	
P_s (C m^{-2})	−0.350		−0.945		−0.369		−0.878		0.350		0.945		0.369		0.878	

Acknowledgments

The authors would like to acknowledge the useful discussions with Dr Claude Ederer from ETH, Zurich that helped clarify the theoretical and practical aspects of the Berry phase polarization theory.

The authors would also like to acknowledge the funding by the Romanian Ministry of Education Executive Unit for Funding High Education, Research, Development and Innovation (MEN-UEFISCDI) through the Young Research Team Grant PNII-RU-TE-2012-3-0320 (Contract No. 11). And the financial support from the NIMP Core Program nr. PN18-110101 and the PCCF project nr. PN-III-P4-ID-PCCF-2016-0047 funded by the Ministry of Research and Innovation though UEFISCDI executive unit. 6.

ORCID iDs

Lucian D Filip https://orcid.org/0000-0001-7319-1758

References

[1] Scott J F and de Araujo C A P 1989 *Science* **246** 4936
[2] Hidaka T 1992 *Ferroelectrics* **137** 291–5
[3] Glinchuk M D, Kirichenko E V, Stephanovich V A and Zaulychny B Y 2009 *J. Appl. Phys.* **105** 104101
[4] Kumari P, Rai R, Sharma S, Shandilya M and Tiwari A 2015 *Adv. Mater. Lett.* **6** 453–84
[5] Rong Y, Li M, Chen J, Zhou M, Lin K, Hu L, Yuan W, Duan W, Deng J and Xing X 2016 *Phys. Chem. Chem. Phys.* **18** 6247–51
[6] Scott J F 2007 *Science* **315** 954–9
[7] Choi T, Lee S, Choi Y J, Kiryukhin V and Cheong S W 2009 *Science* **324** 63–6
[8] Garcia V, Fusil S, Bouzehouane K, Enouz-Vedrenne S, Mathur N D, Barthélémy A and Bibes M 2009 *Nature* **460** 81–4
[9] Huang H 2010 *Nat. Photon.* **4** 134–5
[10] Yuan Y, Reece T J, Sharma P, Poddar S, Ducharme S, Gruverman A, Yang Y and Huang J 2011 *Nat. Mater.* **10** 296–302
[11] Liu F, Wang W, Wang L and Yang G 2014 *Appl. Phys. Lett.* **104** 103907
[12] Chen B, Zheng X, Yang M, Zhou Y, Kundu S, Shi J, Zhu K and Priya S 2015 *Nano Energy* **13** 582–91
[13] Kim W Y, Kim H D, Kim T T, Park H S, Lee K, Choi H J, Lee S H, Son J, Park N and Min B 2016 *Nat. Commun.* **7** 10429
[14] Moure C and Peña O 2015 *Prog. Solid State Chem.* **43** 123–48
[15] Pintilie L, Vrejoiu I, Le Rhun G and Alexe M 2007 *J. Appl. Phys.* **101** 064109
[16] Kundu S *et al* 2015 *Sci. Rep.* **5** 12415
[17] Volonakis G, Filip M R, Haghighirad A A, Sakai N, Wenger B, Snaith H J and Giustino F 2016 *J. Phys.Chem. Lett.* **7** 1254–9
[18] Filip M R and Giustino F 2016 *J. Phys. Chem.* C **120** 166–73
[19] Filip M R, Hillman S, Haghighirad A A, Snaith H J and Giustino F 2016 *J. Phys. Chem. Lett.* **7** 2579–85
[20] Berry M V 1984 *Proc. R. Soc.* A **392** 45–57
[21] Resta R 1992 *Ferroelectrics* **136** 51–5
[22] King-Smith R and Vanderbilt D 1993 *Phys. Rev.* B **47** 1651–4
[23] Resta R, Posternak M and Baldereschi A 1993 *Phys. Rev. Lett.* **70** 1010–3
[24] Resta R 1993 *Europhys. Lett.* **22** 133
[25] Resta R 1994 *Rev. Mod. Phys.* **66** 899–915
[26] Resta R and Vanderbilt D 2007 Theory of polarization: a modern approach *Physics of Ferroelectrics: A Modern Perspective* (Berlin: Springer) pp 31–68
[27] Neaton J, Ederer C, Waghmare U, Spaldin N and Rabe K 2005 *Phys. Rev.* B **71** 014113

[28] Hohenberg P and Kohn W 1964 *Phys. Rev.* **136** B864–71
[29] Giannozzi P *et al* 2009 *J. Phys.: Condens. Matter* **21** 395502
[30] Perdew J P, Ruzsinszky A, Csonka G I, Vydrov O A, Scuseria G E, Constantin L A, Zhou X and Burke K 2008 *Phys. Rev. Lett.* **100** 136406
[31] THEOS Theory and Simulation of Materials 2017 Pseudopotentials http://theossrv1.epfl.ch/Main/Pseudopotentials
[32] Monkhorst H J and Pack J D 1976 *Phys. Rev.* B **13** 5188
[33] Wang J J, Meng F Y, Ma X Q, Xu M X and Chen L Q 2010 *J. Appl. Phys.* **108** 034107
[34] Sághi-Szabó G, Cohen R E and Krakauer H 1998 *Phys. Rev. Lett.* **80** 4321
[35] Dall'Olio S, Dovesi R and Resta R 1997 *Phys. Rev.* B **56** 10105–14
[36] Spaldin N A 2012 *J. Solid State Chem.* **195** 2–10
[37] Gonze X and Lee C 1997 *Phys. Rev.* B **55** 10355–68
[38] Ghosez P, Michenaud J P and Gonze X 1998 *Phys. Rev.* B **58** 6224–40
[39] Born effective charges calculated using Quantum Espresso https://github.com/maxhutch/quantum-espresso/tree/master/PW/examples/example04

Anexa 4

ARTICLE IN PRESS

Ceramics International xxx (xxxx) xxx–xxx

Contents lists available at ScienceDirect

Ceramics International

journal homepage: www.elsevier.com/locate/ceramint

(Ba,Sr)TiO_3 solid solutions sintered from sol-gel derived powders: An insight into the composition and temperature dependent dielectric behavior

Roxana Elena Patru[a], Constantin Paul Ganea[a], Catalina-Andreea Stanciu[b], Vasile-Adrian Surdu[b], Roxana Trusca[b], Adelina-Carmen Ianculescu[b,**], Ioana Pintilie[a,*], Lucian Pintilie[a]

[a] National Institute of Materials Physics, Atomistilor 405A, Magurele, 077125, Romania
[b] Department of Oxide Materials Science & Engineering, Faculty of Applied Chemistry and Materials Science, "Politehnica" University of Bucharest, 1-7 Gh. Polizu, Bucharest, 011061, Romania

ARTICLE INFO

Keywords:
BST ceramics
Phase-transition
Thermal hysteresis
Dielectric relaxation
Impedance-spectroscopy

ABSTRACT

Single-phase $Ba_{1-x}Sr_xTiO_3$ (BST) perovskite ceramics with $0.3 \leq x \leq 0.4$ were prepared from powders synthesized via sol-gel route. The compositions have the ferroelectric-paraelectric phase transition close to room temperature. At 20 °C the BST ceramics are ferroelectric for $0.3 \leq x \leq 0.35$ and paraelectric for $x = 0.375$ and $x = 0.40$. The study follows the relation between the structural changes produced when increasing the Sr content and the dielectric properties at low intensity electric fields. It is found that the grain size and tetragonality decreases as the Sr content increases. Analyses of complex permittivity and impedance spectroscopy reveal the temperature and frequency dependencies of the dielectric properties. The phase transitions seem to be of first order for all compositions, with a thermal hysteresis that decreases with increasing the Sr content, fact attributed to the corresponding increase of the grain boundaries weight allowing a more efficient stress relaxation in the structure during the change of the symmetry from cubic to tetragonal. The diffusiveness degree during the phase transition is increasing with Sr content, suggesting some relaxor-type contribution attributed to smaller grain size. The ac conductivity follows the universal Jonscher law, with an ac component having the power parameter *s* independent of Sr content, and a dc component that it is thermally activated with an activation energy of about 0.7–0.77 eV attributed to oxygen vacancies acting as donor-like defects. The fit of impedance spectra at different temperatures and frequencies is obtained by using an equivalent circuit accounting the grains, grain boundaries, electrode interfaces and the local contributions produced by reorientation of defect dipoles or defect clusters. All the component circuits have significant variations around phase transitions. These are discussed in relation to structural changes occurring during transition and considering the changes in the distribution of various charges when polarization vanishes.

1. Introduction

Ferroelectric materials are very interesting not only for fundamental research, but for due to their specific features and multi-functionality, they are promising candidates for a large number of applications in microelectronics [1]. The ability of being nonlinear and hysteretic with the dielectric permittivity and polarization dependent on the applied field is a main feature that makes these materials interesting and suitable for wireless communications and for microwave devices, data storage, random access memories, ferroelectric tunneling barriers and ferroelectric gate transistors [2–5]. In addition, ferroelectric materials show pyroelectricity, piezoelectricity and specific electro-optic properties that lead to a broad spectrum of applications as transducers, medical imaging, ultrasonic devices, modulator switches, etc. [1–5].

Barium strontium titanate (BST) is one of the most common and studied ferroelectric oxide alongside the solid solutions of barium titanate (BT) [6–8] since the discovery of ferroelectricity in BT [9]. With their promising composition-dependent nonlinear dielectric and hysteretic properties, the BST materials have been the subject of many previous studies. Therefore, thorough research works were dedicated to dielectric properties, frequency- and electric field-dependences, as well as to dielectric relaxation phenomena related to the ferroelectric - paraelectric phase transition in a large range of temperatures [7,10–12]. Nevertheless, the dielectric properties of BST materials still

*Corresponding author.
**Corresponding author.
E-mail addresses: adelina.ianculescu@upb.ro (A.-C. Ianculescu), ioana@infim.ro (I. Pintilie).

https://doi.org/10.1016/j.ceramint.2019.10.136
Received 6 September 2019; Accepted 15 October 2019

Please cite this article as: Roxana Elena Patru, et al., Ceramics International, https://doi.org/10.1016/j.ceramint.2019.10.136

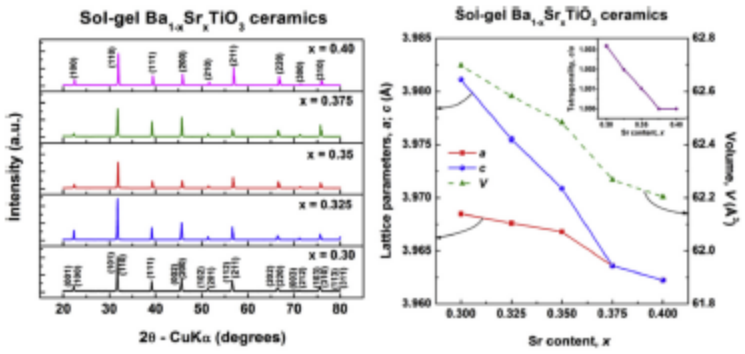

(a) (b)

Fig. 1. Room-temperature X-ray diffraction patterns of the sol-gel BST ceramics (a) and evolution of structural parameters *vs.* Sr content (b); inset of Fig. 1(b) - dependence of the tetragonality (c/a) as a function of Sr addition.

present aspects that deserve a closer insight. In the light of the critical role played by temperature in the ferroelectric state or close to the Curie point, where relative permittivity and dielectric losses reaches their maximum values, a complex analysis on the low field properties *via* broadband impedance spectroscopy is proposed.

To investigate ferroelectrics at temperatures below, close to and above their phase transitions is an appealing task for a better understanding of the low field functional properties in relationship with specific structural and microstructural characteristics. The present study involves a detailed investigation of several $Ba_{1-x}Sr_xTiO_3$ compositions having the ferroelectric-paraelectric phase transition located at temperatures near the room temperature (RT = 20 °C). They are: *(i)* compositions that exhibit a paraelectric behavior at RT (x = 0.4 and x = 0.375), *(ii)* a composition facing the ferroelectric-paraelectric phase transition at RT (x = 0.35), and *(iii)* compositions that are in the ferroelectric state at RT (x = 0.325 and x = 0.3).

Irrespective of heterogeneities type in the ferroelectric materials (structural defects, solutes/dopants, charged vacancies, localized polar species) the short and long-range interactions are affected when increasing the temperature. In addition, the dielectric relaxation mechanisms may change according to the amount of free charge carriers in the oxide ceramic material [13]. Several thermally activated physical processes (e.g. charges migration, reorientation and disorder of dipoles) are influencing the electrical polarization and have impact on the electrical conductivity. Considering these aspects, our experimental study on the complex low-field properties aims to elucidate in which way the charged species at the boundaries of ferroelectric phases affect the functional properties of the BST materials.

2. Experimental methods

The $Ba_{1-x}Sr_xTiO_3$ ceramics, with x = 0.3, 0.325, 0.35, 0.375, 0.4, and abbreviated in the following as BST30, BST32.5, BST35, BST37.5 and BST40, respectively have been prepared in a parallel plate-capacitor configuration from powders synthesized *via* sol-gel route. The preparation process details were previously described elsewhere [14].

X-ray diffraction (XRD) measurements were performed at room temperature (RT = 20 °C) in order to investigate the phase purity and crystal structure of the sol-gel ceramics. For this purpose, a SHIMADZU XRD 6000 diffractometer (Kyoto, Japan) with Ni-filtered CuKα radiation (λ = 1.5406 Å) was used. The measurements were performed in θ – 2θ mode, with a scan step increment of 0.02° and a counting time of 1s/step, in the 2θ range of (20–80) °. Phase identification was performed using HighScore Plus 3.0e software, connected to the ICDD PDF-4+ 2017 database. Lattice parameters were refined by the Rietveld method.

The microstructure of the BST ceramics was analyzed by means of a high-resolution FEI QUANTA INSPECT F microscope with field emission gun (FEI Co., the Nederlands). The grain size of the ceramics was determined as the mean intercept length by taking into account measurements on ~70–80 grains (from images of appropriate magnifications obtained from various microscopic fields). The relative density values of the sintered ceramic pellets were roughly determined as the ratio between the apparent density measured by Archimedes' principle and their crystallographic density calculated from the diffraction data.

Dielectric spectroscopy measurements, in the 10^0 Hz–10^6 Hz frequencies range, with 0.5 V amplitude of the a.c. signal and between −50 °C and +100 °C using an Alpha-A Novocontrol low frequency impedance-meter system, have been carried out. The polished ceramic specimens were covered with silver electrodes on both sides. Dielectric data were recorded during heating and cooling with a rate of 0.6 °C·min^{-1}, low enough to ensure a homogeneous temperature inside the bulk of the studied ceramics.

3. Results and discussions

3.1. Phase purity, structure and microstructure

The X-ray diffraction patterns shown in Fig. 1 were recorded at ambient temperature and they show that all the ceramics are single phase BST. The presence of the well-crystallized perovskite solid solution as unique phase was revealed by the main reflections, which are shifted toward higher diffraction angles as the Sr addition increases, proving the complete homovalent incorporation of Sr^{2+} on Ba sites (Fig. 1(a)).

Even if for the samples with a lower solute content ($0.30 \leq x \leq 0.35$) no clear splitting of the (200) reflection was observed, the best fits of the Rietveld refinement were obtained for the tetragonal symmetry of the unit cell (ICDD no. 04-015-0356 and ICDD 04-021-6861), suggesting that the BST30, BST32.5 and BST35 ceramics are in the ferroelectric state at RT. However, the low values of the tetragonality degree (expressed as c/a ratio) which decreases from 1.0032 for BST30 to 1.002 for BST32.5 and, finally, to 1.001 for BST35 seem to indicate that the ferroelectric-paraelectric phase transition is approaching room temperature. Increasing the Sr concentration (x = 0.375 and x = 0.40) a cubic structure is determined (ICDD no. 04-016-6476 and ICDD no. 04-015-0441), indicating the paraelectric state for the BST37.5 and BST40 samples (inset of Fig. 1(b)). Taking into account the difference in the ionic radius values of the substituent and substituted species ($r(Sr^{2+}) = 1.44$ Å and $r(Ba^{2+} = 1.61$ Å) [15], it

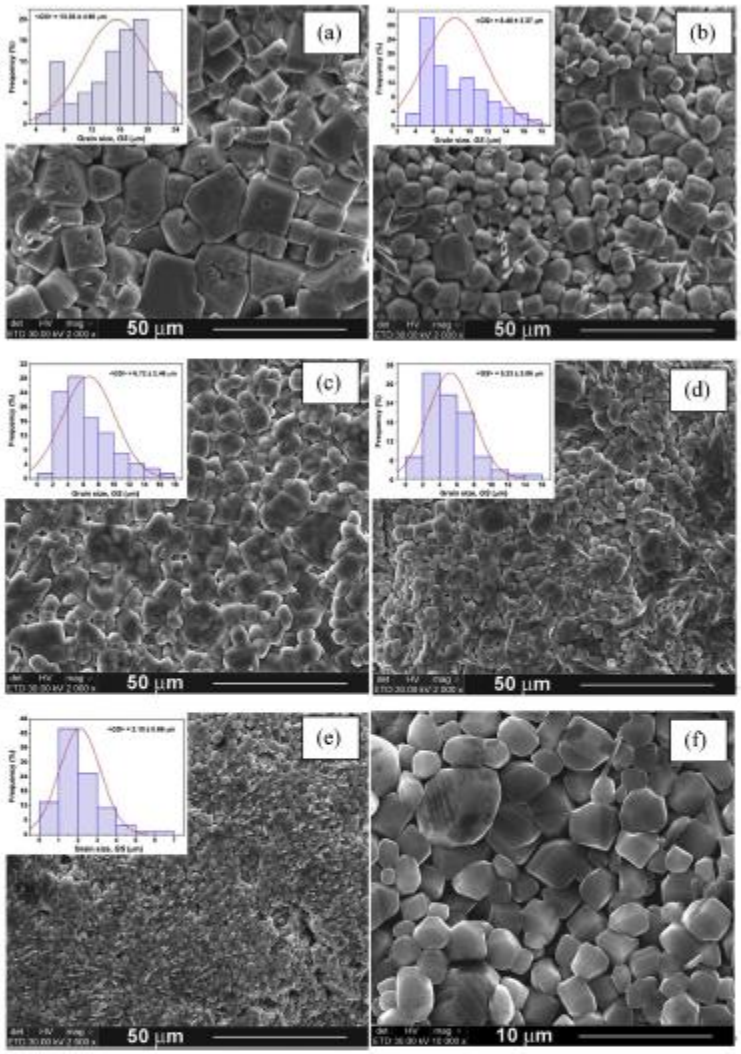

Fig. 2. FE-SEM images of BST ceramics derived from sol-gel powders: (a) BST30; (b) BST32.5; (c) BST35; (d) BST37.5; (e) BST40 - overall view and (f) BST40 - detail. The insets show the distribution of the grain sizes.

result that the increase of the fraction of Sr^{2+} ions incorporated on barium sites induces the reduction of the lattice parameters and, consequently, the shrinkage of the unit cell volume. The latter is gradually decreasing from 62.697 $Å^3$ for BST30 to 62.203 $Å^3$ for BST40 (Fig. 1(b)).

For all the BST specimens under investigation, the FE-SEM images reveal dense and uniform microstructures, consisting of well faceted polyhedral grains and a variable amount of intergranular porosity (see Fig. 2(a)-(f)). The increase of the Sr amount incorporated in the perovskite lattice induces: (*i*) the decrease of the grain size; (ii) the change of grains morphology, from cubes and parallelepipeds in BST30 sample to irregular polyhedral shapes in BST32.5 – BST40 ceramics; (iii) a gradual narrowing of the maximum specific to the unimodal grain size distribution (the top-left insets of Fig. 2(a)-(e)). It is worthy to mention that even in the fine-grained BST40 specimen the ceramic grains preserve the polyhedral morphology (see the higher magnification FE-SEM image of Fig. 2(f)). In addition, according to Fig. 3, the average grain size $< GS >$ decreases from 15.6 µm in BST30 to 2.1 µm in BST40 ceramic sample, meaning that the Sr solute continues to act as grain growth inhibitor also for concentrations $x > 0.3$, higher than those reported earlier ($0.1 \leq x \leq 0.3$) [14]. Relative density values, as determined from the ratio between apparent and theoretical density values, are in the 87–92% range.

3.2 *Dielectric properties*

3.2.1. *Temperature dependence of dielectric properties and Curie – Weiss analysis*

The macroscopic properties are strongly influenced by the partial substitution of Ba with Sr^{2+} on the *A* – site in ABX_3 lattice of BT,

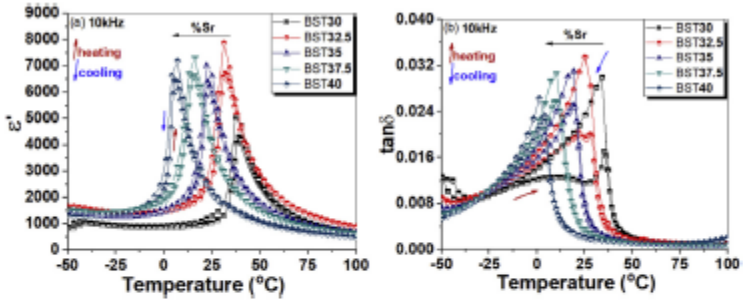

Fig. 3. Temperature dependence of real part of dielectric permittivity $\varepsilon'(T)$ (a) and of dielectric losses (b) for BST ceramics specimens at 10 kHz during heating and cooling. The arrows show the increase of Sr content.

becoming possible this way to modulate the tetragonal (ferroelectric) to cubic (paraelectric) phase transitions. The transitions between ordered states in a ferroelectric material are accompanied by strong variations of dielectric properties (dielectric permittivity, losses and conductivity) with temperature. The temperature dependence of the real part of the dielectric permittivity $\varepsilon'(T)$ depicted i tan $\delta(T)$n Fig. 3(a) shows that the sharp peak associated with the phase transition is shifting towards lower temperatures with increasing the Sr content.

At room temperature the specimens BST30, BST32.5 and BST35 are in the ferroelectric state and those with a higher Sr content (BST37.5 and BST40) are in the paraelectric phase. These results are in good agreement with the room temperature XRD structural data (see Fig. 1(b)) which indicated a decreased tetragonality of the unit cell with the increase of Sr content from 30 to 35% and a cubic symmetry of the unit cell for the BST specimens with 37.5 and 40% Sr concentrations. The maximum value of the real part of dielectric permittivity ε' was found to be ~7000 for all samples, excepting the BST30 specimen, for which ε' is ~5000 [14]. The increase of the dielectric permittivity over the temperature range corresponding to the ferroelectric state of the BST specimens with $x \geq 0.325$ might be correlated with the observed decrease of the grain size (see Fig. 2). According to the study performed by Arlt et al. on pure $BaTiO_3$ ceramics internal strains are induced due to the transition from a multi-domain (twined) toward a single-domain structure when the average grain size is dropping to ~ 1 μm [16,17].

The loss tangent measured close to the phase transitions during the heating and cooling processes reaches maximum values of about 2.5% and 3.4%, respectively, while it is below 1% for the rest of the temperature range (see Fig. 3(b)). Thus, when the dielectric permittivity reaches maximum values close to the phase transition, the dielectric losses still have low values, which is a desired attribute in electroceramics.

The continuum heating - cooling cycles were carefully monitored near the narrow temperature range of the phase transitions, in an attempt to clarify how the composition influences the Curie temperature (T_C). Fig. 4(a) shows the temperature dependences of $\varepsilon'(T)$ and tan $\delta(T)$ for a frequency of 10 kHz. The ferroelectric to paraelectric phase transition was closely followed for each composition, the dielectric response for different frequencies being shown in Fig. 4(b)–(f). A slight frequency dispersion in the region specific to the ferroelectric state, without shifting the transition temperature, is noticed for all the ceramic samples starting with BST30, where the difference between ε' ($f = 10^0$ Hz) and ε' ($f = 10^6$ Hz) is of about 500, and it reaches ~1100 in case the of BST40 sample. A similar behavior is observed for the dielectric losses.

More interesting aspects concern the thermal hysteresis (see Fig. 4(b)–(f) and Fig. S1 in Support Information -SI). This seems to drop in a monotonic way with Sr addition, allowing also, a correlation with the size of the grains and their distribution, as it will be described further. The evolution of average grain size and hysteresis with Sr content is represented in Fig. 5. The T_m temperature has larger values during heating (T_m^h) than during cooling (T_m^c). The difference $\Delta T_m = T_m^h - T_m^c$ is a measure of the thermal hysteresis. The relationship between microstructural aspects and ΔT_m needs a closer insight. The observed reduction in thermal hysteresis with increasing the Sr content (see Fig. 5) correlates well with the changes induced by the addition of this solute in the evolution of structural properties and microstructural features as: (*i*) reduction of tetragonality; (*ii*) reduction in the volume of the unit cell and (*iii*) reduction in the grain size (see Fig. 2(a)–(e)). One can assume that all these changes can lead to a more efficient release of the stress induced by the phase transition from cubic paraelectric to tetragonal ferroelectric, reducing the thermal hysteresis as the Sr content increases. This is in agreement with previous reports on similar ceramic materials [18–20], although other reports noticed a maximum in the value of the hysteresis for a certain grain size [21,22].

The frequency dispersions presented in Fig. 4(b)–(f) only characterizes the phase transition. Once the samples are in the paraelectric state, the frequency dependence is disappearing, and the ceramics fully satisfy the Curie - Weiss law for $T > T_C$:

$$\varepsilon'(T) = \frac{C}{T - T_0} \tag{1}$$

where C is the Curie constant, a measure of ferroelectricity, and T_0 is the Curie-Weiss temperature. Regarding the diffuseness and the character of a phase transition, we have considered the Curie-Weiss law modified according to Santos - Eiras [23] which addresses both, the classical and the relaxor ferroelectrics. In this case the real part of the electrical permittivity is given by:

$$\varepsilon'(T) = \frac{\varepsilon'_m}{1 + \left(\frac{T - T_m}{\delta_\gamma}\right)^\gamma} \tag{2}$$

where ε'_m is the maximum value of the measured $\varepsilon'(T)$ corresponding to the T_m temperature. The two parameters γ and δ_γ are related to the transition character. The γ parameter takes values between 1 and 2, $\gamma = 1$ being a typical value for a classic ferroelectric material while $\gamma = 2$ is associated with a complete relaxor material. The δ_γ parameter represents the diffuseness degree of the paraelectric-ferroelectric phase transition and is determined from the peak broadening in $\varepsilon'(T)$.

The temperature dependence of $\varepsilon'(T)$ have been analyzed according to the above equations, the γ and δ_γ parameters being determined by fitting (see Fig. 6). The few critical parameters for a phase transition in a ferroelectric material were determined as a function of frequency, in accordance with the solute content and based on the data measured during the different thermal cycles. The diffuseness degree δ_γ is determined by using the modified Curie – Weiss law, while the C constant and the Curie-Weiss temperature T_0 were calculated from the linear regression fits of $10^3/\varepsilon'(T)$ in the paraelectric state, as shown in Fig. 6(a). The Curie temperatures were determined from the intersection of the $10^3/\varepsilon'(T)$ linear representations in the proximity of the

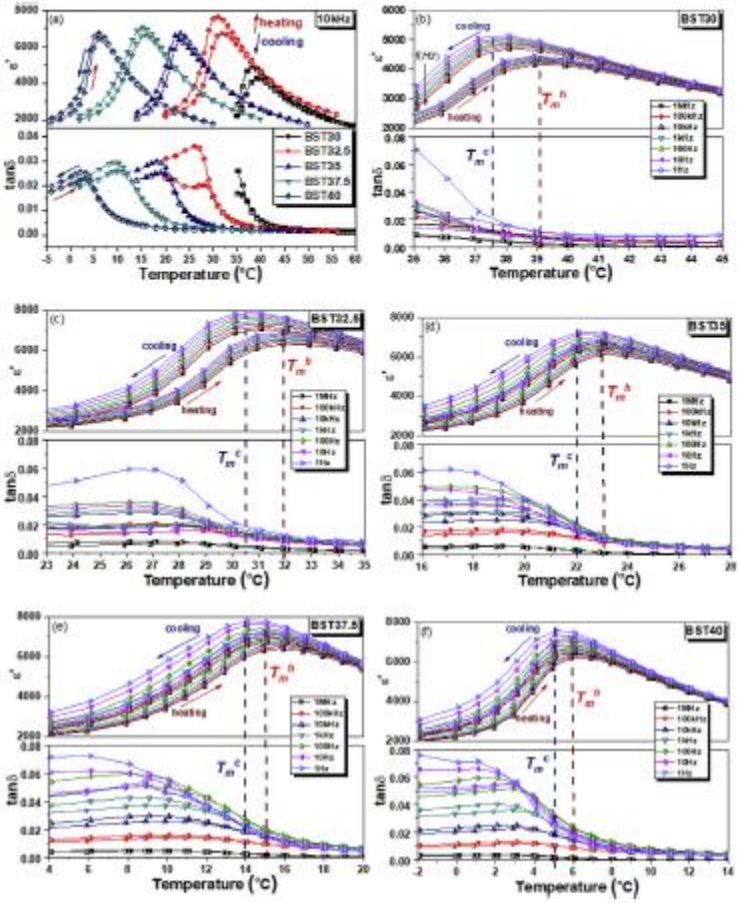

Fig. 4. Temperature dependence of $\varepsilon'(T)$ and $\tan\delta(T)$ on both heating and cooling cycles for all the BST compositions at 10 kHz (a) and for each composition and different frequencies, from 1 Hz to 10^6 Hz, (b)–(f). The dashed lines mark the temperatures corresponding to the maximum value of ε' during heating (T_m^h) and cooling (T_m^c).

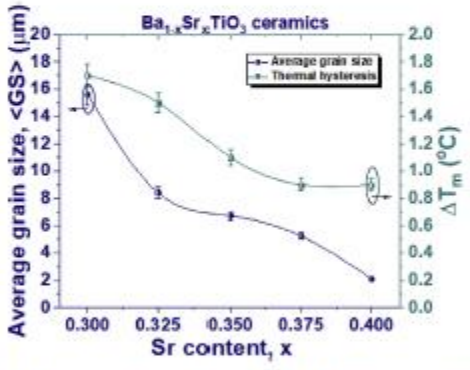

Fig. 5. The average grain size $< GS >$ and thermal hysteresis ΔT_m as a function of Sr content.

phase transition (see the Curie–Weiss fit in Fig. 6(a)). They are 39 °C in the case of BST30, 31 °C for BST32.5, 23 °C for BST35, 15 °C for BST37.5 and 6 °C for BST40.

The frequency dispersion of $\varepsilon'(T)$ shown in Fig. 4(b)–(f) produces effects on γ and the diffuseness degree of the phase transition. For all the compositions, the γ and δ_γ parameters are slightly increasing with frequency (see e.g. the case of BST32.5 in Fig. 6(b)). The γ parameter, for example, is increasing from −1.05 for 1 Hz to no more than −1.3 for 1 MHz, meaning that the more increases the frequency the more the transition moves away from that one specific to a classical ferroelectric. Both T_C and T_0 temperatures show an almost linear decrease as the Sr content increases and T_0 is always lower than T_C, as expected for a first order phase transition. The only parameter that is significantly influenced by the cooling-heating thermal cycles is the maximum value of the dielectric constant $\varepsilon'_m(\nu)$ (inset of Fig. 6(b)).

The calculated Curie constant is presented in Fig. 6(c). It appears uninfluenced by the repeated thermal cycles of measurements. Instead, the calculated results are closely related to the dielectric data presented in Fig. 4(a), where BST specimens have different values for the measured dielectric permittivity, the sample with the highest value of permittivity, BST32.5, exhibiting also the highest Curie constant

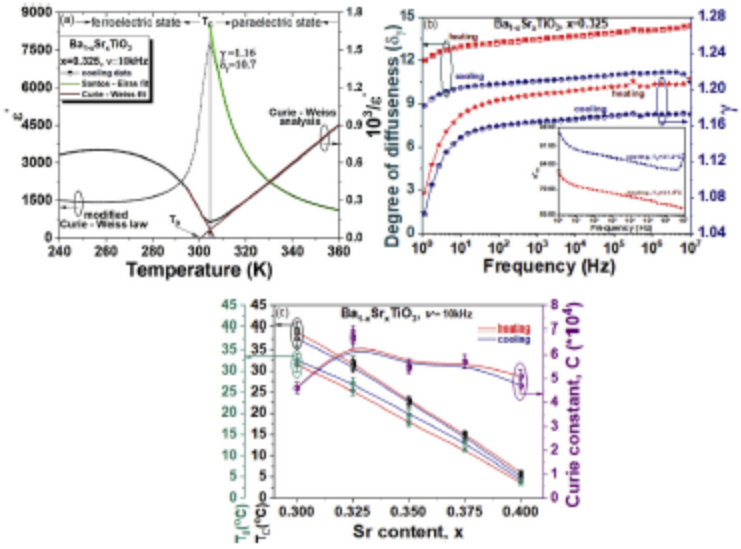

Fig. 6. Example of Curie-Weiss data analyses for BST32.5, at 10 kHz during heating and cooling (a); frequency dependence of the γ and δ_γ fitting parameters calculated for BST32.5 with $\varepsilon'_m(\nu)$ in inset (b); calculated Curie constant and critical temperatures T_C and T_0 as a function of Sr content for the investigated BST ceramics (c).

(Fig. 6(c)).

3.2.2. Dielectric relaxation and AC conductivity

The dependence of the imaginary part of the complex permittivity on frequency, $\varepsilon''(\nu)$, provides information about the relaxation mechanisms inside the BST ceramic specimens. The dielectric data, are represented in Fig. 7 for three temperatures, T_C, with 20 °C below and above T_C of each of the BST compositions. The frequency dependencies of $\varepsilon'(\nu)$ and $\varepsilon''(\nu)$ measured on all the samples at the same temperature (25 °C and 100 °C) are given in Fig. S2 from SI.

In Fig. 7(a and b) all the specimens are in the ferroelectric phase, the temperature being with 20 °C below their own Curie point. A slight decrease of $\varepsilon'(\nu)$ with frequency is accompanied by dielectric relaxations in $\varepsilon''(\nu)$which extends downward over the entire frequency range. The data presented in Fig. 7(c and d) correspond to the Curie point specific to each of the BST specimens. The Curie temperatures for each BST composition are labeled in Fig. 7(d). The phase transition is marked by an increase of the loss factor and by the occurrence of very large dielectric relaxations in $\varepsilon''(\nu)$ with 2 maxima, near 10^2 Hz and 10^5 Hz, associated to several polarization mechanisms. For temperatures with 20° above their own Curie point the specimens have just overcome the phase transition and are settled in the paraelectric state (see Fig. 7(e and f)). In this case, the real part $\varepsilon'(\nu)$is virtually constant with frequency, while the imaginary part show relaxation at low frequencies, probably related to structural defects acting as traps.

The dynamics of both, the ferroelectric domains below T_C, and of the atoms inflicting polar fluctuations near T_C, materialize through several maxima in $\varepsilon''(\nu)$. These mechanisms also manifest at temperatures above T_C (see Fig. 7 (f)) but without reaching the same magnitude as during the phase transition.

Previous studies of electron density distribution have demonstrated that by increasing the Sr^{2+} content and achieving a homogeneous diffusion into the $(Ba,Sr)TiO_3$ lattice, the ionic nature of the bond between Ba^{2+}/Sr^{2+} and O^{2-} species is growing while the one between the Ti^{4+} and O^{2-} is diminished [24]. This way, the thermally activated mechanism of free charge carriers' transfer may be favored at sufficiently elevated temperatures, leading also to a frequency dispersion of conductivity, especially in the low frequency range. This frequency dispersion was attributed to a reversible storage of charge in the bulk material or at interfaces, which is not exactly a dc conduction, even if the isotherms keep a similar trend [25–27].

The complex permittivity expressed for a capacitor with losses contains also the conductive component. Thereby, the contribution of charge transport in terms of the loss factor is quantitatively expressed as function of frequency, as in the equation below [28]:

$$\varepsilon''(\nu) = \frac{\sigma'(\nu)}{\omega\varepsilon_0} \tag{3}$$

where $\omega = 2\pi\nu$ is the angular frequency, ε_0 is the free space permittivity, and $\sigma'(\nu)$ is the real part of the total conductivity. Consequently, $\sigma'(\nu)$ can be written based on the complex permittivity as:

$$\sigma'(\nu) = \omega\varepsilon_0\varepsilon'(\nu)\tan\delta(\nu) \tag{4}$$

while the loss tangent $\tan\delta(\nu)$ is calculated using $\tan\delta(\nu) = \frac{\varepsilon''(\nu)}{\varepsilon'(\nu)}$ formula.

Further, $\sigma'(\nu)$ is described by a relation between the frequency-independent conductivity part σ_{dc} and the frequency-dispersive one $\sigma_{ac}(\nu)$:

$$\sigma'(\nu) = \sigma_{dc} + \sigma_{ac}(\nu) \tag{5}$$

The σ_{dc} represents the ionic conductivity of a material and is usually highlighted in the plateau found in $\sigma'(\nu)$ versus frequency plots in the low-frequency region.

If dielectric relaxations appear in the log/log conductivity *vs.* frequency plot, then the frequency dependent part of conductivity $\sigma_{ac}(\nu)$may be analyzed based on Jonscher's universal conductivity expression [29,30], and $\sigma'(\nu)$ becomes:

$$\sigma'(\nu) = \sigma_{dc} + A\omega^{s(T)} \tag{6}$$

where A is the pre-exponential factor that determines the strength of polarization, ω is the angular velocity, and $s(T)$, with values between 0 and 1, reflects the interaction degree between mobile ions and the environment. Both the A and $s(T)$ factors depend on the type of relaxation processes, temperature and composition.

Dielectric relaxations in the ferroelectric phase are mainly due to

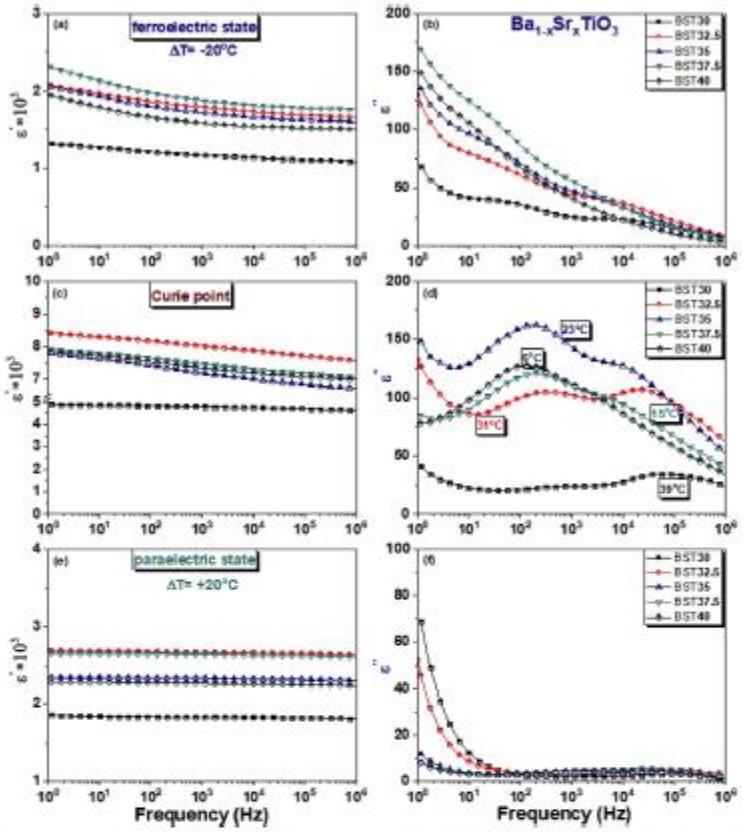

Fig. 7. Frequency-dependences of $\varepsilon'(\nu)$ and $\varepsilon''(\nu)$ for temperatures $T = T_C - 20$ °C (a, b); $T = T_C$ (c, d); $T = T_C + 20$ °C (e, f).

the modification of the material's polarization, an intrinsic compositional/structural effect related to the interactions between conductive electrons and ionic species. Particularly, for BST ceramics, the tetragonal distortion is reduced by increasing the Sr addition and disappears by increasing the temperature above the Curie point. In paraelectric state other thermally activated processes prevail (relaxation of the ion blocking effect [31,32], migration of space charges and defects). The ion blocking effect, for example, manifests at the grain boundaries and relaxes at high temperatures. As the grain size is reducing by the addition of Sr, the frequency response of the grain boundaries increases.

Examples of the investigated frequency-dependent conductivity isotherms and the determined $s(T)$ values are given in Fig. 8 (a, b). The conductivity isotherms shown in Fig. 8(a) were measured at 100 °C, well above the T_C of each of the BST compositions. In the intermediate range of the frequency, a slight relaxation is observed, being much more pronounced for BST40 than for any other composition. As mentioned above, a larger contribution of the grain-boundaries in BST40 is expected since this composition resulted in the smallest size of the

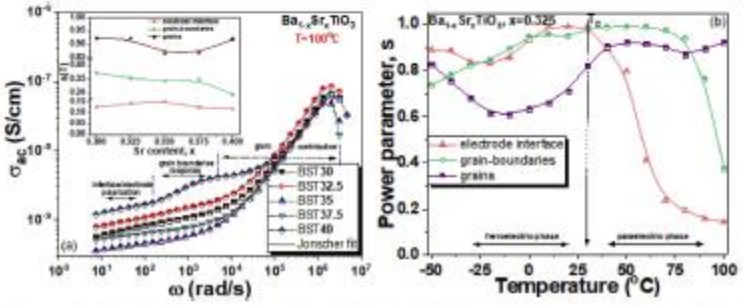

Fig. 8. The real part of complex conductivity dependence on the angular velocity at 100 °C along with the corresponding Jonscher's analysis for each of the BST compositions in inset (a), the temperature-dependent power parameter $s(T)$ calculated for BST32.5 ceramic sample (b).

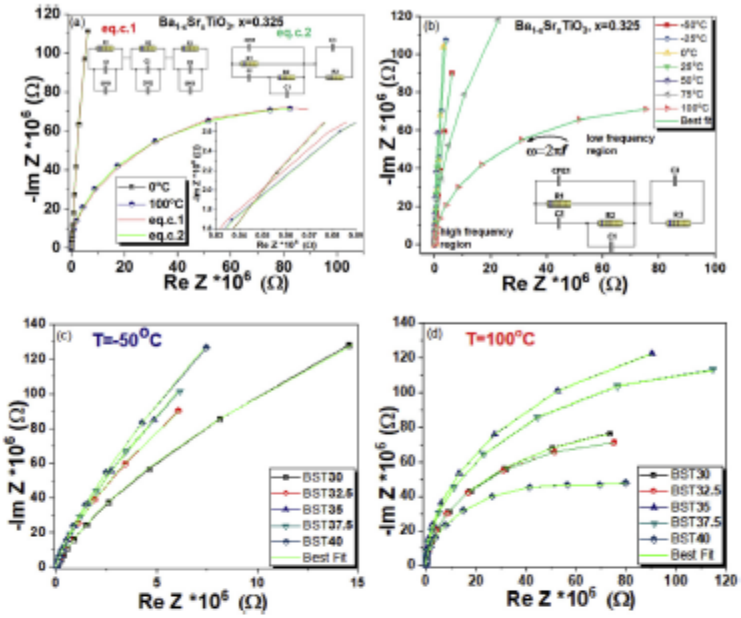

Fig. 9. Nyquist plots of the complex impedance recorded on: BST32.5 ceramics at 0 °C and 100 °C (a), BST32.5 ceramics at different temperatures (b); all the BST ceramics at the extreme temperatures of −50 °C (c) and 100 °C (d). Experimental data are drawn with markers, while the solid red and green lines are the fitting results based on the equivalent circuits shown in the inset of Fig. 9(a) and (b) (red for the equivalent circuit 1 and green for the equivalent circuit 2). (For interpretation of the references to colour in this figure legend, the reader is referred to the Web version of this article.)

grains among the investigated specimens.

In the high-frequency region, the conductivity strongly increases and reaches peak values (see also Fig. S3 in SI). Similar trends in the frequency dependence have been reported earlier for different oxide materials [33,34] and it was attributed to a hopping mechanism through oxygen vacancies. It has been demonstrated that the excess of electrons donated by oxygen vacancies in $SrTiO_3$ are trapped on the Ti sites at low temperature and become mobile when the temperature increases [35,36].

Interfaces, boundaries and grains generate responses in different frequency ranges. Accordingly, the frequency spectrum can be divided into three regions [28], each of them corresponding to different conduction and relaxation processes. The interfaces, boundaries and grains bring effective contributions to the real parts of frequency-dependent conductivity [37] confirmed in Bode plots [38] by the isotherms of the impedance data and phase angle (see Fig. S4 in SI). Thus, according to isotherms recorded between −50 °C and +100 °C for each of the compositions (see Fig. S3 in SI) certain contributions given by specific regions in the sample were ascertain, as depicted in Fig. 8(a). It should be mentioned that the frequency domains refer to the predominant conductivity sources, regions with cumulative contributions coming from interfaces and boundaries at low frequencies (below 50 Hz) and from boundaries and grains at intermediate frequencies (around 10^3 Hz) existing always.

The interaction degree between mobile ions and the media was calculated using eq. (6) and it is represented as a function of temperature in Fig. 8(b) for the BST32.5 specimens. Regarding the physical values the $s(T)$ parameter can take, one has to mention that a value of $s = 1$ corresponds to a situation when no mobile ions exist or when their mobility is completely inhibited by the interaction with the environment (an ideal dielectric). A value of $s = 0$ is associated with the absolute mobility in the absence of any constraint or interaction with the environment (an ideal ionic crystal) [39]. However, both situations are idealistic and values between 0 and 1 are expected for the $s(T)$ parameter in real experiments (see Fig. 8(b)).

Further, a clear distinction between the ferroelectric and paraelectric states in conjunction with the ferroelectric domains needs to be made: below T_C the ferroelectric domains alignment evolves with temperature after which they completely disappear. This is the most likely explanation for the deep decay of the $s(T)$ given by grains calculated below T_C and its returning to approximately constant values close to unity after T_C.

In the same time, the release of spatial charges accumulated at the boundaries and interfaces is also a thermally activated process, which may be clearly observed when other contributions disappear. Thus, according to Fig. 8(b) such processes are activated above T_C. The polarization of the electrodes at the interface with the material occurs at lower temperatures than the ion migration from boundaries. The delayed response of the boundaries could be attributed to ion relaxation process in the bulk followed by an ion blocking effect at grain and subgrain boundaries of the ceramic. The latter process is relaxing with increasing the temperature and is causing the $\sigma_{ac}(\nu)$dispersion in the intermediate frequency range (see Fig. 8(a)).

Concerning the composition, the strontium addition have only a weak influence on the $s(T)$ parameter, as revealed by the inset of Fig. 8(a). The activation energies E_a (eV) of the discussed relaxation mechanisms were calculated according to the Arrhenius law for thermally activated conduction processes [40]:

$$\sigma_{dc} * T = \sigma_0 * \exp\left(-\frac{Ea}{k_B * T}\right)$$

where T is the absolute temperature (K), $k_B \sim 8.617 * 10^{-5}$ is the Boltzmann constant (eV/K) and σ_0 is the pre-exponential factor (S/cm). The increase in Sr content has led to a slight increase of the energies necessary to activate the conduction processes above T_C, from 0.70 eV up to 0.77 eV (see Fig. S5 in SI). Previous studies on the same conduction mechanisms in different perovskite systems and compositions [41] have attributed such E_a values to the energy required to set into motion the electrons resulted from the ionization of oxygen vacancies.

3.2.3. Impedance spectroscopy analysis

The particular contributions of the grains, grain/sub-grain

boundaries and material–electrode interfaces to the overall measured electrical response of the samples can be separated by performing impedance spectroscopy analysis. Therefore, the values of the real (ReZ) and imaginary (ImZ) parts of the impedance were recorded at different temperature set points from −50 °C up to 100 °C in the 10^0 Hz–10^6 Hz frequency range.

Nyquist plots –ImZ – ReZ are represented in Fig. 9. Fig. 9(a) and (b) correspond to BST32.5 ceramics while Fig. 9(c) and (d) refers to the whole set of BST compositions. In all the cases, the -ImZ = *f*(ReZ) plots are changing when increasing the temperature and are reaching the shape of a semicircular arc for the maximum studied temperature of 100 °C. Such modifications confirm the presence of thermally activated phenomena.

The equivalent circuit 1 (eq. c. 1) in Fig. 9(a) is the standard circuit used for a polycrystalline ceramic with metal electrodes. It contains a serial connection of three parallel R–C circuits associated to grains, grain boundaries and electrode interfaces respectively. A constant phase element (CPE) is added to each parallel R–C circuit to take into account the fact that the centers of the semicircular arcs represented in Fig. 9 are located below the ReZ axis, as it is the case for non-ideal Debye-type relaxation processes [33,41]. The equivalent circuit 2 (eq. c. 2) in Fig. 9(a) contains, similar to Ref. [42], a serial connection of: (i) two parallel R–C circuits, R_1-C_1 and R_3-C_3, corresponding to grains and grain boundaries/electrode interfaces, respectively; and (ii) a series R–C circuit (R_2-C_2) accounting for local changes in the orientation of dipolar defects or defect clusters (e.g. V_O-Ti^{3+} dipolar defects or V_O clusters). The experimental data were fitted with the two equivalent circuits and the best fit was obtained using the equivalent circuit 2, as can be seen from Fig. 9(a) and (b) (eq. c. 2 is also shown in the inset of Fig. 9(b)).

Another interesting aspect observed in Fig. 9 is that the diameter of the semicircular arcs changes significantly with temperature, for all BST ceramics, indicating that the interfacial charge transfer enhances with increasing the temperature [41,43]. Thus, the main contributions to the impedance values in the low frequency domain and at elevated temperatures come from the grain boundaries or electrode interfaces, while the grains respond in the high frequency domain, irrespective of the temperature values.

The elements in the equivalent circuit that best describes the impedance behavior of the present BST ceramic samples are: resistors with R (Ohm) resistance contributing to the real part of the impedance Z (ω) = R; capacitors C which contributes to the imaginary part of the impedance by formula $Z(\omega) = (j^*\omega^*C)^{-1}$, and constant phase elements (CPE) defined by formula $Z(\omega) = Q^{-1}(j^*\omega)^{-n}$. This type of element behaves identically to a capacitor, maintaining the phase constant and displaced by 90° at variable frequencies (see Table 1 in SI, where the fitting parameters Q and n for CPE_1 in equivalent circuit 2 are listed).

One has to mention that the elements of the equivalent circuits presented in Fig. 9(a) and (b) are frequency independent but can be temperature dependent. Therefore, the experimentally recorded impedance values in the 10^0 Hz–10^6 Hz frequency range were fitted, at different temperatures, with the equivalent circuit 2. The temperature dependence of the resistances and capacitances determined by fitting are represented in Fig. 10.

One can observe from Fig. 10 that for all the circuit elements there are significant variations with temperature, especially in the proximity of T_C, where the crystalline structure changes from tetragonal to cubic, the material losing its spontaneous polarization. The temperature variations are in opposite directions for capacitances and resistances, in the sense that the capacitances are all increasing at T_C and the resistances are all decreasing. This changes at transition temperature can have various causes such as: changes in the band structure associated to the change in the crystalline symmetry; changes in the distribution of mobile and trapped charges, one can expect that, with increasing the temperature, the amount of mobile charges will increase while the amount of trapped charges will decrease, this changes reflecting in the capacitance and resistance values; the presence or disappearance of the spontaneous dielectric polarization (when present, the polarization needs charges to compensate local depolarization fields, charges that redistributes between grains and grain boundaries when the polarization is vanishing at the phase transition). One can also notice that the grain capacitance C_1 is significantly larger than that of the grain boundaries C_3, while the resistance R_1 is significantly smaller than R_3. This can be attributed to potential barriers that can exist at the grain boundaries or electrode interfaces, and to the associated space charge regions, leading to a higher resistance of the grain boundaries or other interfaces present in the sample. Regarding C_2 and R_2, one can notice that R_2 is significantly smaller than R_1 and R_3, while C_2 is in between C_1 and C_3. As mentioned above, the serial connection C_2-R_2 takes into account changes in the direction of defect dipoles or defect clusters. For example, and oxygen vacancy V_O may associate with a Ti^{3+} ion forming a defect dipole. The V_O may change position around Ti^{3+} ion in the oxygen octahedral places thus the orientation of the dipole will change. This change can be affected by the presence of the ferroelectric polarization and may be less probable at low temperatures in the ferroelectric phase, as the ferroelectric polarization has the tendency to block the surrounding charges for compensating the depolarization field. In the paraelectric phase the polarization does not exist anymore and the local charges may move easier (low resistance) until they are blocked either by trapping or at the internal interfaces with potential barriers.

Regarding the behavior at high temperature, close to 100 °C, one can notice the following:

- For grains, the capacitance decreases with temperature, due to the decrease of the dielectric constant, while the resistance increases as it happens in $BaTiO_3$ based ceramics with positive temperature coefficient [44].
- For grain boundaries, the resistance decreases with temperature, probably due to the release of trapped charges in the grain boundary region as well due to the reduction of the width of the space charge regions associated to potential barriers. The last can produce also an increase in capacitance at high temperature as observed in Fig. 10(b).
- For the serial R_2-C_2 connection, the capacitance decreases and the resistance increases significantly with temperature. One can presume that associated defects may separate, leading to smaller density of defect dipoles or defect clusters. For example, dissociation of a V_O-Ti^{3+} defect will release a V_O that may participate to conduction however, with low mobility, leading to a resistance increase and to a capacitance decrease.

The impedance study reveal that both grains and grain boundaries have impact on the macroscopic electric properties, and that local defects can also affect the overall impedance of the ceramic and its temperature dependence.

4. Conclusions

The dielectric properties at low electric fields of $Ba_{1-x}Sr_xTiO_3$ ceramics, with x = 0.3, 0.325, 0.35, 0.375, 0.4, were investigated on a wide range of temperatures and frequencies and correlated with the structural features. It was found that:

- Increased addition of Sr produces structural changes such as reduction of tetragonality c/a, reduction of the unit cell volume and reduction of the grain size accompanied by an increased weight of grain boundaries.
- Increased Sr addition leads to a reduction of the transition temperature such that the compositions with x = 0.375 and 0.4 Sr are in the cubic paraelectric phase at room temperature, in agreement with the fact that the tetragonality for this samples is unity.
- The thermal hysteresis observed in the temperature dependence of

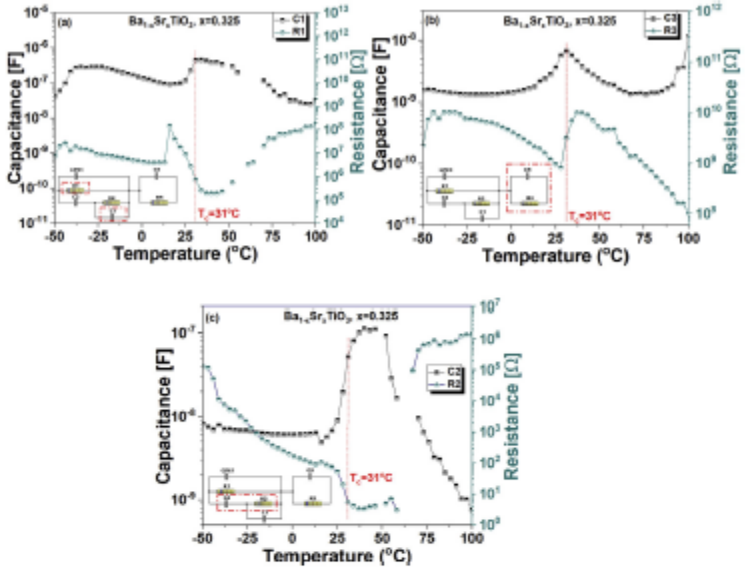

Fig. 10. Parallel resistances and capacitances of grains (a), and grain boundaries (b), and serial R_2-C_2 elements (c) as a function of temperature, calculated for BST32.5 specimens using the proposed equivalent circuit.

the dielectric constant reduces with increasing the Sr content, attributed to smaller size of the crystalline grains and larger weight of grain boundaries allowing a more rapid relaxation of the structural stress occurring at transition from cubic paraelectric to tetragonal ferroelectric phase.

- The analysis of the behavior of the dielectric constant around transition temperature reveals that the transitions are more likely of the first order, with a Curie constant virtually independent on the Sr content and with a slight increase of the frequency dispersion (relaxor-like behavior) as the Sr content increases, attributed to smaller grains and larger weight of the grain boundaries.
- The analysis of the electrical conductivity revealed that the dc part is thermally activated, with activation energy of 0.7–0.77 eV depending on Sr content, attributed to oxygen vacancies, while the ac part follows the Jonscher's universal dispersion law with a power parameter s that it is almost independent on the Sr content. The fact that the activation energy for the dc part is slightly increasing with the Sr content was attributed to possible changes in the band diagram as the unit cell shrinks and tetragonality becomes unity.
- The various contributions (grains, grain boundaries, electrode interfaces) to the macroscopic electric properties were separated by performing impedance spectroscopy analysis and by fitting the experimental data to a specific equivalent circuit including two parallel R–C circuits connected in series (one for grains and one for grain boundaries), a constant phase element in parallel with the parallel R–C circuit for grains, and a serial R–C circuit in parallel with R for grains. This serial R–C circuit takes into account local changes in the orientations of defect dipoles or defect clusters, while R takes into account long range conduction in grains. All the elements of the equivalent circuit show a strong temperature dependence especially in the transition region, with large increase in capacitances and decrease in resistances.

This study shows that the electric/dielectric properties of BST-type ceramics can be fine-tuned by Sr content. It appears that the increase of the Sr content not only changes the transition temperature, but leads also to a more dispersive nature of the dielectric properties attributed to the increased weight of the grain boundaries in the ceramics with large Sr content. Regarding the equivalent circuit used for impedance analysis, one has to mention that further studies are needed to fully understand the physical basis of the component elements together with their temperature dependencies. This can bring further clarifications on the fundamental phenomenon responsible for conduction and relaxation processes in this type of ceramics.

Acknowledgements

Lucian Pintilie, Ioana Pintilie and Roxana Patru acknowledge the financial support of the Romanian Ministry of Research and Innovation (MCI) and of the Executive Unit for Funding High Education, Research, Development and Innovation, Romania (UEFISCDI) through the grant PCCF 16/2018. Catalina-Andreea Stanciu, Vasile-Adrian Surdu, Roxana Trusca, Adelina-Carmen Ianculescu acknowledge the financial support of MCI and UEFISCDI through the project PN–III–P4–ID–PCE–2016–0072. Constantin Paul Ganea acknowledges the financial support of MCI through the PN19-03 Core Program of NIMP.

Appendix A. Supplementary data

Supplementary data to this article can be found online at https://doi.org/10.1016/j.ceramint.2019.10.136.

References

[1] N. Setter, D. Damjanovic, L. Eng, G. Fox, S. Gevorgian, S. Hong, A. Kingon, H. Kohlstedt, N.Y. Park, G.B. Stephenson, I. Stolitchnov, A.K. Taganstev, D.V. Taylor, T. Yamada, S. Streiffer, Ferroelectric thin films: review of materials, properties, and applications, J. Appl. Phys. 100 (2006), https://doi.org/10.1063/1.2336999 051606 1-051606 46.

[2] M.Y. Zhuravlev, R.F. Sabirianov, S.S. Jaswal, E.Y. Tsymbal, Giant electroresistance in ferroelectric tunnel junctions, Phys. Rev. Lett. 94 (24) (2005) 246802, https://doi.org/10.1103/PhysRevLett.94.246802 1–4.

[3] Y. Tarui, T. Hirai, K. Tenmoto, H. Koike, K. Nagashima, Application of the ferroelectric materials to ULSI memories, Appl. Surf. Sci. 113 (1997) 656–663, https://doi.org/10.1016/S0169-4332(96)00963-4.

[4] J. Im, O. Auciello, P.K. Baumann, S.K. Streiffer, D.Y. Kaufman, A.R. Krauss,

Composition-control of magnetron-sputter-deposited $(Ba_xSr_{1-x})Ti_{1+y}O_{3+z}$ thin films for voltage tunable devices, Appl. Phys. Lett. 76 (5) (2000) 625–627, https://doi.org/10.1063/1.125839.

[5] C.L. Canedy, H. Li, S.P. Alpay, L. Salamanca-Riba, A.L. Roytburd, R. Ramesh, Dielectric properties in heteroepitaxial $Ba_{0.6}Sr_{0.4}TiO_3$ thin films: effect of internal stresses and dislocation-type defects, Appl. Phys. Lett. 77 (11) (2000) 1695–1697, https://doi.org/10.1063/1.1308531.

[6] D. Damjanovic, Ferroelectric, dielectric and piezoelectric properties of ferroelectric thin films and ceramics, Rep. Prog. Phys. 61 (1998) 1267–1324, https://doi.org/10.1088/0034-4885/61/9/002.

[7] J.X. Wang, C. Zhang, J.-M. Liu, Revisiting the phase transitions in $Ba_xSr_{1-x}TiO_3$ at low doping range (x≤ 0.1), J. Alloy. Comp. 749 (2018) 276–282, https://doi.org/10.1016/j.jallcom.2018.03.185.

[8] J. Čirković, K. Vojisavljević, N. Nikolić, P. Vulić, Z. Branković, T. Srećković, G. Branković, Dielectric and ferroelectric properties of BST ceramics obtained by a hydrothermally assisted complex polymerization method, Ceram. Int. 41 9A (2015) 11306–11313, https://doi.org/10.1016/j.ceramint.2015.05.068.

[9] A. Von Hippel, R.G. Breckenridge, F.G. Chesley, L. Tisza, High dielectric constant ceramics, Ind. Eng. Chem. 38 (1946) 1097–1109, https://doi.org/10.1021/ie50443a009.

[10] C. Liu, P. Liu, Microstructure and dielectric properties of BST ceramics derived from high-energy ball-milling, J. Alloy. Comp. 584 (2014) 114–118, https://doi.org/10.1016/j.jallcom.2013.09.031.

[11] I.P. Curecheriu, L. Mitoseriu, A. Ianculescu, Nonlinear dielectric properties of $Ba_{1-x}Sr_xTiO_3$ ceramics, J. Alloy. Comp. 482 (1–2) (2009) 1–4, https://doi.org/10.1016/j.jallcom.2009.04.036.

[12] L. Mitoseriu, L. Stoleriu, M. Viviani, D. Piazza, M.T. Buscaglia, R. Calderone, V. Buscaglia, A. Stancu, P. Nanni, C. Galassi, Influence of stoichiometry on the dielectric and ferroelectric properties of the tunable $(Ba,Sr)TiO_3$ ceramics investigated by First Order Reversal Curves method, J. Eur. Ceram. Soc. 26 (14) (2006) 2915–2921, https://doi.org/10.1016/j.jeurceramsoc.2006.02.025.

[13] A.K. JONSCHER, A new understanding of the dielectric relaxation of solids, J. Mater. Sci. 16 (1981) 2037–2060, https://doi.org/10.1007/BF00542364.

[14] A. Ianculescu, I. Pintilie, C.A. Vasilescu, M. Botea, A. Iuga, A. Melinescu, N. Dragan, L. Pintilie, Intrinsic pyroelectric properties of thick, coarse grained $Ba_{1-x}Sr_xTiO_3$ ceramics, Ceram. Int. 42 (2016) 10338–10348, https://doi.org/10.1016/j.ceramint.2016.03.152.

[15] R.D. Shannon, Revised effective ionic radii and systematic studies of interatomic distances in halides and chalcogenides, Acta Crystallogr. A 32 (1976) 751–767, https://doi.org/10.1107/S0567739476001551.

[16] G. Arlt, D. Hennings, G. de With, Dielectric properties of fine-grained barium titanate ceramics, J. Appl. Phys. 58 (4) (1990) 1619–1625, https://doi.org/10.1063/1.336051.

[17] G. Arlt, Twinning in ferroelectric and ferroelastic ceramics: stress relief, J. Mater. Sci. 25 (6) (1985) 2655–2666, https://doi.org/10.1007/BF00584864.

[18] M. Hagiwara, S. Fujihara, Grain-size-dependent spontaneous relaxor-to-ferroelectric phase transition in $(Bi_{1/2}K_{1/2})TiO_3$ ceramics, Appl. Phys. Lett. 107 (107) (2015) 12903–12911, https://doi.org/10.1063/1.4926496.

[19] C.E. Ciomaga, M.T. Buscaglia, M. Viviani, V. Buscaglia, L. Mitoseriu, A. Stancu, P. Nanni, Preparation and dielectric properties of $BaZr_{0.1}Ti_{0.9}O_3$ ceramics with different grain sizes, Phase Transitions 79 (2006) 389–397, https://doi.org/10.1080/01411590600892120.

[20] Y. Zhai, X. Xie, R. Zhou, Li Xu, X. Liu, S. Liu, High performance room temperature ferroelectric barium strontium titanate ceramics by spark-plasma-sintering ultrafine nanocrystals, Ceram. Int. 45 (12) (2019) 15526–15531, https://doi.org/10.1016/j.ceramint.2019.05.057.

[21] V. Tura, L. Mitoseriu, C. Papusoi, T. Osaka, M. Okuyama, Investigation of grain-size influence on the ferroelectric-to-paraelectric phase transition in $BaTiO_3$ ceramics by means of AC calorimetry, Jpn. J. Appl. Phys. 37 (1998) 1950–1954, https://doi.org/10.1143/JJAP.37.1950.

[22] D. Ricinschi, V. Tura, L. Mitoseriu, M. Okuyama, Landau theory-based analysis of grain-size dependence of ferroelectric-to-paraelectric phase transition and its thermal hysteresis in barium titanate ceramics, J. Phys. Condens. Matter 11 (1999) 1601–1613, https://doi.org/10.1088/0953-8984/11/6/024.

[23] I.A. Santos, D. Garcia, J.A. Eiras, Features of diffuse phase transition in lead barium niobate ferroelectric ceramics, J. Appl. Phys. 93 (2003) 1701–1706, https://doi.org/10.1063/1.1530366.

[24] R. Saravanan, J. Mangalaraj karasi, Synthesis and analysis of electron density distribution in $Ba_{1-x}Sr_xTiO_3$ ceramics, J. Mater. Sci. Mater. Electron. 27 (2016) 2523–2533, https://doi.org/10.1007/s10854-015-4053-5.

[25] A.K. Jonscher, Dielectric relaxation in solids, J. Phys. D Appl. Phys. 32 (1999) R57–R70, https://doi.org/10.1088/0022-3727/32/14/201.

[26] A.K. Jonscher, The 'universal' dielectric response, Nature 267 (1977) 673–679, https://doi.org/10.1038/267673a0.

[27] E. Fabbri, D. Pergolesi, E. Traversa, Ionic conductivity in oxide heterostructures: the role of interfaces, Sci. Technol. Adv. Mater. 11 (5) (2010), https://doi.org/10.1088/1468-6996/11/5/054503 054503-9.

[28] X. Song, T. Zhang, Y. Zhang, K. Hu, Z. Zhao, I. Baturin, Impedance spectroscopy and thermally simulated depolarization current study of barium strontium titanate glass ceramics: effect of thermal annealing atmosphere on dielectric property, Ceram. Int. 44 (5) (2018) 5668–5672, https://doi.org/10.1016/j.ceramint.2017.12.218.

[29] A.K. Jonscher, The interpretation of non-ideal dielectric admittance and impedance diagrams, Phys. Status Solidi 32 (1975) 665, https://doi.org/10.1002/pssa.2210320241.

[30] A.K. Jonscher, Analysis of the alternating current properties of ionic conductors, J. Mater. Sci. 13 (3) (1978) 553–562, https://doi.org/10.1007/BF00541805.

[31] W. Heywang, Semiconducting barium titanate, J. Mater. Sci. 6 (1971) 1214–1224, https://doi.org/10.1007/BF00550094.

[32] K. Watanabe, I. Sakaguchi, S. Hishita, N. Ohashi, H. Haneda, Visualization of grain boundary as blocking layer for oxygen tracer diffusion and a proposed defect model in non doped $BaTiO_3$ ceramics, APEX 4 (2011), https://doi.org/10.1143/APEX.4.055801 055801-3.

[33] C.Y. Hsu, J.C.A. Huang, Y.H. Lee, S.F. Chen, C.P. Liu, S.J. Sun, Y. Tzeng, Interfacial defects controlled electrical and magnetotransport in Co/ZnO nanocomposites, Appl. Phys. Lett. 94 (2009), https://doi.org/10.1063/1.3077312 052504-3.

[34] K.-I. Yan, R.-H. Fan, M. Chen, K. Sun, L.-W. Yin, H. Li, S.-B. Pana, M.-X. Yu, Perovskite (La,Sr)MnO_3 with tunable electrical properties by the Sr-doping effect, J. Alloy. Comp. 628 (2015) 429–432, https://doi.org/10.1016/j.jallcom.2014.12.137.

[35] X. Hao, Z. Wang, M. Schmid, U. Diebold, C. Franchini, Coexistence of trapped and free excess electrons in $SrTiO_3$, Phys. Rev. B 91 (2015), https://doi.org/10.1103/PhysRevB.91.085204 085204-6.

[36] C. Ang, Z. Yu, L.E. Cross, Oxygen-vacancy-related low-frequency dielectric relaxation and electrical conduction in Bi:$SrTiO_3$, Phys. Rev. B 62 (1) (2000) 228–236, https://doi.org/10.1103/PhysRevB.62.228.

[37] F.S.M. Sinfronio, J.A.O. Rodrigues, F.C. Silva, R.S.P. Fonseca, A.S. De Menezes, R. Moura, S.K. Sharma, M.C. Castro Junior, Effect of Co-substitution on the vibrational, magnetic, and dielectric properties of copper ferrites obtained by microwave-assisted hydrothermal method, J. Electron. Mater. 47 (11) (2018) 6821–6832, https://doi.org/10.1007/s11664-018-6598-6.

[38] A. Rahal, S. MeglicheBorchani, K. Guidara, M. Megdiche, Electrical, dielectric properties and study of AC electrical conduction mechanism of $Li_{0.6}\square_{0.1}NiV_{0.3}P_{0.7}O_4$, R. Soc. Open Sci. 5 (2018), https://doi.org/10.1098/rsos.171472 171472-13.

[39] Adrian Radoń, Dariusz Łukowiec, Marek Kremzer, Jarosław Mikuła, Patryk Włodarczyk, Electrical conduction mechanism and dielectric properties of spherical shaped Fe3O4 nanoparticles synthesized by Co-precipitation method, Materials 11 (2018) 735–812, https://doi.org/10.3390/ma11050735.

[40] D.P. Almond, A.R. West, Anomalous conductivity prefactors in fast ion conductors, Nature 306 (1983) 456–457, https://doi.org/10.1038/306456a0.

[41] E. Barsoukov, J.R. Macdonald, Impedance Spectroscopy: Theory, Experiment, and Applications, Wiley, 978-0-471-64749-2, 2005.

[42] M.A. Hernandez, A.R. West, Dipolar relaxation and impedance of an yttria stabilised zirconia ceramic electrolyte, J. Mater. Chem. 4 (2016) 1298–1305, https://doi.org/10.1039/C5TA08990E.

[43] X.M. Feng, X.P. Ai, H.X. Yang, A positive-temperature-coefficient electrode with thermal cut-off mechanism for use in rechargeable lithium batteries, Electrochem. Commun. 6 (2004) 1021–1024, https://doi.org/10.1016/j.elecom.2004.07.021.

[44] J. Nowotny, M. Rekas, Positive temperature coefficient of resistivity for $BaTiO_3$-based materials, Ceram. Int. 17 (1991) 227–241, https://doi.org/10.1016/0272-8842(91)90017-T.

Anexa 5

RAPID RESEARCH LETTER

Metal–Ferroelectric Interfaces

physica status solidi rrl

www.pss-rapid.com

Impact on Ferroelectricity and Band Alignment of Gradually Grown Au on $BaTiO_3$

Dana Georgeta Popescu, Marius Adrian Husanu, Cristina Chirila, Lucian Pintilie, and Cristian Mihail Teodorescu*

The competition between interface barrier in the Schottky–Mott limit and polarization driven mechanism is established during gradual formation of metal (Au) – ferroelectric ($BaTiO_3$) interface. X-ray photoelectron spectroscopy provides core level energies and valence band positions in the contact region, to monitor the band alignment from the very first stages of metal deposition on $BaTiO_3$. The band bending at metal/ferroelectric (FE) interface is extracted from the shift of core levels (Ba 3*d*, Ti 2*p*) as a function of the metal thickness. It is shown that the interface band alignment mechanism involves a well-defined polarization orientation washing out the bending expected from the work function difference. The sudden modification of the binding energies within ferroelectric at the first 2 Å Au indicates that the ferroelectric compensation mechanism triggered by the metal overlayer initiates already at ultrathin top layer, while subsequent growth contributes only at a gradual correction of the potential in the FE. The emerging picture is confirmed in first-principle calculation indicating the preferences of Au to grow preferentially to different terminated regions and to stabilize distinct ferroelectric polarization.

Ferroelectric materials exhibit a spontaneous polarization, which can be reversed by applying a voltage exceeding the coercive field.[1] They are used in a wide number of applications such as sensors and actuators,[2,3] in ferroelectric capacitors[4] and non-volatile memories.[5,6] In most of these applications, the ferroelectric (FE) system is in direct contact with a metal electrode, and the device physics is strongly influenced by the metal-ferroelectric interface. Consequently, understanding the mechanism of metal/FE interface formation is of central importance in device design. Ferroelectric thin films may present a particular single-domain ferroelectric state with the polarization perpendicular to the film, which is connected to the existence of free charge carriers into the film.[7] Electrons and holes from the ferroelectric thin film may then be transferred by the internal field (P/ε, where P = polarization perpendicular to the surface of the FE, $\varepsilon = \varepsilon_0\varepsilon_r$ = dielectric permittivity of the FE), opposed to the polarization, close to the surface or across the interface. These mobile charge carriers form layers screening the depolarization field inside the film, in absence of any other sources of extrinsic screening.[8] As a consequence, near the free FE surface a band bending arises, with the magnitude $eP\delta/\varepsilon$ (δ is the distance between the polarization charge sheet and the physical termination of the FE and e the elementary charge). When the polarization is oriented inwards, the bands bend upwards and the signature is seen in photoemission as shifts toward lower binding energies (LBE) near surfaces, while in the outwards polarization case they bend downwards accompanied by shifts toward higher binding energies (HBE).[9] Core levels shift rigidly with respect the vacuum level together with the valence band maximum (VBM), following the band alignment direction.[9–13] X-ray Photoelectron Spectroscopy (XPS) emerges as the tool to directly extract such signatures close to the surfaces and their corresponding interfaces with different electrodes.[14–16] When a metal is grown on a semiconductor, the Schottky–Mott mechanism controls the way electrons migrate from the system with lower work function into the one with a higher work function, until an internal field appears at the interface, preventing further charge migration. Thus, an interface band bending is induced in the semiconductor, equal to the difference of work functions between the metal and the semiconductor (in absence of any ferroelectric polarization). The mechanism can be extended for ferroelectrics by corroborating the effect of the depolarization charge-induced bending at free ferroelectric surfaces having polarization perpendicular to the surface.[9,17] Recent experiments evidenced the importance of the build-in-potential at metal/ferroelectric interface depending on the nature of the electrode used in these contacts.[17,18] An ongoing effort in technology is devoted to seeking environment-friendly solutions and $BaTiO_3$ (BTO) is one of the candidates, in counterpart with Pb-based ferroelectrics. For this material, in spite of its considerably lower saturation polarization, it was found that by in situ biasing of a FE sample, all core levels vary as a function of the ferroelectric polarization.[18]

Although joining materials with different work-functions has been shown to create new functionality,[19] here we show that the

D. G. Popescu, M. A. Husanu, C. Chirila, L. Pintilie, C. M. Teodorescu
National Institute of Materials Physics
Atomistilor 405A, 077125 Magurele, Romania
E-mail: dana.popescu@infim.ro

The ORCID identification number(s) for the author(s) of this article can be found under https://doi.org/10.1002/pssr.201900077.

DOI: 10.1002/pssr.201900077

Schottky barrier height (SBH) for Au/BTO interfaces depends mainly on the FE polarization, with the Schottky–Mott mechanism playing only a correction role. Starting from the early stages of the heterostructure formation, the gradual band alignment effect is inferred from the shift of the XPS core levels with respect the Fermi level of the metal. Our findings add a new perspective concerning the washing out the bending expected solely on work function difference, due to FE polarization effects. The results are supplemented by ab-initio calculations, with information of the preferences of the metal layers deposition on the different polarization domains of BTO substrate.

A 150 nm thick $BaTiO_3$ film was grown by pulsed laser deposition (PLD) on $SrTiO_3$(100) (STO) with $SrRuO_3$ bottom electrode. The PLD parameters used are KrF radiation (248 nm wavelength), 5000 pulses, repetition rate 5 Hz, laser fluence 1.5 J cm^{-2}. During the BTO growth, the substrate was heated at 700 °C and the partial O_2 pressure was 14 Pa. After the preparation, the sample was introduced into a XPS and molecular beam epitaxy (MBE) surface science cluster (Specs). Surface contamination was partly reduced by flashing the samples at about 180 °C. Gold was gradually deposited (2, 4, 16, 24, 40, 100 Å) at room temperature in the MBE chamber, connected in vacuum to the analysis XPS chamber. The XPS experiments were performed in ultrahigh vacuum at a base pressure of 2×10^{-8} Pa by using a monochromatized Al $K\alpha_1$ X-ray source (1486.74 eV), with the photoelectrons recorded by a Phoibos (150 mm radius) electron energy analyzer operating in fixed analyzer transmission mode with pass energy of 30 eV.

First principles calculations were performed using Quantum Espresso code,[20] by employing ultrasoft pseudopotentials and the generalized gradient approximation functional in Perdew-Burke-Ernzerhof (PBE) parameterization[21] of the exchange and correlation term. Calculations were performed on 8 unit cell ferroelectric slabs with two different FE polarization states, allowing them to relax along the *z*-axis until the Hellman-Feynman forces on each atom are less than 30 meV $Å^{-1}$ while keeping the coordinates of the first unit cell fixed at the bulk-relaxed values. The in-plane lattice constant value was fixed to the $SrTiO_3$ substrate, deduced from a previous bulk calculation to be $a = 3.936$ Å. Calculations were performed using a 30 Ry cutoff for the plane wave expansion of the wave functions and 400 Ry for the charge density integration. A $7 \times 7 \times 1$ *k*-point mesh for relaxation of the coordinates in the supercell was enough to achieve the convergence.

Figure 1a and b presents the XPS spectra of Au/BTO system, in the increasing order of Au thickness, deposited on ferroelectric BTO sample. Each XPS spectrum is simulated with Voigt lines.[22] Ba 3*d*, Ti 2*p* spectra being fitted with two components with a relative binding energy (BE) shift of 1.14 ± 0.01 eV.[23] One can see the evolution of the BE for each component in Figure 1c and d. We assign the main component of Ba 3*d* (Figure 1a) at LBE (green curve) to Ba atoms in the perovskite structure and the one at HBE (blue curve) to surface related emission due to uncoordinated surface Ba atoms.[24,25] The main component of Ti 2*p* spectra (Figure 1b) is associated to Ti ions in perovskite phase having a +4 valence state and the smaller component at HBE is attributed to TiO_2 surface termination, meaning that our BTO surface has mixed termination.

A first observation is that the Ba 3*d* and Ti 2*p* intensities do no drop to zero after Au deposition, even after growing an Au overlayer equivalent of 10 nm. At this thickness the signal of the substrate Ba 3*d* and Ti 2*p* spectra would attenuate to $\approx 4 \times 10^{-5}$ of their initial amplitudes.[10] This indicates that Au films grow as discontinuous coating – clusters or nanoparticles connected by thinner Au regions. The amplitude variation of both components (LBE/HBE) with Au thickness is quite similar, obeying, as expected from the inelastic mean free path (IMFP) of the photoelectrons, an exponential attenuation law (see Figure S2, Supporting Information). All BE of the substrate are featured by

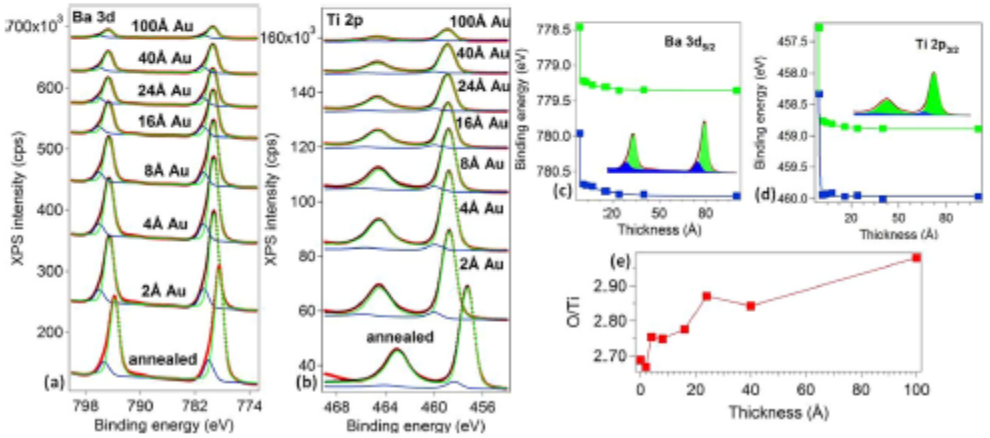

Figure 1. Ba 3d (a) and Ti 2p (b) XPS spectra after successive Au deposition on BTO. Red symbols are experimental data, black lines are fits, green and blue lines are individual components. (c) Ba $3d_{5/2}$ and (d) Ti $2p_{3/2}$ BE variations of different XPS components resulted from the fit of spectra recorded in (a,b) as function on the Au nominal thickness; (e) O/Ti ratio after successive Au deposition.

gradual shifts toward HBE with increasing metal thickness, up to 0.9 eV at 100 Å Au (Figure 1c and d). The values of the core levels obtained for the main component of the clean surface ($E_{Ba} \cong 779.96$ eV for Ba $3d_{5/2}$, $E_{Ti} \cong 457.27$ eV for Ti $2p_{3/2}$)[13] are in reasonable agreement with previous data. For more details about the Au and O 1s evolution during layer growth see the Supporting Information.

Surprisingly, the shift toward HBE upon Au deposition is opposed to the trend expected from the values of their work functions and corresponds to downwards band bending in absolute values, indicating the stabilization of a polarization state pointing away from the surface (P^+).[10,23] The BE variation of Ba 3*d* is about half of the shift induced in the Ti core levels, and is probably due to the smaller probing depth of Ba 3*d* (λ_{Ba}=12.46 Å) than of Ti 2*p* photoelectrons (λ_{Ti}=15.81 Å). The former are then able to capture the extensive ferroelectric-induced bending over the whole thickness δ, while Ba 3d photoelectrons probe a significantly smaller depth. Close to the surface, a dead layer has been reported with the thickness of about 2–3 unit cells where the FE activity decreases[8,26,27] (see also Figure S5, Supporting Information), and this effect may account for the apparent smaller shift of Ba 3*d* electrons.

The evolution of the $r = O/Ti$ ratio in the order of increasing Au thickness starting from the annealed state (Figure 1e) indicate the initial deviation from the expected Stoichiometry ($r = 3$), gradually recovering the ideal one around the thickness of 100 Å of the overlayer. We can expect that vacuum annealing may create some oxygen vacancies in BTO[28] and a consequent release of mobile charges of $2e^-$/unit cell. More importantly, the evolution of r with Au thickness indicates the different contribution of those intrinsic charge carriers at the compensation of the depolarization field inside the ferroelectric BTO.

The increase of r at high Au overlayer cannot be accounted as coming from the top metal, nor from the MBE chamber as the pressure during the deposition was $\approx 10^{-8}$ Pa and the temperature ≈300 K. The only possibility is the migration of oxygen vacancies from close to the surface where they, initially build-up as charge sheet in order to compensate the depolarization field, toward the bulk at higher Au coverage.

Two compensation mechanisms may be taken into account to stabilize the out-of-plane polarization state: an intrinsic one, relying on the presence of charge carriers near surface whose origin is from the semiconductor bulk (electrons for outwards polarization) and an extrinsic one, where compensating charge carriers are stabilized in the metal overlayer.[17] With the increase of the effective thickness of the metal deposited, the extrinsic contribution will prevail. Hence, less oxygen vacancies are needed to create electrons near surface. During Au deposition, it is expected that the BTO surface is additionally heated by the thermal radiation from the evaporation cell by about 30–40 K. It seems that this deposition temperature is sufficient to favor oxygen migration from the bulk toward the surface, when, owing to the extrinsic screening, no self-doping is anymore needed in this region to ensure the intrinsic screening.[7]

In **Figure 2** we sketched the mechanism to explain the evolution of the BE seen in Figure 1c and d assuming a combination of FE induced band bending and formation of a Schottky contact. We first consider only the bending involving

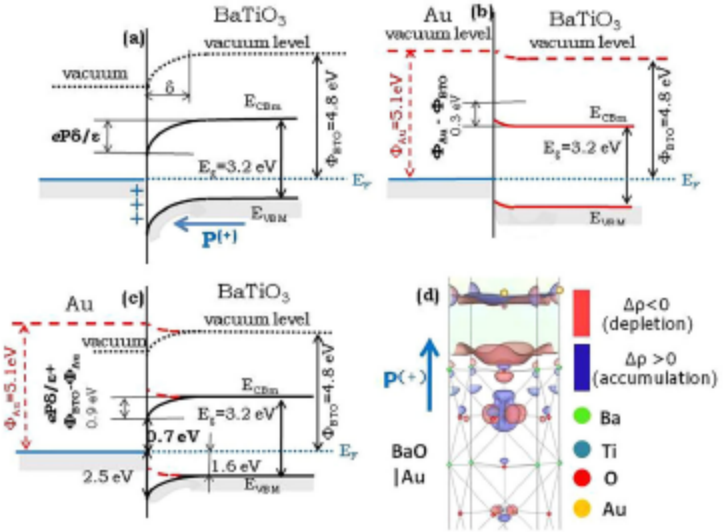

Figure 2. Proposed mechanism to explain the evolution of BE from Figure 1. (a) Energy band diagram of BTO exhibiting a FE polarization oriented outwards (↑) with its corresponding band bending; (b) the Schottky–Mott mechanism involving the work-function difference; (c) our case when the FE keeps its polarization, washing out some of the bending due to the Schottky junction. With red lines is depicted the scenario of a band bending based on the different work-functions only. The black lines represent the observed behaviour at Au/BTO interface; (d) calculated bonding charge distribution of the Au/BTO interface. Au presumably prefers the $P^{(+)}$ polarization domains on the TiO_2 terminated surface.

the out-of-plane ferroelectric polarization, P^+ (a), or the Schottky–Mott mechanism involving the work-function difference (b). Scenario (b) would lead to a shift toward LBE, which is not our observed case, while (a) alone would have most probably lead to shifts toward even higher HBE. Then we can assume that in our case the FE-induced contribution plays the leading role, with only minor contribution from the work function difference. The VBM is extracted from valence band spectra of the clean, bare BTO substrate $E_F - E_{VBM} = 1.6$ eV. Assuming a rigid shift of VBM and core-levels, we deduce the Schottky barrier height of the interface, $\phi_e^{Au/BTO} = 0.7$ eV. Indeed, the shifts in BE after gold deposition (Figue 1c and d) are consistent with a band bending downwards at the interface due to the combined effect of a stabilized $P^{(+)}$ polarization orientation of the film and different work-functions in the metal-semiconductor interface ($\Phi_{Au} = 5.1$ eV,[29] $\Phi_{BTO} = 4.8$ eV[30]). The resulting Schottky barrier has the height $ePS/\varepsilon + (\Phi_{BTO} - \Phi_{Au})$, where ePS/ε is the modification of the 'apparent built-in potential' at the FE interface and $\Phi_{Au} - \Phi_{BTO} = 0.3$ eV. According to the mechanism suggested in Figure 2 derived from our experimental data, the apparent BE shift of the Au covered surface by 0.9 eV toward HBE,[13] allows to extract the ferroelectric term $ePS/\varepsilon = 1.2$ eV with $P = 25\ \mu C/cm^2$[18] and effective dielectric constant $\varepsilon_r = 140$[31] and, deduce that $\delta_{Au/BTO(P+)} \approx 6$ nm. This is larger by a factor of 2-3 compared to PZT.[12,33]

A final observation addresses the stability of the interface formation as deduced from DFT calculations.[34,35] Au lattice constant $a_{Au} = 4.078$ Å is close to that of BTO strained at the in-plane STO lattice constant,[23] $a_{STO} = 3.905$ Å. Consequently, one would expect that the epitaxy condition is rather easily fulfilled for Au growth. However, the calculations of the formation energy reveal that Au strongly prefers only a well-defined termination domains, namely BaO-termination (Figure 2d), stabilizing a P+ polarization state (See Figure S4, Supporting Information), with significant differences for the formation energy in the case of other regions. As thick BTO layers are generally featured with mixed termination domains, it is likely that the growth tendency will be where the energy is most favorable, resulting in islands or grains as revealed by previous TEM studies.[10,23] Indeed, this assumption is in line with the attenuation of the substrate signal at thick metal coverage which shows that 100 Å Au depositions translates into a 88.9% attenuation.

In summary, we have presented photoemission results of the contact formation on Au at $BaTiO_3$ surface. After the metal deposition, the BTO VBM at the interface varies slightly around 1.6 eV, indicating similar SBH for electrons and holes. Direct quantitative measurements of SBH dependence of ferroelectric polarization are obtained from XPS, with value of 0.7 eV. The anticipated effect was a band bending toward lower energy in the Au/BTO contact. Nevertheless, we find that the opposite process takes place. The bending expected from the difference of work function is vanishing, due to a leading term associated to FE – induced band bending in the opposite direction. The mechanism is accompanied by gradual transition from intrinsic screening to extrinsic screening of the ferroelectricity by the thick enough metal contact. First principles calculations point toward a scenario with Au growing more likely on the BaO terminated domains. Understanding such delicate interplay of the ferroelectricity with the interface electronic structure is of central importance for creating new functionality in the context of non-volatile memories based on field effect and tunnel junctions.

Supporting Information

Supporting Information is available from the Wiley Online Library or from the author.

Acknowledgements

This work was funded by the Romanian Ministry of Research and Innovation through Project PN-III-P4-ID-PCCF2016-0047 granted through the UEFISCDI Agency, and by the Project 18-ELI/2016 granted through the Institute of Atomic Physics. D.G. Popescu acknowledges the partial funding from the PN-II-RU-TE-2014-4-1117.

Conflict of Interest

The authors declare no conflict of interest.

Keywords

band bending, barium titanate, ferroelectrics, X-ray photoelectron spectroscopy

Received: February 7, 2019
Revised: March 20, 2019
Published online: April 01, 2019

[1] M. E. Lines, A. M. Glass, *Principles and Applications of Ferroelectrics and Related Materials*. Clarendon, Oxford **1977**.
[2] S. Trolier-McKinstry, P. Muralt, *J. Electroceram.* **2004**, *12*, 7.
[3] G. H. Haertling, *J. Am. Ceram. Soc.* **1999**, *82*, 797.
[4] R. Bruchhaus, D. Pitzer, M. Schreiter, W. Wersing, *J. Electroceram.* **1999**, *3*, 151.
[5] J. F. Scott, *Ferroelectric Memories*. Springer, Berlin **2000**.
[6] T. Nakamura, Y. Nakao, A. Kamisawa, H. Takasu, *Appl. Phys. Lett.* **1994**, *65*, 1522.
[7] L. Pintilie, C. Ghica, C. M. Teodorescu, I. Pintilie, C. Chirila, I. Pasuk, L. Trupina, L. Hrib, A. G. Boni, N. G. Apostol, L. E. Abramiuc, R. Negrea, M. Stefan, D. Ghica, *Sci. Rep.* **2015**, *5*, 14974.
[8] L. Pintilie, M. Alexe, *J. Appl. Phys.* **2005**, *98*, 124103.
[9] N. G. Apostol, L. E. Stoflea, G. A. Lungu, C. A. Tache, D. G. Popescu, L. Pintilie, C. M. Teodorescu, *Mater. Sci. Eng. B* **2013**, *178*, 1317.
[10] N. G. Apostol, L. E. Stoflea, G. A. Lungu, C. Chirila, L. Trupina, R. F. Negrea, C. Ghica, L. Pintilie, C. M. Teodorescu, *Appl. Surf. Sci.* **2013**, *273*, 415.
[11] C. Fares, F. Ren, D. C. Hays, B. P. Gila, M. Tadjer, K. D. Hobart, S. J. Pearton, *Appl. Phys. Lett.* **2018**, *113*, 182101.
[12] F. Chen, R. Schafranek, A. Wachau, S. Zhukov, J. Glaum, T. Granzow, H. von Seggern, A. Klein, *J. Appl. Phys.* **2010**, *108*, 104106.
[13] D. G. Popescu, N. Barrett, C. Chirila, I. Pasuk, M. A. Husanu, *Phys. Rev. B* **2015**, *92*, 235442.
[14] J. Zhang, S. Han, W. Luo, S. Xiang, J. Zou, F. E. Oropeza, M. Gu, K. H. L. Zhang, *Appl. Phys. Lett.* **2018**, *112*, 171605.
[15] M. H. S. Owen, M. A. Bhuiyan, Z. Zhang, J. S. Pan, E. S. Tok, Y. C. Yeo, *Appl. Phys. Lett.* **2014**, *105*, 031602.

[16] S. Hüfner, *Photoelectron Spectroscopy: Principles and Applications*. Springer, Berlin **2003**.
[17] L. C. Tanase, L. E. Abramiuc, D. G. Popescu, A. M. Trandafir, N. G. Apostol, I. C. Bucur, L. Hrib, L. Pintilie, I. Pasuk, L. Trupina, C. M. Teodorescu, *Phys. Rev. Appl.* **2018**, *10*, 034020.
[18] F. Chen, A. Klein, *Phys. Rev. B* **2012**, *86*, 094105.
[19] D. C. Vaz, *Adv. Mater.* **2017**, *29*, 1700486.
[20] P. Gianozzi, S. Baroni, N. Bonini, M. Calandra, R. Car, C. Cavazzoni, D. Ceresoli, G. L. Chiarotti, M. Cococcioni, I. Dabo, A. Dal Corso, S. de Gironcoli, S. Fabris, G. Fratesi, R. Gebauer, U. Gerstmann, C. Gougoussis, A. Kokalj, M. Lazzeri, L. Martin-Samos, N. Marzari, F. Mauri, R. Mazzarello, S. Paolini, A. Pasquarello, L. Paulatto, C. Sbraccia, S. Scandolo, G. Sclauzero, A. P. Seitsonen, A. Smogunov, P. Umari, R. M. Wentzcovitch, *J. Phys. C* **2009**, *21*, 395502.
[21] J. P. Perdew, K. Burke, M. Ernzerhof, *Phys. Rev. Lett.* **1996**, *77*, 3865.
[22] C. M. Teodorescu, J. M. Esteva, R. C. Karnatak, A. El Afif, *Nucl. Instrum. Methods Phys. Res. A* **1994**, *345*, 141.
[23] I. Pintilie, C. M. Teodorescu, C. Ghica, C. Chirila, A. G. Boni, L. Hrib, I. Pasuk, R. Negrea, N. Apostol, L. Pintilie, *ACS Appl. Mater. Interfaces* **2014**, *6*, 2929.
[24] S. M. Mukhopadhyay, T. C. S. Chen, *J. Mater. Res.* **1995**, *10*, 1502.
[25] K. Morikawa, T. Mizokawa, A. Fujimori, Y. Taguchi, Y. Tokura, *Phys. Rev. B* **1996**, *54*, 8446.
[26] Y. Wang, M. K. Niranjan, K. Janicka, J. P. Velev, M. Ye. Zhuravlev, S. S. Jaswal, E. Y. Tsymbal, *Phys. Rev. B* **2010**, *82*, 094114.
[27] Q. Yang, J. Cao, Y. Zhou, L. Sun, X. Lou, *Acta Mater.* **2016**, *112*, 216.
[28] N. Barrett, J. Dionot, D. Martinotti, E. K. H. Salje, C. Mathieu, *Appl. Phys. Lett.* **2018**, *113*, 022901.
[29] D. E. Eastman, *Phys. Rev. B* **1970**, *2*, 1.
[30] T. Schulmeyer, S. A. Paniagua, P. A. Veneman, S. C. Jones, P. J. Hotchkiss, A. Mudalige, J. E. Pemberton, S. R. Marder, N. R. Armstrong, *J. Mater. Chem.* **2017**, *17*, 4563.
[31] Y. Qi, S. M. Anlage, H. Zheng, R. Ramesh, *J. Mater. Res.* **2007**, *22*, 1193.
[32] L. Pintilie, I. Boerasu, M. J. M. Gomes, T. Zhao, R. Ramesh, M. Alexe, *J. Appl. Phys.* **2005**, *98*, 124104.
[33] C. M. Teodorescu, L. Pintilie, N. G. Apostol, R. M. Costescu, G. A. Lungu, L. Hrib, L. Trupină, L. C. Tănase, I. C. Bucur, A. E. Bocirnea, *Phys. Rev. B* **2017**, *96*, 115438.
[34] D. G. Popescu, M. A. Husanu, *Thin Solid Films* **2014**, *552*, 241.
[35] D. G. Popescu, M. A. Husanu, *Phys. Status Solidi RRL* **2013**, *7*, 274.

Anexa 6

www.nature.com/scientificreports

SCIENTIFIC REPORTS
natureresearch

OPEN

Low value for the static background dielectric constant in epitaxial PZT thin films

Received: 20 February 2019
Accepted: 27 September 2019
Published online: 11 October 2019

Georgia Andra Boni, Cristina Florentina Chirila, Luminita Hrib, Raluca Negrea, Lucian Dragos Filip, Ioana Pintilie & Lucian Pintilie

Ferroelectrics are intensively studied materials due to their unique properties with high potential for applications. Despite all efforts devoted to obtain the values of ferroelectric material constants, the problem of the magnitude of static dielectric constant remains unsolved. In this article it is shown that the value of the static dielectric constant at zero electric field and with negligible contribution from the ferroelectric polarization (also called static background dielectric constant, or just background dielectric constant) can be very low (between 10 and 15), possibly converging towards the value in the optical domain. It is also found that the natural state of an ideal, mono-domain, epitaxial ferroelectric is that of full depletion with constant capacitance at voltages outside the switching domain. The findings are based on experimental results obtained from a new custom method designed to measure the capacitance-voltage characteristic in static conditions, as well from Rayleigh analysis. These results have important implications in future analysis of conduction mechanisms in ferroelectrics and theoretical modeling of ferroelectric-based devices.

Although ferroelectric materials have been studied for the better part of the last 100 years, the magnitude of the static dielectric constant of these materials is still a matter of debate and controversy. For a long time, it was thought that ferroelectrics are materials with large values of the static dielectric constant[1]. However, this is valid for ceramics or polycrystalline films, while in the case of epitaxial layers it was found that the dielectric constant is significantly smaller[2–4]. Even when considering the same material, e.g. $BaTiO_3$ (BTO), the reported values for the dielectric constant span an interval of at least one order of magnitude, from about 100 to more than 1000, generating difficulties in developing theoretical models involving this quantity[5–7]. Therefore, it is fair to consider that the static dielectric constant in ferroelectric materials is very much sample dependent, being affected by extrinsic contributions coming from various structural defects that may act as trapping centers for electric charges that may be able to respond to the small amplitude *ac* signal used for standard capacitance measurements[8]. It immediately follows that, if one intends to get closer to the intrinsic value of the dielectric constant in ferroelectrics, it has to prepare single crystal or epitaxial samples with reduced density of structural defects[9]. Values well below 100 can be obtained in epitaxial films of reduced thickness[4,9,10], and as low as 17 in a 12 nm thick $(Ba,Sr)TiO_3$ thin film[11].

The reduction of the dielectric constant with the thickness of the epitaxial ferroelectric layers was attributed to the presence of so called dead-layers at the electrode interfaces, namely layers that are not ferroelectric and, therefore, have low value of dielectric constant[12–15]. The debate on whether dead-layers are present at the electrode interfaces is closely related to the debate regarding the partial or total depletion of the ferroelectric capacitors, and it is largely accepted that ferroelectric-metal interfaces behave as Schottky contacts[16–20]. Therefore, many experimental and theoretical studies were devoted to these problems for the past 20 years, some considering only dead-layers at the interfaces, some showing that there are no such things as dead-layers, some considering only depletion regions, and some considering both depletion and dead-layers[1,21–35].

Returning to the subject of this study, it is known that the static dielectric constant can be estimated from the results of capacitance measurements, such as capacitance-voltage (C-V) characteristics, also the presence of ferroelectricity can be assessed if well-known butterfly shape is obtained. Standard C-V measurements involve simultaneous applications of two voltages on the sample: a *dc* voltage used to set the polarization value and direction, and a small amplitude (relative to the coercive voltage) *ac* voltage for determining the capacitive response measured with a standard LRC bridge. The C-V measurement described above is a type of dynamic measurement,

National Institute of Materials Physics, Atomistilor 405A, Magurele, Ilfov, Romania. Correspondence and requests for materials should be addressed to L.P. (email: pintilie@infim.ro)

as the *dc* voltage is varied step by step, such that the *dc* voltage is set to a certain value and the capacitance is measured using the small amplitude *ac* voltage. After recording the capacitance value, the *dc* voltage is set to the next value and the procedure is repeated until the full C-V characteristic is obtained[34–37]. The problem that arises is the parasitic contributions appearing in the measured capacitance due to transitory phenomena induced by the step change of the *dc* voltage (e.g. charge carriers released from traps able to respond to the frequency and amplitude of the *ac* voltage)[38]. All these issues will be reflected in the value of the calculated dielectric constant!

It is fair to assume that, in a ferroelectric capacitor, the dielectric constant can be divided in two parts: one related to ferroelectric polarization and one related to the dielectric response when there is no contribution from ferroelectric polarization (the case of complete saturation). The static dielectric constant, when there is no contribution from ferroelectric polarization, is sometimes called background static dielectric constant and should be related to the linear dielectric response associated to any non-ferroelectric material[39,40].

The background static dielectric constant can be introduced with the help of the following equation:

$$D = \varepsilon_0 E + P \tag{1}$$

here, D is the electric displacement, E is the electric field, ε_0 is the vacuum permittivity, and P is the total polarization, including the linear part P_L specific for any dielectric/semiconductor material, and the non-linear ferroelectric part characterized by the spontaneous polarization P_S. Replacing P_L with $\varepsilon_0 \chi E$ (χ is the electric susceptibility), Eq. (1) can be written as:

$$D = \varepsilon_0(1 + \chi)E + P_S = \varepsilon_0 \varepsilon_b E + P_S \tag{2}$$

here ε_b is the static background dielectric constant. The total static dielectric constant of a ferroelectric ε_f can be defined as:

$$\varepsilon_f = \varepsilon_b + \frac{1}{\varepsilon_0}\frac{\partial P_S}{\partial E} \tag{3}$$

It is clear from Eq. (3) that, if the spontaneous polarization is saturated and no longer varies with the applied electric field, then ε_f reduces to ε_b.

The question is: how large is the static background dielectric constant? In this paper we suggest that the static background dielectric constant of an epitaxial ferroelectric layer can have values as low as 10–15 and may converge towards the optical dielectric constant, even in the low frequency domain, in defect free, very thin epitaxial films. In order to sustain this claim, a new C-V measurement procedure, named "static" C-V, was developed to estimate the values of the dielectric constant in conditions as close as possible to the electrostatic ones. The differences compared to the results of standard C-V measurements are discussed in terms of Schottky contacts that are present at the electrode interfaces. Rayleigh analysis was also performed to confirm the results and, by comparing them with those extracted from static C-V, it was possible to estimate the polarization contribution at small amplitude ac electric fields used for capacitance measurements.

Results

The results were obtained on a set of epitaxial $Pb(Zr_{0.2}Ti_{0.8})O_3$ (PZT) films having thicknesses of 20, 50 and 150 nm. The proposed "static" C-V measurement uses the following procedure: a pre-poling pulse of a certain period is applied on the sample in order to set the polarization in the $-P$ state; the pre-poling voltage is removed and the capacitance is measured with the small amplitude *ac* signal after a waiting time (this is the first point, corresponding to 0 V, thus to the remnant polarization; the waiting time is necessary to allow relaxation of transitory phenomena); the *dc* voltage is set to a positive value slightly higher than zero and it is applied on the capacitor for a certain period of time; the *dc* voltage is removed and the capacitance is measured again, after the waiting time, at zero volt but with polarization set by the positive voltage previously applied on the sample; the *dc* voltage is set to a positive value slightly higher than the previous one and applied to the sample for the same period of time as the previous one; the *dc* voltage is removed again and the capacitance is measured after the same waiting time; the procedure is repeated step by step until a full hysteresis cycle is obtained (see the *dc* voltage sequence in Fig. 1a). One can observe that, contrary to the standard dynamic C-V, in this case no *dc* bias is applied on the sample while the capacitance is measured with the small amplitude *ac* signal. The resulting C-V characteristic is presented in Fig. 1b) together with the one obtained after a standard C-V measurement using staircase like increase of the *dc* voltage. The waiting time was set to 1 second after checking that it is long enough to allow relaxation of all transitory phenomena (see Supplementary Information SI).

It can be seen that the C-V characteristic obtained using "static" C-V measurement retains the butterfly shape but, contrary to the standard C-V measurement (which from now on will be referred to as "dynamic"), the capacitance value has a very small variation with the *dc* voltage after achieving the saturation of the ferroelectric polarization. In fact, when the *dc* voltage is swept down from maximum value to zero, the capacitance variation is below 1%, being virtually voltage independent as it should be if the polarization is saturated. Similar results were obtained on samples with other thicknesses (see Fig. 2a) and for different frequencies (see details in SI). One can see that the capacitance remains constant after switching, once the polarization is saturated.

An interesting observation is that, for the samples of 20 and 50 nm thickness, the "static" capacitance has different values for sweeping the voltage up and down between maximum negative and positive voltage values. This may be related to the presence of an internal electric field, as evidenced from the hysteresis loops presented in Fig. 2b). As the thickness increases, the intensity of the internal electric field reduces, the hysteresis loop becomes more symmetric and the differences in the capacitance values obtained when the *dc* voltage is swept up and down becomes negligible as it is the case for the 150 nm thick sample.

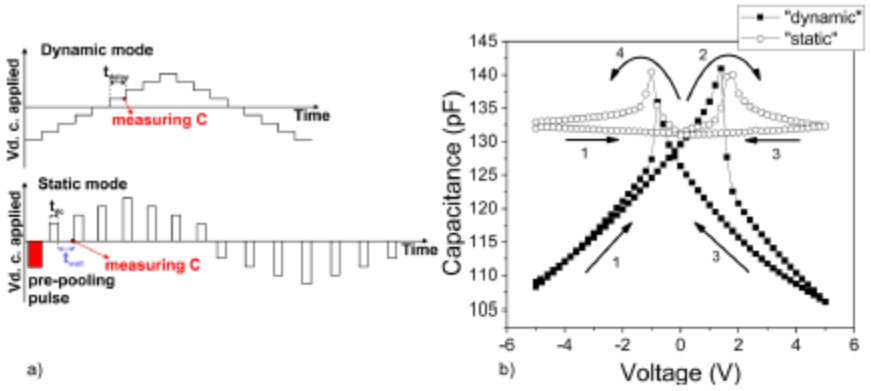

Figure 1. (**a**) The voltage pulse sequence for the "dynamic" and "static" C-V: t_{delay} is the delay time between changing the *dc* voltage and measuring the capacitance in the "dynamic" mode; t_{dc} is the time for applying the *dc* voltage that sets the polarization state in the "static" mode; t_w is the waiting time after removing the *dc* voltage; (**b**) the "static" and "dynamic" C-V characteristics for the 150 nm thick sample (pre-poling pulse of 0.1s; $t_{dc} = 0.1$s; $t_w = 1$s; frequency of the *ac* voltage of 100 kHz).

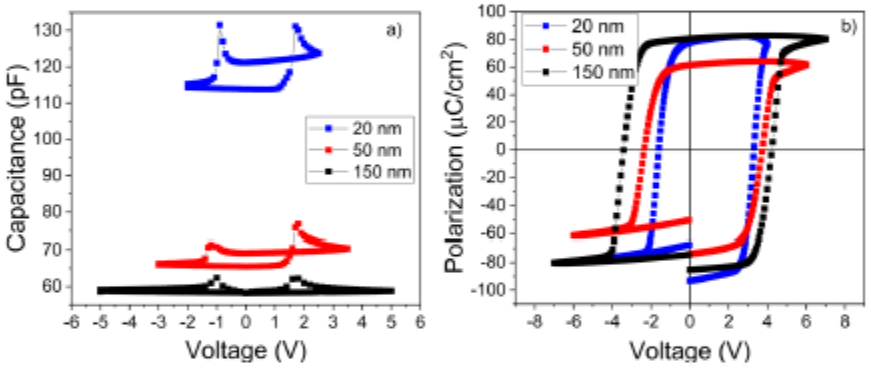

Figure 2. (**a**) The "static" C-V characteristics for epitaxial PZT layers of different thicknesses (the measuring times are the same as in Fig. 1b; the frequency of the ac voltage was 100 kHz); (**b**) the hysteresis loops recorded for epitaxial PZT films of different thicknesses (triangular voltage with 1 kHz frequency).

The dielectric constant was estimated from capacitance values for several situations: at 0 V-"static" measurement (average between capacitances measured while sweeping up and down the dc voltage); at 0 V-"dynamic" measurement (average between capacitances measured while sweeping up and down the dc voltage); at maximum applied V-"dynamic" measurement (average between capacitances corresponding to maximum negative and positive *dc* voltages). The results are presented in Fig. 3a) as function of sample thickness.

Considering that the hysteresis loops are almost rectangular (see Fig. 2b), one can assume that the ferroelectric polarization is saturated when the voltage goes down to zero from the maximum applied *dc* voltage. The amplitude of the *ac* voltage used for capacitance measurements is of 100 mV, at least one order of magnitude smaller than the coercive voltage. One can be tempted to assume that the polarization contribution is negligible in the case of the three situations mentioned above, and that the estimated value is the static background dielectric constant ε_b. However, one cannot exclude small, reversible, polarization variations at electric fields below the coercive one (usually below half of the coercive field, as it is the case for the amplitude of the *ac* voltage used for capacitance measurements). These may contribute to the static dielectric constant even the *dc* bias is removed, as it is the case for static C-V. Therefore, Rayleigh analysis was performed on the three samples, following the procedure described in refs[41,42] (see details in SI). The values estimated for the dielectric constant at zero field, using the Rayleigh analysis, are also presented in Fig. 3a).

One can observe from Fig. 3a) that the values estimated from the C-V characteristics at zero volt are about the same, while the values at maximum applied *dc* voltage during dynamic measurements are significantly lower, especially as the thickness increases. Also, one can observe that all the methods give about the same value for

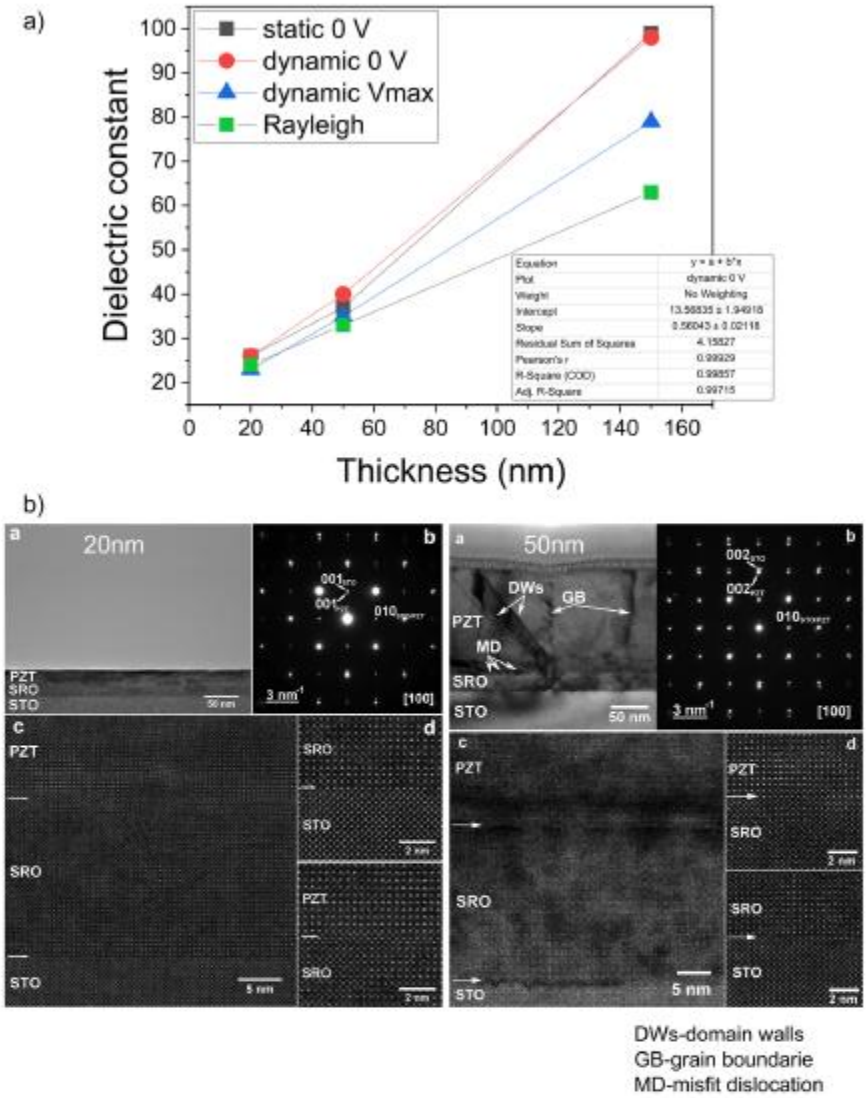

Figure 3. (**a**) The thickness dependence of the dielectric constant evaluated from C-V measurements performed at 100 kHz. Evaluation was performed in three cases: at 0 V "static"; at 0 V "dynamic"; at maximum applied voltage "dynamic". (**b**) TEM images for 20 nm and 150 nm thick samples (inside each image the notations are a-low magnification image cross-section; b-SAED image; c-low magnification HR-TEM image; d-high magnification HR-TEM image of PZT/SRO interface and SRO/STO interfaces; these images demonstrate the high quality of the epitaxial growth).

the thinnest sample, around 23–25, while for the thicker samples the values obtained from C-V measurements are slightly higher than those obtained from Rayleigh analysis. One may infer that the difference is due to the response of the ferroelectric polarization to the small ac voltage used for capacitance measurements. The contribution of the ferroelectric polarization is increasing with thickness as 90° domains start to develop in the sample of 150 nm thickness, as shown in TEM investigations presented in Fig. 3b). Based on these results, one may assume that the values obtained from Rayleigh analysis are closest to the static background dielectric constant, and that in very thin epitaxial films the polarization contribution to the static dielectric constant estimated from C-V measurements can be well below 10% (see SI). These results will be further discussed in the next section.

Discussion

Figure 3a) suggests a linear dependence of the dielectric constant on sample thickness (see the inset, showing that the linear fitting has a confidence factor of 0.99). Assuming that this empirical dependence continues to remain true for lower thicknesses, then a value of about 14–15 is obtained for the background dielectric constant in samples around 1.2 nm in thickness, which are still ferroelectric according to literature[43–46]. This value is about twice the value of 6–7 reported to date for the optical dielectric constant of PZT type materials[47].

Therefore, the value of ε_b can be as low as 14–15 in ultra-thin epitaxial layers, possibly including a minimal contribution from polarization (well below 10%) if a small amplitude *ac* voltage is used to measure the capacitance. A value virtually free of polarization contribution may be obtained using Rayleigh analysis, but this is hard to apply to very thin films due to larger leakage compared to thicker films. Another contribution comes from the structural defects that may be charged and may still respond to the low amplitude *ac* signal used for capacitance measurements in the low frequency domain. Such defects, especially point defects (e.g. vacancies), are present even in high quality, very thin epitaxial films. More defects (e.g. dislocations) can form as the thickness increases and the film start to relax from the strain imposed by the substrate, as can be seen in TEM images presented in Fig. 3b). This can also contribute to the larger static dielectric constant in thicker films. In a perfect epitaxial film, the contribution from structural defects vanishes and the value of the dielectric constant can be lower. One can imagine the extreme case of an ideal mono-domain ferroelectric film where the static background dielectric constant is only slightly larger than the optical dielectric constant, due to a very small contribution of the ferroelectric polarization. This result, based on experimental findings, confirms the early predictions of Watanabe *et al.* that the value of background permittivity in ferroelectrics may be close to the vacuum permittivity[48].

Theoretical calculations performed on bulk crystal, as well as early experimental findings based on Raman measurements performed on bulk samples, report values of the dielectric constant of about 80 (thermodynamic theory applied to PZT with Zr/Ti ratio of 20/80)[49], or around 30–35 (first principle calculations, Raman measurements combined with Liddane-Sachs-Teller equation)[50–52]. The values experimentally reported for thin films can go down to 15–20 (see ref.[11]. and the present study). There are some theoretical studies suggesting a hardening of the soft modes in epitaxial thin films[53]. This can potentially lead to lower values of the dielectric constant along the direction perpendicular to the electrodes due to the strain constrains imposed by the substrate, especially in the case of ultra-thin films. Other theoretical studies suggest that it is possible to reach values as low as 10 in thin films[54]. One can conclude that our experimental results, based on the "static" C-V measurement, are in agreement with previous reports in literature regarding the value of the static dielectric constant in very low thickness thin films.

In order to further test the results presented until now, we have calculated the static dielectric constant using density functional perturbation theory calculations implemented in the Quantum Espresso simulation package[55]. The method for calculating the static dielectric constant has been developed by Gonze *et al.*[56] and has been used successfully to calculate the dielectric function for hybrid organic/inorganic halide perovskites[57]. For simplicity's sake, we have used $PbTiO_3$ as a test material in three scenarios: completely relaxed bulk, strained bulk and thin film. The obtained values are approximately 29 in the case of a bulk unstrained crystal, 32.35 for the strained bulk and about 32.3 for a 5 unit cells film with SRO contacts with the same basal strain as in the previous bulk case. These results are comparable to the experimental values and confirm that the background dielectric constant in PZT crystals or epitaxial films is very low. The details of the calculations can be found in the SI.

There are other aspects that have to be discussed:

- The increase of the static background dielectric constant as the thickness increases. This can be explained by the occurrence of structural defects as revealed by the TEM investigations (results presented in Fig. 3b). One can see in the low magnification TEM images that, as the thickness increases, more and more defects occur in the film (dislocations, grain boundaries, domains and domain walls).
- The constant capacitance in the case of "static" C-V compared to the voltage dependent capacitance in the case of the "dynamic" C-V. This behavior can be explained assuming the presence of Schottky type contacts at the electrode interfaces. As already mentioned in the Introduction section, the presence of Schottky type contacts at electrode interfaces in ferroelectric capacitors is already demonstrated and accepted in the literature[16–20,58,59]. Schottky contacts assume the presence of space charge (depletion) regions at the electrode interfaces, with voltage dependent thickness translated into voltage dependent capacitance[60] as can be seen in "dynamic" C-V characteristics (Fig. 2a). The relative capacitance variation with the applied voltage, after polarization switching (saturated polarization), reduces from about 15% for the 150 nm thick sample to about 5% for the 20 nm thick sample. This result suggests that, as the thickness decreases, the metal-ferroelectric-metal (MFM) structure tends towards full depletion. Therefore, in the case of "dynamic" C-V, the effect of the Schottky contacts will be less visible at small thicknesses and it is expected to disappear in very thin films, these being fully depleted at any voltage except the voltage range where the polarization switching takes place. On the other hand, in the case of "static" C-V, the films are fully depleted at any thickness because the free carriers from the ferroelectric film are blocked at the interfaces to compensate the polarization charges. As a consequence, the capacitance is nearly constant at any voltage outside the range where the polarization switching takes place.
- The frequency dependence of the dielectric constant confirms that this quantity decreases as the thickness of the epitaxial film is decreased (see details in SI). One interesting aspect is that, for the 20 nm thick film the frequency dependence can be fairly well simulated with a simple Debye equation, as shown in the Supplementary Information.

In summary, it was shown that the static background dielectric constant at low frequencies, in ultra-thin epitaxial ferroelectrics, can have low values, of about 10–15, and can be even lower in ideal, defect free, mono-domain

ferroelectric layers. The large values reported in the literature are resulting from extrinsic contributions associated to structural defects, mainly ferroelectric domains and domain walls, but also other structural defects, that occur as the films start to relax when the thickness is increased. It was also evidenced that the natural state of an epitaxial ferroelectric in mono-domain state, with no applied *dc* voltage, is that of full depletion. Once step *dc* voltage is applied the state may change to partial depletion in thick films but remains of full depletion in very thin films. These findings can have an important impact in the analysis of conduction mechanisms in ferroelectrics as well in developing models to simulate the characteristics of ferroelectric-based devices.

Methods

Samples. The samples were grown by pulse laser deposition (PLD) on single crystal $SrTiO_3$ (STO) substrates. The bottom electrode was a 20 nm thick layer of $SrRuO_3$ (SRO). Top SRO/Pt electrodes were deposited for electrical measurements, with area of 0.01 mm^2. The epitaxial quality of the structures was analyzed by transmission electron microscopy (ARM-200F from JEOL). Details about the deposition process and about the structural characterization can be found in previous publications[61,62].

Electric measurements. Polarization and current hysteresis loops were recorded using a model TF2000 ferritester from AixACCT. Capacitance and dielectric losses were recorded using a LCR bridge model Hioki 3536 or a HP 4194A impedance analyzer. The voltage pulses were applied using a Keithley 6517 electrometer. All data were recorded using special designed acquisition programs. All the measurements were performed at room temperature.

Numerical calculations. Density functional perturbation theory calculations were performed using the Quantum Espresso distribution and the included Phonon package.

References

1. Waser, R. Dielectric analysis of integrated ceramic thin film capacitors. *Integrated Ferroelectrics* **15**, 39–51 (1997).
2. Petzelt, J. Dielectric Grain-Size Effect in High-Permittivity Ceramics. *Ferroelectrics* **400**, 117–134 (2010).
3. Setter, N. *et al.* Ferroelectric thin films: Review of materials, properties, and applications. *J. Appl. Phys.* **100**, 051606 (2006).
4. Khan, A. I. *et al.* Negative capacitance in a ferroelectric capacitor. *Nat. Mater.* **14**, 182 (2015).
5. Zhu, J., Zheng, L., Luo, W. B., Li, Y. R. & Zhang, Y. Microstructural and electrical properties of $BaTiO_3$ epitaxial films on $SrTiO_3$ substructures with a $LaNiO_3$ conductive layer as a template. *J. Phys. D: Appl. Phys.* **39**, 2438–2443 (2006).
6. Wang, X. W. *et al.* Microstructure and ferroelectric properties of epitaxial $BaTiO_3/SrRuO_3/SrTiO_3$ (001) films grown by pulsed laser deposition under high oxygen pressure. *Thin Solid Films* **520**, 2785–2788 (2012).
7. Yu, J. *et al.* Extrinsic origin of giant permittivity in hexagonal $BaTiO_3$ single crystals: Contributions of interfacial layer and depletion layer. *Appl. Phys. Lett.* **87**, 252904 (2005).
8. Chilibon, I. & Marat-Mendes, J. N. Ferroelectric ceramics by sol–gel methods and applications: a review. *J. Sol-Gel Sci. Technol.* **64**, 571–611 (2012).
9. Vrejoiu, I. *et al.* Intrinsic Ferroelectric Properties of Strained Tetragonal $PbZr_{0.2}Ti_{0.8}O_3$ Obtained on Layer–by–Layer Grown, Defect–Free Single–Crystalline Films. *Adv. Mater.* **18**, 1657–1661 (2006).
10. Khan, A. I. *et al.* The effects of strain relaxation on the dielectric properties of epitaxial ferroelectric $Pb(Zr_{0.2}Ti_{0.8})TiO_3$ thin films. *Appl. Phys. Lett.* **105**, 022903 (2014).
11. Saad, M. M. *et al.* Investigating the Effects of Reduced Size on the Properties of Ferroelectrics. *IEEE T. Ultrason. F.* **53**, 2208–2225 (2006).
12. Kim, S. H. *et al.* Thickness effects on imprint in chemical-solution-derived (Pb, La)(Zr, Ti)O_3 thin films. *Appl. Phys. Lett.* **78**, 2885–2887 (2001).
13. Cho, H. J. & Kim, H. J. Improvement of dielectric properties of (Ba, Sr)TiO_3 thin films deposited by pulse injection chemical vapor deposition. *Appl. Phys. Lett.* **72**, 786 (1998).
14. Larsen, P. K., Dormans, J. M., Taylor, D. J. & van Veldhoven, P. J. Ferroelectric properties and fatigue of $PbZr_{0.51}Ti_{0.49}O_3$ thin films of varying thickness: Blocking layer model. *J. Appl. Phys.* **76**, 2405 (1994).
15. Bouregba, R., Le Rhun, G., Poullain, G. & Leclerc, G. Investigation of thickness dependence of the ferroelectric properties of $Pb(Zr_{0.4}Ti_{0.6})O_3$ thin-film capacitors. *J. Appl. Phys.* **99**, 034102 (2006).
16. Hwang, C. S. *et al.* Depletion layer thickness and Schottky type carrier injection at the interface between Pt electrodes and (Ba, Sr)TiO_3 thin films. *J. Appl. Phys.* **85**, 287–295 (1999).
17. Shin, J. C., Hwang, C. S., Kim, H. J. & Park, S. O. Leakage current of sol-gel derived (Pb,Zr)TiO_3 thin films having Pt electrodes. *Appl. Phys. Lett.* **75**, 3411–3413 (1999).
18. Yang, Y. S., Lee, S. J., Kim, S. H., Chae, B. G. & Janga, M. S. Schottky barrier effects in the electronic conduction of sol–gel derived lead zirconate titanate thin film capacitors. *J. Appl. Phys.* **84**, 5005–5011 (1998).
19. Choi, T., Lee, S., Choi, Y. J., Kiryukhin, V. & Cheong, S.-W. Switchable Ferroelectric Diode and Photovoltaic Effect in $BiFeO_3$. *Science* **324**, 63–33 (2009).
20. Liu, X., Wang, Y., Burton, J. D. & Tsymbal, E. Y. Polarization-controlled Ohmic to Schottky transition at a metal/ferroelectric interface. *Phys. Rev. B B* **88**, 165139 (2013).
21. Mihara, T. *et al.* Process Dependent Electrical Characteristics and Equivalent Circuit Model of Sol-Gel Based PZT Capacitors. *Proc. 3rd International Symposium On Integrated Ferroelectrics (ISIF)*, 116–138 (1991).
22. Brennan, C. J. A Physical Model for The Electrical Ferroelectric Capacitors. *Ferroelectrics* **132**, 245–257 (1992).
23. Brennan, C. J. Characterization and Modelling of Thin-Film Ferroelectric Capacitors Using C-V Analysis. *Integrated Ferroelectrics* **2**, 73–82 (1992).
24. Miller, S. L., Nasby, R. D., Schwank, J. R., Rodgers, M. S. & Dessendorfer, P. V. Device modelling of ferroelectric capacitors. *J. Appl. Phys.* **68**, 6463–6471 (1990).
25. Evans, J. T. & Bullington, J. A. A ferroelectric capacitor simulation model. *Proc. IEEE 7th International Symposium on Applications of Ferroelectrics* 692–697 (1990).
26. Scott, J. F. Depletion width in $SrTiO_3$ and $BaxSr_{1-x}TiO_3$ films. *Ferroelectrics* **232**, 905–914 (1999).
27. Ng, N., Ahluwalia, R. & Srolovitz, D. J. Depletion-layer-induced size effects in ferroelectric thin films: A Ginzburg-Landau model study. *Phys. Rev. B* **86**, 094104 (2012).
28. Liang, K. *et al.* The conductivity mechanism and an improved C-V model of ferroelectric PZT thin film. *J. Appl. Phys.* **117**, 174107 (2015).
29. Filip, L. D., Pintilie, P., Stancu, V. & Pintilie, I. Simulation of the capacitance-voltage characteristic in the case of epitaxial ferroelectric films with Schottky contacts. *Thin Solid Films* **592**, 200–206 (2015).

30. Saad, M. M. *et al.* Intrinsic dielectric response in ferroelectric nano-capacitors. *J. Phys.: Condens. Matter* **16**, L451–L456 (2004).
31. Nagarajan, V. *et al.* Scaling of structure and electrical properties in ultrathin epitaxial ferroelectric heterostructures. *J. Appl. Phys.* **100**, 051609 (2006).
32. Chang, L., Alexe, M., Scott, J. F. & Gregg, J. M. Settling the "Dead Layer" Debate in Nanoscale Capacitors. *Adv. Mater.* **21**, 4911–4914 (2009).
33. Pintilie, L., Vrejoiu, I., Hesse, D., Le Rhun, G. & Alexe, M. Extrinsic contributions to the apparent thickness dependence of the dielectric constant in epitaxial Pb(Zr, Ti)O_3 thin films. *Phys. Rev. B* **B 75**, 224113 (2007).
34. Bell, J. M., Knight, P. C. & Johnston, G. R. Ferroelectric-electrode interactions. In *Ferroelectric Thin Films: Synthesis and Basic Properties*, editors Paz de Araujo, C., Scott, J. F. & Taylor, G. W., 93–134, Gordon and Breach Publishers (1996).
35. Chai, F. K., Brews, J. R., Schrimpf, R. D. & Birnie, D. P. Profiling of electrical doping concentration in ferroelectrics. *J. Appl. Phys.* **82**, 2517–2527 (1997).
36. Nguyen C. A. & Lee P. S. Capacitance-voltage measurement in memory devices using ferroelectric polymer. *Proc. of SPIE Vol.* **6037**, 603708-1-8 (2005).
37. Li, H. & Subramanyam, G. Capacitance of Thin-Film Ferroelectrics Under Different Drive Signals. *IEEE T. Ultrason. F.* **59**, 1861–1867 (2009).
38. Kim, H.-S., Polla, D. L. & Campbell, S. A. Charge Trapping and Degradation Properties of PZT Thin Films for MEMS. *MRS Proc.* **444**, 161–166 (1997).
39. Levanyuk, A. P., Strukov, B. A. & Cano, A. Background dielectric permittivity: Material constant or fitting parameter? *Ferroelectrics* **503**, 94–103 (2016).
40. Tagantsev, A. K. The role of the background dielectric susceptibility in uniaxial ferroelectrics. *Ferroelectrics.* **69**, 321–323 (1986).
41. Hall, D. A., Ben-Omran, M. M. & Stevenson, P. J. Field and temperature dependence of dielectric properties in BaTiO3-based piezoceramics. *J. Phys.: Condens. Matter* **10**, 461–476 (1998).
42. Hall, D. A. & Stevenson, P. J. High field dielectric behaviour of ferroelectric ceramics. *Ferroelectrics* **228**, 139–158 (1999).
43. Zhang, S. *et al.* Giant Polarization Sustainability in Ultrathin Ferroelectric Films Stabilized by Charge Transfer. *Adv. Mater.* **29**, 1703563 (2017).
44. Xi, Z. *et al.* Giant tunnelling electroresistance in metal/ferroelectric/semiconductor tunnel junctions by engineering the Schottky barrier. *Nat. Comm.* **8**, 15217 (2017).
45. Gerra, G., Tagantsev, A. K., Setter, N. & Parlinski, K. Ionic Polarizability of Conductive Metal Oxides and Critical Thickness for Ferroelectricity in $BaTiO_3$. *Phys. Rev. Lett.* **96**, 107603 (2006).
46. Fong, D. D. *et al.* Stabilization of Monodomain Polarization in Ultrathin $PbTiO_3$ Films. *Phys. Rev. Lett.* **96**, 127601 (2006).
47. Moret, M. P., Devillers, M. A. C., Worhoff, K. & Larsen, P. K. Optical properties of $PbTiO_3$, $PbZr_xTi_{1-x}O_3$, and $PbZrO_3$ films deposited by metalorganic chemical vapor on $SrTiO_3$. *J. Appl. Phys.* **92**, 468 (2002).
48. Watanabe, Y. Proper Permittivity for Depolarization Field in Perfectly Insulating Ferroelectric and Examination of Background Permittivity. *Ferroelectrics* **461**, 38–43 (2014).
49. Haun, M. J., Furman, E., Jang, S. J. & Cross, L. E. Thermodynamic theory of the lead zirconate-titanate solid solution system, part V: theoretical calculations. *Ferroelectrics* **99**, 63–86 (1989).
50. Sai, N., Rabe, K. M. & Vanderbilt, D. Theory of structural response to macroscopic electric fields in ferroelectric systems. *Phys. Rev. B* **66**, 104108 (2002).
51. Burns, G. & Scott, B. A. 'Dirty' Displacive Ferroelectrics. *Solid State Comm.* **13**, 417–421 (1973).
52. Frey, R. A. & Silberman, E. The Raman Spectrum of Ferroelectric $PbTiO_3$. *Helvetica Physica Acta* **49**, 1–11 (1976).
53. Sun, L. *et al.* Phonon-mode hardening in epitaxial $PbTiO_3$ ferroelectric thin films. *Phys. Rev. B* **55**, 218–222 (1997).
54. Baudry, L. & Tournier, J. Model for ferroelectric semiconductors thin films accounting for the space, varying permittivity. *J. Appl. Phys.* **97**, 024104 (2005).
55. Giannozzi, P. *et al.* Quantum Espresso: a modular and open-source software project for quantum simulations of materials. *J. Phys. Condens. Matter.* **21**(39), 395502 (2009).
56. Gonze, X. & Lee, C. Dynamical matrices, Born effective charges, dielectric permittivity tensors, and interatomic force constants from density-functional perturbation theory. *Phys. Rev. B* **55**, 10355 (1997).
57. Perez-Osorio, M. A. *et al.* Vibrational Properties of the Organic-Inorganic Halide Perovskite $CH_3NH_3PbI_3$ from Theory and Experiment: Factor Group Analysis, First-Principles Calculations, and Low-Temperature Infrared Spectra. *J. Phys. Chem. C* **119**, 25703–25718 (2015).
58. Robertson, J. & Chen, C. W. Schottky barrier heights of tantalum oxide, barium strontium titanate, lead titanate, and strontium bismuth tantalite. *Appl. Phys. Lett.* **74**, 1168 (1999).
59. Chen, F., Schafranek, R., Wu, W. & Klein, A. Formation and modification of Schottky barriers at the PZT/Pt interface. *J. Phys. D: Appl. Phys.* **42**, 215302 (2009).
60. Sze, S. M. *Physics of Semiconductor Devices*, 2nd ed. Wiley, New York, chap. 5 (1981).
61. Pintilie, I. *et al.* Polarization-Control of the Potential Barrier at the Electrode Interfaces in Epitaxial Ferroelectric Thin Films. *ACS Appl. Mater. Interfaces* **6**, 2929–2939 (2014).
62. Pintilie, L. *et al.* Polarization induced self-doping in epitaxial $Pb(Zr_{0.28}Ti_{0.80})O_3$ thin films. *Sci. Rep.* **5**, 14974 (2015).

Acknowledgements

The authors acknowledge the financial support of the Romanian Ministry of Research and Innovation through the project CEPROFER/PN-III-P4-ID-PCCF-2016-0047 (contract 16/2018, funded UEFISCDI) and the Core Program of NIMP. Publication fee from project 12PFE/2018.

Author Contributions

L.P. had the idea of the manuscript, designed the "static" C-V method, collected and analyzed the experimental data, and wrote the manuscript. C.C. and L.H. grew the samples and deposited the top electrodes. I.P. and G.A.B. have arranged the set-ups for electrical measurements, performed these measurements, and contributed to data analysis. R.N. had performed the TEM investigations. L.D.F. has performed some theoretical calculations and helped with the English language. All the authors have commented on the manuscript.

Additional Information

Supplementary information accompanies this paper at https://doi.org/10.1038/s41598-019-51312-8.

Competing Interests: The authors declare no competing interests.

Publisher's note Springer Nature remains neutral with regard to jurisdictional claims in published maps and institutional affiliations.

Anexa 7

PHYSICAL REVIEW APPLIED 12, 024053 (2019)

Memcomputing and Nondestructive Reading in Functional Ferroelectric Heterostructures

Georgia A. Boni, Lucian D. Filip,* Cristina Chirila, Alin Iuga, Iuliana Pasuk, Luminita Hrib, Lucian Trupina, Ioana Pintilie, and Lucian Pintilie
National Institute of Materials Physics, Atomistilor str. 405A, PO Box MG7, Magurele, Ilfov 077125, Romania

(Received 27 March 2019; revised manuscript received 24 July 2019; published 26 August 2019)

Multiple nonvolatile and well-separated capacitive states can be obtained in a two-terminal ferroelectric capacitor setup by fine tuning the polarization switching process. This approach allows for the implementation of memcomputing (same platform for storage and computing) capable ferroelectric structures. Digital and analog storage modes are exemplified in this work together with an algorithm for simple binary computation functions such as OR/NOR and AND/NAND for data processing on the same device. Results are obtained by controlling the polarization switching process in ferroelectric multilayers such as $Pb(Zr_{0.2}Ti_{0.8})O_3/SrTiO_3/Pb(Zr_{0.2}Ti_{0.8})O_3$ and $Pb(Zr_{0.2}Ti_{0.8})O_3/BaTiO_3/Pb(Zr_{0.2}Ti_{0.8})O_3$. Besides memcomputing, these results can be used for nondestructive capacitive reading of information in simple ferroelectric capacitors or can open the way toward applications such as neuromorphic and chaotic circuits.

DOI: 10.1103/PhysRevApplied.12.024053

I. INTRODUCTION

One of the realities of present and future technologies is the ever-increasing need for computing speed and high-density information storage. This technological race gives rise to numerous challenges related to various limitations of Moore's law, such as the rising cost of chip manufacturing and physical limitations due to size reduction [1]. For these reasons the concept of memcomputing is gaining traction since the processing and storing of information is performed on the same physical platform [2,3]. This new paradigm relies on passive circuit elements with memory function, such as memristors, memcapacitors and meminductors [4,5]. Unfortunately, there are only a small number of systems exhibiting capacitive switching behavior [6–11]. Conceptually, memcapacitors are different from already existing electrically programmable capacitors such as varactors and typical ferroelectric capacitors: the set capacitance values are maintained without a power supply and, most importantly, the read operation for each state is nondestructive [12].

Ferroelectric materials have shown great promise for nonvolatile memory applications, considering that the two polarization orientations can be associated to the two Boolean bits used in digital computing. The exploitation of commercial ferroelectric random access memory to its full potential is severely hindered by the destructive reading process of the stored information, which requires multiple rewriting operations. These repeated cycles will eventually alter the stability of the ferroelectric phase and compromise device operation [13,14]. A nondestructive capacitive reading will resolve this disadvantage; however, inducing different capacitive states in a ferroelectric structure can be associated with the partial switching of polarization or with a shifting of a capacitance-voltage loop due to an internal field, leading to different capacitance values for the two stable polarization states. Unfortunately, the first case is a transitory phenomenon for ideal structures, and for the second case the capacitance difference between the two values is insignificant and cannot be used effectively. Currently, the link between the memcomputing field and ferroelectric materials is realized with ferroelectric-based memory structures exhibiting resistive switching behavior [15–20]. For logic gates, ferroelectric-based structures (e.g., graphene-ferroelectric metamaterials and organic ferroelectric multilayers) can be used for digital computing [21,22].

In this article we demonstrate memcapacitive effects in structures based on ferroelectric-insulator-ferroelectric (*F-I-F*) thin-film layers. The findings are corroborated by repeatable experimental measurements and theoretical modeling demonstrating the presence of multiple, stable and individually addressable capacitive states. In addition, the capacitance states for these structures depend on the past states along the system evolution path. This property can be harnessed for logic operations such as OR/NOR and AND/NAND while storing the result on the same physical device, in accordance with the parallel computation

*lucian.filip@infim.ro

philosophy [23]. Finally, it is shown that intermediate capacitance states can be obtained in between two extreme values, which is the equivalent of an analog-type memory, a behavior that can be exploited in neural networks mimicking the functionality of the brain.

II. THEORETICAL ASPECTS

Sequential switching of ferroelectric polarization in three-layer structures such as $Pb(Zr_{0.2}Ti_{0.8})O_3$ (PZT)/$SrTiO_3$ (STO)/$Pb(Zr_{0.2}Ti_{0.8})O_3$ (PZT) was demonstrated both experimentally and theoretically in [24]. It was shown that there are four different polarization states that are stable in time and available for information storage. The theoretical arguments for proving the multi-polarization states in the *F-I-F* structures are based on the Landau-Ginzburg-Devonshire (LGD) model [24].

The free energy of the three-layer structure was obtained as a function of the polarization state in each ferroelectric layer, revealing that the *F-I-F* device studied has four equilibrium states with distinct polarizations [Fig. 1(a)]. In addition, it will be shown below that this setup also has distinct capacitance states. Starting from a given state of the structure, it is possible to map its evolution as the voltage is modified. Figure 1(b) shows the positive branch of the theoretical hysteresis curve obtained using the LGD theory detailed in [24]. In order to prove the nondestructive reading operation in the *F-I-F* structure, one must obtain different capacitance values between the available polarization states. If the system is initially set in a stable state where the polarizations in both ferroelectric layers are set to point in the upward direction (toward the top electrode), as the voltage is continuously increased, the system will remain in the initial state [see the corresponding minimum of the free-energy function in Fig. 1(a)] until $V = V_{C1}$. At this point the system is able to switch to the next available equilibrium state that corresponds to the case where the polarization in each ferroelectric layer has different orientation (i.e., one is pointing downwards while the other is point upwards). One important note is that the new state is considered stable because it is maintained when the voltage is slowly returned to 0 [see the red curve hysteresis in Fig. 1(b)]. Continuing to increase the voltage beyond V_{C1}, the system will eventually reach its final state where the two polarizations are pointing downwards at $V = V_{C2}$. By approximating the entire structure with an equivalent circuit of three capacitors connected in series one can write the total equivalent dielectric constant of the three-layer structure as follows:

$$\varepsilon(V) = (d_1 + d_t + d_2)\left[d_1\left(\frac{1}{\varepsilon_0}\frac{dP_1(V)}{dE_1(V)} + 1\right)^{-1} + \frac{d_t}{\varepsilon_t} + d_2\left(\frac{1}{\varepsilon_0}\frac{dP_2(V)}{dE_2(V)} + 1\right)^{-1}\right]^{-1}, \quad (1)$$

where ε_t is the dielectric constant of the insulator interlayer, and $P_1(V)$, $E_1(V)$, $P_2(V)$, and $E_2(V)$ are the polarizations and electric fields in the two ferroelectric layers. Using Eq. (1) and the theoretical model for the three-layer heterostructure [24], one can determine that the partial reversal of polarization [i.e., the intermediate state in Fig. 1(b)] leads to an increased dielectric constant of the structure compared to the initial and final states. This result is fundamentally different than the simple ferroelectric capacitor case where the two available polarization states have indistinguishable capacitance values. Thus the theoretical description demonstrates the existence of *four* stable polarization states and, more crucially, two distinct capacitance states: a high capacitance state (HCS) and a low capacitance state (LCS).

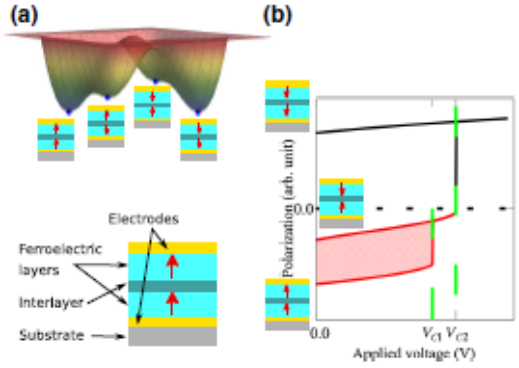

FIG. 1. The theoretical description of stable ferroelectric states and the switching between them based on the LGD model. (a) The free-energy landscape (energy vs polarization of each ferroelectric layer) of an *F-I-F* structure in equilibrium. (b) The positive polarization hysteresis branch of an *F-I-F* heterostructure and the schematic representation of the polarization orientation in each ferroelectric layer for different states.

III. THE MEMCAPACITIVE EFFECT

It is now clear from the theoretical results that the nondestructive reading process could be achievable in *F-I-F* structures by a capacitance measurement that is a nondestructive process, where the amplitude of the signal is much lower than a coercive voltage; however, a more compelling argument is the experimental verification. For this reason *F-I-F* capacitors have been fabricated using $Pb(Zr_{0.2}Ti_{0.8})O_3$ as the ferroelectric material and two types of insulating materials: STO and $BaTiO_3$ (BTO). While the latter is known to be ferroelectric at room temperature, it has a much lower saturated polarization compared to the PZT layers such that its electrostatic contributions at the PZT interfaces are similar to an insulator.

The main result in Fig. 2(a) is the dynamic hysteresis measurement for the PZT-BTO-PZT structure, showing the clear decoupling of polarization switching in the two ferroelectric layers predicted by the theoretical model in Fig. 1. Changing the capacitive state can be achieved with a simple pulse sequence shown in Fig. 2(c). A negative −18-V dc pulse will set the polarization toward the top electrode interface in both ferroelectric layers, which is attributed to an LCS. The following positive +7-V dc pulse will reverse the polarization toward the bottom electrode in only one ferroelectric layer, which brings the structure to an HCS. Moreover, the two states have different dielectric losses, suggesting that the loss mechanism depends on the relative orientation of polarizations in the two PZT layers (see the Supplemental Material [25]). For a quantitative description of the differences between the dielectric properties of the two states, one can define the relative variation of capacitance between the two polarization states (RPC):

$$\delta_{\mathrm{RPC}}(\%) = \frac{C_{\mathrm{HC}} - C_{\mathrm{LC}}}{C_{\mathrm{LC}}} \times 100, \tag{2}$$

where C_{HC} and C_{LC} are the HCS and LCS capacitance values, respectively. The RPC values for both structures are shown in Fig. 2(d) for different frequencies and amplitudes of ac signals. The BTO interlayer case has higher RPC values in the lower-frequency regime and they become approximately equal to the STO case toward 100 kHz. For both cases the RPC decreases at higher frequencies, the differentiation between the two capacitive states being significant in the low-frequency regime. The dielectric behavior of the two states is better represented as a capacitance vs frequency measurement in the 100 Hz to 1 MHz range, presented in Fig. 2(b) (the dielectric loss for the same frequency range is shown in Fig. S2 in the Supplemental Material [25]). It is clear that the most important contribution to the capacitance of the structure is achieved toward the static frequency regime due to the different relative orientations of polarization in each ferroelectric layer and the induced electrostatic boundary conditions at the interfaces. When the frequency is increased, the charges contributing to the compensation of polarization charges and associated depolarization field, as well as the space charge regions that may develop at ferroelectric-insulator or ferroelectric-electrode interfaces, cannot follow the rapid changes of the ac field, and the capacitive response is diminished, evolving toward the intrinsic dielectric properties of the constituent layers. This behavior, together with the two capacitance states with different capacitance and dielectric loss values, is observed for both the PZT-STO-PZT and PZT-BTO-PZT structures. Figure 2(d) also shows that the relative difference between LCS and HCS, measured by the RPC value, becomes larger toward higher values of the ac signal amplitude. This can be associated with the increase of capacitance as the ac signal amplitude approaches the magnitude of the coercive voltage.

An important aspect of information storage is the retention property, which was monitored over time for both the

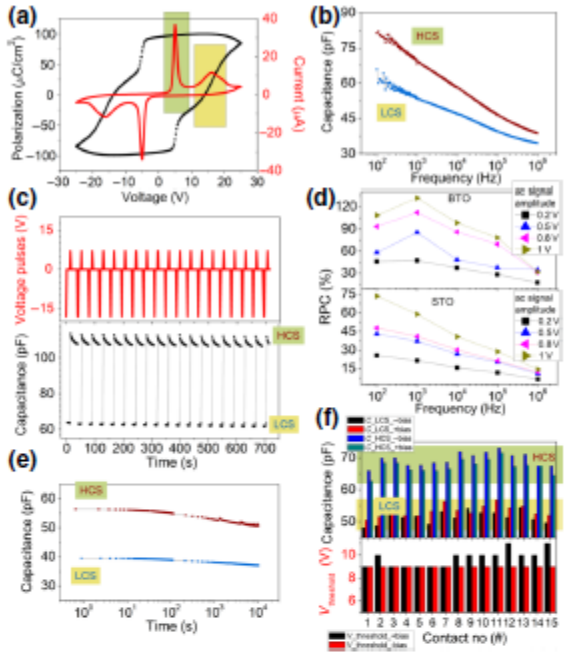

FIG. 2. Two different capacitance states. (a) The hysteresis loops obtained for a complete switching cycle for the case of a BTO interlayer exhibiting four switching peaks in current-voltage characteristics accompanied by a steplike increase in the polarization loop; the extreme peaks situated at higher voltages correspond to a totally reversed polarization, where the ferroelectric polarization is either oriented *up*, toward the top interface in both ferroelectric layers, for negative voltages, or *down*, toward the bottom electrode in both ferroelectric layers, for positive voltages; the intermediate peaks are obtained when the applied voltage changes its polarity and indicates a partial reversal of polarization in only one ferroelectric layer, generating either a head-to-head or a tail-to-tail configuration between the polarizations of the two ferroelectric layers. (b) The capacitance vs frequency, using 0.2-V ac signal, measured after setting HCS and LCS states, respectively. (c) Voltage pulse sequence, combining high-amplitude and low-amplitude pulses with 0.1 s duration, used to repeatedly change the capacitance of the system between LCS and HCS; the capacitance values are measured at 1 kHz frequency and with 0.5-V ac signal. (d) RPC ratios for the BTO and STO interlayer cases, respectively, for different frequencies and ac signal amplitudes. (e) evolution of the two distinct capacitance states, during the 104 s time period, measured at 1 kHz frequency and 0.2 V amplitude of the ac signal. (f) Distribution of capacitance values for HCS and LCS, measured at 1 kHz and 0.5-V ac signal, and distribution of the voltage threshold defined as the voltage necessary for switching from LCS to HCS for 15 different contacts.

HCS and the LCS states [see Fig. 2(e)] for up to 10^4 s. The nondestructive aspect of the reading operation is also emphasized. It can be observed that during the continuous 10^4 s capacitance measurement, there is only a 10% drop in the capacitance of HCS; however, the net difference between the two states is clearly maintained. This behavior reflects that the partially reversed states of the system, while stable from an energy point of view, will tend to evolve toward the totally reversed states that are energetically more stable and in consequence have a lower capacitance. The ability to differentiate between the HCS and LCS is repeatable for many contacts, as can be seen in Fig. 2(f).

IV. OPERATING LOGIC FUNCTIONS

As was shown above, the three-layer heterostructures clearly exhibit four polarization states but only two different capacitance states. Changing between these system states is schematically illustrated in Fig. 3.

The possibility of switching between polarization states with distinct associated capacitance values using two different voltage pulses can be used to build algorithms for logic functions. The logic operation is determined by an appropriate choice of the initial state followed by two particularly defined pulses with different amplitudes and polarities as input logic "0" (L0) or input logic "1" (L1), which can lead to stabilization of different system states that can be read nondestructively by the capacitive method. It is therefore possible to realize Boolean logic functions

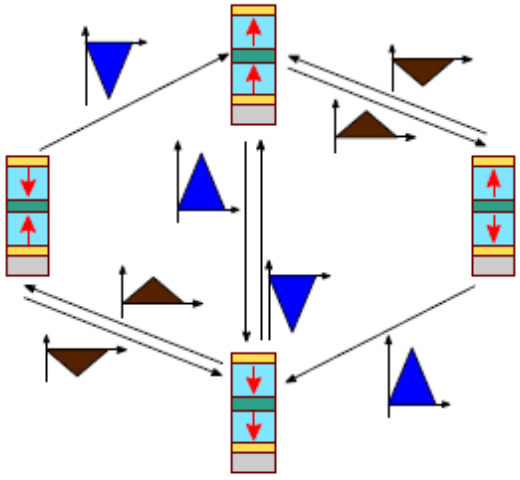

FIG. 3. Schematic representation of the switching possibilities between the four polarization states with the two different capacitive values using corresponding signals. The red and blue triangular pulses are the low- and high-amplitude voltage pulses, respectively.

AND/NAND and OR/NOR using two binary input signals, as illustrated in Figs. 4(a) and 4(b).

Thus, in Fig. 4(a) the system is initially set in a low capacitive state by applying a negative high-amplitude pulse, for which the polarization is oriented in the same direction in both PZT layers. If a positive low-amplitude voltage pulse defined as L0 is applied, the system will evolve into a partially reversed polarization state with a high capacitance value. Furthermore, the system can remain in the same state if the same pulse is applied or can be changed to a totally reversed polarization state with a low capacitance value if a positive high-voltage pulse is applied, defined as L1. If the initial state is subjected to an L1 pulse, the system will change to a totally reversed state with low capacitance where it will remain whether a logic L0 or L1 pulse is further applied. Thus,

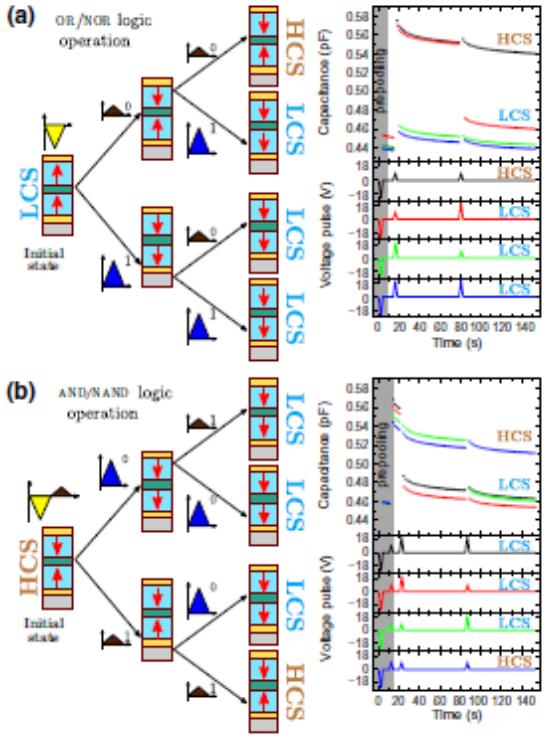

FIG. 4. Logic operation using an *F-I-F* capacitor. The representation of the polarization states in an *F-I-F* structure during different stages (initialization and computation) of a logic operation for the OR/NOR case (a) and for the AND/NAND case (b), together with the corresponding simulations of the logic operations obtained by changing the capacitance state (HCS or LCS) of the system using different combinations of pulses. The HCS and LCS states can have 0 or 1 values associated for logic operations and the results are memorized on the computation cell and can be accessed at any time.

the system will be set to an HCS if only two consecutive L0 pulses are applied, otherwise the system will be in an LCS for any other combination of two pulses. By associating the two capacitive states with Boolean values, the final states are the result of an OR(HCS, 0; LCS, 1) or NOR (HCS, 1; LCS, 0) logic operation, as summarized in Table S1 in the Supplemental Material [25]. Similarly, in Fig. 4(b) the initial state of the device is set to a partially reversed polarization configuration with a corresponding high capacitance value using a negative high-amplitude voltage pulse followed by a positive low- amplitude one. This scenario allows the implementation of an AND/NAND logic operation. The L0 and L1 are defined for this case as a positive high-amplitude voltage pulse and a positive low- amplitude voltage pulse, respectively. It is clear from Fig. 4(b) that only the consecutive appliance of two L1 inputs determines a final HCS, while for the remaining three input combinations an LCS is obtained (see also Table S2 in the Supplemental Material [25]).

At this point, the proposed *F-I-F* structure shows simultaneous information storage and computation functions, since the result of the logic OR/NOR or AND/NAND operations can be stored as HCS or LCS. Furthermore, such devices can be used to realize cascade computations for defined operations. It can be easily verified that for the case of an OR operation, multiple combinations of L1 or of L1 with L0 inputs will leave the system in a low capacitive state and only a combination of L0 inputs will change it to a high capacitive state. The same results apply for multiple AND operations.

V. ANALOG STORING SCHEME

The remarkable properties of the *F-I-F* devices presented thus far can be regarded as extreme cases, in that the multi-polarization states used until now are fully saturated.

Further investigations reveal that intermediate capacitance states can be set using different voltage amplitudes for the writing pulses [see Fig. 5(a)]. Until now, an intermediate state referred to the case where the polarizations in the two ferroelectric layers of the *F-I-F* device had opposite orientations but are fully saturated. For this case, however, the intermediate values of capacitance can be associated to the partial reversal of polarization in the two PZT layers, as schematically presented in Fig. 5, where ferroelectric layers are formed by multiple domain regions. After the −25-V prepolarization pulse, the system is in a complete reversal of polarization toward the top electrode interface. When positive voltage pulses are applied, different ferroelectric domains will start to reverse toward the bottom electrode interface. From an electrostatic point of view any combination of ferroelectric polarization orientations is possible between the monodomain ferroelectric layers, as it was shown in Secs. II and III. Thus, for any complete or partially reversed polarization in the ferroelectric layers, the structure has areas with high capacitance states and areas with low capacitance states, respectively.

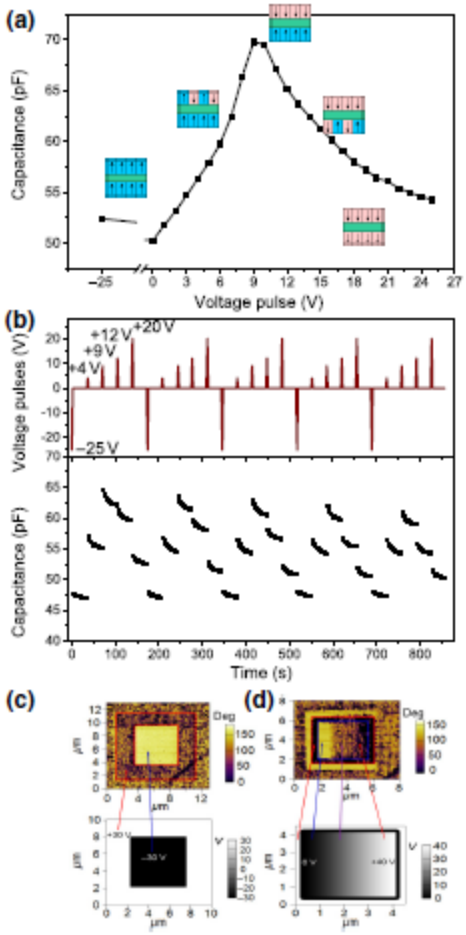

FIG. 5. Multiple stable states with continuous capacitive values. (a) A continuous spectrum of capacitance values, with stable intermediate states measured for the STO interlayer case at 1 kHz frequency with 0.5-V ac signal; insets show schematic illustrations of polarization configurations associated with distinct capacitive states. (b) An example of a voltage sequence combining pulses with different amplitudes and polarities used to access different capacitive states. (c) The piezoresponse phase signal obtained using the poling map: the upper PZT layer present totally reverses polarization toward the surface for negative applied bias (bright central rectangular zone) while for positive bias the polarization remains partially reversed, forming with 180° domain structure. (d) The piezoresponse phase signal obtained by applying the poling map with a voltage gradient on the totally reversed polarization area from (c): the switching of polarization takes place gradually with increasing the amplitude of voltage; different degrees of partial switching of polarization are obtained in the 8–37 V range.

The equivalent capacitance of the structure will cover the range between the LCS and the HCS, such that

$$C_{LC} \leq \alpha C_{LC} + \beta C_{HC} \leq C_{HC}, \quad (3)$$

where $\alpha + \beta = 1$ are the ratios of the areas corresponding to LCS and HCS, respectively. The sum $\alpha C_{LC} + \beta C_{HC}$ is the equivalent capacitance of the structure, considering that the multiple areas with C_{LC} and C_{HC} form a parallel capacitance connected circuit. These intermediary polarization states have been evidenced in current-voltage and polarization-voltage characteristics shown in Fig. S4 within the Supplemental Material. All data exhibit different remnant polarization values, with an almost rectangular shape and no significant back-switching contribution when the voltage drops to zero. This assumption is also experimentally verified by performing piezoresponse atomic force microscopy (PFM) investigations in the three-layer structure. A special poling procedure is designed. Firstly, a rectangular area is subjected to −40 V applied voltage in order to ensure a complete reversal of polarization. After this treatment, the PFM tip is used to scan the same area from left to right while the applied voltage on the tip is gradually increased [see Fig. 5(d)]. The PFM scan in the phase mode revealed that the polarization switching, reflected in the domain structure, took place gradually from a totally up state to totally down one, with a mixed structure of 180° domains in between.

The PFM results are in very good agreement with multiple studies in the literature showing the apparition of 180° nanoscale poly-domain configurations in multilayered ferroelectric-insulator structures [26,27]. Such nonhomogeneous systems also present stable intermediary states, corresponding to incompletely switched polarization, over long periods of time, due to a wide distribution of coercive voltages in different nanoscale regions [28,29]. These results can be used for constructing an analog-type ferroelectric memory or artificial synaptic circuits, with the demonstrated property of nondestructive reading [30].

All partially switched polarization states in the head-to-head and tail-to-tail polarization configurations of the two constituent layers exhibit a relaxation on the values of the attributed capacitance with time. The drop is significant in the first seconds before converging toward a stable value. This phenomenon is related to the presence of the insulator interlayer and the discontinuity of the polarization charges, which is mandatory for obtaining this sequential polarization switching and different capacitive states. In addition, large depolarization fields are not uniformly distributed in the ferroelectric (FE) layers (since one interface is in contact with a metallic electrode and the other with an insulator layer). Also, different defects and structural differences (domains, domain walls, pinning centers, etc.) will appear in these structures compared to simple FE layers. These defects have a significant role in the switching dynamics, for example a voltage pulse sets a particular configuration of polarization and domain distribution, but reducing the voltage to zero could determine a back-switching of polarization in a certain volume of the layers in such a way that the system evolves toward a minimum energy. Another explanation could be related to the redistribution of charges inside the structures during switching in order to compensate the newly induced polarization state. This process could be continued after removing the applied voltage or could be delayed compared with the moment of the switching. Even if this relaxation seems to be a general phenomenon for all polarization states, the fact remains that these systems present a good separation and differentiation between the states at all measured moments.

One should also keep in mind that this study is a proof of concept for nondestructive reading of polarization states and many aspects such as the relaxation of the capacitance are suitable for separate study. A better choice of constituent materials, optimization of layer thicknesses and operational optimization (time duration of the voltage pulse, ac signal amplitude, frequency) could solve the capacitance relaxation problem.

VI. CONCLUSION

Information storage and processing with nondestructive reading operation are demonstrated in *F-I-F* thin-film multilayered heterostructures. Two distinct, well-separated and nonvolatile capacitive states have been obtained for two test devices, PZT-STO-PZT and PZT-BTO-PZT, associated with different polarization configurations of the two ferroelectric layers. The capacitor memory setup presented has a wide variety of uses, with demonstrated capabilities as nonvolatile memory with nondestructive reading and the ability to perform binary logic operations on the same chip. These properties open the way for building parallel computation systems extending beyond the von Neumann architecture. Also, by specially designed algorithms the current circuit architecture based on classic logic gates can be simplified and optimized, leading also to significantly reduced power consumption and reduced cost of manufacturing.

Furthermore, by switching the polarization in each ferroelectric layer gradually, quasistable states can be obtained, presenting a continuum of capacitance values. This opens the way for nonvolatile analog memory development with nondestructive reading capabilities for constructing neuromorphic or chaotic circuits.

ACKNOWLEDGMENTS

The authors acknowledge the financial support of the Romanian Ministry of Research and Innovation through the Core Program of NIMP (Contract No. PN18-110101) and the PCCF project no. PN-III-P4-ID-PCCF-2016-0047

funded by the Ministry of Research and Innovation though UEFISCDI Executive Unit 6.

[1] Moore's Law Reaches Its Limit! Developing a New Architecture to Solve the Combinatorial Optimization Problem, http://journal.jp.fujitsu.com/en/2017/02/15/01/ (2017).

[2] Y. V. Pershin and M. D. Ventra, in 2014 International Workshop on Computational Electronics (IWCE) (IEEE, Paris, France, 2014), pp. 1–2.

[3] M. Di Ventra and F. L. Traversa, Perspective: Memcomputing: Leveraging memory and physics to compute efficiently, J. Appl. Phys. **123**, 180901 (2018).

[4] L. Chua, Memristor-the missing circuit element, IEEE Trans. Circuit Theory **18**, 507 (1971).

[5] M. D. Ventra, Y. V. Pershin, and L. O. Chua, Circuit elements with memory: Memristors, memcapacitors, and meminductors, Proc. IEEE **97**, 1717 (2009).

[6] Y. V. Pershin and M. D. Ventra, Memory effects in complex materials and nanoscale systems, Adv. Phys. **60**, 145 (2011).

[7] Z. B. Yan and J. M. Liu, Coexistence of high performance resistance and capacitance memory based on multilayered metal-oxide structures, Sci. Rep. **3**, 2482 (2013).

[8] H. Nieminen, V. Ermolov, K. Nybergh, S. Silanto, and T. Ryhänen, Microelectromechanical capacitors for RF applications, J. Micromech. Microeng. **12**, 177 (2002).

[9] I. Salaoru, Q. Li, A. Khiat, and T. Prodromakis, Coexistence of memory resistance and memory capacitance in TiO2 solid-state devices, Nanoscale Res. Lett. **9**, 552 (2014).

[10] Y. V. Pershin and M. D. Ventra, Memristive circuits simulate memcapacitors and meminductors, Electron. Lett. **46**, 517 (2010).

[11] J. Martinez-Rincon, M. Di Ventra, and Y. V. Pershin, Solid-state memcapacitive system with negative and diverging capacitance, Phys. Rev. B. **81**, 195430 (2010).

[12] Electrically Variable or Programmable Nonvolatile Capacitors, https://www.techbriefs.com/component/content/article/tb/techbriefs/electronics-and-computers/5773.

[13] J. F. Scott, *Ferroelectric Memories* (Springer, Berlin, New York, 2000).

[14] H. Ishiwara, M. Okuyama, and Y. Arimoto, Ferroelectric Random Access Memories: Fundamentals and Applications, Topics in Applied Physics Vol. 93 (Springer, Berlin, New York, 2004).

[15] P. Hou, J. Wang, X. Zhong, and Y. Wu, A ferroelectric memristor based on the migration of oxygen vacancies, RSC Adv. **6**, 54113 (2016).

[16] V. Garcia and M. Bibes, Ferroelectric tunnel junctions for information storage and processing, Nat. Commun. **5**, 4289 (2014).

[17] Z. Wen, C. Li, D. Wu, A. Li, and N. Ming, Ferroelectric-field-effect-enhanced electroresistance inmetal/ferroelectric/semiconductor tunnel junctions, Nat. Mater. **12**, 617 (2013).

[18] S. Boyn, J. Grollier, G. Lecerf, B. Xu, N. Locatelli, S. Fusil, S. Girod, C. Carrétéro, K. Garcia, S. Xavier, J. Tomas, L. Bellaiche, M. Bibes, A. Barthélémy, S. Saïghi, and V. Garcia, Learning through ferroelectric domain dynamics in solid-state synapses, Nat. Commun. **8**, 14736 (2017).

[19] A. Chanthbouala, V. Garcia, R. O. Cherifi, K. Bouzehouane, S. Fusil, X. Moya, S. Xavier, H. Yamada, C. Deranlot, N. D. Mathur, M. Bibes, A. Barthélémy, and J. Grollier, A ferroelectric memristor, Nat. Mater. **11**, 860 (2012).

[20] Y. Nishitani, Y. Kaneko, and M. Ueda, in 72nd Device Research Conference (IEEE, Santa Barbara, CA, USA, 2014), pp. 297–298.

[21] S. Horie, K. Noda, H. Yamada, K. Matsushige, K. Ishida, and S. Kuwajima, Flexible programmable logic gate using organic ferroelectric multilayer, Appl. Phys. Lett. **91**, 193506 (2007).

[22] W. Y. Kim, H.-D. Kim, T.-T. Kim, H.-S. Park, K. Lee, H. J. Choi, S. H. Lee, J. Son, N. Park, and B. Min, Graphene-ferroelectric meta devices for nonvolatile memory and reconfigurable logic-gate operations, Nat. Commun. **7**, 10429 (2016).

[23] M. Di Ventra and Y. V. Pershin, The parallel approach, Nat. Phys. **9**, 200 (2013).

[24] A.-G. Boni, L. Filip, C. Chirila, I. Pasuk, R. Negrea, I. Pintilie, and L. Pintilie, Multiple polarization states in symmetric ferroelectric heterostructures for multi-bit non-volatile memories, Nanoscale **9**, 19271 (2017).

[25] See Supplemental Material at http://link.aps.org/supplemental/10.1103/PhysRevApplied.12.024053 for descriptions on the materials and methods, electric and PFM measurements.

[26] C. Lichtensteiger, S. Fernandez-Pena, C. Weymann, P. Zubko, and J.-M. Triscone, Tuning of the depolarization field and nanodomain structure in ferroelectric thin films, Nano Lett. **14**, 4205 (2014).

[27] G. Liu, J. Chen, C. Lichtensteiger, J.-M. Triscone, P. Aguado-Puente, J. Junquera, and N. Valanoor, Positive effect of an internal depolarization field in ultrathin epitaxial ferroelectric films, Adv. Electron. Mater. **2**, 1500288 (2016).

[28] A. Ghosh, G. Koster, and G. Rijnders, Multistability in bistable ferroelectric materials toward adaptive applications, Adv. Funct. Mater. **26**, 5748 (2016).

[29] D. Zhao, I. Katsouras, K. Asadi, W. A. Groen, P. W. M. Blom, and D. M. de Leeuw, Retention of intermediate polarization states in ferroelectric materials enabling memories for multi-bit data storage, Appl. Phys. Lett. **108**, 232907 (2016).

[30] S. Ambrogio, P. Narayanan, H. Tsai, R. M. Shelby, I. Boybat, C. di Nolfo, S. Sidler, M. Giordano, M. Bodini, N. C. P. Farinha, B. Killeen, C. Cheng, Y. Jaoudi, and G. W. Burr, Equivalent-accuracy accelerated neural-network training using analogue memory, Nature **558**, 60 (2018).